Multi-modal Assessment of Myofascial Trigger Point Response to Osteopathic Manipulation in the Anterior Forearm

by

Chandhana Pedapati

A Dissertation Presented in Partial Fulfillment
of the Requirements for the Degree
Doctor of Philosophy

Approved March 2024 by the
Graduate Supervisory Committee:

Inder Raj S. Makin, Co-Chair
Jitendran Muthuswamy, Co-Chair
Vikram D. Kodibagkar
Christopher A. Buneo
Bruce Towe

ARIZONA STATE UNIVERSITY

May 2024

ABSTRACT

Work-related muscle disorders are a main cause of missed work, globally, and are costly for public health systems. However, development of musculoskeletal tissue diagnostics is lagging compared to other tissues and organs. Myofascial trigger points (MTP) are unique muscle tissue phenomenon that are challenging to address due to a lack of objective assessment methodology. This study seeks to meet this need by devising a non-invasive, objective methodology for evaluating musculoskeletal tissue following intervention or physical provocation, specific to the anterior forearm region. In Aim 1, current literature on MTP pathophysiology informs a multi-modal assessment approach, including: 1) pain pressure threshold (PPT), 2) power Doppler (PD) ultrasound, 3) strain elastography (SE), and 4) surface electromyography (sEMG). In Aim 2, controlled ultrasound image acquisition and standardization techniques are developed for imaging muscle tissue with PD (Aim 2a) and SE (Aim 2b) . These techniques improved differentiability of vascularity and compliance estimation after physical provocation or intervention. In Aim 3, the multi-modal approach is implemented in a human pilot study (n=34) investigating MTP response to osteopathic manipulative treatment, compared to rest and light exercise. Positive trends and significant changes are detected after OMT and rest. PPT significantly increased after OMT ($p = 0.021$). Tissue compliance significantly increase after rest ($p \ll 0.0001$) and after OMT($p = 0.002$). Principal component analysis finds 9 of 13 outcome measures to be salient features of MTP treatment effect. The data suggests high and low responders, yielding insights for improved patient screening and study design for future work. With further optimization and development, this method may be applied to a broad array of clinical scenarios for musculoskeletal tissue evaluation directed towards amelioration of neuromuscular symptoms.

ACKNOWLEDGEMENTS

I am grateful to my graduate committee members who supported my journey as a non-traditional graduate student at Arizona State University's School of Biological and Health Systems Engineering (ASU SBHSE) and as a research associate at A.T. Still University's School of Osteopathic Medicine in Mesa, Arizona (ATSU SOMA).

I am sincerely grateful for the invitation to collaborate in advancing objective evaluation in OMT research. I thank Dr. Makin and Dr. Heath for the opportunities to engage in osteopathic principles and practice education as an instructor and as a researcher. Dr. Deborah Heath has a visionary approach for integrating physiologic measurement into osteopathic practice. Dr. Makin generously provided laboratory resources, flexibility, and research opportunities. It has been an honor to contribute to this pioneering work.

Dr. Muthuswamy's constant encouragement, guidance, and willingness to champion my endeavors have been indispensable throughout this pursuit. My teaching practicum in Dr. Kodibagkar's challenging course cultivated a steadfast commitment to excellence and inspired me to strive for the highest standards. Dr. Towe's pragmatic, incisive, and impartial counsel at every stage of my doctoral journey strengthened my work with thoughtful consideration. Dr. Bueno's clear communication and calm guidance directed my inquiry towards impactful research. As the department chair, his approval to puruse my graduate studies was a significant endorsement. To Laura Hawes and Roberto Reynoso, your compassion and tireless efforts in navigating administrative processes have been invaluable.

Dr. Micheal Caplan's mentorship went above and beyond, from principle component analysis to guidance in finalizing my doctoral studies. You helped frame my work as a rigorous preliminary study serving to provide guidance for future work.

Dr. Douglas Mast's image and signal processing expertise has been essential. I aspire write code as elegant as yours. Dr. Curt Bay, your mentorship in statistical analysis refined my research conduct.

Dr. Kellie Huxel Bliven, your meticulous mentorship and unwavering support throughout the dissertation process can not be overstated. I am profoundly grateful for the opportunity to work with you.

I extend my gratitude to the Osteopathic physicians, fellows, and students, including William Erico, Dylan Kassenbrock, Timothy Durr, Weston Burrup, Breena Miller, Fego Galvan, and Drs. James Keane and Deborah Heath. Their insights into osteopathic principles were invaluable contributions to this research endeavor. My sincere appreciation goes to Dr. James Keane and Breena Miller for their assistance during the human participant study, especially during a period while I was injured.

The opportunity to study myofascial trigger points in women presents unique challenges. I extend my gratitude to the research participants who generously volunteered their forearms, a majority of whom were women.

I express my gratitude to Debra Loguda-Summers for her assistance in printing the transducer boots. To Ezer Lichtenstein, Geetha Pedapati, and Travis Tibbs, thank you for your contributions to the experimental setup.

Dr. Priya Yenebere, your insights into the broader implications of this research on medical practice and patient care are enlightening. I am grateful for your recognition of the value of my work and for your belief in me.

To my exemplary role models: my parents, Prakash J. Pedapati, MD, Pushpa Pedapati, MD, my sister's Anita, Jyothi, and Geetha, and Dr. Mani and Padma Venkata - thank you for being a cornerstone of strength and reassurance throughout this endeavor.

To Alan Carter, thank you for your friendship. As my sounding board, your

insights have enhanced the depth and quality of my work. Your strategic input were instrumental in navigating challenges and achieving success. Cheers!

To my son, Sanjai, no one worked harder than you. Despite facing numerous challenges, you have demonstrated remarkable composure, patience, and understanding. Witnessing your growth into the talented and poised young man you are today fills me with immense pride. Credit must be given where it's due, and you deserve recognition for naming the "transducer boot."

To my nephew and neice, Anish P. Venkata and Eira P. Lichtenstein, thank you for bringing such joy into my world and helping me remember what all this hard work is for.

TABLE OF CONTENTS

CHAPTER Page

CHAPTER Page

CHAPTER Page

LIST OF TABLES

Table Page

Table Page

LIST OF FIGURES

Figure Page

Figure Page

Figure Page

Figure Page

Chapter 1

INTRODUCTION

1.1 Context

The World Health Organization reports that work-related muscle disorders are a main cause of missed work, globally, and are a "considerable cost for the public health system" [175]. Muscle disorders arising from repetitive strain use, overloading and prolonged holding postures are frequently dismissed as pathological conditions largely due to their predominantly behavioral etiology and because work-related musculoskeletal tissue disorders are not typically considered life-threatening. This work delves into the unique muscle tissue phenomenon known as myofascial trigger points (MTP) that arise from work-related strain, and are characterized by muscle weakness, dysfunction, loss of range of motion and pain. Addressing these disorders leads to an improvement in quality of life, treatment directed towards the underlying mechanisms of pain, and a reduction the overall burden of cost to the public health systems.

1.2 MTP Diagnosis and Treatment

MTP present as symptomatic muscle tissue "knots" that are diagnosed with patient history and physical exam [8, 63]. During physical examination muscle weakness, loss of function and local and referred pain are assessed subjectively [148]. MTP are regularly misdiagnosed or under-diagnosed [8, 1] because they may mimic other pain conditions [8, 21, 11].

Two health care paradigms that address MTP are the allopathic and osteopathic medical practices. In allopathic medicine, MTP falls under the umbrella of myofascial

pain syndrome (MPS). MPS presents similarly to fibromyalgia, another pain condition that presents in musculoskeletal tissues, but does not include MTP as a symptom [1]. Management of MPS symptoms relies on pain management, postural modifications, physical therapy and strength training, and in severe cases, surgical interventions. Conversely, osteopathic manipulative medicine (OMM) recognizes MTP as a distinct pathology wherein diagnosis and treatment are accomplished in a holistic approach including manual (hands-on) treatments.

1.3 Problem Statement

The challenge with the allopathic approach to MTP treatment stems from the absence of a proven causal relationship between MTP and MPS [148]; MPS may arise without the presence of MTP and MTP may present without MPS. Both the allopathic and osteopathic approaches rely on subjective techniques for diagnosing MTP, i.e. physical exam and patient history. To date, no medical imaging or diagnostic test has been developed and approved for MTP evaluation [1]. OMT is clinically observed to alleviate pain and restore function in muscle tissue presenting with MTP, without the side effects of surgery and pain medications. However, there is low quality of evidence due to a low number and low quality of investigations [117].

Despite the paucity of evidence-based research, in 2012, more adults with musculoskeletal disorder sought alternative care/complementary medicine - such as acupuncture, chiropractic, OMM, and holistic medicine [32]. Between 2002-2012, adults with musculoskeletal disorders seeking complementary medicine increased the most among those without health insurance coverage [118]. These data point to a failure in allopathic medicine to address work-related muscle tissue disorders, and a strong pull towards alternative care.

In systematic reviews of MTP research, strong evidence supports the following: 1)"MTP and taut bands do exist and are indeed local areas of increased muscle stiffness" [107]. 2) Evidence of OMT efficacy is promising but evidence is limited due in part to low number of studies, low quality of studies, and non-standard outcome measures [117, 16]. 3) "There is a need for biomarkers to improve diagnosis and treatment assessment through objective means" [107]. While research on work-related musculoskeletal disorders such as MTP, and alternative and integrated treatments such as OMT exist, development of multi-modal, non-invasive, objective assessment methodologies are warranted. This thesis seeks to address the overarching need for first-order controlled studies that establish recommendations in study design and participant screening[148, 171, 107]. The motivation for this project is to improve the quality of evidence in muscle tissue investigation through the development of optimal research methodology.

Recently, efforts to support the development of musculoskeletal tissue diagnostics have grown among notable research entities including: National Center for Complementary and Integrative Health (NCCIH), the National Institute of Arthritis and Musculoskeletal and Skin Diseases (NIAMS), the National Institute of Biomedical Imaging and Bioengineering (NIBIB), the National Institute of Dental and Craniofacial Research (NIDCR), the National Institute of Neurological Disorders and Stroke (NINDS), and the Eunice Kennedy Shriver National Institute of Child Health and Human Development (NICHD), and the Helping to End Addiction Long-term (HEAL) initiative from the National Institutes of Health (NIH). Within these initiatives lies a specific effort towards developing quantitative imaging and relevant biomarkers for muscle tissue with MTP.

1.4 Project Overview

The work is directed towards devising quantitative methods for assessing muscle tissue characteristics that change as a function of pathology. The proposed method should be easily translatable to the clinic. This necessitates the use of non-invasive, minimally interrogative instruments. Given the limited understanding of the pathophysiology of MTP, investigating with multiple modalities may offer a comprehensive perspective to build experimental knowledge.

The forearm was selected for this proof-of-concept study because it is 1) easily accessible for ultrasonic and sEMG investigation, 2) there is a high prevalence of MTP in the anterior forearm in the general population [53, 52, 68], and 3) because the OMT procedures for MTP in the forearm are well established with empirical evidence of an expected response [73]. See Figure 1.1 describing the anatomical region examined throughout this study.

The multiple modalities include pressure algometry, diagnostic ultrasound imaging and surface electromyography (sEMG) for measuring measure pain pressure threshold, vascularity, tissue stiffness and myogenic activity. See Figure 1.2.

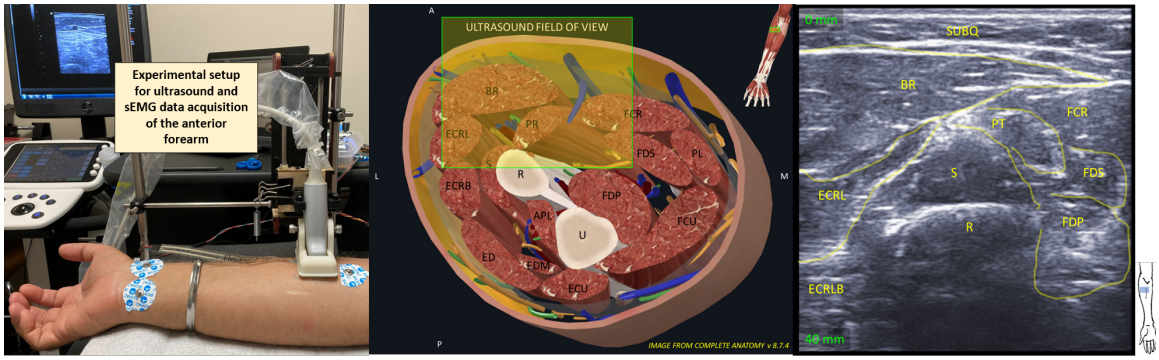

Figure 1.1: The anterior forearm selected as the anatomical region of interest in this study, (left) Controlled experimental setup, (middle) cross-sectional anatomy and (right) B-mode image of the anterior forearm. Structures (middle and right) are labeled as follows: structures labeled as follows:BR-brachioradialis, PR-pronator teres, FCR-flexor carpi radialis, FDS-flexor digitorium profundus, FCU-flexor carpi ulnaris, PL-palmaris longus, s-supinator, R-radius, U-ulna, APL-abductor pollicis longus, ECRL-extensor carpi radialis longus, ED-extensor digitorum minimus, ECU-extensor carpi ulnaris.

The proposed approach was distilled from the established of physical examination and palpatory findings, the current evidence of MTP pathology and the theoretical bases of OMT. The rational for using each modality in MTP assessment is summarized as follows:

- **Pain Pressure Threshold**: MTP are identified as painful nodules within taut bands of muscle tissue. The pressure algometer is a validated tool for assessing MTP pain and has been widely used in MTP literature [84, 101, 127]. This modality was included as an adjunct to the other modalities.

- **Vascularity Assessment:** Regional blood flow and interstitial tissue fluid changes are observed in MTP pathology throughout onset, progression and

healing processes [20, 147, 179]. Power Doppler ultrasound is used to image vascularity of the muscle tissue in the anterior forearm.

- **Tissue Compliance Estimate:** MTP are found within a taut band of muscle tissue [8, 21, 63]. Strain elastography (SE) estimates relative tissue stiffness differences by detecting motion of tissue upon application of a quasi-static pressure. SE estimates tissue elasticity (Young's modulus, E). However, in SE imaging, strain is estimated, but the stress applied is unknown. To better approximate Young's modulus, the stress applied during elastography imaging, or the tissue resistance, is estimated using a force sensitive resistor (FSR). Using the tissue resistance estimate (TRE) to scale the SE image, we obtain an estimate of tissue compliance (J), or the inverse of Young's Modulus.

- **Muscle fatigue:** Left unattended, MTP ultimately impact muscle function, contractility and endurance, but with proper care and therapeutic intervention these conditions are known to improve or even reverse [28, 63]. To evaluate the effect of OMT on MTP, the myogenic activity during a voluntary sustained hand grip (clench) is evaluated with surface electromyography (sEMG) and a clench force transducer. During a sustained hand grip muscles fatigue. Fatigue is characterized as increased sEMG amplitude and decreased muscle firing frequencies. The time to fatigue and spectral shift provide measures of endurance and fatigability, respectively.

The novelty of this work lies in the controlled experimental setup for ultrasound image acquisition, and in the ultrasound image (power Doppler and strain elastography) standardization techniques.

1.5 Specific Aims

This thesis comprises two main phases: development and implementation. Aims 1 and 2 are dedicated to the development phase, while Aim 3 focuses on the implementation in a human pilot study.

In the development phase, an in-depth comprehension of the pathology and symptom presentation of MTP delineates appropriate modalities for muscle tissue measurement (Aim 1). Chapter 2 contains a topical background on muscle anatomy and physiology of skeletal muscle tissue. Chapter 3 provides a Background on MTP pathology and a brief discussion of OMT and theoretical basis for efficacy using current state of research methods. The central hypothesis of this work is formulated from these chapters.

Hypothesis: The combination of algometry, regional blood flow, tissue compliance and myogenic activity provides insight into mechanical properties of musculoskeletal tissue that are quantifiable and clinically useful in assessing the effect of osteopathic manipulative treatment on myofascial trigger points in the forearm.

Figure 1.2 provides a flow diagram of the multi-modal approach.

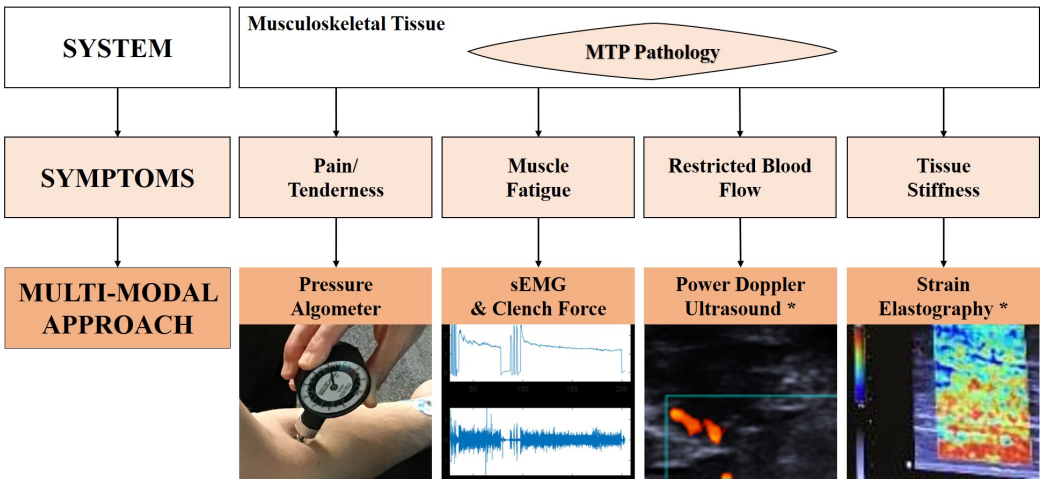

Figure 1.2: Flow diagram of the multi-modal approach for non-invasive, objective MTP assessment (Aim 1). *Novel technique development, see Figure 1.3 for description.

These ultrasound imaging modalities present inherent limitations for repeated-measures design study, specifically, image acquisition is user dependent and comparability before and after intervention or physiologic provocation is limited. Aim 2 seeks to mitigate these limitations by developing controlled experimental setups and establishing standardization techniques. In Aim 2a, power Doppler ultrasound images are standardized with area of detected flow and ultrasound optimization settings (Chapter 4). In Aim 2b, strain elastography is standardized with a measure of the stress applied to the tissue during SE imaging (Chapter 5). These methods are tested on phantoms and on human forearms. Their limitations for evaluating OMT treatment effect on MTP in the forearm are discussed. Figures 1.3, 1.4, and 1.5 depict flow charts outlining the experiments conducted in this bench-top development work.

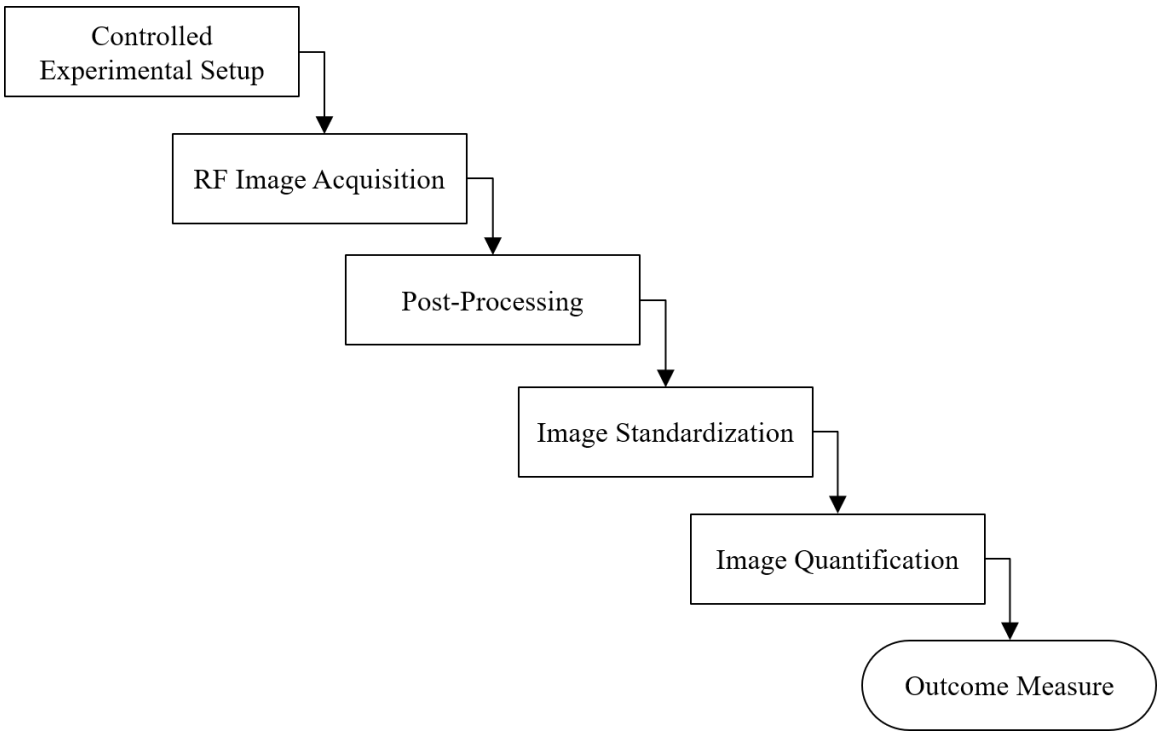

Figure 1.3: Process step for developing techniques for Regional Blood Flow (Aim 2a) and Tissue Compliance (Aim 2b) estimation.

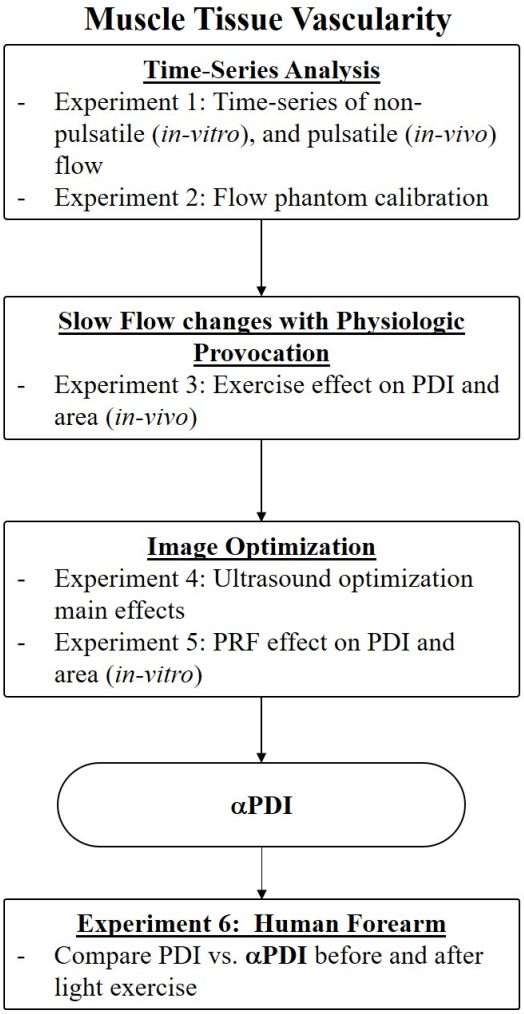

Figure 1.4: Flow diagram describing the technique for time-series analysis of power Doppler ultrasound images for regional blood flow estimation (Aim 2a). The scaled power Doppler outcome measure, αPDI is shown circled. PRF - pulse repetition frequency, PDI - power Doppler intensity

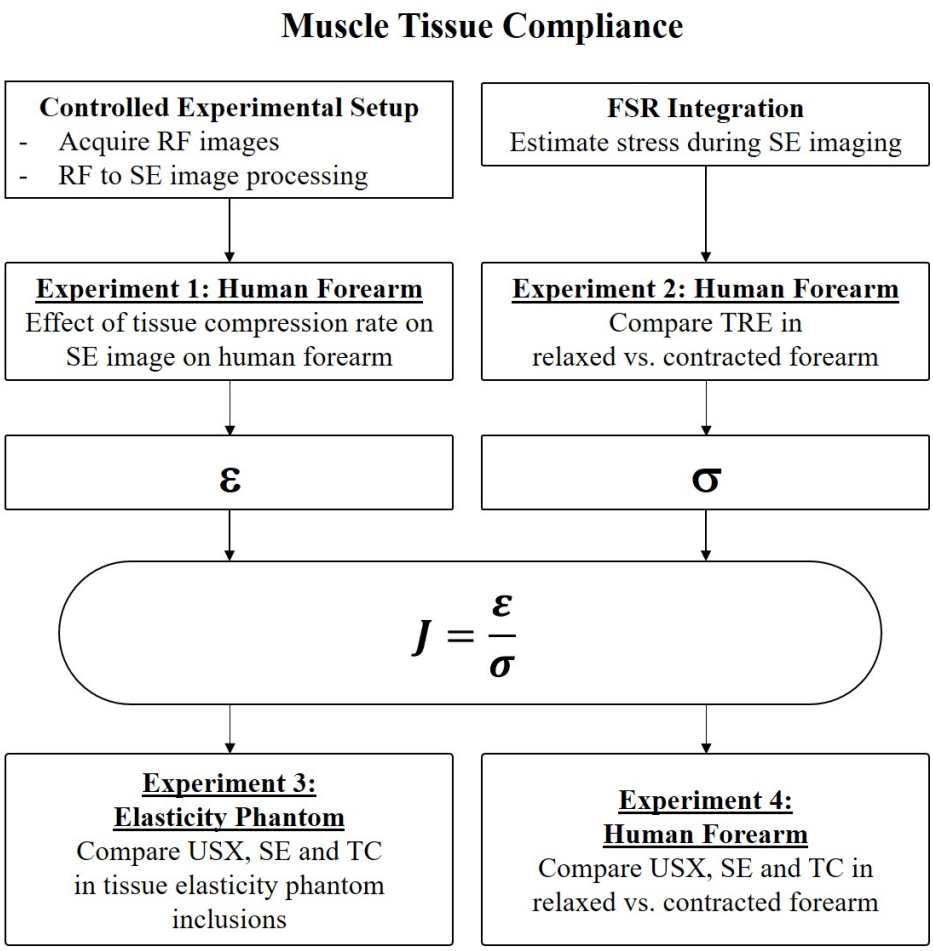

Figure 1.5: Flow diagram describing the development of the tissue compliance estimate (TC) (Aim 2b). The scaled SE, or tissue compliance (TC), J, is shown circled. Abbreviations are as follows: radiofrequency (RF) echo data, force sensitive resistor (FSR), tissue resistance (TR), strain (ε), stress (σ), tissue resistance estimate (TRE), Ultrasonix built-in strain elastography function (USX), strain elastography using basic normalized cross-correlation strain elastography (SE) method.

In Aim 3, the performance of the multi-modal approach is evaluated in a pilot human-subject study, where we assess the response of MTP in the anterior forearm to OMT, compared to rest and exercise (Chapter 6). Figure 1.6 depicts the study design. The four modalities used provides 13 outcome measures. Principal component analysis identifies 9 of the 13 parameters as salient features muscle tissue changes. Baseline values of the 9 parameters reveal possible responders and non-responders. The data suggests participant screening parameters that are likely to improve response for future investigations.

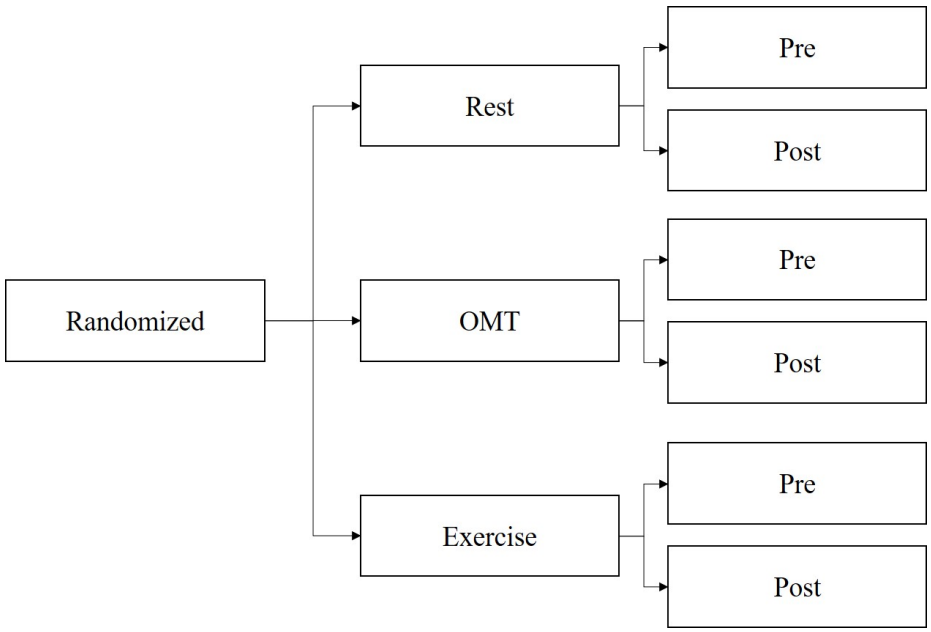

Figure 1.6: Comparative design for pilot human study (Aim 3).

The major contributions and overall impact of this research are provided in the final chapter (Chapter 7). This approach may apply to a broad array of clinical scenarios for musculoskeletal tissue evaluation including physical medicine, biomechanics, stroke rehabilitation, neuromuscular diseases, and therapeutic techniques directed towards amelioration of neuromuscular symptoms.

Chapter 2

SKELETAL MUSCLE

Skeletal muscle is a unique biological tissue that relies on highly coordinated neurological, vascular, structural (tissue morphology), biochemical and mechanical processes to produce dynamic (reflexive, rhythmic and voluntary locomotion), and static work (posture, balance) [122]. Alterations in these systems and their interactions result in dysfunction and disease states as well as healing and tissue regeneration. Constant demand (repetitive strain and overuse) predisposes skeletal muscle to microtrauma that leads to structural changes at the cellular level which cascade into functional disability observed in myofascial trigger point pathology (Chapter 3). This chapter provides a topical overview of skeletal muscle anatomy, describes mechanisms of contraction and support in healthy tissues as well as changes elicited by trauma, acute exercise and tissue regeneration. Table 2.1 lists four interconnected systems in muscle tissue and their major functions.

MUSCLE TISSUE	- Structure - Contraction/Relaxation - Tension - Force transmission - Energy storage/supply - Endocrine secretion
SOMATIC NERVOUS SYSTEM	- Neural signaling for motor control - Receive and process sensory information - Sympathetic innervation of vascular system - Sympathetic influence on biochemical expression - Regenerate tissues
VASCULATURE	- Support muscle metabolism - Maintain interstitial fluid biochemical homeostasis - Maintain nerve, myocyte and vascular tissue health - Maintain blood pressure - Regenerates tissues - Heat dissipation
CONNECTIVE TISSUE	- Contains and regulates biochemicals - Regulates response to internal and external stimuli - Supports muscle tissue structure - Regenerates tissues

Table 2.1: Overview of integrated systems of skeletal muscle tissue.

2.1 Anatomy

Force generation and movement is produced by both muscle contraction (contractile elements) and force transmission (connective tissues). The contractile components of muscle tissue include extrafusal (motor) and intrafusal fibers (muscle spindle). The non-contractile tissues, connective tissues and tendons, provide structural support and contribute to tissue regeneration [122].

2.1.1 Muscle fibers

Extrafusal fibers form the bulk of the muscle fiber, contracting on demand, generating force and movement. Mostly non-contractile with contractile ends, the intrafusal fibers wrap around the extrafusal fibers in fusiform shape acting as sensory elements. Intrafusal fibers detect muscle stretch and communicating this signal to the central nervous system (CNS) via gamma-motor neurons. The ends of muscle fibers attach to tendons and aponeuroses, which are thick collagen connective tissues distributing tension, generating a passive force and providing sensory information to the CNS for proprioception via Golgi tendon organs. The interplay between the extrafusal and intrafusal fibers forms a range of movement from smooth wide sweeping motion to quick reflexive guarded maneuvers. Pathological states can be detected by characterizing motion abnormalities, i.e., reduced range of motion or slow reflexes.

Extrafusal Fibers

The muscle tissue is composed of a hierarchy of fibril structures bundled in parallel arrangements by membranes. The smallest contractile unit of muscle tissue is the sarcomere. Sarcomeres are formed from myosin and actin myofilaments, Figure 2.1. Myosin, an anisotropic protein, is a thick filament with a tail, neck and

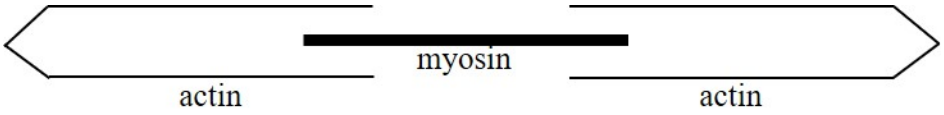

Figure 2.1: Arrangement of actin and myosin in sarcomere

head. Actin, an isotropic protein, is a thin filament composed of globular proteins held in helical chains, called tropomyosin, and a three-part protein complex called troponin. Troponin-I, troponin-T, and troponin-C regulate actin, tropomyosin and calcium binding, respectively.

Chains of sarcomerers form myofibrils. The myofibril is further divisible by the characteristic arrangement of the myofilaments into A- and I-bands, referring to the anisotropic and isotropic regions. A-bands contain the myosin and actin, appear darker and shorten during muscle contraction. The I-band contains no myosin, appear lighter, and the length remains unchanged during contraction. Actin filaments anchor on a dark line in the middle of the I-band, called the Z-line. Connectin, thin, elastic fibers anchor myosin to Z-lines, maintain the alignment of actin and myosin and provide a restoring force when muscles are passively stretched [88]. The region between two Z-lines forms the sarcomere, the smallest functional unit of muscle.

The muscle fiber, myofiber, or myocyte, is the multinucleated cell. The myocyte is composed of thousands of myofibris. It is filled with sarcoplasm and surrounded by the sarcoplasmic reticulum that stores calcium ions for triggering muscle contraction. A plasma membrane surrounding the myocte forms the sarcolemma. The sarcoplasmic reticulum and a portion of the sarcolema called the T-Tubule, form the triad, which exchanges ions to transmits action potentials (AP). Each myocyte contains mitochondria and lipids which provide energy to the cell [124] and cytoskeletal proteins which provide structural support and regenerate muscle tissue, among other functions [27, 26]. Proper muscle contraction or various disease states are dictated by

the myocyte structure, the mitochondria shape and quantity, lipid distribution in the myocyte, and cytoskeletal morphology [183, 24, 77, 78]. The myocyte is further encased in a collagen layer of connective tissue, called the endomysium, that distributes tension.

Bundles of muscle fibers, encased in endomysium, form fascicles. Bundles of fascicles encased in perimysium form the muscle. The muscle at large is encased in epimysium.

Intrafusal Fibers

Intrafusal fibers have non-contractile centers and contractile endings. They sense fiber length change and rate of length change [91]. Three types of intrafusal fibers - nuclear chain and nuclear bag static and nuclear bag dynamic - combine to form the muscle spindle. There are about 2-3 nuclear bag fibers and about 5 nuclear chain fibers per muscle spindle [51]. The intrafusal fibers contribute to the spinal reflex, a behavior produced pathways contained within the spinal cord via interneurons. Muscle spindle activation increases tension in the skeletal muscle [128].

Muscle fiber types

There are different types of muscle fibers, Type I and IIa, IIb IIx and hybrids, which have different functions. Type I are slow twitch, red muscle fibers, that have less contractile force and slower force production rate. These fibers maintain low tension for long periods of time without energy loss due to the large number of mitochondria and capillaries which fuel fatigue-resistance with oxidative enzymes and myoglobin. Type II are fast twitch, white muscle fibers, whose myosin protein produces force at rapid shortening velocities. Type II fibers further classify into fast fatigue-resistant, IIA, fast fatigable, IIB, and IIx and hybrids. Type IIA have an aerobic capacity to

resist fatigue for several minutes. Type IIB fatigue quickly due to large stores of glycogen phosphorylate ADP and lactic acid production. These fibers deplete energy, build up waste inducing fatigue and require long recovery time[18, 130].

2.1.2 Neural Organization

Skeletal muscle is the only tissue type under voluntary (somatic) control although it is subject to autonomic regulation (sympathetic and parasympathetic neurotransmitters). The somatic nervous system further divides into the sensory (vision, hearing, touch, taste, smell, balance and visceral sensation, perception, interoception), and somatosensory (thermoception, proprioception, nociception) systems which are organized in a hierarchy to receive and interpret sensory information and achieve motor control [3]. At the top of the hierarchy lies the cortex and brain stem wherein the dorsolateral frontal cortex drives the purpose of movement, the posterior and parietal premotor areas forms a motor plan and is responsible for proprioception, the cerebellum and basal ganglia and thalamus coordinate input and output between the cortex and brain stem [122]. The motor circuits within the spinal cord execute the plan using afferent neurons (sensory), efferent neurons (motor) and interneurons.

Afferent nerves bring sensory input from the periphery (muscle, connective tissues, vasculature, and skin) to the CNS. Efferent nerves bring control signals from the CNS to the muscles. Sensory and motor neuron cell bodies lie within the gray matter of the spinal cord and brain stem, and their axons exit the spinal cord on the dorsal and ventral roots, respectively [88]. Axons of the upper motor neuron exit the ventral root of the spinal cord and join sensory nerve axons entering at the same intervertebral foramen to form the spinal nerve. A group of muscles innervated by a single spinal nerve root forms a myotome. The sensory neurons include proprioceptors, mechanoreceptors nociceptors and thermoceptors [92]. The lower motor neuron,

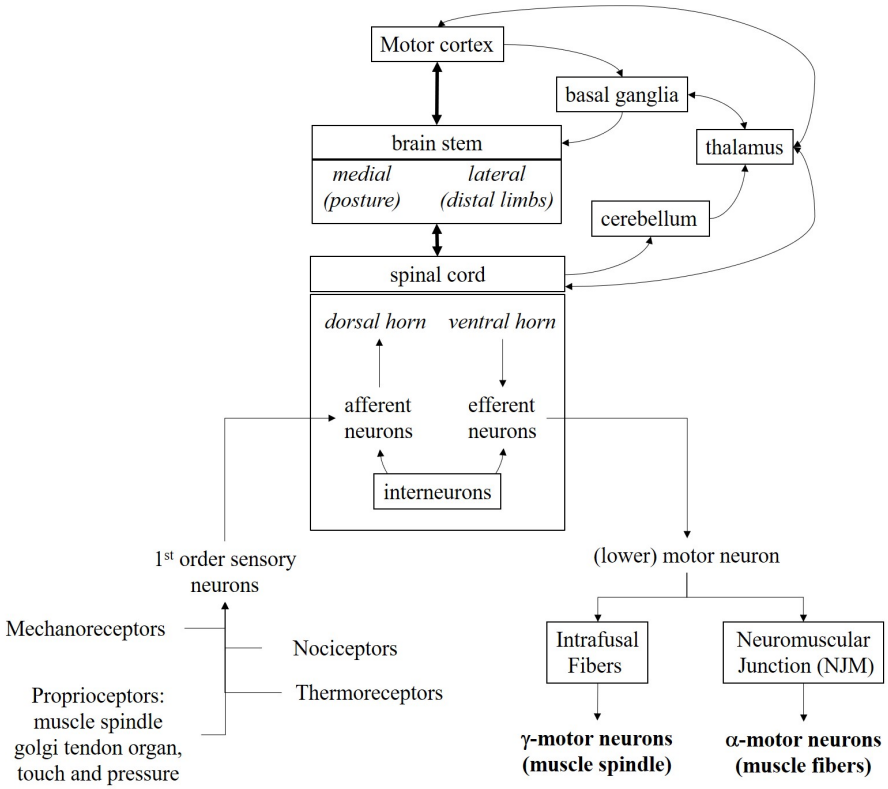

Figure 2.2: Flow diagram describing neural organization of the somatic nervous system from the cortex to the motor and sensory neurons in skeletal muscle.

α-motoneuron, traverses from the spinal cord to the neuromuscular junction (NMJ) innervating the muscle fibers. A single motor neuron innervates multiple muscle fibers within a muscle to form a motor unit. Figure 2.2 provides a flow diagram of the neural organization.

Neural Innervation

The extrafusal fibers are innervated by α-motor neurons transmitting action potentials (AP) which elicit muscle contraction, and the intrafusal fibers are innervated by γ-motor neurons, transmitting muscle spindle length and rate of length change [88]. Interneurons located within the spinal cord modulate signals from sensory neu-

rons to brain, form brain to motor neurons and from motor-to-motor neural pathways. Type Ia, the primary afferent nerve, has stretch activated channels, and increases or decreases firing rate when stretched or shortened, respectively. The primary afferent nerve coactivates with the α-motoneuron to resist changes in muscle length, such as with the myotatic reflex (knee-jerk reflex), however this is overridden during voluntary movement. Type IIa, the secondary afferent nerve, is a medium myelinated and slower to respond, and is found on the nucleated chain fiber and nuclear bag static fibers only, and communicates information about the static length of muscle.

Henneman's size principle

Motor neurons size and length vary with fiber types that they innervate. Small motor neurons innervate fewer muscle fibers, activating smaller motor units to generate less force. Larger motor neurons innervate a greater number of muscle fibers, activating larger motor units to generate greater force. Henneman's size principle relates the motor neuron size with motor unit recruitment order and other electrophysiological properties of motor neurons [76, 108, 22]. Three major fiber types are Type I, Type IIa and Type IIb. Motor neurons of Type I are thinner and innervate fewer muscle fibers and have lower force generating capabilities. The motor neurons of Type IIA have intermediate cell bodies and thicker axon to generate intermediate velocity, while those for Type IIB have large cell bodies and thicker axon to generate high velocity action potentials.

In order to produce a required amount of force while minimizing fatigue, muscles are recruited in order from weakest to strongest, i.e. starting with slow twitch fibers, then fast fatigue-resistant and finally fast fatigable, and by conduction velocity, slowest to fastest. As the muscles fatigue, force production drops and conduction velocity slows. The fiber types also drop out in the opposite order, from strongest to

weakest. order of recruitment is from slowest to fast, and derecruitment from fastest to slowest. The slow twitch fibers are the last to drop out. [108, 76, 22]. Fatigue is also observed as a decrease in action potential frequency seen in the electromyogram spectrum [66, 6, 39].

2.1.3 Vasculature

Due to its large mass, skeletal muscle receives 25% of cardiac output at rest [93]. The wide ranging metabolic requirements of skeletal muscle are met by a highly coordinated vasoregulatory mechanisms varying blood supply at rest (5-10 ml/min/100g) to strenuous activity (80-100 ml/min/100g) while maintaining blood pressure[93, 4]. Consequently, adverse alterations in the percent of cardiac output directed towards skeletal muscle, blood vessel structure and function, vascular resistance, and microvacsular exchange properties contribute to muscle tissue dysfunction and pathology. Figure 2.3 illustrates the vascular branching within skeletal muscle, from the primary arteries. The primary arteries are the last branch of arterial supply before tissue entry into the microvascular unit (group of capillaries perfused by a terminal arteriole). The microvascular unit is the smallest functional unit for blood flow regulation, where fluid filtration to skeletal muscle occurs [93, 130].

Several interconnected capillaries surround each muscle fiber in a highly variable array, where the density and number of interconnections of capillaries are greater in oxidative muscle (fatigue-resistant), Type I and IIa, than anaerobic muscle (fatigueable), Type IIb. Lymphatic vessels in skeletal muscle begin as endothelial tubes adjacent to post-capillary venules which penetrate the perimysium to connect to larger lymph vessels [83]. Lacking smooth muscle, non-contractile lymph vessels rely on muscle movement and arteriole pulsation for fluid propagation [93].

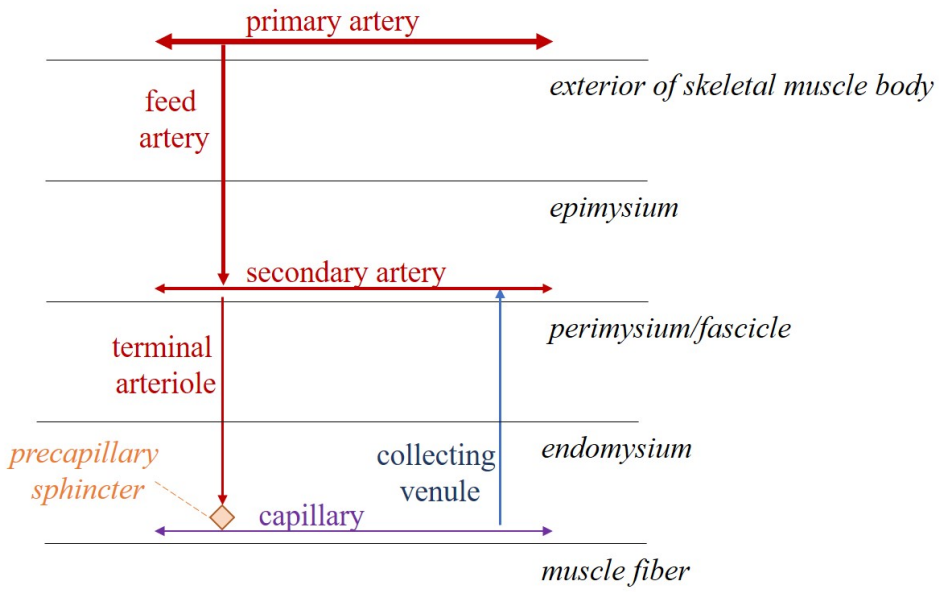

Figure 2.3: Flow diagram of vasculature branches supplying blood to skeletal muscle.

2.1.4 Connective tissue

A variety of connective tissue cells play a vital role in structural maintenance, force transmission, tissue regeneration and maintenance of homeostasis in skeletal muscle. Among these connective tissue cells are fibroblasts, myofibroblasts and myoblasts. These produce extracellular matrix (ECM) and collagen [122, 164].

Fibroblasts reside within the collagen fibers of the ECM where they secrete collagen and other molecules for regenerating muscle tissue [122]. Myofiberblasts are activated fibroblasts that are contractile, found in would healing, for example, [142]. The myoblast is a precursor cell that differentiates to give rise to muscle cells. This is accomplished by myoblasts fusing to form myotubes that will mature into myofibers [26].

ECM is 70% water and 30% solids (collagen, ground substance and elastin), however the composition varies by structure depending on the function. Tendons and

ligaments are generally composed of 75-80% extracellular matrix and 25-20% cells (fibroblasts) [27]. Tendon in extremities, however may have up to 99% collagen content in the solids of ECM [122]. The epi-, peri- and endomysium around the muscle are formed from varying compositions of ECM constituents. ECM also surrounds the muscle fibers and fascicles. Collagen is synthesized by fibroblasts and cross-linked to form microfibril structures which provide support and transmit forces. The newly formed collagen is soluble in acidic and neutral salt-solutions and the cross-links are easily denatured by heat. Mature collagen has longer chains and fewer cross-links, and is not easily denatured - not soluble in acidic or neutral salt solutions and can withstand higher temperatures before denaturing [122].

2.2 Mechanisms

2.2.1 Muscle contraction

Muscle contraction is initiated by an action potential (AP) from the upper motor neuron (brain to spinal column) the with the process steps as follows:

1. AP travels from the upper motor neuron to lower motor neuron and ends at the neuromuscular junction (NMJ).

2. Vesicles containing acetylcholine (ACh) are released into the synaptic space.

3. ACh binds to the nicotinic-M receptors in post-synaptic cleft, or the motor endplate, opening channels in the sarcolemma.

4. AcH triggers potassium ions (K^+) to exit the muscle cell and a greater amount of sodium ions (Na^+) stored in the sarcolemma to enter the muscle cell, causing a potential difference in electric charge across the cell membrane. The (Na^+) -(K^+) pump is vital for a) maintaining cell membrane potential gradient to

achieve a) a resting potential, b) AP propagation and for c) achieving excitation contraction coupling (ECC). The (Na^+) -(K^+) pump dysfunction impacts muscle contractility [33].

5. When the critical amount of sodium ion (Na+) conductance is reached the sarcolemma depolarizes in all directions.

6. Excitation-contraction coupling (ECC). The AP from the sarcolemma travels along the T-tubules, which connecting the sarcolemma to the sarcoplasmic reticulum, causing the sarcoplasmic reticulum to also depolarize. The ECC is the process whereby electrical activity is converted to force generation. ECC latency has been linked to pathology and muscle weakness [18]. ECC amplitude depends on the Na+ channel dynamics. The latency of this AP depends on the speed of the depolarization [18].

7. The ECC opens dihydropyridine (DHP) channels in the sarcoplasmic reticulum. The small electrical potential of the sarcoplasmic reticulum is called the intramembranous charge movement [18].

8. The DHP channels open ryanodine receptors, producing an influx of calcium ions (Ca^{2+}) from the sarcoplasmic reticulum into the cytosol.

9. The influx of Ca^{2+} produces sarcomere contraction, explained by the sliding filament hypothesis. When myofilaments, myosin and actin, slide past each other in a cross-bridge cycle, the sarcomeres shorten and ultimately contracts the muscle at large. The cross-bridge cycle initiates with the influx of Ca^{2+}.

10. Ca^{2+} binds to troponin-C, displacing the tropomyosin off of actin.

11. ATP binds to the myosin head.

12. The enzyme ATPase in the myosin head hydrolyzes ATP into adenosine diphosphate (ADP) and inorganic phosphate (Pi).

13. Energy released during ATP hydrolysis pivots the myosin head in a cocked-back position, leaving it available to bind to a new actin site.

14. The myosin head binds to the exposed actin site in a cross-bridge.

15. The release of Pi causes the myosin head to pivot, pulling the actin filament in a power stroke.

16. ADP releases from the myosin head.

17. Myosin head is still attached to actin in a state known as rigor.

18. A new ATP molecule binds to myosin in order to release it from the actin protein, returning it to the original position, completing the cross-bridge cycle.

19. The enzyme acetylcholinesterase (AChE) hydrolyzes ACh into acetate and choline. This inhibits further signaling at the sarcolemma. If ACh remains in the synaptic cleft, the cell membrane will continue to signal [168].

As this cycle repeats the myosin and actin filaments slid together, shortening the A-bands which shortens the sarcomere, and ultimately contracting the muscle. This process occurs as long as Ca^{2+} ions are present and bound to troponin-C [131].

Resting Tone

When muscle relaxes Ca^{2+} returns to the sarcoplasmic reticulum storage for future use [131]. Some fibers remain contracted in order to create resting muscle tone [67]. The muscle spindle and Golgi tendon reflexes participate in maintaining resting tone.

MEPP

If ACh remains in the pre-synaptic cleft, if for example, not hydrolyzed by AChe, it will continue to produce APs stimulating small muscle contractions, called miniature endplate potential (MEPP) [18]. MEPP frequency increases with temperature, depolarization of motor nerve terminal and calcium availability. MEPP amplitude relies on the number of ACh molecules available in vesicles, ACh receptor sensitivity, as well as endplate structure [18]. MEPP is below the needed threshold for depolarization of the nerve ending to initiate complete muscle contraction. MEPP have been measured to be about 3%of EPP, and is not detected with denervation or with anesthetics, suggesting central activity.

Force generation

Force is produced from muscle fiber activation level, length and velocity [88], and passive tension from the non-contractile elements.

The force generated is a result of persistent release of Ca^{2+} from the triad (a structure formed by the T-tubule and sarcolemma), enabling a higher frequency of action potentials leading to continuous activation of cross bridges.

Muscles have an optimal length-to-tension ratio. The strength of contraction or tension grows as a muscle approaches optimal length. If a muscle is stretched beyond optimal length no force can be generated, or no tension in the muscle fiber exists. This relationship between length and tension occurs as a result of the sarcomere length, or amount of overlap between the myosin and actin filament and length of the titin fiber, a protein that stabilizes myosin and prevents over stretching and recoils the muscle fiber when contracting. If the myosin and actin filaments are stretched apart with no overlap, no force can be generated. If myosin and actin overlap completely,

there is no room to pull the z-disks, the junction between two scarcomeres, together no more force can be generated.

With active lengthening of the muscle, actin rips away from cross-bridges without the ATP biding, or without consuming energy. Myosin then automatically binds to actin continually contributing to the contraction, resisting stretch of the muscle regardless of stretch velocity.

The contraction velocity (sarcomere shortening) contributes to force generation as well. The contraction velocity of the cross-bridges is proportional to the energy consumed by the muscle. The faster the sarcomere shortens, the less force can be produced, because the fiber length is decreasing.

Passive tension is produced by the non-contractile elements – tendons, aponeuroses, z-disks, connectin and endomysia [88]. When these constituents are compromised with cell damage, force production and contractility suffer [33]

Contraction and relaxation time

During contraction, muscle fibers are stimulated in patterns. While some fibers contract while other fibers recover, the muscle as a whole may maintain a longer contraction. This prevents fatigue, uses energy efficiently and generates smooth movement [67]. Skeletal muscles work in agonist and antagonist groups made possible by the spinal reflexes. Coactivation of agonist and antagonistic muscle groups provides stability. Any misstep in this complex process may result in fatigue, inefficiency, or dysfunctional motion.

2.2.2 Vasoregulation

Vascular resistance is inversely proportional to the 4^{th} power of the vessel radius; small changes in vessel diameter result in large blood flow changes [93]. Vasomotor

control mechanisms lie within the two major types of cells in the blood vessel walls - vascular smooth muscle and endothelial cells. The veasomotor control mechanisms are divided into central (neural, humoral) and local drivers (metabolic, mechanical, endothelial, paracrine). Baroreceptors are low pressure stretch-sensitive mechanoreceptors that communicate vessel distention and heart rate to the autonomic nervous system. Increases in blood pressure increase the barroreceptor firing rate [12].

Vasodilation also results from elevated blood flow inducing shear-stress on the vascular wall. This effect is independent of vascular pressure or vasodilator responses. Mechanoreceptors in the endothelial wall detect shear-stresses, releasing epoxyeicosatrienoic acids, which diffuse to vascular smooth muscle cells, inducing vasodilation.

Central drivers

Release of Ca^{2+} from the sarcoplasmic reticulum into the cytoplasm activates myosin-actin cross-bridge cycling of vascular smooth muscles as well. This contraction results in vasoconstriction. Constriction or relaxation of the vascular smooth muscles are a function of the level of Ca^{2+} present in the cytoplasm. Vasoactive factors like prostacyclin (PGI_2), nitric oxide (NO), carbon monoxide (CO), and hydrogen sulfide (H_2S), are among the endothelium-derived factors that modulate vascular smooth muscle tone. Vasoactive facturs modulate the cytosolic concentration of and sensitivity of proteins to Ca^{2+} by altering cell membrane receptivity (depolarization and hyperpolarization by altering gating of potassium channels).

Endothelial cell functions include modulating vascular permeability, inflammation, homeostasis, vascular growth, cell migration, forming and interacting with ECM, lipid metabolism and vasomotion (regulating blood flow). The endothelium detects both internal and external chemical and mechanical changes, and responds by releasing

substances or generating electrical signals which modulate blood vessel structure.

Biochemicals released during exercise and trauma activate endothelial nitric oxide synthase (eNOS) resulting in vasodilation. Biochemicals activated by pressure (form exercise or trauma) include adenosine, acetylcholine, and norepinephrine. Biochemicals released during inflammatory/pain processes include inflammatory peptides, bradykinin, calcitonin gene-related peptide (CGRP) and substance-P.

Local drivers

Local processes including 1) myogenic regulation, 2) metabolic control, 3) flow/shear stress-induced vasodilation, 4) neural signal conducted vasomotor responses control vessel tone.

Myogenic regulation. Besides vascular controls, muscles can also induce vasomotion, referred to as myogenic regulation. Pressure against the vessel can cause vasoconstrction, relaxation can cause vasodilation.

Metabolic Control. Contracting skeletal muscle produces vasodilator byproducts such as hydrogen peroxide (H_2O_2), which diffuse from myocyte to arteriole. Increased metabolite concentration induces vasodilation, relaxing terminal arterioles. In order to maintain homeostasis, capillaries are recruited to 1) increase the surface area of metabolite diffusion, and 2) to increase blood supply to meet oxygen demand of the active muscles. As muscle activity decreases the hyperemic state sustains until metabolite concentration washes out from the interstitium. The absence of vasodilators results in derecruiting capillaries and restoring vascular flow to a lower level.

The extracellular matrix (ECM) surrounding tissue and vascular cells may also influence vasomotion depending on the binding proteins. The juxtaposition of proteins adjust and interact during muscle contraction. Interestingly, fibrocenection may support hyperemia during muscle contraction, as NO, a vasodilator, is produced when

ECM experiences tensile force from muscle contraction [93].

Flow/Shear stress. Blood flow exerts shear stress against the blood vessel, inducing vasodilation. As arterioles dilate, blood flow through capillaries increases, thereby increasing venous return. To compensate for the increased preload to the right side of the heart, the left side of the heart must match cardiac output thereby augmenting arterial supply in larger vessels.

Blood vessels are sympathetically regulated. Sympathetically modulated adrenergic receptors produce vasoconstriction by norepinephrine. Reducing sympathetic tone causes vasodilation in skeletal muscle.

2.2.3 Cytoskeletal proteins

Mutations in cytoskeletal proteins underlie dysfunction and disease in muscle tissues. Desmin is a well studied intermediate filament protein that, among many functions, connects adjacent myofibrils and connects the sarcolemma to the myofibrils. With mechanical stress, it is hypothesized that force transmission within the myocyte is compromised due to disruption of desmin. Titin, or connectin, is the largest protein in the human genome, spans half the length of the sarcomere, and has been found to support a number of functions including structural integrity, force transmission, mechanical sensing and reflex. Muscle weakness has been characterized by mutations in titin. Dystrophin-associated glycoprotein complex (DGC) connects the sarcolemma to the endomysium and the myofibril cytoskeleton to the ECM [26]. Myopathies such as Duchenne muscular dystrophy and Becker muscular dystrophy result from the complete or partial depletion of dystrophin, the major component of DGC [74]. A growing body of evidence suggests that these supportive elements contribute to normal function of muscle and that pathological alterations reflect the status of those elements. The role of myofibroblasts in fascial tissues have been implicate in

muscle tissue support as well as myoneural coordination [142]. This study, [142], suggested that the contractility of the fascial tissues contributes to "tissue contractures and matrix remodeling" which impact proprioception, coordination and contribute risk of injury [142].

2.2.4 Damage and Regeneration

Muscle damage from trauma or acute exercise elicits an inflammatory response. Excessive damage requires therapeutic intervention for eliciting wound healing responses [184]. Mechanisms of trauma, acute exercise and tissue regeneration are described.

Trauma

Injury occurs when myofibrils are stretched or contracted to the point of compromising cell integrity. Disrupted sarcoplasmic reticulum and transverse tubules increases extracellular calcium concentration, while damage to myofibrils release inflammatory markers such as substance P, mytokines (cytokines within skeletal muscle)[4]. These alterations activate proteases and hydrolases which further damage myofibers [27]. Endothelial-satellite cell niche disruption dysregulates blood flow, causing hypoxia and apoptosis. Trauma, external compression, also activates fibroblasts to produce ECM [27]. Chronic fibroblast activation causes fibro/adipogenic progenitor (FAP) cells to rapidly differentiate upon injury, producing fibrotic and fatty tissues, which present clinically as loss of range of motion and weakness [27].

Static-stretching has been shown to cause fascial tissues hardening through connective tissues (fibroblasts, myoblasts and myofibroblast) activity as well as fluid content changes at the cellular level [141, 102]. *In vivo* studies reported that when the cell is compressed [102] or stretched [141] fluid content within the cell reduces,

and increases more than baseline after rest. The amount of fluid exchange is related to the rate and magnitude of compression or stretch. The immediate impact of increased fluid content was found to be a temporary increase in fascial tissue stiffness [141].

Acute Exercise

Acute exercise increases skeletal muscle metabolism [4], increases core body temperature [93], increases glucose uptake independent of insulin [140], and modulates vasomotion and inflammatory processes (resulting from mitochondria uncoupling) [4]. Exercise hyperemia occurs via local and central regulation. Pressure induced response reduces vascular wall tension by an unknown mechanism, resulting in vasodilation [93].

After an acute bout of exercise there is an increase nitric oxide expression through shear wave flow in endothelial cells [99], which can stimulates glucose transport [140] and increase tissue stiffness [35].

It has been suggested that extramuscular connective tissues, epimysium and deep fascia, increase in thickness after eccentric exercise due to tissue inflammation and collagen breakdown leading to edema. Restriction in gliding between deep fascia and muscle may result in mobility issues and pain [167]. Fascial tissues are also able to contract via myofibroblasts, directly contributing to motion [142]. Myofibroblasts are able to sustain contraction for a long duration. Combined with ECM collagen expression, myofibroblasts stiffens tissues and may lead to muscle contractures [142].

Tissue Regeneration

Skeletal muscle is able to regenerate following trauma, which have been summarized in three phases [130]: 1) degeneration of myofibers, capillary fragmentation

and inflammation, 2) regeneration of myofibers and microvasculature, 3) remodeling/maturation of myofibers and reorganization of microvasculature.

Satellite cells in muscle tissue generate myotubules which form new myofibers [10]. Regeneration of myofibers and their vasculature also involves endothelial cells, immune cells (neutrophils and macrophages) and FAP cells.

Satellite cells located below the endomysium (basal lamina) and close to capillaries support angiomyogenesis, and endothelial cells that are close to satellite cells proliferate after injury and initiate regeneration of myofibers [130].

Fibroblasts organize the proteins into fibrillar structures of ECM and along with satellite cells may regenerate skeletal muscle [27]. The FAP cells differentiate into fibroblasts or adipocytes to promote muscle regeneration [27]. Necrotic tissues initiate an immune response of macrophages and neutrophils [4].

The function of nitric oxide (NO) in skeletal muscle is ubiquitous. Its various forms contribute to muscle metabolism, ECC, immunity, tissue regeneration, and neural signaling [99, 10]. NO 1) protects endothelial cells that participate in tissue repair and angiogenesis [99], 2) alters mitochondria Ca^{2+} uptake to make it more energy efficient, 3) enhances insulin sensitivity and stimulates glucose oxidation, reducing oxidative stress, 4) prevents proinflammatory cytokines activation and mediates satellite cells post injury. These mechanisms protect skeletal muscle cells and endothelium from constant insult [99, 10].

Chapter 3

MYOFASCIAL TRIGGER POINTS

3.1 Introduction

Myofascial trigger points (MTP) are discrete, hyperirritable, palpable nodules found in a taut band of muscle tissue [155]. Chronic MTP weakens muscles, reduces range of motion, causes debilitation and refers pain down related muscles. Documentation of MTP has been found as early as the 1500's [148], yet, the pathophysiology is still not well understood. Consensus on diagnostic criteria and etiology is still not fully established, rather these exist as widely accepted paradigms. Developing an objective evaluation method for MTP treatment response requires an understanding of the underlying mechanisms of the pathology itself.

Three major hypotheses of MTP formation are described - 1) the Cinderella Hypothesis, 2) the integrated trigger point hypothesis and 3) the neurogenic/neurophysiologic hypothesis. These hypotheses have areas of disagreement. The areas of overlap among these hypotheses were used in the development of the approach used in this study. Current MTP pathophysiology research focuses on the fundamental mechanisms of muscle tissue biochemical interaction, neurophysiology and ultrastructural components - myocyte, mitochondria, membranes, fibroblasts and myoblasts. A full understanding of the fundamental mechanisms may provide insight into MTP formation and inactivation. Figure 3.1 provides a schematic diagram of MTP clinical profile and the underlying functions involved. This chapter provides a brief history of MTP research. Evidence of the internal functions and ultrastructural alterations in MTP pathology are summarized in this chapter.

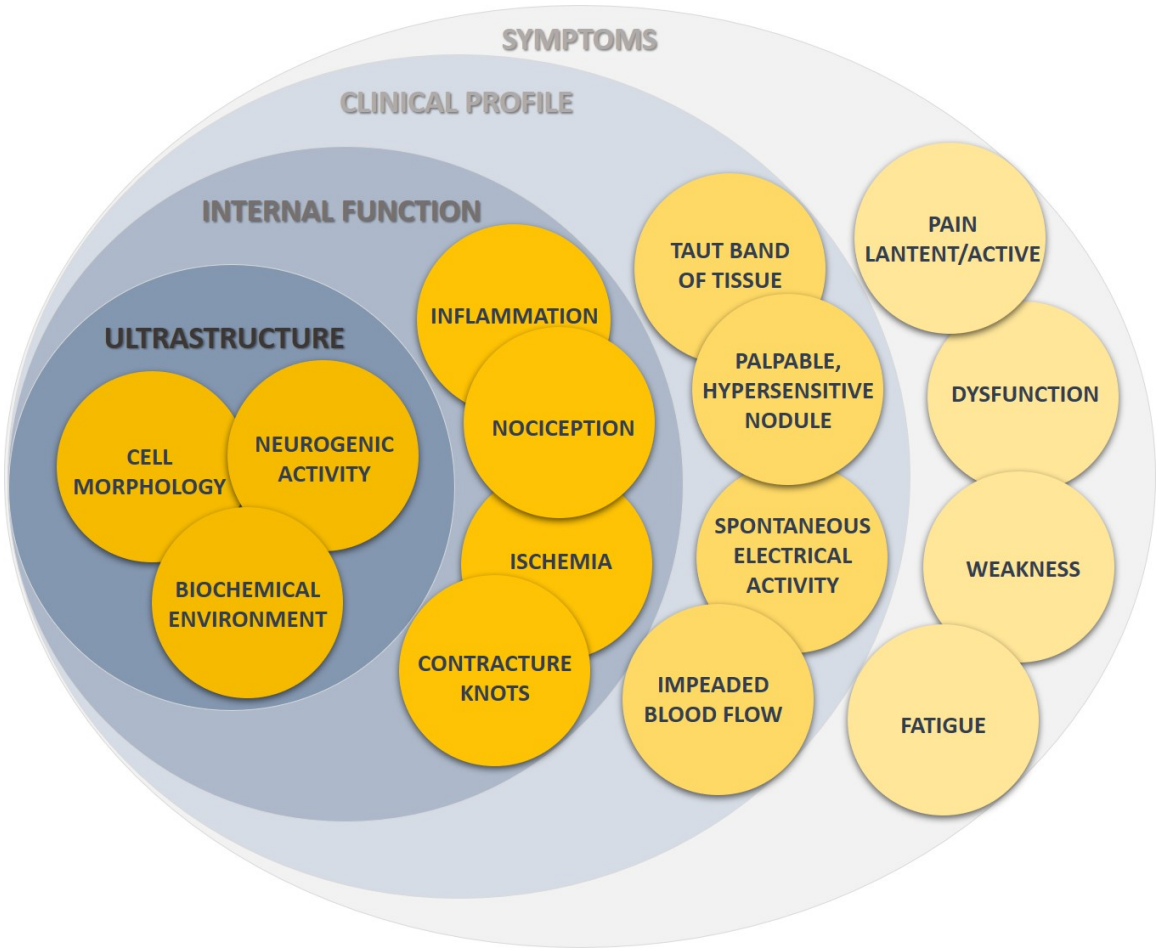

Figure 3.1: Schematic diagram of MTP symptoms with underlying clinical profile, internal function and ultrastructural alterations.

3.1.1 History

To some extent, MTP pathology has been documented for centuries, but a lack of common terminology and objective diagnostic methods have stifled advancements in treatments. In the 1960s, prominent physicians, Janet G. Travell (1901-1997), White House physician to President Kennedy, 1961-65, and David G. Simons (1922-2010), Chief of the Flight Medicine Branch, Aerospace Medical Sciences Division, at the School of Aerospace Medicine at Brooks, 1962-65, brought scientific rigor towards

understanding and treating MTP. Drs. Travell and Simons' work, spanning over four decades, lead to their co-authoring *The Myofascial Pain and Dysfunction: The Trigger Point Manual*, considered to be the preeminent resource for non-pharmacological, non-surgical treatment of MTP. Table 3.1 summaries notable events in the history of MTP research.

3.1.2 MPS and TP

Within MTP literature, references to myofascial pain syndrome (MPS) and tender points (TP) has been used interchangeably with myofascial trigger points. The following is a point of clarification for these terms.

A common pain disorder associated with MTP is myofascial pain syndrome (MPS). MPS is separate from acute soft tissue injury - fibromyalgia, bursitis, tendinitis [1, 148]. But it may be a secondary condition. Like MTP, MPS is diagnosed with physical exam and patient history and found to improve with stretching and manual therapies. A causal relationship between MTP and MPS has been debated [1, 148].

While concomitant occurrence of MTP and MPS is widely observed, MTP may be present in a taut band without MPS [63]. Similar to MTP, MPS is widely attributed to muscle overload, yet clinical observation indicates that MPS may arise without muscle overload and without the presence of MTP [1]. Evidence for a causal relationship is insufficient, and further research is needed to better understand the relationship between MTP and MPS.

Within the physical medicine fields, MTP and TP both describe hypersensitive spots in muscle tissue, and have been used interchangeably, however, these are distinct phenomena. The term MTP was developed by Travell and Rinzler in 1950, to define the hypersensitive nodule which may occur within the muscle tissue and surrounding connective tissue (fascia), but are predominantly found in taut bands of muscle belly

Year	Notable Event
1500's	France, Guillaume de Baillous describes muscle pain disorders [148].
1816	Great Britan, Balfour describes muscle thickening and nodules with pain [148].
1843	Germany, Froriep describes muscle callouses [148].
1904	England, Gowers, neurologist, uses the term fibrositis to describe hard nodules caused by inflammation of fibrous tissue, but was discredited for lack of evidence [148].
1919	Germany, Schade proposes that nodules, or "myogeloses", are a result of increased muscle tissue viscosity [148].
1900's	America, Kellegren documented referred pain patterns [148].
1938	America, Kellegren uses procaine injection to alleviate MTP pain [154].
1941	Germany, Kraus demonstrates that ethyl chloride spray alleviates myocardial infarction pain. America, Travell applies this technique to alleviate MTP pain [154].
1950's	America, Travell and Rinzler use the term "myofascial trigger point" to describe nodules present with referred pain in muscle and fascia [148].
1963	America, Travell presents a 2-day lecture and demonstration on myofascial trigger points, where it is highlighted that myogenic pain is overlooked but can be identified and treated manually by an experienced practitioner. David Simons meets Travell.
1970	Travell and Simons begin writing trigger point manual in order to train practitioners in diagnosis and treatment of MTP at Simon's myofascial pain clinic, Houston [154].
1981	Travell and Simons publish a hypothesis on the mechanism of MTP formation as the "energy crisis hypothesis" [156].
1993-94	Pain referral mechanisms were demonstrated to be contained within the spinal cord in a rat model [79, 109]. Needle EMG study demonstrated sustained spontaneous electrical activity in MTP compared to normal tissue 1cm from MTP [81]. First edition of Travell and Simons' Myofascial Pain and Dysfunction: The Trigger Point Manual [169].
1999	Second edition of Travell and Simons' Myofascial Pain and Dysfunction: The Trigger Point Manual [157].
2019	Third edition of Travell and Simons' Myofascial Pain and Dysfunction: The Trigger Point Manual [155].

Table 3.1: Notable events in myofascial trigger point research

[21]. MTP have acute and chronic phases, where sensitivity is either localized and painful with applied pressure, classified as latent MTP, or pain is spontaneous and refers pain to distant sites, classified as active MTP. The term *tender point* was coined by osteopathic physician, Lawrence Jones in 1955, to describe areas of tissue-texture abnormality with tenderness. Unlike MTP, TP are found at muscle insertion points and do not refer pain [21]. TP also reach beyond muscle and may be localized on bone and within joint structures [143]. Dr. Jones developed the strain-counterstrain method to treat TP. Patterns of distribution of muscle tissue sites between Jones' TP and Travell's MTPs may overlap. Both may be treated with positional release techniques [116].

3.2 Diagnosis

MTP are diagnosed with physical examination and patient history [63, 64, 1, 148]. The patient will present with mainly pain complaints but may also have other symptoms including numbness, tingling and motor dysfunction. The motor dysfunction is characterized by limited range of motion, muscle fatigue, weakness, and autonomic phenomena - cooling, sweating, pilomotor activation at the target level, persistent lacrimation, imbalance, dizziness, tinnitus [64]. Patients may also present with asymmetry, postural deviations, disproportionate loading, reduced joint mobility, protective or guarded positions and mental attitudes [64]. The location of the trigger point is determined by palpation and the patient's perceived pain [8]. Briefly, the clinician palpates the taut band to locate the stiff MTP nodule [64]. The affected muscle may present with a twitch response (TR), which is a muscle contraction visible as dimpling of the muscle and skin and/or palpable upon pressure [8]. The TR is elicited by placing fingers perpendicular to the band and applying direct pressure on or sweeping pressure in a transverse direction, snapping the band. The pain presentation further

classify the MTP as active or latent. Active MTP are spontaneously painful and latent MTP are painful upon stimulation (palpation or needle) [21, 8]. It is postulated that latent MTP is an early phase and active MTP is the chronic phase [64].

3.3 Treatment

The first courses of action in treating MTP are behavior and postural modifications, and warm or cold compress. This is commonly followed by pain management (analgesics, muscle relaxants, sleep aids, anti-depressants, neuroleptics and pain management with non-steroidal anti-inflammatory to opioids)[8]. In chronic cases lidocaine injection or surgical intervention are sought. Complementary medicine and integrative therapies like acupuncture, osteopathic manipulative treatment, therapeutic ultrasound, vapocoolant spray, and stretch [8] seek to inactivate the MTP and provide pain relief and restore function.

3.4 Pathophysiology

3.4.1 Etiology

It is widely agreed that MTP form from trauma such as muscle strain or overuse [21, 8]. Primary MTP form from muscle strain, i.e. use extending beyond normal capacity, muscle overload, repetitive-use strain, long periods of sustained posture, sustained low-level contractions using the same muscles, chronic injury, and chronic sports injury. Secondary MTP form from sites of pain referral from visceral or somatic structures [64, 105] connected neurogenically or in antagonist muscle to the primary MTP. Nutritional deficiencies, dysfunctional sleep, physical and psychological stress, infection and gene mutation also promote MTP formation [8, 61, 64, 185]. Prevalence increases with age, reduced daily level of activity, lack of exercise, postural deficiencies,

improper body mechanics while performing weight bearing or dynamic tasks, surgical scars and tissue tension post-surgery [8, 21, 61, 185].

3.4.2 Hypotheses

Several mechanisms have been proposed to describe MTP formation and maintenance. The following are hypotheses are commonly discussed in literature:

1. Cinderella Hypothesis
2. Integrated trigger point hypothesis
3. Neurogenic hypothesis

Cinderella hypothesis

The Cinderella hypothesis describes the mechanism of injury that initiates MTP formation, where fibers recruited first and derecruited last are vulnerable and sustain damage before other fibers. The Cinderella hypothesis is based on Henneman's size principle. Henneman demonstrated in a cat model that the motor-neuron recruitment and derecruitment occurred in order of increasing size [76], where smaller fibers, i.e. Type I, are subject to prolonged activation. The Cinderella hypothesis, described by Haggs, stated that due to recruitment order smaller fibers are most vulnerable to MTP formation [21, 87]. Kadefors and Roland supported this hypothesis by showing evidence of constant activation of small motor-neurons in low-threshold electrical signals using fine-wire electromyography (EMG) [87]. Minerbi and Vulfson challenged this postulate with "the shift model", a numerical model of postural muscle fibers. In this hypothesis, trauma on motor units initiate prolong contraction, and, more importantly, reduce relaxation time. Interestingly, they found that fibers with less relaxation time were found to be more susceptible over Type I or smaller motor-neuron

size [110]. Recruitment/decruitment order based on relaxation time may be specific to postural fibers. This theory suggests that further investigation on recruitment order by different muscle fibers may be warranted to better understand MTP mechanisms.

Integrated trigger point hypothesis

The most widely accepted hypothesis is the integrated trigger point formation hypothesis, postulated by Travell and Simons'. The integrated trigger point hypothesis describes the mechanism of MTP formation as an "energy crisis", where energy demand from shortened sarcomeres exceeds energy supply, and compressed capillary beds impede energy replenishment and metabolic waste removal [21]. This sets off a cascade of events often referred to as a "vicious cycle" where MTP forming events are self-perpetuated. Sustained muscle contraction releases excess calcium ions, Ca^{+}, shortening the sarcomeres. Trauma may not damage muscle tissue but it may disrupt ultrastructures - cell membrane, sarcoplasmic reticulum (SR) [21]. As a result, Ca^{+} reuptake to the SR diminishes. Contracted sarcomeres deplete ATP. This hypercontraction also compresses the arerial, venous, and lymph microvasculature within the muscle cells promoting hypoxia and apoptosis, impeding supply of oxygen and myoglobin, thereby inhibiting ATP generation. Without available ATP, myosin heads do not detach from actin leaving sarcomeres in hypercontracted states. These shortened sarcomeres, often referred to as contracture knots, simultaneously increase energy demand and reduce energy supply, creating the energy crisis. In addition, the lack of tissue perfusion results in lactic acid build-up, lowering the pH. This acidic environment upregulates ACh receptors (AChR) increasing the firing rate in the motor endplates, and downregulates AChE sustaining motor endplate activity. This shortened sarcomere also segments the muscle fiber [63], limiting the effective fiber length, diminishing force production capacity, clinically observed as muscle weakness.

Neurogenic theory

The neurogenic hypothesis proposes that central sensitization triggers inflammatory response in muscle tissue, and that MTP formation is secondary to the neurogenic activity [159, 128]. The neurogenic or neurophysiological hypothesis centers on the role of muscle spindles in pain and endplate activity, specifically endplate spikes (EPS) and miniature endplate potentials (MEPPs). Prolonged overload in skeletal muscle produces neural inflammation (release of neuropeptides and substance P) and sensitizes afferent muscle spindles [128]. The intrafusal fibers have a blood/nervous barrier so that capillaries supplying nerves do not leak into the fibers, as do those supplying extrafusal fibers. Also, intrafusal fibers contain fewer capillaries in the intraparietal space, compared to extrafusal fibers. When inflammatory substances enter the intrafusal space, it may be more concentrated and have a longer wash out period than compared to extrafusal space. This results in excitation and pain. Sustained isometric contraction or overload leads to fusimotor activation. Chronic activation leading to inflammation and sensitization. These sources of excitation may explain the EPS and MEPPS of intrafusal origin [128].

3.4.3 Mechanisms

Gerwin et.al. suggested that the mechanism of MTP resulting in reduced force-generating capacity must be reversible because strength is restored upon inactivation of MTP [63]. Understanding the mechanism of MTP is important for developing an objective assessment method or approach. While there is disagreement on MTP initiating processes, commonalities across the hypotheses can be examined. These commonalities include manifestation of pain, regional blood flow changes, tissue stiffness, and myogenic activity alterations.

Pain

Active MTP sites have been shown to have elevated acidic pH levels, ischemia, hypoxia, which are known to be associated with pain. Metabolic waste such as lactic acid that would normally diffuse from muscle to blood stream, builds up in the tissue, lowering the pH [21]. This acidic environment promotes the release of inflammatory mediators and nociceptive substances. Shah, et. al. (2005,2008) developed a microdialysis technique to investigate biochemical milieu of MTP. Their studies revealed elevated inflammatory markers, nociceptors, and acidic pH levels in active MTP, compared to latent MTP and normal tissue - H^+ concentration, Bradykinin, TNF-α, IL-1β, serotonin, and norepinephrine. Elevated levels of neuropeptides such as calcitonin gene-related peptide (CGRP) and substance P (SP), were also found in active MTP. The release of CGRP and SP into muscle stimulates nociceptive markers and inflammation.

Neural activity is reflected in pain mechanisms. Nociception in tissues may alter receptors thresholds, developing hypersensitivity via neurogenic mechanisms [61]. Muscle tissue nociceptors have multiple receptors - vanilloid, sensing heat and H^+, acid sensing ion channels (ASCI) and purinergic, sensitive to ATP, adenosine diphosphate and adenosine. Thus, inflammation in muscle may trigger pain in one nociceptor for multiple reasons. This nociceptive input exposes a range of neurons and interneurons within the spinal cord. This may explain the mechanism of how nociception is enhanced with a wider range of impact, i.e. across muscles fibers, connective tissue, fascia and skin, as well as viscera through somato-visceral pathways. Neuropeptides, SP and CGRP, are produced in the dorsal root ganglion, transmitted through the axon and stored in the muscle nociceptors.

As a result, any stimulus activating the nociceptors will release these substances into muscle tissue, further promoting inflammation [62, 63, 147]. The presence of SEA may also contribute to local and referred pain [59] by triggering the release of inflammatory and nociceptive substances. Pain was found to follow electrodiagnostic measurements when placing needles into active MTP [128].

Regional Blood Flow

In normal dynamic muscle activity, rhythmic contraction-relaxation cycles serve as a fluid pump, compressing and releasing capillary beds. In a sustained contraction the capillary bed is compressed and muscle tissue becomes hypoperfused [69, 21]. Prolonged hypoperfusion grows into an ischemic condition. The oxygen and glucose supplies, needed for adenosine triposphate (ATP) production, do not replenish leading to the energy crisis [21]. Sikdar et. al. measured blood flow in MTP site using doppler ultrasound and found that systolic and diastolic velocities and resistivity index (RI) were significantly increased in active MTP compared to normal tissue and latent MTP [151]. A lumped parameter simulation attributed these increases to the increased outflow resistance from capillary compression on the venous side and increased vascular volume of the compliant vessel on the arterial side.

Tissue Stiffness

Pressure gradients from traumatic activity damage the cell membrane and SR releases calcium ions, Ca^{+}, further sustaining contraction. The increased Ca^{+} supply produces low-level activity maintaining a muscle in a hypertonic state, which may contribute to the taut band [63]. It is hypothesized that without ATP, the muscle tissue enters a state of rigor, reducing elasticity. The homeostasis of the muscle tissue is locally compromised further damaging ultrastructures. Studies have demonstrated

morphological changes in cytoskeletal proteins, desmin, tintin and dystrophin [21]. Desmin destruction has been observed after 5 minutes of unaccustomed eccentric exercise resulting in disorganized myofibrils, Z-band streaming and A-band disorganization [63]. Zhang et. al. imaged histopathological changes in MTP muscle tissue in a rat model. Transmission electron microscopy (TEM) images of normal muscle fibers showed uniform shape and size, while those in MTP tissue were rounded. MTP muscle fibers presented with fewer mitochondria that also displayed morphological changes. Normal mitochondria are oval with ridged edges. Those in MTP tissue appeared circular with smooth or diminished ridged edges[185].

Continual nociceptive input also leads to guarding behaviors maintaining muscle tone from posture holding patterns. The taut band may also be a result of increased muscle tone due to neural signaling. The gamma-gain may participate in dysfunction as it relates to fiber length and rate of length change. Gamma-motoneurons synapse to anterior horn cells and co-activate with alpha motor-neurons via interneurons to maintain appropriate tension during contraction. The stretch reflex has short and long latency components, where over-activity in the long component may increase muscle tone [59]. Whether the tissue damage or nociceptive input occurs first has not yet been determined.

Hemodynamic activity alters pH and skin temperature. Collagen fibers are known to denature in acidic solution and elevated temperatures which may contribute to supportive structure changes (ECM, fibroblasts and myoblast activity) [122, 27]. *In vitro* studies on fibroblasts and myoblasts suggest mechanisms of tissue texture change and nociceptor release from altered non-contractile connective tissue structure [40]. Dodd, et. al. (2006) investigated effects of strain on shape and proliferation on human fibroblasts in order to develop a model for injury and OMT-related strain *in vitro*. They found that inflammatory cytokines, IL-6 and nitric oxide, are released with

strain of 10% or more and altered the fibroblast shape. At 30% strain or more cell viability partially or completely diminished. The cells were found to undergo hyperplasia, increased clustering, altered cell shape to fusiform shape and lacked elongated pseudopodia, the portion of the cell containing actin. These are characteristic fibrous tissue texture changes (fibromyalgia) and were suggested by this study to also be characteristic of changes observed in MTP pathology.

Tissue contractures may be supported by myofibroblast behavior, where fascial tissue contraction mediated by myofibroblasts results in collagen expression and matrix remodeling, where lax collagen are digested and new fibers expressed. If the contraction is beneath the threshold for mechanosensation the sympathetic nervous system fails to activate and respond with cytokine expression to relieve the contraction. The contracted fibers are then neurally and structurally supported, producing contractures within the muscle fibers [142].

Myogenic Activity

Henneman's first paper from 1957 relating size of neuron and discharge susceptibility, stated that "[The] tendency to be continuously active is perhaps an indication that small cells are so susceptible to excitation that the spontaneous activity of the spinal cord is sufficient to keep them firing" [76]. More recently, the Cinderella hypothesis, supported this statement, where smaller fibers continuously performing sub-maximal work for long periods of time leads to muscle damage and disruption to $Ca+$ dynamics [147, 21]. Hubbard and Berkoff demonstrated SEA with needle EMG in 1993. Since then SEA in MTPs has been well documented with electrodiagnostic studies [54, 59]. This phenomena has been demonstrated to occur within the endplates of extrafusal fibers (alpha-motor neurons) [59]. Acidic levels associated with pain and ischemia, lower the nociceptive threshold and inhibit acetylcholine esterase (AChe).

This leaves excess ACh remaining in the pre synaptic space, increasing the motor endplate activity. [148, 63]. Also, the hypercontracted sarcomeres occur near plasma membrane lesions which increase Na^+ permeability and membrane depolarization [59]. The Na^+ and Ca^+ produce endplate spikes and endplate noise, respectively, which together form spontaneous electrical activity (SEA) of the muscle at rest[59].

Histopathological studies demonstrated that structural alterations in the muscle fibers in MTP sites of rat models included shortened sarcomeres and fewer mitochondria [185]. This morphological change at the muscle fibers and myofilament level, and fewer quantity and deformed mitochondria may serve to explain the reduced aerobic capacity observed with contracture knots. The lipid content serving mitochondria may also be of importance. Ozgocment and Ardicoglu found a significantly elevated lipid profiles in MTP compared to fibromyalgia syndrome (FPS) and healthy tissue [125]. In a more recent study, mitochondrial and fat droplet morphology of upper trapezius were investigated to determine if lipid droplets may provide information on metabolic changes in MTP. The authors found more mitochondria in the subsarcolemmal and intermyofibrillar spaces, and less lipid droplets in the subsarcolemmal space. In MTP, the amount of lipid droplets touching the mitochondria were significantly greater than the control, and also had greater cytochrome c oxidase-deficient muscle fibers. The authors hypothesized that theses alterations with mitochondria and fewer lipid droplets in MTP tissue explained reductions in metabolic capacity. Aggregation of lipid droplets near mitochondria was hypothesized to be a compensatory optimization mechanism assisting in energy production [37]. The reduced metabolic activity may explain the muscle weakness and fatigue observed with MTP.

Chapter 4

VASCULAR ASSESSMENT

4.1 Introduction

The relationship between pathological tissue and altered tissue perfusion is well known [2]. Myofascial trigger points (MTP) also exhibit alterations in muscle tissue vascularity. These alterations include: 1) ischemic conditions within the MTP site [113, 21], 2) fluid collections seen as hypoechoic regions in B-mode ultrasound images [152] with 3) inflammatory and nociceptive markers [147], and 4) increased retrograde flow as seen in the the spectral Doppler waveform [151]. Osteopathic manipulative treatments (OMT) aim to restore homeostatic tissue perfusion [28], however, thus far, only a few studies have investigated MTP treatment effect on musculoskeletal tissue vascularity.

Tissue perfusion is complex, referring to movement of all fluids through a volume of tissue; it has been further described as the "nutrition/waste exchange" at the capillary level [85]. While capillary exchange is difficult to measure, power Doppler ultrasound (PD) has been shown to closely approximate tissue perfusion [85, 23]. In PD ultrasound images, the color pixel intensity depends upon the ultrasound settings and tissue attenuation. PD imaging is suitable for imaging musculoskeletal disorders due to its sensitivity to slow flow and ability to image small and scattered vessels [158], however, the images are qualitative and are not comparable without standardization [173]. This chapter proposes a new technique for standardizing PD images for musculoskeletal tissue vascularity assessment, specific to imaging MTP treatment effect in a pre-post test.

4.1.1 Doppler Ultrasound

Ultrasound is transmitted into tissue at a certain frequency. Reflections off of moving scatterers in the blood stream shift in frequency depending on the velocity. The difference between the transmitted and reflected signal is the Doppler frequency. Higher velocity scatterers produces higher Doppler shifts. The Doppler velocity of blood flow is related to the Doppler frequency shift by the following equation [49, 89]:

$$v = \frac{cf_D}{f_t cos\theta} \tag{4.1}$$

where c is the speed of sound through soft tissue, f_D is the Doppler frequency defined as difference between the transmitted, f_t, and reflected, f_r, frequencies, and θ is the angle of insonation between the ultrasound beam and moving scatterers, e.g. erythrocytes [161, 163].

Spectral Doppler Ultrasound

Doppler frequencies from a small sample volume are viewed on a time scale, shown in spectral Doppler ultrasound waveform, where maximum and minimum frequencies correlate with peak systole and end diastole. Figure **??** describes this one cardiac cycle of a spectral Doppler waveform. Because Doppler frequency is related to the Doppler velocity, the spectral Doppler waveform provides the same shape as a velocity distribution plot [49]. The spectral Doppler ultrasound sample volume is user defined and typically placed at the center of the vessel, at the peak of the parabolic flow profile.

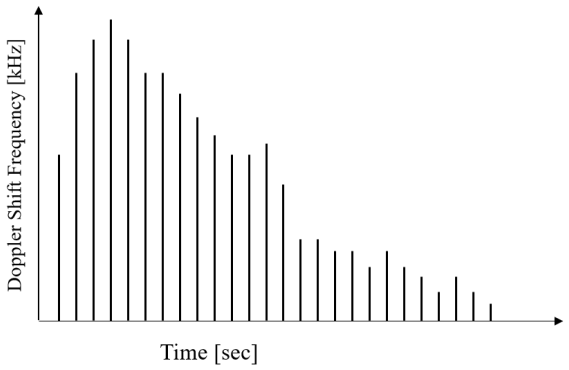

Figure 4.1: Representation of the spectral Doppler waveform over one cardiac cycle. The variation of the frequency shift over time is proportional to the "velocity profile" within a prescribed sample volume.

Color Doppler Ultrasound

The average Doppler velocities per pixel are displayed in 2-D color flow imaging (CFI). In color Doppler (CD) ultrasound, the color intensity depicts the velocity $[cm/s]$, and the color map depicts direction of flow with respect to the transducer angle of insonation. Colors values from top to bottom of the color map indicate flow towards and away, respectively. Color values to the left or right of the color map represent variance of flow, where left-most values represent laminar or parabolic flow (normal) and right-most represent turbulent (pathologic) [46]. In practice, the Doppler frequency (kHz) is demodulated from the carrier (MHz) frequency, and the mean frequency of N samples is estimated through IQ quadrature process [163]. The phase-based mean estimator efficiently approximates instantaneous Doppler frequency at a spatial location [163]. Equation 4.2 provides the Doppler frequency estimation using IQ demodulated components. Multiple ensembles or packets improve accuracy of the velocity estimation and slow flow sensitivity [46]. Increasing the number of ensembles decreases the frame rate and temporal resolution [46].

$$\bar{f}_d = \arctan\left(\frac{I\frac{dQ}{dt} - Q\frac{dI}{dt}}{I^2 + Q^2}\right) \tag{4.2}$$

where, $I = cos(\omega_c t + \theta)$, and $Q = sin(\omega_c t + \theta)$, and $\omega_c = 2\pi f_c$, f_c is the carrier signal [98].

The discrete approximation of the Doppler frequency is as follows (Equation 4.3) [163]:

$$\bar{f}_d = \arctan\left[\frac{\sum_{n-1}^{N} I(n)Q(n-1) - Q(n)I(n-1)}{\sum_{n-1}^{N} I(n)I(n-1) + Q(n)Q(n-1)}\right] \tag{4.3}$$

where N is the number of ensembles.

Color Doppler ultrasound quantifies the instantaneous blood velocity in large vessels, where beam angle is adjusted to optimize flow detection. Doppler ultrasound imaging is not suitable for detecting flow in small vessels with tortuous paths due to the angle dependence. PD ultrasound is independent of angle, so it effectively visualizes small vessel blood flow [23] even at 90 degrees [163, 158]. Additionally, PD and is sensitive to slow or low amplitude flows [158].

Power Doppler Ultrasound

The Doppler shifted frequency is proportional to the blood velocity. The power of a particular frequency band is proportional to the number of erythrocytes producing those Doppler frequencies [49]. The spectral Doppler waveform, therefore, provides the variation of the power profile over time within a prescribed volume. The spectral Doppler waveform relationship with the power Doppler image is analogous to the Amplitude-mode waveform to B-mode image [49].

Equation 4.4 [163] provides the power Doppler calculation from the Doppler velocity.

The power of the Doppler velocity is closely approximated by the sum of the squares of the sine and cosine demodulated signal, the I and Q components, shown in Equation 4.4.

$$\int_{-\infty}^{\infty} P(f)df = \int_{-\infty}^{\infty} |V_{Doppler}(f)|^2 \approx \sum_{n-1}^{N} I^2 + Q^2 \tag{4.4}$$

The PD ultrasound image displays the log compressed power, producing the relative power Doppler intensity (PDI) [163]. See Equation 4.5.

$$PDI = 20log_{10}\left(\sum_{n-1}^{N} I^2 + Q^2\right)[dB] \tag{4.5}$$

PD imaging has been used in musculoskeletal tissue applications to visualize fluid collections [166, 158], inflammation[158] and intramuscular blood flow changes with activity [41]. Equation 4.4 shows that power is related to the Doppler velocity amplitude [163]. The Doppler velocity amplitude is dependent on to the density or speed of moving scatterers, which decreases with depth or increased tissue attenuation [158]. As a result, sampling impacts image outcomes. Power Doppler images are sensitive to image optimization.

4.1.2 Image Optimization

In CFI, the color pixel intensity depends on tissue attenuation and ultrasound settings, e.g., depth, focus, gain, color gain, and pulse repetition frequency (PRF), which can under- or overestimate blood flow [166]. CFI optimization is dictated by the range of Doppler frequencies detected in the sample volume [46]. The range of frequencies depends on the speed and depth of flow. If signal attenuation is significant, depth may be compensated for using time gain compensation to amplify the signal.

PRF

Under ideal and uniform sampling conditions, the power Doppler image should reflect the same shape as the velocity profile, or the spectral Doppler ultrasound waveform [49]. CFI uses pulsed wave (PW) ultrasound. The advantage of PW over continuous wave (CW), is that PW can discern the depth of the echoes received, while CW depicts all echos that fall within the ultrasound beam, regardless of point of origin.

In spectral Doppler ultrasound, the sample volume is limited, so all spectra contained only within that sample volume are plotted over time. In power Doppler images, spectra are not limited by space, but limited in time. The number of pulses transmitted per second, or the pulse repetition frequency (PRF), is vital to image outcomes. Many factors contribute to why the power Doppler image does not accurately reflect the velocity distribution, including spectral resolution and variance of the spectral estimate [49].

The maximum Doppler shift frequency that can be detected by the transducer is equal to the Nyquist limit, or half the pulse repetition frequency (PRF) [7],

$$PRF_{max} = \frac{c}{2R} \tag{4.6}$$

where R is the maximum depth sampled.

PRF impacts aliasing, range resolution, temporal resolution and depth penetration. In power Doppler imaging, spectral aliasing has less of an impact, as the direction and frequencies are not represented [7].

In practice, PRF is manually adjusted to capture the expected range velocities, where PRF is increased with higher velocities. In clinical practice PRF is described as a scaling factor [46, 146].

Artifact

At suboptimal gain, the degree of vascularity is underestimated, whereas an over-increased gain can increase the noise floor, resulting in erroneous color pixels and color bleeding, called ghosting [95]. A non-optimal PRF setting results in spectral aliasing in pulsed wave ultrasound (CD image), and under- or over-sampling in PD images. Under-sampling produces color bleeding (color beyond vessel boundaries) and increase noise floor, while oversampling results in range ambiguity (echoes incorrectly located more superficially), decreased penetration and loss of color in the vessel (not detecting moving scatters). Techniques for ensuring weak flow detection while minimizing noise is necessary to accurately image tissue blood flow [158]. PRF has been recognized as a main effect for minimizing artifact.

4.1.3 Quasi-Quantitative Methods

The first-order analysis of PD images involves qualitatively interpreting area and pixel intensity changes by visual inspection. Increases in area may indicate increases in blood volume and increases in color pixel intensity may indicate increased speed. Because PDI values are qualitative, the need for standardizing images has been acknowledged and attempted. Quantification techniques are not well established. Vascularity metrics from PD develop on an as-needed basis, and tend to be application specific. Techniques used in musculoskeletal applications are summarized.

A common method used in musculoskeletal and visceral organ tissue imaging is identifying the maximum PDI at systole by visual inspection. The PD pixel color values represent the density or speed of moving scatterers [85]. The higher dB values indicate faster flow or higher density of moving scatterers, regardless of direction. When using pixel intensity as the metric for vascularity changes, randomized controlled tri-

als have most often standardized images by using a constant PRF (1kHz), as much as possible. This technique has been shown to have a high interoperator-reliability in detecting musculoskeletal synovial fluid collections in inflamed joints [20, 50, 160], acute and chronic knee arthritis [65], and hyperemia in acute focal musculoskeletal pain [121]. However, 1kHz PRF is not always the optimal image setting, so a fair comparison between images is not guaranteed. PD image optimization is subject to the underlying tissue attenuation factors which may be altered with intervention or physical provocation. Maintaining a PRF of 1kHz for repeated measures design may fail to represent vascularity of the underlying tissue, misleading interpretation of and diminishing the diagnostic value PD imaging.

Another common metric is the colored pixel density. Flow may be quantified using the ratio of colored-to-non-colored pixels, the quantity of visible vessels in transverse view, the sum total of color pixel values in a frame [41, 173], or the percent of region of interest (ROI) coverage. Color pixel density has been interpreted as a tissue perfusion metric used to grade severity of pathology [19]. These techniques used PD images to infer the presence or lack of flow, independent of pixel intensity (speed or density of scatterers). The limitation with this methodology is that it still-quasi-quantitative. While the number of color pixels is made available, the color pixel size is not available, and is area is not quantified. These data are obtainable with diagnostic ultrasound, however manufacturers fail to provide this information to the end user.

The fractional moving blood volume (FMBV) technique employs a reference value to normalize the color map for for within-frame comparison. The reference color pixel value is selected from largest vessel in-frame, and is defined as the maximum (100%) detectable amplitude [138, 173, 174]. The limitation of this method is that a large vessel within the frame may not be available. Also, this reference value is subject to change when comparing two images, i.e. before and after an intervention. Due to the

inherent variability of the cardiovascular system, the stability of the reference value is not guaranteed. For these reasons, FMBV is inadequate for repeated measures design investigation of muscle tissue.

Clinically relevant data are often excluded from PD image quantification. In many PD imaging applications, the maximum PDI values from peak systole are the primary metric of interest. This approach neglects to consider low PDI values, representing slow flow, and variations (pulsatility) throughout the cardiac cycle. It is widely known that the blood flow waveforms - for example, those obtained with continuous wave Doppler ultrasound, finger pulse plethysmography, laser Doppler flowmetry or spectral Doppler ultrasound - represent clinically relevant information, specifically on the diastolic portion of the waveform. To better understand what data are available in PD data, the anterior forearm was imaged before and after light exercise. See Appendix C). This preliminary data showed increases in pixel intensities, quantity of color pixels, range of pixel intensities (low to high dB values), and variance after exercise. Using conventional methods, these changes may have been overlooked.

Few commercially available software packages allow for ultrasound cine data processing. One software package (Color Quantifier, Kinetic Imaging, Liverpool United Kingdom), utilized both pixel intensity and area for quantifying vascularity in tissues, defining vascularity as the integration of color energy per square millimeter. Vascular changes of the uterus, ovaries and follicles throughout the menstrual cycle was investigated with this software package and found it to be a feasible and reproducible technique for estimating vascularity of these organs [9]. The limitation in this technique is that, area is inversely proportional to the primary outcome measure. If area of blood flow increases, this technique will interpret the PD image as a reduction in vascularity. Furthermore, this technique requires the standardized ultrasound image settings to compare images. The area of blood flow may be under- or overesti-

mated at suboptimal settings. This technique does not accurately reflect the impact of vasomotion on blood flow through compliant vessels.

The current techniques for quantifying PD images are inadequate for comparing muscle tissue vascularity in pre-post tests. Fortunately, these limitations can be addressed. Table 4.1 summarizes the limitations and how these limitations may be overcome.

Limitation	**Mitigation**
omission of pixel intensities across all levels (low to high dB)	all pixel value intensities are accessible in PD images
failure to account for variations throughout the cardiac cycle	ultrasound cine allows for visualization of blood flow variations throughout the cardiac cycle. Quantification is possible with an open-source ultrasound unit.
lack of a direct measure of area, yielding a quantitative value	pixel size and depth are available in diagnostic ultrasound from which area can be calculated
discounting the influence of image optimization settings in PD imaging	main factors may be investigated on any conventional ultrasound unit

Table 4.1: Limitations and mitigation of PD quantification techniques.

Methodology have not yet been developed to take full advantage of clinically relevant data available in PD ultrasound. The purpose of this study is develop new quantitative methodology for investigating muscle tissue vascularity with PD. The techniques include a quantitative metric for vascularity and histogram analysis of the PD image.

4.2 Methods

Development of these techniques involve a series of experiments to determine: 1. time-series analysis 2. main factors optimizing Doppler ultrasound images with fractional factorial design *in-vivo* 3. effect of optimization on PDI and area detected with

PD using histogram by PD intensity bands *in-vitro* 4. effect of physiologic provocation on PDI and area histogram *in-vivo* 5. include optimization setting in vascularity metric, using a mapping function 6. demonstrate effectiveness of vascularity metric and histogram analysis in single case *in-vivo*

4.2.1 Instrumentation

For all experiments excluding Experiment 4, RF images were acquired with an open-source ultrasound unit with research platform, (Ultrasonix SonixTouch Q+, BK Medical, Burlington, MA), and linear transducer (L14-5/38), at $13.3MHz$. B-mode, color, power and spectral Doppler images were also acquired, depending on the experiment. All imaging was performed with a by an experienced ultrasound operator.

RF images were acquired from a peripheral flow phantom in three experiments as follows:

Experiment 1: Calibrate the peripheral vascular flow phantom

Experiment 2: Observe the effect of PRF on PDI and area of CFIs of flow phantom.

Experiment 3: Apply αPDI standardization using PRF Mapping function on flow phantom images. Compare PDI and αPDI on images of the anterior forearm at rest and after light exercise.

4.2.2 Experimental setup

Peripheral vascular flow phantom

For Experiments 1, 2, and 5, PD images were acquired from a peripheral vascular Doppler flow phantom (ATS 524, CIRS Inc., Norfolk Virginia) with variable vessel

diameters (2, 4, 6 mm). A peristaltic pump moved blood mimic fluid (Doppler test fluid, Model 707, ATS Laboratories, Inc.) through a closed circuit with non-pulsatile flow. The experimental setup is shown in Figure 2. The transducer position was fixed by a gooseneck arm and photography grip claw. Pump vibration noise was mitigated by placing the pump on a separate table with rubber wheels, and by placing both the transducer grip fixture and flow phantom on vibration isolation pads. The depth and color gain were held constant for all image sets, at 3 cm and 50% respectively. One focal point was positioned at the center depth of the tube where maximum flow profile is expected, 1.5cm + half the diameter of the vessel. The region of interest included all pixels in-frame. See Figure 4.2.

Anterior forearm

The forearm experiment used the same controlled setup and imaging parameters as the flow phantom, except that the transducer was mounted to an apparatus beneath which the subjects' arm rested in supine position. A custom transducer boot maintained the transducer position on the forearm throughout imaging. See Figure 4.3

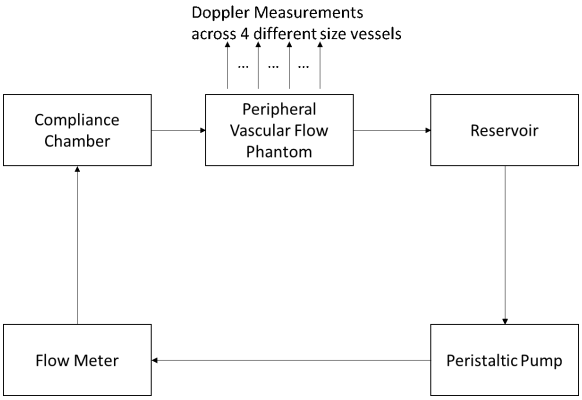

(a)

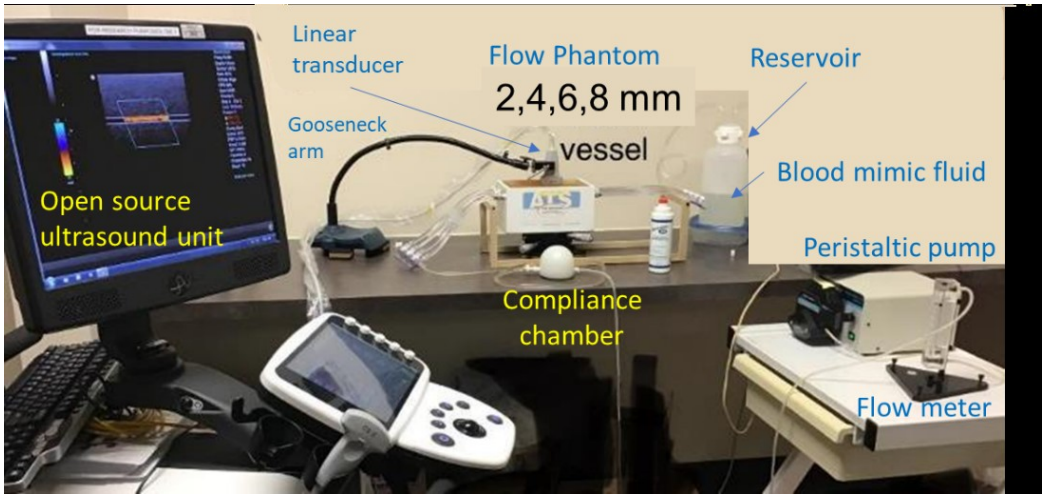

(b)

Figure 4.2: Experimental setup for peripheral vascular flow phantom imaging, (a) connection diagram, and (b) actual.

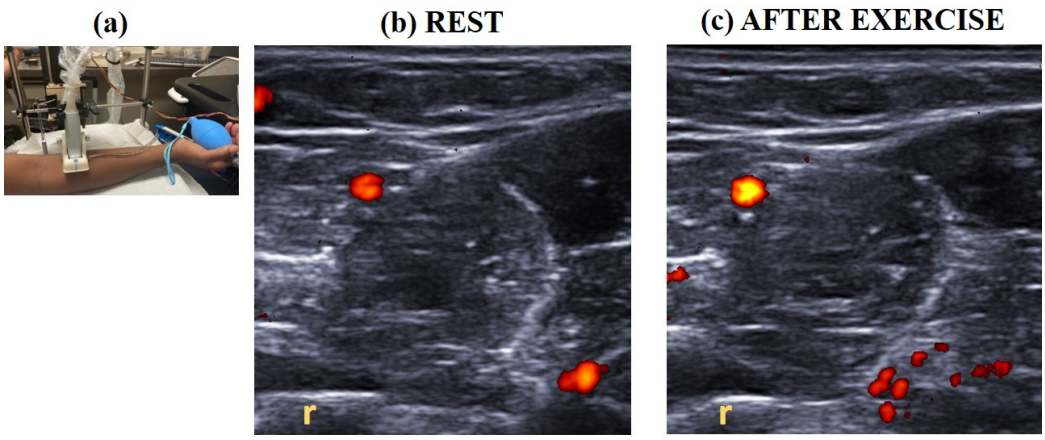

Figure 4.3: (a) Experimental setup for anterior forearm imaging; transducer is fixed in a grip claw and stabilization boot. A clench bulb shown in the subject's hand is used to perform light exercise. (b-c) The Power Doppler images of the anterior forearm in transverse view at rest (b) and after exercise (c). The radius is labeled with a yellow 'r'.

4.2.3 Image processing

RF images were post-processed off-line to obtain and quantify PD images using Matlab R2016a and R2020a (Mathworks Inc., Natick, MA). PD was calculated from the RF images using code provided by Ultrasonix software development kit (SDK), with some minor changes to optimize for the region of interest imaged (superficial). In brief, the IQ data is calculated with sine and cosine demodulation of RF data, and used to calculate the power of the Doppler signal on a frame-by frame and scanline-by-scanline basis, using the Equation 4.5. The PD image was log compressed to obtain the final PDI values. See Figure 4.4.

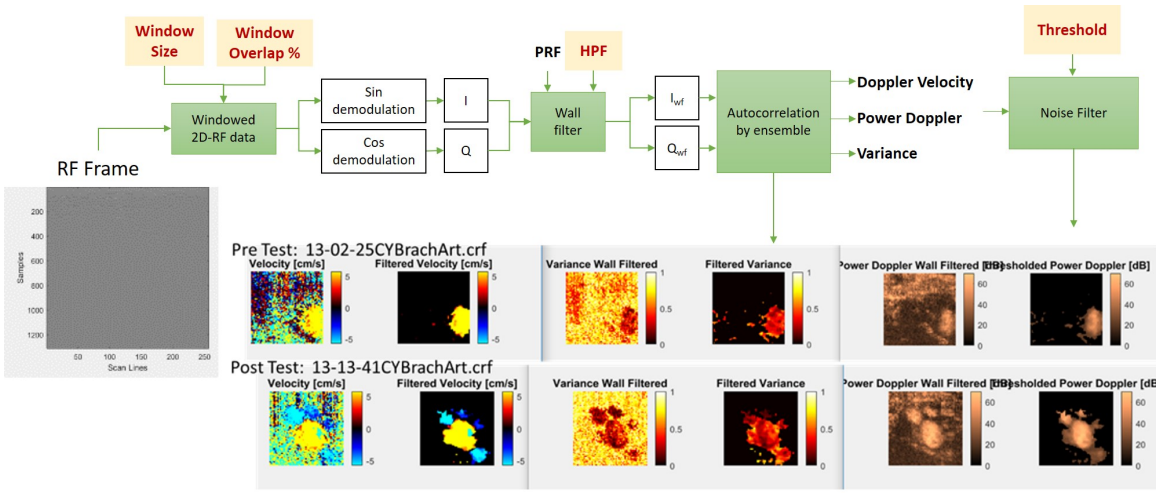

Figure 4.4: Flow diagram of image processing steps converting an RF image to velocity, variance and PD ultrasound images. Image processing optimization parameters are highlighted in yellow box with red bold font. The top row of images shows the filtered and unfiltered images of the brachial artery at rest (top row) and after exercise(bottom row).

4.2.4 Experiments and Statistical Analysis

Experiment 1: Time-series analysis

Ultrasound cine was captured from a flow phantom vessel (1-second) and anterior forearm (6-seconds) to visualize the time-series data. Area of colored pixels was plot over time to illustrate non-pulsatile and pulsatile flow from the rigid tube and *in-vivo*, respectively.

Experiment 2: Flow phantom calibration

The flow phantom was calibrated with spectral Doppler ultrasound at variable velocities $(5-, 10-, 15-, 20-, 25 cm/sec)$ through the $2-, 4-, 6mm$ diameter phantom vessels. The color Doppler pixel size was determined. The lowest detectable flow was

determined using linear regression with Pearson's coefficient. See Figure 4.2 for flow phantom experimental setup.

Experiment 3: Effect of exercise on PD image of the forearm

Five seconds of RF echo data were acquired from the anterior forearm at rest and after light exercise at frame rates of 5 and 6 FPS, respectively. The image depth was set to 4cm with one focus positioned at 2.5 cm. The transducer was fixed to an apparatus and placed in a grip claw. Position was further stabilized with a boot fixed to the foot of the transducer. The outline of the boot was marked with a surgical pen to ensure proper position after exercise. The transducer was placed 2 cm distal to the cubital fossa and was outlined on the arm with a surgical pen to ensure accurate angle and repositioning between exams. The participant was provided a soft clench bulb and asked to perform repeated isometric clenches (approximately 40-60 clenches) to facilitate blood flow changes in the anterior forearm muscles. Figure 4.3 below presents the experimental setup and PD images of the anterior forearm at rest and after exercise.

The PDI distribution were visualized with with box-whisker plots and with histograms. Box-whisker plots display the central tendency of the PDI values, comparing 5 seconds of data from rest and exercise (including all pixels from all PD frames). Statistical differences are compared with Wilcoxon rank-sum test. Histograms of PD images depicting quantity of color-pixels detected (y-axis) within an intensity band (x-axis) from 20-70 dB, in 10 dB increments, displays the power Doppler intensity distribution per intensity band. Histograms of the power Doppler images of rest and after exercise were visually compared.

Experiment 4: Main effects in image optimization

Optimization parameters are known to impact repeatability and reliability of Doppler ultrasound imaging [103]. Optimization settings are difficult to standardize as they are unit and application specific. A screening experiment was used to identify the main effects in Doppler ultrasound imaging optimization using a fractional factorial design experiment.

The carotid artery was imaged bilaterally with spectral Doppler ultrasound using a Logiq p6 (General Electric Healthcare, Chicago, IL) and linear transducer (ML6-15) in 1 subject. The resistivity index (RI) (response) was assessed by varying six optimization parameters (factors). Levels were aggressively distanced (lo and hi) around the carotid preset (default setting). See Figure 4.5 for experimental setup and RI calculation. The Resolution III 1/8 Fractional Factorial Design, with 6 factors, is used. The base design has three factors, and there are three design generators. There were 8 runs total, with 2 replicates. The design generators were selected based upon [112], which have a minimum aberration and high resolution (D = AB, E = AC, F = BC).

The transducer frequency was set to 12 MHz for all imaging. The depth was set to 2cm, sample volume length was set to 6 (unitless), and a focus was placed at 1.25cm, centered at mid vessel depth. It is well documented in literature, although not well understood, that the human body exhibits bilateral asymmetry in flow. Therefore, it is reasonable to select bilateral vasculature for replication.

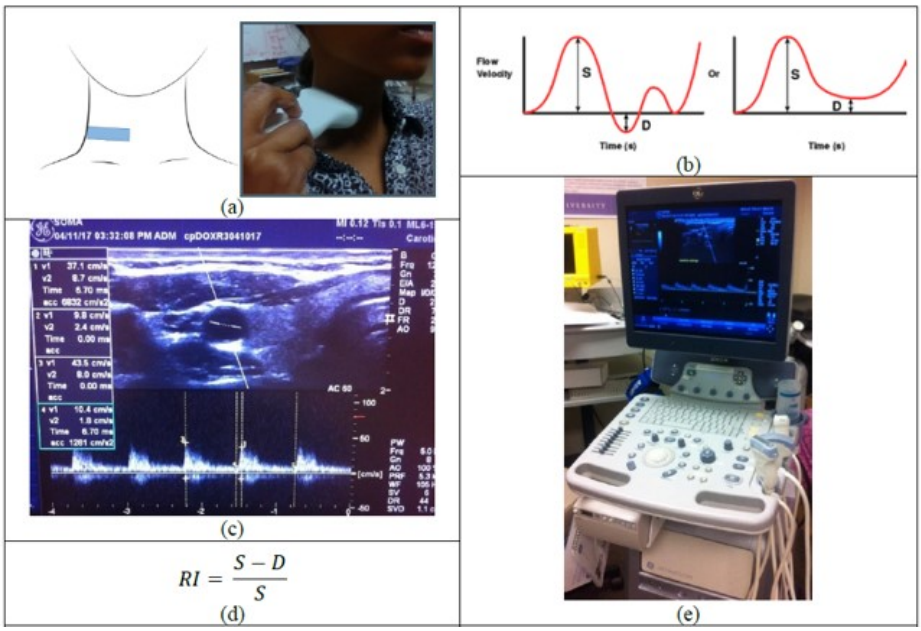

Figure 4.5: Experiment 4 setup for assessing optimization parameters. (a) Probe position on carotid artery (transverse view), (b) ultrasound Doppler waveform characteristics for RI calculation. (c) B-mode and spectral Doppler ultrasound with PSV and ESV measurements, (d) Resistivity Index equation, S = peak systolic and D = end diastolic velocities, (e) GE Logiq-P6 Ultrasound unit and ML-6-15 Linear Probe.

The pulse wave (PW) Doppler settings were not orthogonal; specifically, the PW PRF and wall filter (WF) adjust with the PW frequency, and the wall filter adjusts with the PRF. The ultrasound unit was reset to default after each experimental run to minimize operator error during data collection. The optimization parameters (factors) and levels are listed in Table 4.2. The factors were selected based upon literature and trial and error experimentation.

Factor	Standard order Run #	1	2	3	4	5	6	7	8
A	Probe Gain	40	98	40	98	40	98	40	98
B	Dynamic Range	48	48	105	105	48	48	105	105
C	PW Gain	0	0	0	0	32	32	32	32
D	PW Frequency [MHz]	8	5	5	8	8	5	5	8
E	PW PRF [kHz]	12.4	2.6	47.7	4.1	4.1	7.7	2.6	12.4
F	PW Wall Filter [Hz]	750	200	154	83	83	154	200	750

Table 4.2: Experiment 4: Factors and levels used in fractional factorial design experiment.

Experiment 5: Power Doppler image dependence on PRF

PD images were acquired from a 4mm diameter tube in the peripheral vascular flow phantom, using the setup shown in Figure 4.2. Images of blood mimic fluid through the rigid tube was captured at variable flow rates (75-, 135- and 185 ccm, or mL/min) and variable PRF settings (low, medium and high, with respect to the flow rate). Flow rates and PRF settings are shown in the PD images in Figure 4.6. The mean PDI and area per flow rate and PRF setting are plotted, and trends are visually compared.

The vascular flow phantom vessels (2-, 4- and 6mm diameter) with blood mimic fluid were imaged at variable flow speeds, 5-, 10-, 15-, 20-, 25 cm/s, imaged at variable PRF settings, 0.2-, 0.3-, 0.4-, 0.5-, 0.6-, 0.7-, 1.0-, 1.3-, 1.4-, 1.7-, 2.0kHz. The effect of the PRF setting on quantity of pixels by intensity band is represented with histograms.

The histograms of PDI values per frame showed the number of pixels by intensity-band, from 20-80 dB in 10 dB increment bins, for each PRF setting. The inflection point of the histogram was used to as the noise floor threshold at 27dB for the flow phantom images [173].

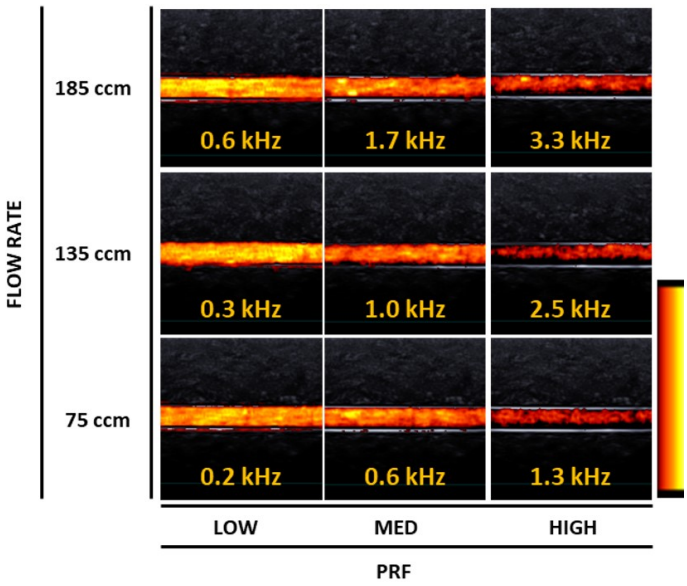

Figure 4.6: Sample PD images of blood mimic fluid through 4 mm vessel at variable flow rate imaged with variable PRF settings. The actual PRF settings are shown in yellow text.

Experiment 6: Vascularity metric, αPDI

The proposed vascularity metric, αPDI, was devised to quantify PD images. It serves to establish a method for standardizing the qualitative data using information typically overlooked, but readily available. Table 4.3 provides the criteria for standardizing power Doppler images. The interpretation of each variable is described:

In order to improve slow flow differentiability, i.e. flow imaged at PRF settings $< 1.0kHz$, a mapping function, $M(PRF)$, was developed through trial and error, to normalize the PRF settings from 0 to 1, that stretches the lower values $< 2.0kHz$. See Figure 4.7.

Criteria	Variable	Interpretation
Magnitude of blood flow	PDI [dB]	High PDI value indicates increased blood supply. Low PDI values represents retrograde flow, slower flow, or blood flow that has slowed from vasodilation
Dimensional Change	Area [mm^2]	Vasoconstriction and vasodilation resulting from sympathetic activity
Flow speed metric	PRF [kHz]	While PRF is optimized for the depth of vessels imaged, in practice, it is adjusted to accommodate the speed of blood flow; PRF is increased when imaging faster flow, and decreased when imaging slower flow.
Time averaged flow	RMS(pulsatile flow)	Variability in the power Doppler spectrum observed over one or more cardiac cycles.

Table 4.3: Criteria used to standardize power Doppler images. These variables are the components of the αPDI vascularity metric.

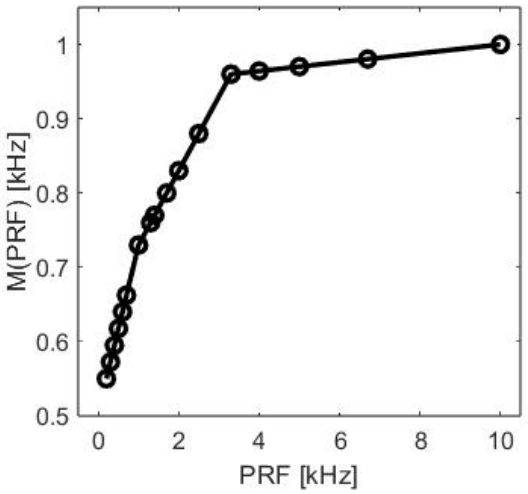

Figure 4.7: Mapping function, $M(PRF)$, used to scale PRF from 0.5 to 1 for standardizing PD images acquired under different PRF settings

PDI values were standardized using Equation 4.7,

$$\alpha PDI = PDI \times A \times M(PRF)[dBmm^2] \tag{4.7}$$

where $M(PRF)$ is the mapping function used to normalize PRF from 0 to 1, and A is the area, or the number of pixels multiplied by the color Doppler pixel size mm^2.

Three seconds of ultrasound cine were collected from the anterior forearm at rest and after exercise at frame rates of 5- and 6FPS, respectively, and at PRF settings of 1kHz and 1.3kHz, respectively. Distribution of αPDI and PDI values from all frames were plotted in box-whisker plots. Rest and exercise image data were compared using wilcoxon rank-sum test.

Histograms of the PDI data, displaying average pixel count (y-axis) per bin, 30-70 dB in 1 dB width bins (x-axis). The noise floor, calculated using the inflection point of the histogram, was identified at 30dB. The average pixel count was calculated as the RMS value over 3 seconds of frames. Similarly, histograms of the αPDI standardized data were used to show pixel counts in equivalent bin sizes. Comparison of rest and exercise image data were compared at each bin using either paired-sample t-test or wilcoxon rank-sum test, depending on normality of data.

4.3 Results

4.3.1 Experiment 1: Time-series analysis

Area of colored pixels over 1-second ultrasound cine clip of flow phantom data shows that flow through the rigid tube is non-pulsatile. Area of colored pixels over 6-second ultrasound cine clip shows the pulsatile flow of the forearm. Time-averaged estimates of non-pulsatile and pulsatile flow should use *mean* and *RMS* respectively. See Figure 4.8.

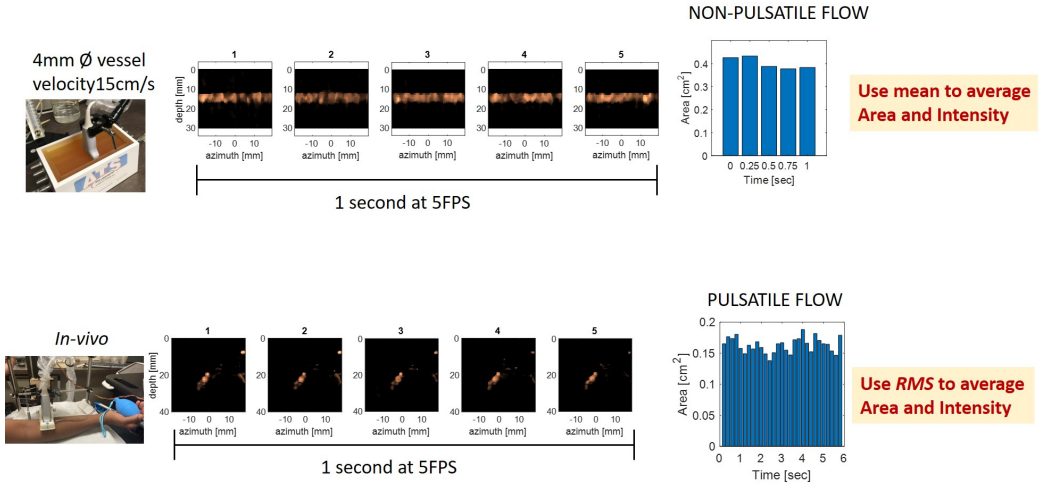

Figure 4.8: Experiment 1: One second of PD images from a flow phantom and forearm. Plots of area over over time, presenting non-pulsatile flow in rigid tube of phantom, and pulsatile flow in forearm.

4.3.2 *Experiment 2: Flow phantom calibration*

PD pixel size was determined to be 200μm x 200μm. The lowest velocities detectable through the 2-, 4- and 6mm vessels were found to be $-5.48, -1.03, -2.46 cm/s$ (flow rates $0.13, 0.6, 0.28 cm^3/sec$ respectively). See Figure 4.9.

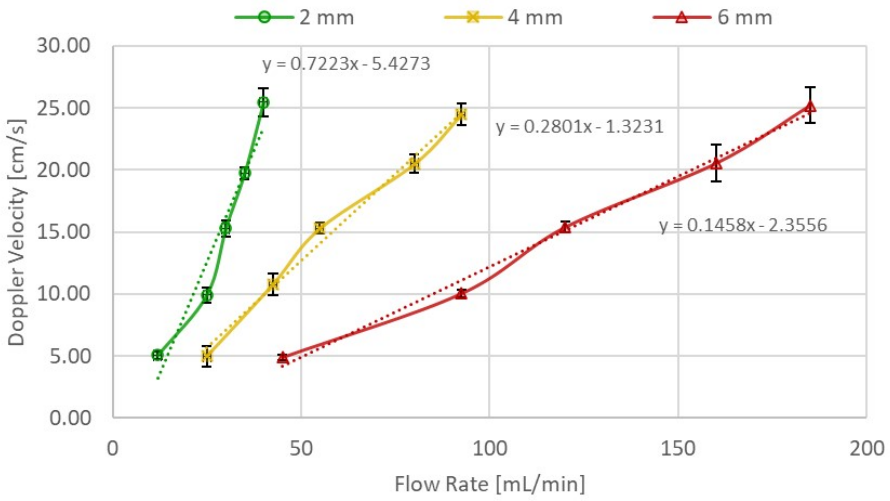

Figure 4.9: Experiment 2: Doppler velocities of blood mimic fluid through flow phantom vessels at variable flow rates.

4.3.3 *Experiment 3: Effect of exercise on PD image of the forearm*

The histograms of the forearm PDI images show that both quantity of pixels (y-axis) and range of intensity values (x-axis) increased after light exercise. Pixel quantity increases were predominant in PDI values less than 40dB. See Figure 4.10. The cumulative power distribution function (CPDF), the performance of PDI and αPDI, and demonstrates that the difference between lower intensity values, less than 35 dB, are statistically different between rest and exercise when scaled with αPDI ($p \ll 0.001$). See Figure 4.14. When comparing all pixels values from all frames, the distribution of rest compared to exercise is not differentiable (p=*0.2441*) with PDI,

compared to αPDI ($p \ll 0.00001$).

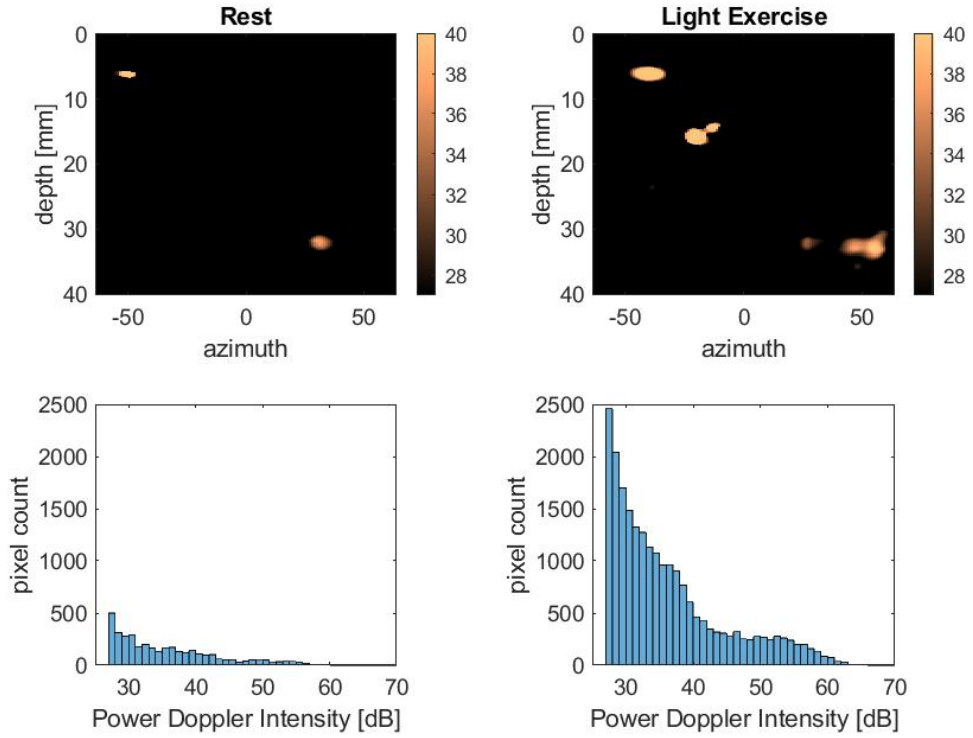

Figure 4.10: Experiment 3. PD images at rest(top left) imaged with PRF of $1kHz$ and after light exercise (top right) imaged with a PRF of $1.3kHz$, and the respective histograms (bottom row), showing pixel quantity (y-axis) by intensity band (x-axis).

4.3.4 Experiment 4: Main effects in image optimization

The experimental runs and responses are shown in Table 4.4. A full detail of the results is provided in Appendix C. The codded coefficients and 2-way ANOVA results are summarized in Table 4.5. The frequency, PRF and wall filter were identified as main factors in this experiment. The frequency settings will not need to be altered in superficial imaging studies. The wall filter is dependent on the PRF setting. The ultrasound unit automatically adjusts the wall filter around the PRF. The main factor identified in this experiment is the PRF *(p=0.039)*.

Tx. Comb.	Run	Run order		A	B	C	D=AB	E=AC	F=BC	RI		Total
		Vessel 1	Vessel 2							Vessel 1	Vessel 2	RI
def	1	1	5	-1	-1	-1	1	1	1	0.929	1.000	1.929
af	2	8	3	1	-1	-1	-1	-1	1	0.803	0.820	1.622
be	3	5	6	-1	1	-1	-1	1	-1	0.682	0.772	1.455
abd	4	4	2	1	1	-1	1	-1	-1	0.823	0.744	1.567
cd	5	2	7	-1	-1	1	1	-1	-1	0.871	0.582	1.453
ace	6	3	1	1	-1	1	-1	1	-1	0.774	0.794	1.569
bcf	7	6	8	-1	1	1	-1	-1	1	0.662	0.792	1.454
abcdef	8	7	4	1	1	1	1	1	1	1.000	1.000	2.000

Table 4.4: Experiment 4. Experimental runs for fractional factorial design experiment.

Term	Effect	Coef	SE Coef	95% CI	T-Value	P-Value	VIF
Constant		0.8156	0.0217	(0.7656, 0.8656)	37.62	0	
A	0.0584	0.0292	0.0217	(-0.0208, 0.0792)	1.35	0.215	1
B	-0.0121	-0.006	0.0217	(-0.0560, 0.0439)	-0.28	0.788	1
C	-0.0122	-0.0061	0.0217	(-0.0561, 0.0439)	-0.28	0.786	1
D	0.1061	0.0531	0.0217	(0.0031, 0.1031)	2.45	0.04	1
E	0.107	0.0535	0.0217	(0.0035, 0.1035)	2.47	0.039	1
F	0.1203	0.0601	0.0217	(0.0101, 0.1101)	2.77	0.024	1
A*F	0.0013	0.0007	0.0217	(-0.0493, 0.0506)	0.03	0.976	1

Table 4.5: Experiment 4. Doppler ultrasound image optimization codded coefficients.

4.3.5 Experiment 5: Power Doppler image dependence on PRF

Images of phantom peripheral vessels with blood mimic fluid moving at a constant flow rate showed that the pixel intensity and pixel quantity varied with PRF setting. In images of the 4mm vessel, imaged with three flow rates at three PRF settings, the PDI values and areas decreased as PRF increased. See Figure 4.11. These data suggest that PRF is inversely related to PDI and area.

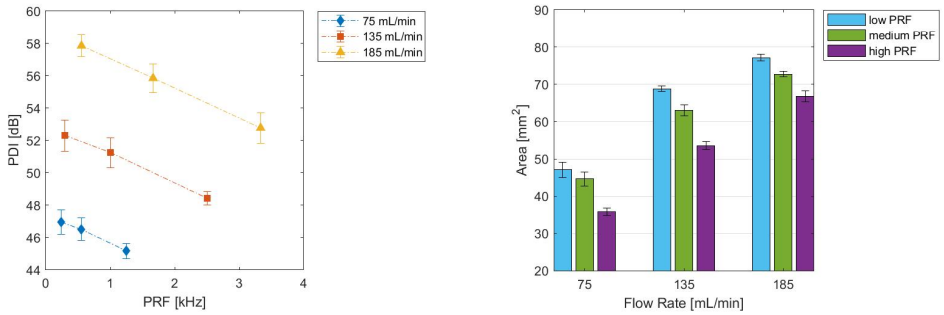

Figure 4.11: (left) PDI and (right) area of detected flow in a 4-mm diameter vessel with variable flow acquired at variable PRF settings.

The effect of variable PRF (0.2-2kHz) on pixel quantity across PDI bands is depicted in Figure 4.12. These figures display the changes in the flow profile through rigid tubes of different diameters, as PRF varies. In small vessels and slower flow speeds, the effect is less prominent. In the 4- and 6mm diameter vessels the number of pixels in the lower intensity bands increases as PRF increases, while the number of pixels in the higher intensity bands decreases. A spike in pixel count occurs at PRF of 0.2-0.4kHz, in all images, suggesting instrumentation artifact.

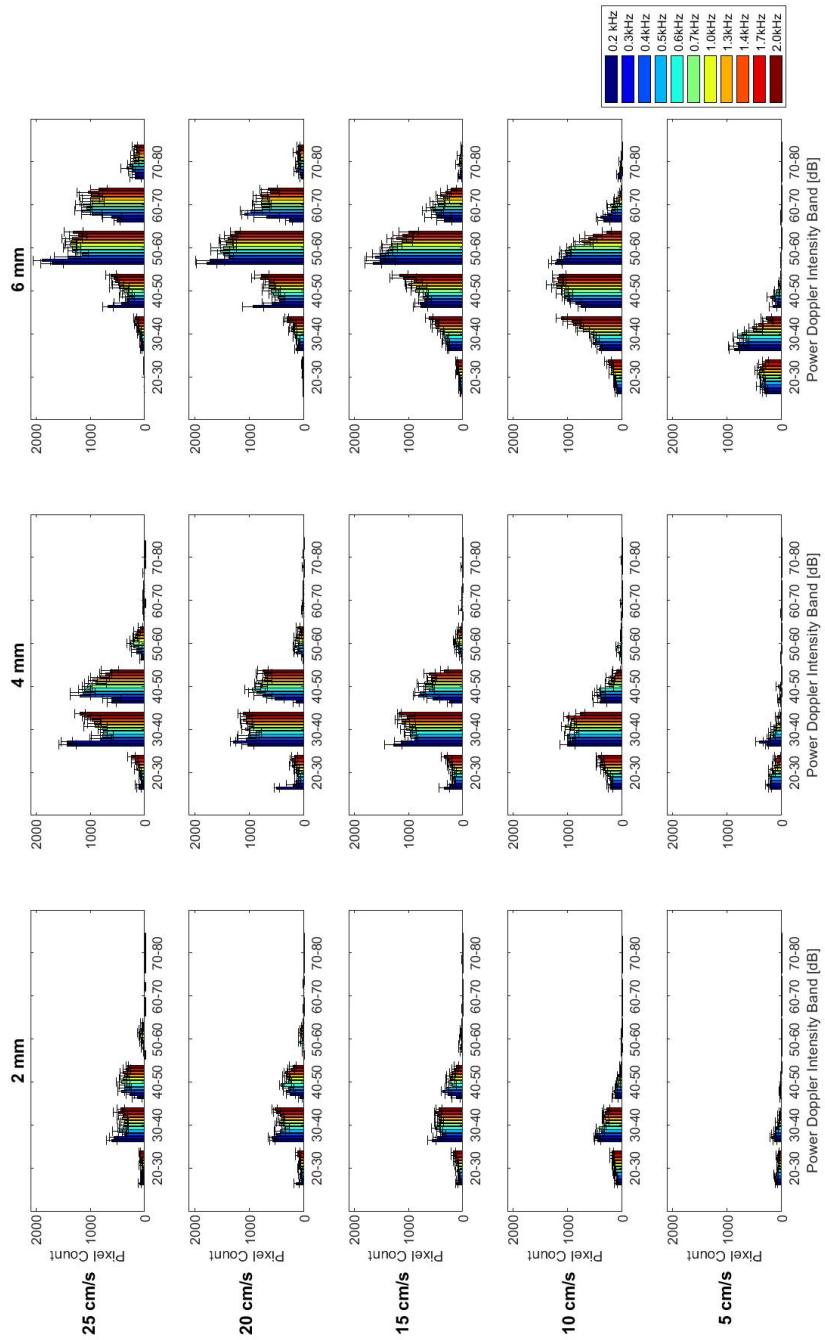

Figure 4.12: Effect of PRF on PDI area and magnitude show in histogram representation - pixel quantity (y-axis) by PD intensity band (x-axis) represents the area by magnitude. Values are shown as mean (bars) and standard deviation (error bars) over 5 frames.

4.3.6 *Experiment 6: Vascularity Metric, αPDI*

The box-whisker plots shows that PDI data from rest and after exercise were not statistically differentiable. However, statistical difference was found after standardizing the data with the αPDI metric. See Figure 4.13.

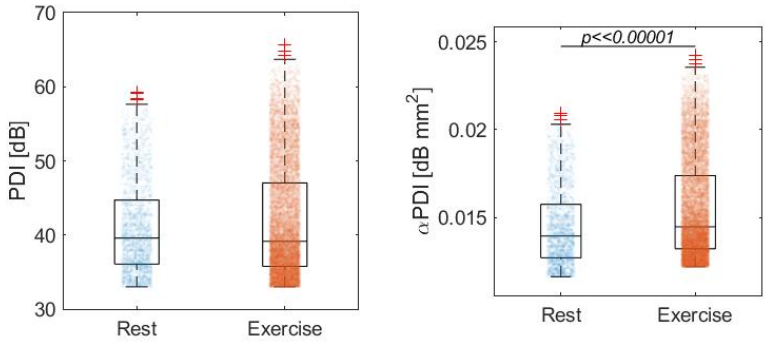

Figure 4.13: Comparison of rest and exercise distribution of all pixels with PDI and αPDI.

With histogram analysis, the PDI and αPDI data both show significant increases pixel counts across all intensity bins after exercise, where the lower intensities, $< 40dB$, more than doubled over the higher dB bins. The αPDI data displayed more pixels in lowest intensity ranges (≤ 0.012) at rest compared to after exercise. These data demonstrate that αPDI differentiated slower flows between rest and exercise compared to PDI alone.

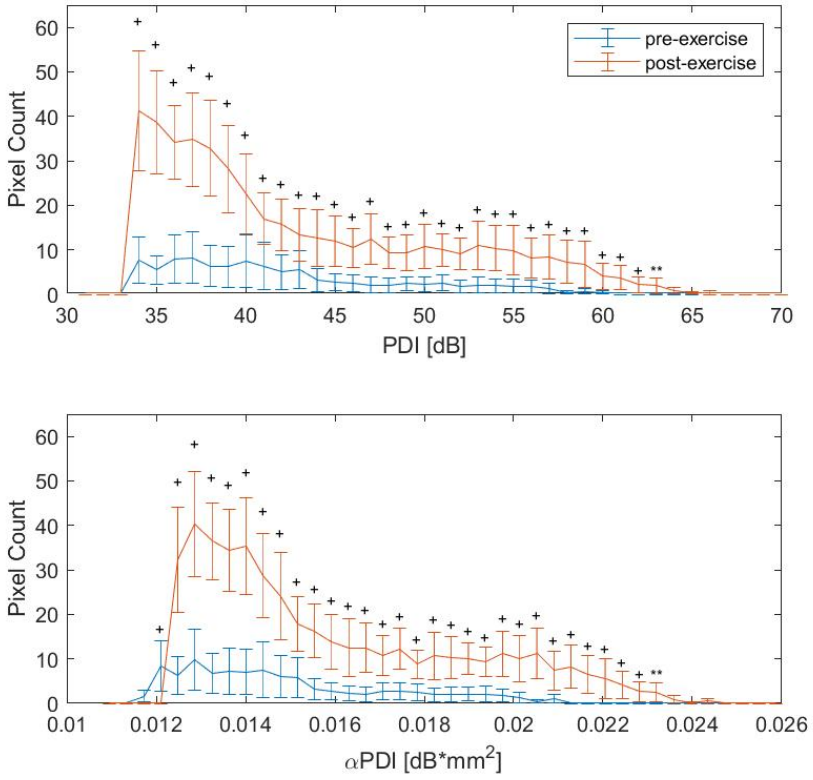

Figure 4.14: Histogram plots showing the quantity of pixels per PDI (top) and per αPDI (bottom), comparing rest and post-exercise. Values are shown with RMS and standard deviation (error bars) of the pixel quantities over 3 seconds of power Doppler ultrasound frames. Rest and post-exercise data were compared by each histogram bin with Wilcoxon-rank sum test, where $^{*}p < 0.05$, $^{**}p < 0.01$, $^{+}p < 0.001$.

4.4 Discussion

This study developed quantitative techniques for investigating muscle tissue vascularity with PD ultrasound. The techniques included a vascularity metric, called αPDI, and explored power Doppler intensity distributions with histogram analysis.

Typically, the maximum intensity values in PD images are of interest. However, clinically relevant information exists throughout the cardiac cycle. Blood flow

waveforms acquired with photo pulse plethysmogram, laser Doppler flowmetry and continuous wave Doppler ultrasound are evaluated for monitoring autonomic activity and screening for peripheral arterial disease. PD ultrasound cine contains clinically relevant data with the added dimension of depth. However, it has not yet been made accessible to the end user. This study demonstrated that time-series analysis of ultrasound cine may be used to evaluate pulsatile flow. In Experiment 1 the time-averaged estimate of pulsatile flow *in-vivo* was calculated using RMS. However, 2-D analogs of metrics such as the pulsatility index and resistivity index may be assessed from this same data. Inferences on diastolic portion of the blood flow waveforms data could be made with proper access of these data.

Experiment 2 used a peripheral vascular flow phantom to simulate expected blood flow velocities in peripheral vasculature. However, the inherent variability and pulsatility of blood flow *in-vivo* is challenging to replicate. Development of realistic phantoms with pulsatile flow and compliant vessels may support further development of PD image quantification.

In Experiment 3, a strong physiologic response was observed in PD images, i.e. increased blood flow after a single bout of light exercise, as expected. When comparing the distribution of pixel intensities in box plots or with descriptive statistics, no difference was found before and after exercise. Rather, differences were best observed using histogram analysis, i.e. the change in the quantity of pixels by intensity band. In the case studies of a preliminary experiment, Appendix C, and Experiment 3, physiologic provocation (light exercise) was shown to significantly impact slower flow (retrograde blood velocity and low dB, respectively) over faster flow (forward blood velocity and high dB, respectively). These studies agrees with 1-D blood flow waveform analysis, in that the entire pixel intensity range contains relevant information. This finding is useful, specifically in the challenging field of small vessel imaging, as

it suggests a that this methodology has merit. For small vessel imaging, Doppler velocity imaging is not suitable for quantifying blood flow, however, area change by PD intensity band is a promising option for quantitative assessment of tissue vascularity. Ultrasound manufacturers should provide the area of detected blood flow to the end user to improve quantitative value of PD imaging in small vessel ultrasound examination.

In practice, image optimization is accomplished by manually adjusting the PRF, as well as other settings. The fractional factorial analysis, Experiment 4, demonstrated that PRF was a main factor in Doppler ultrasound optimization. Experiment 5 then demonstrated the effect of PRF on PD images pixel intensity and area. Increased PRF settings were shown to decrease pixel intensity (PDI) and area of detected flow thought a rigid tube. While blood flow in the tissue is ever-present, it may not necessarily be detectable with PD ultrasound because the flow speed and/or density of moving scatteres are below the threshold of detection. Experiment 5 presented a closer look at this phenomena *in-vitro*. Flow profiles of a constant flow through a rigid tube were altered with PRF settings. This experiment clearly demonstrated the impact of the PRF setting in PD imaging. If manufacturers provide the area of detected flow, the optimal PRF setting may correspond with the maximum area is of detected flow. Area could possibly be used to assist the ultrasound operator in finding the optimal PRF setting. Further investigating is needed to confirm and develop this functionality.

The effect of PRF was explored in a rigid tube. The effect of PRF setting may be even more exaggerated *in-vivo*, where blood flow is variable and pulsatile. Muscle tissue vascular investigations using PD imaging commonly maintains the PRF at one setting , "as much as possible" [20], for all samples. However, Experiment 5 shows that this approach may omit clinically relevant blood flow detection. Maintaining

PRF at one setting may not be an appropriate method for standardizing PD images research and clinical diagnostics. Furthermore, studies using PD ultrasound imaging should report the PRF settings.

While both PDI, i.e. velocity magnitude, and area of detected blood flow were shown to increase after light exercise, these pre- and post-exercise images were acquired at different PRF settings (1kHz and 1.3 kHz, respectively). In Experiment 3, the effect of PRF on PDI magnitude and area was investigated. The PRF setting can be interpreted as flow speed metric. The vascularity metric, αPDI developed in Experiment 6 accounted for the PRF setting. In order to utilize PRF as a scaling factor, a mapping function was developed, optimized for slow flow detection. αPDI successfully detected a significant difference between the pixel intensity distributions, where PDI did not. The αPDI histogram further confirmed that significant change occurred in the slower flows region, or lower intensity values, ¡ 40dB.

This region of detected flow was more differentiable with αPDI compared to PDI. Experiment 6 demonstrated that PRF may be utilized as a scaling factor to help quantify PD images. The mapping function may be customized per clinical application to focus differentiation on the intensity range of interest (lower or higher flows, as needed). The sensitivity and specificity of this technique should be investigated to further develop the diagnostic value of αPDI.

The overall diagnostic value of slow blood flow has been highlighted throughout the experiments presented here. Literature suggests that OMT effects the retrograde flow (diastolic or venous flow) [151], which are generally slower than the forward flow velocities, e.g. arterial flow and systolic peaks compared to venous flow and diastolic waveforms). In PD imaging, increases in small vessel flow may present as additional low dB spots. When quantified, color pixel density has been the metric of choice. αPDI captures both pixel intensity and area changes, demonstrating that

it is a comprehensive metric that values low flow changes. Investigating the effect of OMT on blood flow requires tool capable of discerning even the slightest variations in low velocity flows. Slower flow can be difficult to capture due to low PRF settings and increased noise floor, and lack of functions supporting differentiation in this region of flow. Clinical applicability of slow flow differentiation is ubiquitous and the techniques developed here have demonstrated a possible expansion of PD ultrasound to meet these needs.

Incorporating the area in the standardizing factor assumes the image is absent of artifact encountered with low PRF settings (color bleeding, or erroneous color pixels from motion). In this experiment color gain was constant, and wall filter automatically adjusted with the PRF setting. The background noise in PD images tended to be low intensity, whereby further artifact removal could be completed during post processing. However, other pathologic states or other anatomical regions may impact flow and tissue attenuation in different ways. Therefore, this method may not be generalizable. Defining the appropriate noise-floor threshold for sufficient low amplitude detection is a non-trivial task. The cut-off value may vary from application to application, or from patient to patient. In both tissue phantom and forearm imaging, the noise floor increased with lower PRF settings. This may be of concern when investigating even slower vascularity changes, where PRF settings are low, requiring higher frequency ultrasound, for lower flow resolution.

In the flow phantom experiments, the vessel boundary and background were well defined, so artifact was excluded by assessing pixels strictly within the vessel boundary. In practice, the vessel boundaries may not be visible, especially concerning small irregular vasculature. PD ultrasound is effective at imaging vessel boundaries as the the signal reflects pooling erythrocytes in the center of the vessel due to parabolic flow profiles [158]. In the anterior forearm experiment, the low intensity background

noise values were exponentially greater in quantity than the vascularity values, so the inflection point of the histogram was a natural method for finding the appropriate threshold. Elfarnawany, et. al., developed an automated wall filter selection curve (WFSC) method with adaptive threshold, capable of varying by region within a PD image. This method improves the PD image by automatically removing artifact without intervention of the ultrasound operator. The images are then more suited to being quantified [48]. Automated threshholding was beyond the scope of this project, however, is an important consideration for future investigation.

4.5 Conclusion

Power Doppler images require standardization for comparison. Histogram analysis of PD images showed that the quantity of images per intensity band was able to quantify changes in vascularity significantly more than intensity values alone. To advance PD's applicability in quantifying tissue vascularity, area of detected flow should be made available in conventional CFI. Studies using PD imaging should report PRF values, as PRF has been shown to affect image outcomes. The combination of color pixel intensity, area of detected flow and ultrasound optimization factors comprehensively reflect small vessel flow. Further investigation is needed to examine the diagnostic accuracy of the proposed techniques. With further development power Doppler imaging may be utilized as a quantitative imaging modality, specifically in small vessel imaging.

Chapter 5

TISSUE COMPLIANCE ASSESSMENT

5.1 Introduction

It is well established that MTP presents with tissue stiffness [107], however objective assessments have not yet been standardized for MTP diagnosis and treatment. While palpation is the accepted diagnostic evaluation method, systematic reviews have indicated that manual detection of MTP may be unreliable [107]. Objective evaluation of MTP are warranted. Elastography is an ultrasound and magnetic resonance imaging based technique for measuring tissue stiffness clinically. It is a well established diagnostic tool for assessing for liver, breast and gland pathology [38, 100, 150]. Musculoskeletal applications include joint and muscle tissue degeneration [100]. Quantitative elastography techniques have been used to estimate the elastic modulus of MTP ($12.3-14.7kPa$) compared to adjacent normal tissue ($5-8kPa$) [107] in the neck and upper trapezius muscles. However, few studies have investigated MTP treatment with elastography.

Quantitative elastography techniques such as shear wave elastography (SWE) and acoustic radiation force impulse (ARFI), utilize an external vibration to induce tissue motion. The shear wave velocity propagating through the tissue is deduced from ultrasound cine, providing a quantitative measure of tissue stiffness. In contrast, strain elastography (SE) is a qualitative method that visualizes relative tissue strains in-frame. SE imaging involves calculating the underlying tissue deformation rate, or strain, induced by applying a quasi-static pressure to the tissue using the transducer. While SE imaging offers advantages such as minimal tissue interrogation and ease of

use for the clinician, it is limited in that the stress applied is unknown so the tissue strain is qualitative. In order to enable meaningful comparison of tissue stiffness changes following OMT, standardization of SE images is necessary. The purpose of this study is to propose an SE standardization technique by estimating the applied stress during imaging, termed as the tissue resistance estimate (TRE). This technique is developed and validated in tissue phantoms and human forearms, specifically optimized for superficial muscle tissue evaluation.

5.1.1 Ultrasound and Elastography Principles

Biological tissue is a viscoelastic material where a small applied stresses deform the tissue proportionally (linearly) and predominantly in the axial direction, and a large stress deforms the tissue non-linearly in axial and lateral directions [44]. Shape recovery is almost immediate when compressed within the linear (Hookean) region of the stress-strain curve. In all elastography methods, the ratio of stress (σ) to strain (ε) , or the Young's modulus, $E = \sigma/\varepsilon$, is estimated, [60]. The E approximation is only applicable in the linear range of deformation. To maintain linear tissue deformation during elastography imaging, the compressive force should deform the tissue within $1-2\%$ of the imaged depth [25, 149, 163, 17]. Strain elastography (SE) mimics palpation by manually applying a quasi-static pressure to the tissue with the transducer during imaging. Conventional SE functions provide a visual indicator of tissue deformation to help guide the operator to achieve optimal manual compression (distance and rate) required for SE image rendering. The required motion for SE rendering varies by unit and manufacturer and by the image processing techniques used.

SE is well suited for visualizing relative strain differences between background and target tissue, eg. adipose compared to fibrosis in the breast tissue, muscle to thyroid

nodule [38], or healthy to pathological liver [42], and performs well with solid tumor and cyst detection. While SE is clinically standardized for organs and glands - liver, breast, thyroid, prostate, lymph node, salivary and parathyroid glands [38, 100, 150], musculoskeletal applications are less developed. Applications of SE in joint/tissue degeneration or osteoporosis [100], multiple sclerosis, [82], congenital muscular torticollis, tendinitis [90], plantar fascitis [177], cerebral palsy, and myostosis, and myofascial pain [176, 177] have been found useful but are not yet considered standard care. Muscle tissue poses a challenge to SE imaging compared to other tissues, specifically, muscle tissue lacks a reference/background tissue within frame to standardize the SE color map. While, healthy organ, gland or adipose tissues can serve as a reference tissue, the mechanical properties of muscle tissues alter with physical provocation or intervention or demand, and are highly variable within and between subjects. Normal musculoskeletal tissue stiffness ranges between 5-170 kPa [70], challenging uniformity of background muscle tissue for SE imaging. Standardizing SE images have been proposed, but have not yet been addressed in MTP research.

5.1.2 Quasi-quantitative methods in strain elastography

Quasi-quantitative approaches in SE images focus on comparing relative strain differences within frame. The most common approaches of assessing a strain image is by visual inspection, for example, to determine the presence of a tumor nodule in liver or breast tissue. A widely used technique for quantifying the nodule stiffness compared to background is the target to background tissue strain ratio (SR) [72]. For this technique, cutoff values need to be determine for normal and pathological tissues [115]. Since a reference tissue is not available in muscle tissue, Illomie, et. al. scored the heterogenity of the strain image, from 1 to 4, where 4 denoted the most heterogeneous indicating advanced pathological state of multiple sclerosis (MS)

[82]. This technique was found to highly correlated with actual diagnosis. Chino et. al, proposed a technique using calibrated hard and soft phantom standoffs to calibrated the color pixel values [29, 30]. This technique improved intra- and inter-investigator reliability, and strains measured from the medial gastrocnemius were within comparable with magnetic resonance elastography (MRE).

5.1.3 Limitations

SE imaging poses several limitations with musculoskeletal tissue imaging. These limitations are as follows:

- SE image acquisition is user dependent. Image quality relies on steady and consistent periodic compression which can be challenging to achieve manually. SE imaging is vulnerable to decorrelation noise which may lead to diagnostic errors [144]. Also, the push force required to deform tissue $1-2\%$ of depth to maintain linear response varies with tissue stiffness; hard tissues require greater stress than soft tissues. Strain values may vary with compression and compression rate. Controlled pulsatile motion is needed for SE image acquisition.

- Strain maps produce relative values. The applied stress is unknown [25] and musculoskeletal tissue has no suitable reference/background contrasting tissue to calibrate the SE values. Monitoring pathology is challenging because tissue stiffness alters with pathology or repair [90], and strain images may not be comparable.

- Quantification methods for musculoskeletal SE are not yet standardized, and optimizations are specific clinical application and anatomical regions.

5.1.4 Proposed technique

In strain imaging, the stress applied to the tissue is unknown. We hypothesize that strain images may be scalable with estimation of applied stress during SE imaging. Using this scaled image, quasi-quantitative methods may be employed to compare repeated measures data.

The proposed technique addressed three limitations inherent with SE imaging in repeated measures design for musculoskeletal tissue assessment by:

1. automating transducer motion with a controlled experimental setup,
2. estimating tissue resistance to applied stress with force sensitive resistor,
3. standardizing the strain image using the tissue resistance estimate to obtain a measure of tissue compliance (J), and
4. quantifying the strain image by depth.

5.2 Methods

5.2.1 Controlled Setup

A controlled experimental setup was built to minimize user dependence in SE imaging. In this setup, the ultrasound transducer was mounted to a motorized arm with adjustable step size and speed. A force distribution boot was fixed to the transducer head and applied uniform tissue compression in the axial direction. A force sensitive resistor (FSR) was fastened to the transducer boot to measure pulsatile stress applied during SE imaging. Custom graphical user interfaces (GIU) for FSR calibration and data acquisition were developed in MATLAB, and run on dedicated computer during image acquisition. See appendix for details on the experimental setup. Figure 5.1b displays the boot and motorized arm assemblies.

5.2.2 Instrumentation

SE images were acquired with open-source ultrasound unit (SonixTouch Q+, BK Medical, Burlington, MA), using a linear transducer (L14-5/38) at 15 frames per second. The ultrasound was preset to the general MSK setting. Gain was set to

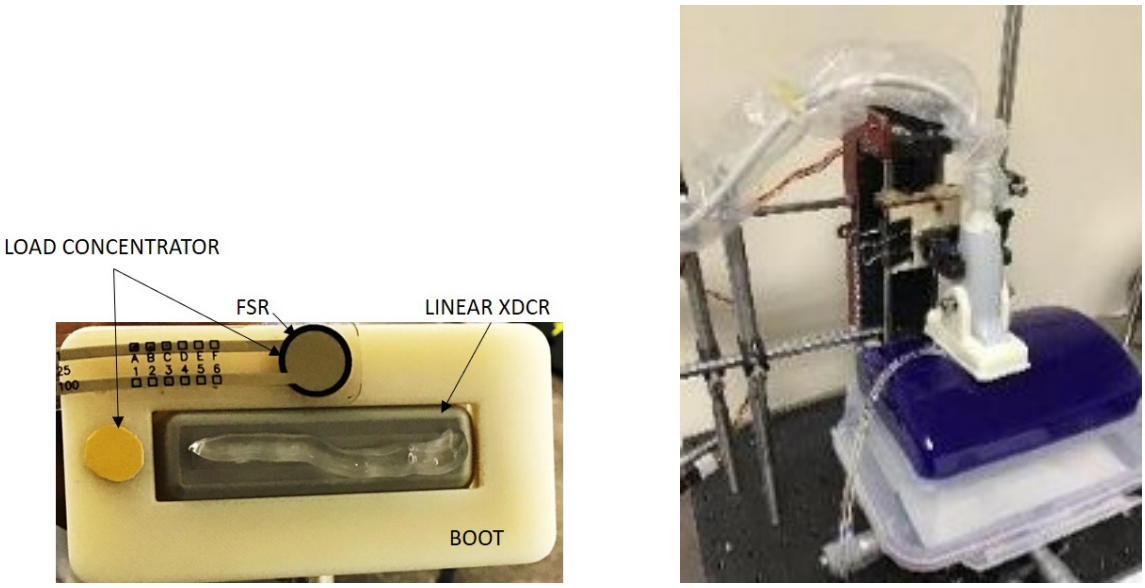

(a) (b)

Figure 5.1: Experimental Setup. (a) Transducer boot assembly with FSR and load concentrator. (b) Transducer in motorized arm, secured to a bread board with optical posts, imaging a tissue phantom

67. Time gain compensation (TGC) was set to increase gain in the lower half of the image (setting 4). One focus was placed mid-depth. The FSR sampling frequency was $10Hz$. Table 5.1 provides the acoustic, mechanical and processing parameters used for tissue phantom and forearm imaging. Figure 5.2 provides the experimental setup of tissue elasticity phantom.

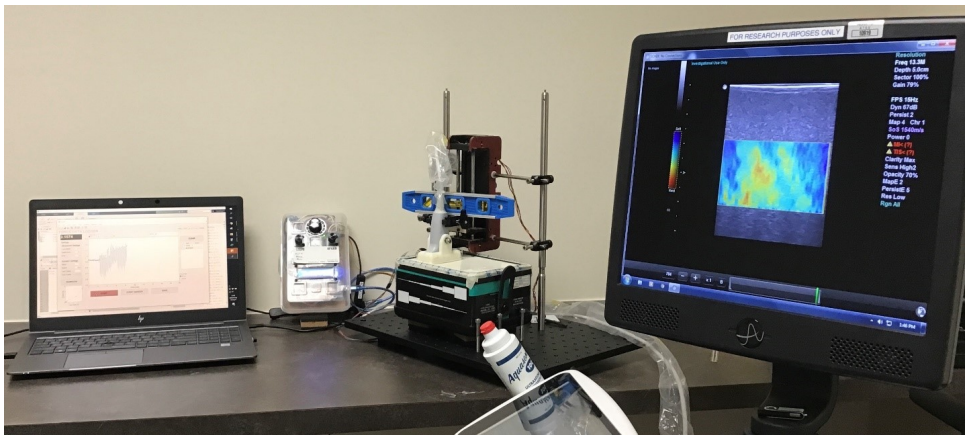

Figure 5.2: Experimental setup for imaging the tissue elasticity phantom

a) ACOUSTIC	Speed of sound through soft tissue		1540 ms^{-1}
	Center frequency		13.3 MHz
	Dynamic Range		67 dB
	Pitch		305
	Element		128
	Focus Depth		30 mm
	Depth		30 - 50 mm
	Length (azimuth)		38 mm
	Elastographic frame rate		15 FPS
	Axial resolution (delta-y pixel size)		0.69-0.106 mm
	Lateral resolution (delta-x pixel size)		0.69-0.106 mm
b) MECHANICAL	Transducer palpatory motion frequency		4-6 Hz
c) PROCESSING	Number of wavelengths per Xcorr window		5-40
	Window overlap:	phantom	60-95 %
		forearm	82%
	Xcorr window size		[2 2] – [20 30]
	Smoothing filters		gauss kernel 1-9
			median filter [8 12]

Table 5.1: SE Imaging Parameters. a) Acoustic parameters of the ultrasound unit, b) mechanical parameters set with the motorized arm for data acquisition, and c) image post-processing parameters.

5.2.3 *Data Acquisition*

A bubble level was used to set the transducer at 90^o to the tissue/phantom. Prior to each test session, the FSR was calibrated with 10-, 20-, 50-, 100-, 200-, 500-, and 1000 g weights and converted to units Newtons. The motorized arm was set to pulsate on the tissue at approximately $5Hz$ without losing contact with tissue. An indicator on the ultrasound screen provided visual feedback for sufficient tissue compression and rate. The FSR trace provided an additional visual feedback indicating suitable compression and rate as well as transducer-to-tissue alignment. RF echo images and FSR data were acquired simultaneously for a duration of 5 seconds. Figure 5.3 shows a schematic diagram of the experimental setup used in both tissue phantom and human forearm imaging (Figure 5.4).

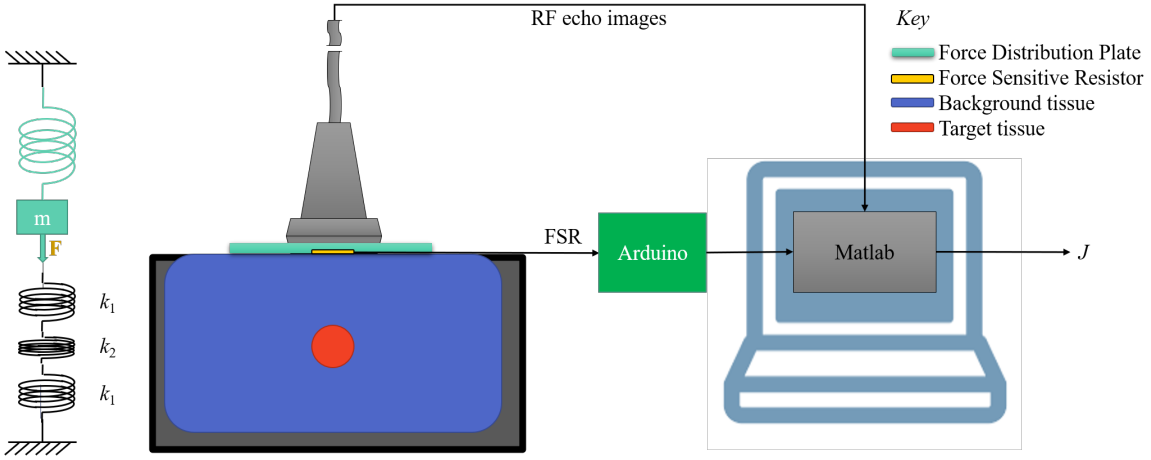

Figure 5.3: Schematic diagram of instrumentation with simultaneous RF echo image and FSR data acquisition, integrated with Arduino board. The spring force body diagram (left) illustrates the applied force with periodic motion in the axial direction, with a 1D spring model, with spring constants of background, k_1, and inclusion (target), k_2, and $k_2 >> k_1$.

When imaging the anterior forearm, the participant was seated, with their arm supinated and positioned beneath the transducer. The arm was placed on a cushion, and the height of the seat was adjusted to subject's comfort to limit postural restrictions on blood flow. See Figure 5.4.

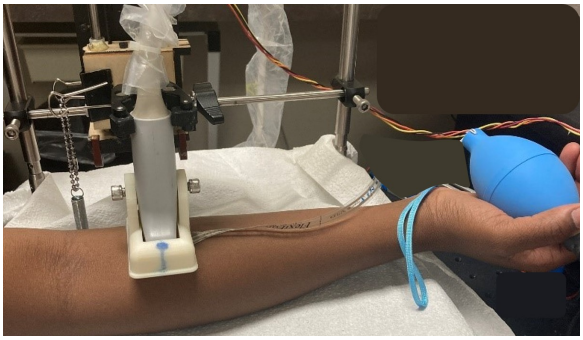

Figure 5.4: Experimental setup for forearm imaging at rest. The soft clench bulb was gripped to image muscle contraction.

5.2.4 Algorithm

The proposed algorithm used estimates of strain (ε) and applied stress (σ) to estimate tissue compliance (J), or inverse Young's modulus. Tissue strain was estimated from the RF-echo images using normalized cross-correlation (NCC). The cross correlation was used estimate tissue displacement, δz, between the windowed pre- and post-compression frames. Then the spatial differentiation of the displacement map was calculated by integrating the displacement map, $\delta z/\delta x$, [123, 149]. The tuning parameters for the NCC method are the window overlap and window size. Gaussian and median filters smoothed and denoised the strain image.

The stress, or tissue resistance estimate (TRE), was calculated from the FSR data. FSR data was first converted from volts to force in Newtons units. Then the mean peak-to-peak amplitude (f_{pp}) was calculated using a peak detector. (f_{pp}) was divided by the surface area of the boot ($A_{boot} = (31.2m^{-}2)$ to obtain the final TRE estimate.

See Equation 5.1. The tuning and mechanical parameters used in the phantom and forearm experiments are provided in Table 5.1.

$$\sigma = \frac{\frac{1}{n}\Sigma f_{pp,n}}{A_{boot}} \tag{5.1}$$

where n is the number of f_{pp} over the duration of the signal (3-5 seconds). The strain map values were scaled with TRE, producing a quasi-quantitative representation of inverse Young's modulus $E^{-1} = \varepsilon/\sigma$, or tissue compliance, J, Equation 5.2.

$$J = \frac{\varepsilon}{\sigma} = \frac{\delta z/\delta x}{F/A} = \frac{\delta z/\delta x}{\frac{\frac{1}{n}\Sigma f_{pp,n}}{A_{boot}}} \tag{5.2}$$

5.2.5 Experiments

Four experiments were conducted to test the data acquisition method (Experiments 1 and 2) and the TC algorithm (Experiments 3 and 4) using conveniences samples of healthy subjects and a tissue elasticity phantom. The anterior forearm anatomy imaged with ultrasound is shown in Figure 1.1.

Figure 5.5 illustrates the major steps for developing the data acquisition and post-processing technique.

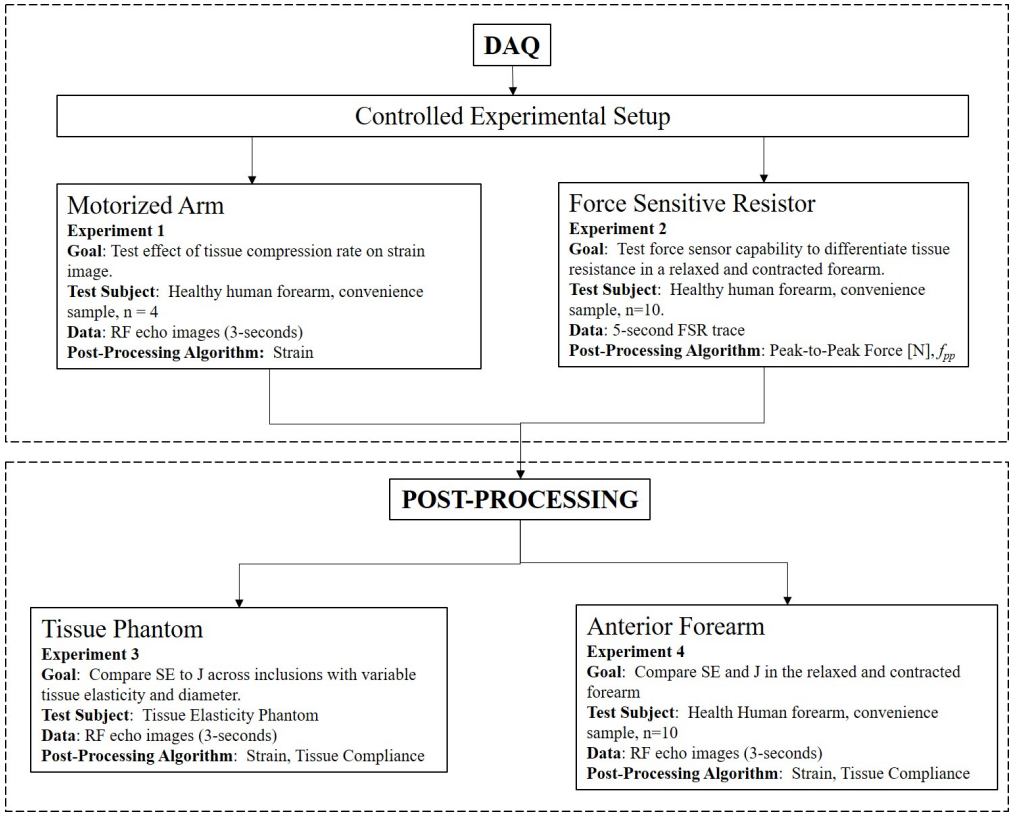

Figure 5.5: Generalized block diagram representing major steps in testing the data acquisition (DAQ) method and the post-processing algorithm

Experiment 1) Effect of tissue compression rate on strain map

The effect of tissue compression rate on the strain map was tested in the anterior forearm in a convenience sample of 4 healthy subjects. The resting forearm was imaged with SE at compression rates of $4-, 5-$ and $6Hz$. The images and histogram representations were compared visually.

Experiment 2) TRE in relaxed and contracted forearm

TRE was measured in the relaxed and contracted forearm in order to determine if soft and hard muscle tissue is differentiable using the FSR. FSR readings from a convenience sample of 10 healthy subjects were collected over 5 seconds during transducer palpatory motion, using the setup shown in Figure 5.4. The average force amplitude (f_{pp}) over 5 seconds was calculated and compared across all 10 subjects. Group means were compared with Wilcoxon ranksum test.

Experiment 3) Elasticity phantom

The experimental setup and the TC algorithm were tested on a tissue elasticity phantom (CIRS Elasticity QA Phantom, Model 049, CIRS Ing, Norfolk, VA). Two $4mm$ inclusions with elastic moduli of $8-$ and $14kPa$ simulated normal and MTP tissue, respectively. The inclusions were sampled 5 times for each post-processing technique compared - the built-in SE image (USX), SE (non-calibrated strain image) and TC. The strain ratios were calculated as the ratio of $non\text{-}MTP$-to-MTP strain, and compared with ttest.

Experiment 4) Relaxed and contracted forearm

The experimental setup and TC algorithm was tested on the anterior forearm in a convenience sample of 5 healthy volunteers. The forearms were imaged in the relaxed

and contracted states to simulate soft and hard tissue, respectively. Images from the three post-processing techniques USX, SE with NCC and TC, were compared. The mean elasticity estimates from superficial ($2 - 11.5mm$) and deep ($11.5 - 25mm$) tissue layers were compared with paired-sample t-test.

5.3 Results

Experiment 1: Effect of tissue compression rate on strain map

The strain maps varied with compression rate. In each test subject, the tissue appeared softer at a different rate. Figure 5.6 shows the strain map of each test subject imaged at $4-, 5-$ and $6Hz$.

Figure 5.7 shows the histogram representation of the strain maps by compression rate, per subject. In Test 1 and 3, the strain distribution shifted towards higher values (soft tissue) as compression rate increased. In Test 2 strain distribution increased at $5Hz$ and decreased with $4-$ and $6Hz$. In Test 4, the strain distribution shifted towards lower values (hard tissue) as compression rate increased. The strain distribution of each tests, shown as histograms, in Figure 5.7.

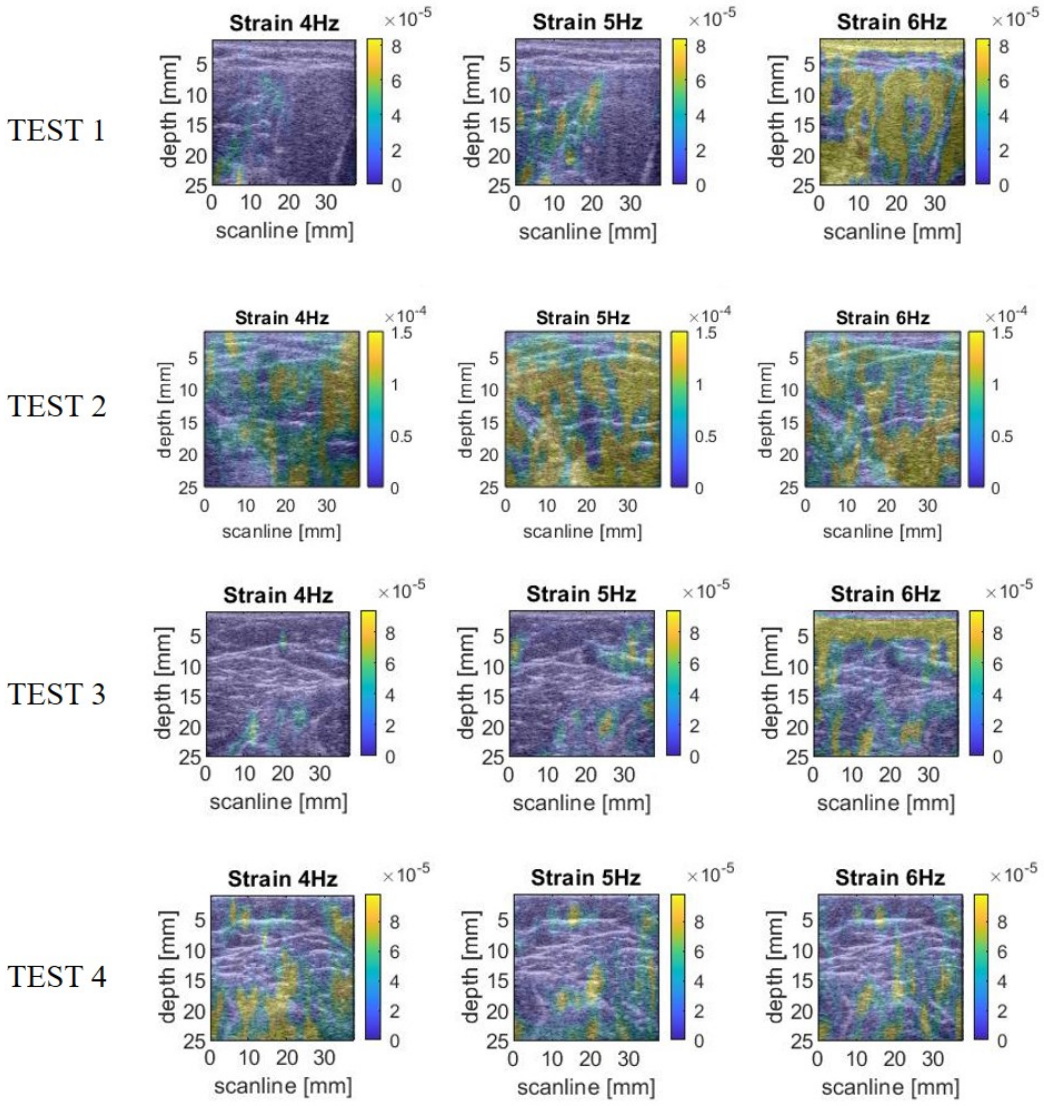

Figure 5.6: Strain images from resting forearms of 4 healthy subjects, at variable compression rates, $4-, 5-$ and $6Hz$. The color bar scales are standardized within each test, where 0 (blue) is hard and higher values (yellow) are soft tissue.

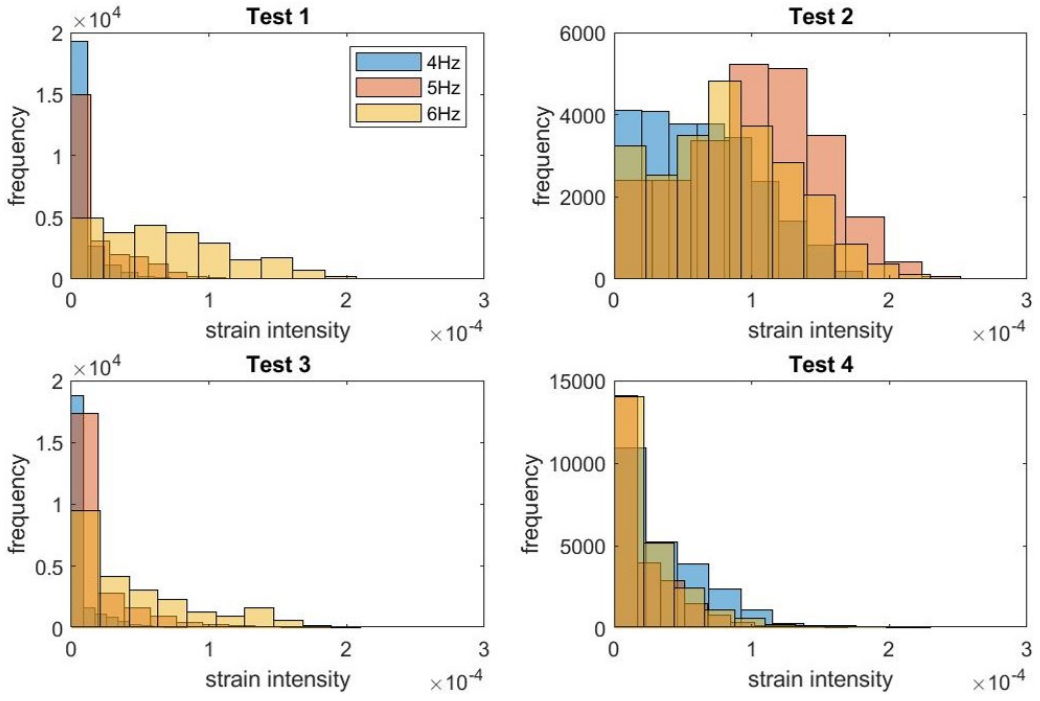

Figure 5.7: Histograms representation of strain distribution comparing variable compression rates $4-, 5-$ and $6Hz$ from 4 tests.

Experiment 2: TRE in relaxed and contracted forearm

The force amplitude increased with muscle contraction. Figure 5.8 shows the oscillating force trend over 5 seconds in the relaxed and contracted tissue. The oscillation visualizes the periodic tissue compression by the transducer-booth assembly used in SE imaging. Figure 5.8 shows the mean force amplitude by subject. The baseline force amplitude (relaxed forearm) varied by subject. The force measured during contraction was greater than the relaxed muscle in 6 of the subjects. For test subjects 1 and 9, the large error bars suggest instrumentation or transducer misalignment. In test subjects 7 and 10, the discrepancy may be a result of the test subject's grip style; flexors were relaxed and therefore the FSR registered a lower resistance. To mitigate this issue in the human pilot study, instructions on how to grip the bulb appropriately

was included in the study protocol (Chapter 6). The group means between relaxed and contracted forearms were nearly significant (p=*0.0022*).

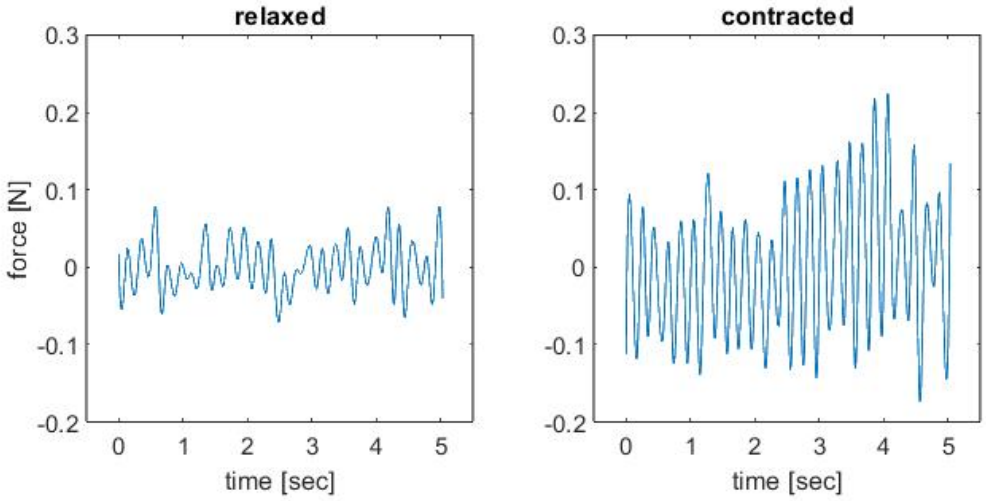

Figure 5.8: Force traces in measured on the relaxed and contracted anterior forearm for 5 seconds.

The mean f_{pp} the relaxed and contracted forearm from 6 tests, over 5 seconds, is shown in Figure 5.9. The relaxed muscle has lower force amplitudes than the contracted muscle.

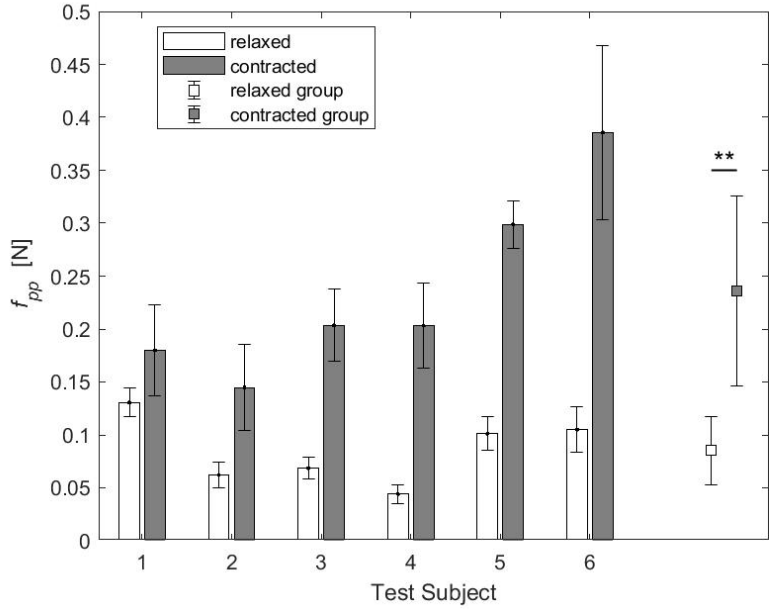

Figure 5.9: Tissue resistance estimates from relaxed and contracted forearms of 6 subjects. The bar plots with error bars represent the mean force amplitude, f_{pp}, and standard deviation from a $5 - second$ interval of FSR data. The group means and standard deviations of relaxed and contracted forearms are represented by the right most error bars. The forearm tissue resistance is statistically higher when contracted than when relaxed, calculated with Wilcoxon-rank sum test, $^{*}p = 0.0022$.

Experiment 3: Elasticity phantom

TRE estimates of the hard $14kPa$ and soft $8kPa$ targets were 137.1 and 56.213 N/m^2, respectively. Images of the $4mm$ diameter inclusions produced with SE and TC had smooth surfaces within the inclusions and poor boundary detection compared to the USX. See Figure 5.10. The color scales are unique for each algorithm: USX is on a 0-256 RGB value scale, SE is on a unitless strain value scale obtained with NCC, and TC is a quasi-quantitative representation of $[kPa^{-1}]$ or inverse Young's elastic modulus units $[m^2/N_{-1}]$.

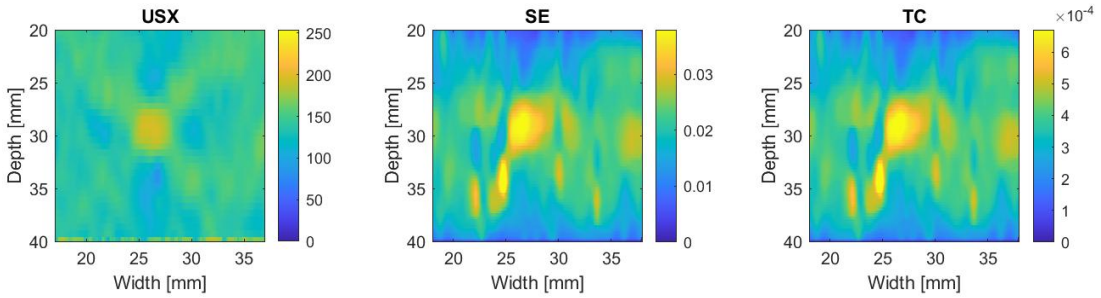

Figure 5.10: Elasticity images of $4mm$, $8kPa$ inclusion in $25kPa$ background obtained with Ultrasonix (USX) built-in SE function, SE (not calibrated with TRE), and TC (SE calibrated with TRE).

Elasticity ratios from the actual Young's modulus, built-in SE (USX), SE using NCC, and TC images of the $8kPa$ and $14kPa$ inclusions are compared in Table 5.2. USX indicated that both the hard and soft targets were approximately $190RBG$. The SE and TC estimates found that the 8kPA inclusion had higher strains than the 14kPa inclusion. The elasticity ratio obtained with USX was was near unity (i.e. no difference between the 8- and 14kPa inclusions), and therefore underestimated the elasticity ratio. The elasticity ratio found using SE, 1.71, nearly matched the actual Young's modulus ratio of 1.75. The TC method overestimated the ratio. Each post-processing technique produced a significantly different elastic ratio.

	Young's Modulus [kPa]	USX [RBG value 0-255]	SE [unitless]	TC [Pa^{-1}]
Normal Tissue Phantom	8	189.97(3.53)	3.77E-02(9.08E-04)	6.71E-04(1.62E-05)
MTP Tissue Phantom	14	187.28(2.34)	2.21E-02(9.70E-05)	1.61E-04(7.08E-07)
Elasticity Ratio	1.75	1.01	1.71	4.17
Normal vs. MTP within-group difference	--	*p=0.222*	*p=0.0079**	*p=0.0079**
Elasticity Ratio between-group difference	--	*p=1.012E-06**		
	--		*p=1.28E-07**	
	--	*p=5.65E-08**		

Table 5.2: Comparison of elasticity estimates and ratios of $4mm$-diameter inclusions with elastic moduli of $8kPa$ and $14kPa$ embedded in 25kPa background, obtained with USX, SE and TC estimators. Elasticity values are represented as mean and (sd) of 5 samples. The elasticity units of measure differ for each estimator - USX provides the RGB values (0-255), SE provides a unitless measure of strain, and TC provides an estimate in Pa^{-1}. Statistical significance was calculated with Wilcoxon-rank sum test, where $^*p < 0.05$.

Experiment 4: Relaxed and contracted forearm

Elasticity values were higher (softer) in the relaxed tissue compared to the contracted tissue, in all three post-processing techniques. See Figure 5.11. The pixel value distribution differed across the techniques, shown in the histogram representations (right-most column) of Figure 5.11. In the USX technique, the relaxed image had a greater quantity of pixels with values between 180-256 (soft tissue) and 0-60 (hard tissue) compared to contracted. The contracted image had a greater quantity of mid-range strain values (60-180) compared to the contracted. In the SE and TC techniques, the relaxed forearm had a greater quantity of pixels across high and mid range values compared to the contracted forearm. The salient feature in the TC histogram was the reduction of pixel value and quantity with the contracted image across.

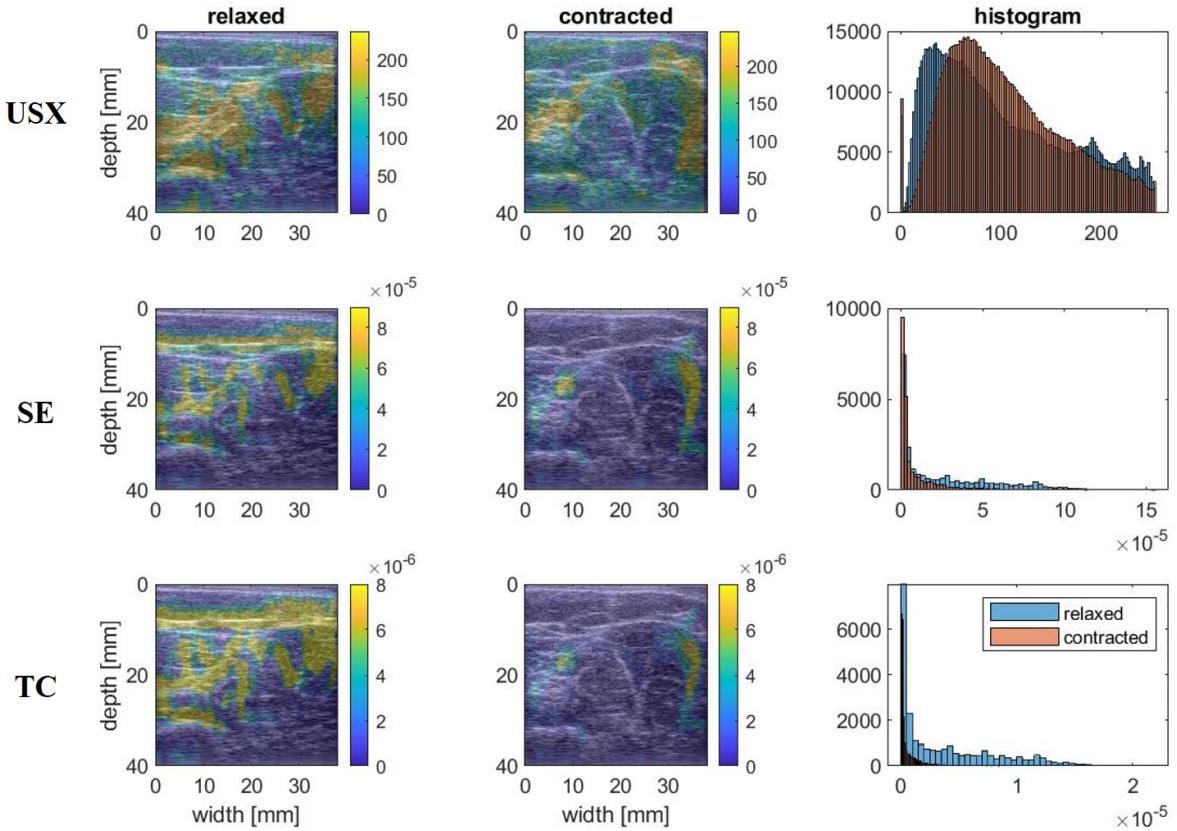

Figure 5.11: Comparison of strain images of relaxed and contracted forearm and the corresponding histograms obtained with USX, SE and TC post-processing algorithms. The histogram representations of relaxed and contracted forearms (right-most column), displays the pixel color value on the x-axis, and quantity of pixels per bin in the y-axis.

Tissue	Trial	USX		SE		TC	
Layer	#	relaxed	contracted	relaxed	contracted	relaxed	contracted
Superficial	*test 1*	107.45	96.75	9.29E-06	4.25E-06	1.95E-07	1.10E-07
	test 2	91.06	95.99	3.82E-05	2.98E-06	1.92E-06	6.42E-08
	test 3	131.54	93.94	4.28E-05	3.64E-05	3.02E-06	5.60E-07
	test 4	120.37	152.00	2.58E-05	4.80E-05	7.95E-07	5.01E-07
	test 5	103.41	78.37	2.72E-05	2.53E-05	2.00E-07	2.22E-07
Deep	*test 1*	101.13	112.78	1.21E-05	8.80E-06	2.55E-07	2.27E-07
	test 2	140.67	97.35	3.55E-05	5.41E-06	1.79E-06	1.17E-07
	test 3	133.91	141.54	6.72E-05	5.37E-05	4.74E-06	8.24E-07
	test 4	149.60	136.39	3.42E-05	6.27E-05	1.05E-06	6.54E-07
	test 5	124.34	117.84	5.32E-05	5.11E-05	3.91E-07	4.48E-07
Superficial	*mean*	110.77	103.41	2.86E-05	2.34E-05	1.23E-06	2.91E-07
	std	15.631567	28.1848	1.299E-05	1.98E-05	1.225E-06	2.27E-07
Deep	*mean*	129.93	121.18	4.04E-05	3.63E-05	1.65E-06	4.54E-07
	std	18.56454	17.99567	2.087E-05	2.7E-05	1.836E-06	2.92E-07

Table 5.3: Comparison of compliance estimates from the relaxed and contracted forearms of 5 subjects, using USX, SE, and TC post-processing techniques. Units of measure differ for each algorithm: USX [0-256 RGB values], SE [unitless], and TC [compliance ($kPa^{-}1$)].

The mean elasticity values in the superficial and deep tissue layers are provided in Table 5.3. The elastic modului estimated from TC (by inverting them) are several orders of magnitude higher than the actual tissue elastic modulus due to the scaling factor, TRE. In harder targets the TRE is large. TC is inversely proportional to TRE, and grows smaller.

The ratio between contracted and relaxed tissues are compared in Table 5.4. The ratio obtained with the USX and SE technique were near unity, at 0.94 and 0.87, respectively. The ratio obtained with TC was 0.54, indicating tissue elasticity with contraction was nearly half of that when relaxed. The TC method was significantly lower than the USX method. See Table 5.4.

Tissue Layer	Trial #	USX	SE	TC
Superficial	*test 1*	0.900	0.457	0.563
	test 2	1.054	0.078	0.033
	test 3	0.714	0.852	0.185
	test 4	1.263	1.863	0.631
	test 5	0.758	0.930	1.108
Deep	*test 1*	1.115	0.724	0.892
	test 2	0.692	0.152	0.065
	test 3	1.057	0.799	0.174
	test 4	0.912	1.834	0.621
	test 5	0.948	0.961	1.145
	mean	0.941	0.865	0.542
	std	0.185	0.602	0.418

Table 5.4: Comparison of compliance ratios, (contracted to relaxed mean compliance value), in the superficial and deep tissue layers, by the USX, SE, and TC post-processing techniques.

TC was significantly lower than USX, while no significant difference was found between USX and SE, and SE to TC. Test 2 compliance values an order of magnitude lower than the other test

USX-SE	*p=0.7064*
USX-TC	*p=0.0128*
SE-TC	*p=0.1801*

Table 5.5: Statistical significance with paired sample t-test comparing the contracted/relaxed rations of USX, SE and TC algorithms.

5.4 Discussion

This study demonstrated a technique for calibrating strain elastography images with tissue resistance estimate, estimating tissue compliance, in order to produce quasi-quantitative images for pre-post-test investigation. The experimental setup developed for controlled SE imaging enabled controlled tissue compression and tissue compression rate.

In Experiment 1, the forearm of four individuals were imaged with 4-, 5- and 6Hz compression rates, producing unique responses between subject tests. In all four tests, a drift in the strain image varying with compression rate was observed. The drift is produced by the ultrasound frame rate (15Hz) and the compression rate (4-6Hz) produced by the motorized arm. At a compression rate of 5Hz, 3 ultrasound frames represent 1 tissue compression cycle, under-sampling the compression cycle. A reduction in tissue compression cycle would increase the number of frames representing a tissue compression cycle, reducing the drift. This suggests another vulnerability of relying on manual SE imaging and underscoring the need for controlled tissue compression rate. In conventional SE imaging, compression rate is currently not tracked or controlled for. This study suggested that compression rate should be controlled in order to obtain objectively comparable images. Further investigation is needed to better understand the relationship between tissue compression rate and the strain elastographic image. A drift compensation technique was proposed for shear wave elastogragphy [36, 162]. This study established that the pilot human subject study should maintain the same tissue compression rate in pre- and post-intervention images. The tissue may soften or harden after intervention and thereby require a different push force to achieve the same tissue deformation. The tissue compression rate should be controlled for pre- and post-intervention SE image.

Experiment 2 demonstrated that TRE was detectable and differentiable between relaxed and contracted muscle in 6 of 10 subjects. The variability in the FSR signal during palpatory motion suggests the need for further motion control to mitigate noise. The stability of the signal may also be a function of the minute position changes of the transducer during palpatory motion, or motion noise introduced by the forearm. In the human forearm, motion noise may be a function of the fatigue during sustained contraction.

Experiment 3 and 4 compared the performance of the TC image with the built-in SE and the non-calibrated SE images. In the tissue phantom experiment, the inclusions simulating normal ($8kPa$) and MTP $14kPa$) tissue were embedded in the same background material ($25kPa$, therefore a difference in elasticity is expected to be detected. Experiment 3 confirmed that the built-in SE function does not differentiate between the hard and soft tissue targets. During post-scan conversion of the ultrasound image with SE overlay, calculated strain values become normalized to the 0-256 RGB values, making values relative within frame. This process results in two images that can not be objectively compared. The actual strain values, demonstrated with the SE method, do detect a difference between the hard and soft targets closely approximating the true elasticity ratio. In the case the the background tissue stiffness alters, these two strains may not be comparable. The TC method calibrated the SE values using a scaling factor with a physiologic basis - the tissue resistance. This method increased the contrast between the hard and soft targets.

Experiment 4 demonstrated the use of TC in obtaining comparable data in the relaxed and contracted forearm when no reference tissue is available to establish objective comparison between images. The combined superficial and deep tissue elasticity ratios obtained with built-in SE function, USX, and SE performed similarly, detecting little difference between relaxed and contracted muscle. TC detected a

significantly lower ratio, indicating that tissue stiffness increased in the contracted muscle compared to the relaxed muscle. Due to the small sample size, data was not statistically analyzed by tissue depth, but only by technique used.

5.4.1 Limitation

An inherent limitation of this technique is that the compliance image may suffer aliasing from the ultrasound unit frame rate. Despite the mitigation employed, the method is still user-dependent. The positioning of the ultrasound probe is highly variable due the natural slope in the forearm muscle. Positioning $2cm$ proximal to the cubital fossa, where tissue curvature is minimal, was attempted in all subjects. Some subjects had limited supinating range of motion. For these cases the probe position needed to accommodate an angle whereby perpendicular position and controlled motion may be compromised. In a symptomatic population, positioning of the forearm in a full supine position may not be feasible.

The change in tissue resistance estimate by depth was not accounted for in this technique. In muscle tissue, stress applied to the tissue surface will attenuate with depth. Further investigation is needed to characterize the stress attenuation with muscle tissue depth.

5.4.2 Future work

Achieving adequate tissue deformation within linear range but sufficient for elasticity image rendering is challenging to achieve with manually SE imaging. Hard and soft tissues require different amounts of pressure to achieve the same tissue deformation. The motorized arm removes user dependent tissue compression. While compression rate was more consistent using the motorized arm, determining the correct pressure still relied on visual inspection of the strain image and the on-screen

indicator and the real-time FSR trace. Automating tissue compression distance using a feedback controller may improve this process. Fully automating the tissue compression method may advance the ease of use and accuracy of SE imaging.

It is known that the tissue displacement estimate (TDE) is pivotal in strain elastography imaging, and that normalized cross-correlation (NCC) is noisy, has poor resolution and is computationally inefficient. For these reasons, NCC is not used in real-time SE imaging. Phase domain algorithms are preferred because of the reduced computation time [181]. The developers of the ultrasound unit used in this study have published techniques called sample tracking (ST) algorithm and time domain with prior estimates (TDPE). In the ST algorithm, TDE is compared to a spline-based interpolated representation of the pre-compression signal, thereby providing higher resolutions and sensitivity over NCC [180]. TDPE is similar to NCC, but uses the TDE peaks from neighboring RF windows to predict the location of the next TDE peak, reducing the search area (within 3 lags) and improving computation time. Rivaz et al. developed machine-learning and dynamic programming based techniques - global ultrasound elastography (GLUE) [71] and second-order ultrasound elastography (SOUL) [14, 13, 15], respectively. GLUE utilizes axial and lateral displacements to obtain a first-order continuity constraint, while SOUL utilizes a second-order continuity constraint. Both methods were shown to vastly improve signal-to-noise and contrast-to-noise ratio over other TDE algorithms. Implementing these algorithms in this clinical application may improve the image quality and accuracy of the tissue elasticity estimate.

5.5 Conclusion

Objective methods for evaluating mechanical properties of muscle tissue are desirable and clinically relevant. Such outcome measures could serve as a valuable adjunct diagnostic tool. Improvements in superficial tissue resolution ($> 8MHz$) imaging have led to an increase in applications in MSK imaging within the physical medicine sphere. However, musculoskeletal tissue diagnostics are in a nascent phase. The technique proposed here is one attempt at a possible area for advancement. Further development and investigation is required to determine its capability for investigating the elusive features of musculoskeletal tissue pathology and response to intervention.

Chapter 6

HUMAN SUBJECT STUDY

6.1 Introduction

Osteopathic manipulative treatment (OMT) is widely used to alleviate MTP and promote self-healing processes [16]. OMT involves application of manual pressure or force to restore the body's structure and function by removing barriers to the body's natural capacity towards self-healing [28, 45]. Homeostasis is restored using a variety of manual techniques including myofascial release, balanced ligamentous tension, positional release, Still method, mobilization and more [28]. However, the mechanisms of MTP treatment with OMT are not well understood due to a lack of objective assessment to support palpatory findings [107].

Strong evidence suggests that MTP formation and alleviation involves a combination of mechanisms altering pain, circulation, tissue mechanical properties and muscle function. *In-vitro* studies have demonstrated OMT simulated stretching induces fibroblast proliferation that enhances wound healing [40, 24, 183, 184]. *In-vivo* studies have demonstrated improved local circulation and contractility and reduced tissue stiffness, pain and muscle tone following OMT [117]. Development of diagnostic imaging for tracking pathology and treatment progression is an active area of research [1]. Sill, few studies utilize multiple modalities to assess MTP treatment.

6.1.1 Challenges in OMT research

Randomized controlled studies aiming to demonstrate tissue response to OMT commonly target the therapeutic effects on pain and muscle dysfunction. These are

quantified with the visual analog scale (VAS) and various disability indices. See Table 6.1. A vast majority of studies quantify pain with pressure algometry (or dolorimeter) that measures MTP pain pressure threshold (PPT). To date, the algometer is the only validated tool for quantifying an MTP symptom [132, 129]; it is not used in clinical diagnostics but it is widely used in MTP treatment research. OMT investigations quantifying pain and disability are limited to patient perceived outcome measures [84]. While pain and disability are prominent features of MTP, MTP may arise without pain symptoms [148]. Tissue stiffness, circulation and muscle function are indicated as prominent clinical symptoms [107, 148]. Modalities for investigating other characteristics of MTP have included: 1) heart rate variability or salivary biomarkers for autonomic activity, 2) ultrasound or near infrared spectroscopy (NIRS) for hemodynamics, 3) ultrasound elastography and digital palpation methods for tissue stiffness, 4) goniometer for range of motion, 5) infrared thermography for skin temperature, 5) electromyography for muscle function, and 6) dynamometer for muscle strength. Table 6.1 summarizes quantitative methods used in MTP research.

MTP Assessment	Clinical Outcome Measure	Quantitative Parameter	Modality	Source
Pain and dysfunction	somatic dysfunction	Tart Score	palpation and physical examination	Gao 2020
	disability and pain	Neck disability Index (NDI), Quebec Back Pain Disability Index (QBPI), Boston Carpal Tunnel Questionnaire (BCTQ), Sensory symptom diagram Disabilities of Arm, Shoulder and Hand (DASH) questionnaire score (VAS-P), Global Perceived Effect (GPE) Frequency, Intensity and duration of headaches, Northwick Park Neck Pain Questionnaire(NPQ) Headache Disability Inventory (HDI)	Self-reported disability questionnaire	Girasol 2018, Nguyen 2021 Burnham 2015, Bron 2011, Korkmaz 2022, Falsiroli Maistrello 2018, Ferira 2017
	pain sensitivity	VAS Score	visual analog scale	Jaeger and Reeves 1986, Perez-Bellmunt 2021, Morikawa 2017, Kostopoulos 2018, Bron 2011, Korkmaz 2022 Muggenborg 2023
	pain pressure threshold (PPT) pain tolerance	force	algometer	Turo 2015, Jaeger and Reeves 1986, Girasol 2018, Perez-Bellmunt 2021, Kostopoulos 2008, Long 2021, Renan-Ordine 2011, Muggenborg 2023, P.Nikam 2021
Vascular function	hemodynamics	Oxy-hemoglobin (Hb), Deoxy-Hb, and total Hb concentrations, skin temperature	Near infrared spectroscopy (NIRS), infrared thermography	Morikawa 2017, Turo 2015
Biomechanical properties	musculoskeletal tissue morphology	transverse carpal ligament length and bowing MTP diameter	ultrasound (B-Mode)	Burnham 2015, Korkmaz 2022
	tissue elasticity/ stiffness	Mechanical Heterogeneity Index, shear wave velocity rate, Muscle tone, stiffness, elasticity and relaxation	Vibration Elastography with color Doppler Variance, shear wave elastography Digital palpation device (Myotone Pro)	Turo 2015, Gao 2020, Perez-Bellmunt 2021
Muscle function	contractility, myoelectric activity during flexion/extension, strength during isometric contraction	shear wave velocity in relaxed and contracted muscle, median frequency, force	shear wave elastography sEMG hand dynamometer	Gao 2020, Girasol 2018, Perez-Bellmunt 2021
	range of motion	amplitude of movement in flexion and extension, dorsiflexion angle and lunge test angle	flexometery, inclinometer	Girasol 2018, Perez-Bellmunt 2021, Muggenborg 2023
	myoelectrical activity at rest/ spontaneous electrical activity (SEA)	RMS of EMG signal, amplitude of EMG signal	sEMG, needle EMG	Girasol 2018, Kostoplous 2018, Ginszt 2020

Table 6.1: Quantitative methods used to evaluate MTP treatment efficacy in-vivo.

Major limitations to conducting controlled studies for muscle tissue evaluation with OMT include establishing a sham or placebo protocol and conducting double-blinded studies. Sham and placebo protocol for OMT research are not yet established. Methods used to date have been highly operator dependent and have produced inconclusive results. In a recent meta-analysis controlled studies investigating OMT on musculoskeletal conditions were found to insufficiently describe sham or placebo procedures, using terms such as "light touch only", challenging replication of the study [16]. Application of light pressure on skin induces significant changes in microvascular blood flow [80]. The amount and location of applied pressure to achieve therapeutic effects is a point of investigation on its own. Roberts et. al. observed that the pattern of applied pressure influenced muscle reactivity. Conditioning with light pressure before deep pressure maintained EMG activity, whereas deep pressure alone increased EMG activity, suggesting that light pressure altered the reactivity to deep pressure possibly by inhibiting the stretch or nociceptive reflexes [136]. Double-blind studies are not possible as the practitioner cannot be blinded to the treatment arm, and the subject may not be naive to the treatment administered.

6.1.2 Objective

The purpose of this study is to implement a non-invasive, multi-modal technique in a healthy adults to evaluate MTP response to OMT treatment. The hypothesis is that MTP alleviation by OMT is detectable and measurable using the combination of evaluation methods: 1) pain pressure threshold with algometry, 2) muscle tissue vascularity with power Doppler, 3) tissue compliance with strain elastography and force sensitive resistor, and 4) myogenic activity with sEMG. In this comparative study design, OMT was compared with rest (no touch control) and with light exercise (repetitive hand grips on soft bulb, as positive control) interventions.

The output of this pilot research is to inform future study design by: 1) identifying likely factors for participant screening, 2) study design, 3) better understanding limitations of the experimental setup and 4) identifying areas for further development. To date, all four MTP symptoms - pain, circulation, tissue mechanical properties and myogenic activity - have not been investigated in parallel within the anterior forearm with MTP using ultrasound and sEMG.

6.2 Methods

6.2.1 Participants

38 participants without recent (within the past year) upper extremity injury or surgery, or known neuromuscular pathology, were recruited from ATSU in Mesa, AZ. Of these, 4 were excluded from the study due to no MPT or active pain present. The remaining 34 participants, 25 female/9 male, age 33.9±12.9, range [22 69], refrained from using pain medication (OTC or prescribed) for 48 hours prior to the test session, and were randomly assigned to Rest ($n = 10$), OMT ($n = 14$), and exercise ($n = 10$) intervention groups.

6.2.2 Protocol

The study protocol was approved by the ATSU IRB Committee (IRB #2022 − 096). After providing formal consent, the participant completed an intake form to self-report daily activity level, types of activity, pain complaints or discomfort in the upper extremity, level of interference with activities due to pain, and previous experience with manual therapy. An experienced osteopathic practitioner completed a bilateral physical examination of the forearms and took patient history. A primary MTP on the anterior forearm (left or right) was identified and marked with a surgical

pen. If more than one MTP was found, the most painful spot was selected as the primary MTP. Three sEMG electrodes with coupling gel were attached to cleaned the skin on the forearm, near the cubital fossa and and two near the carpal tunnel. The PPT and ultrasonic imaging and myogenic activity were collected before and after intervention. See the flow diagram of protocol in Figure 6.1.

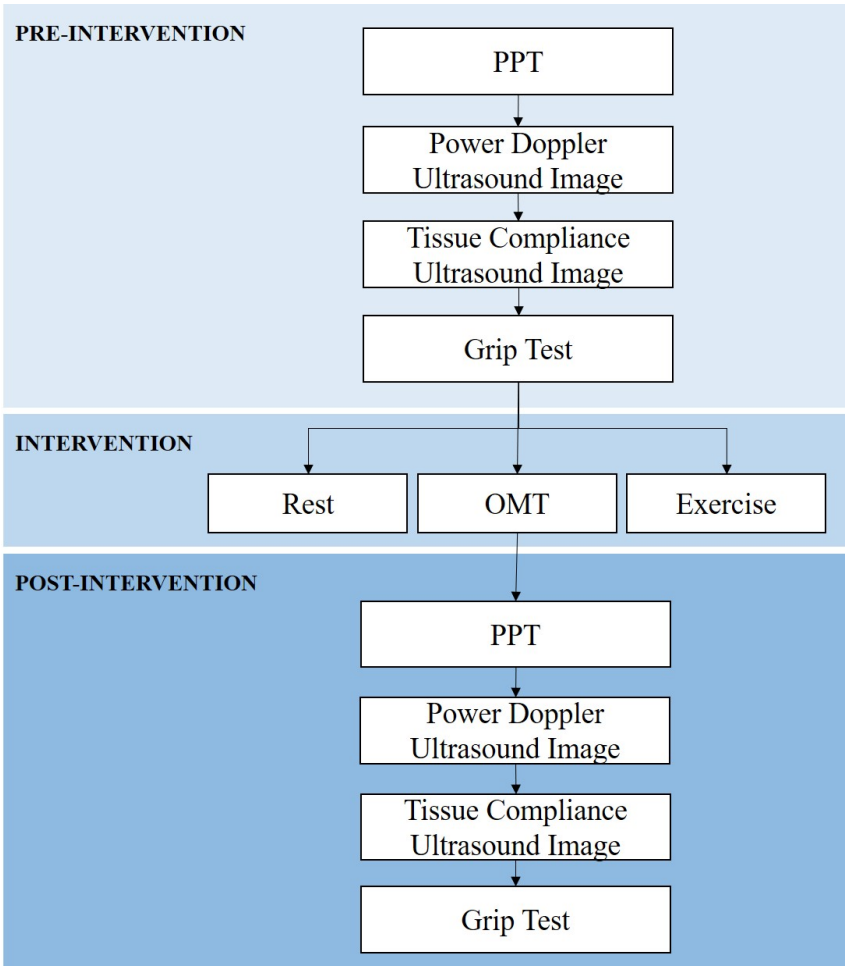

Figure 6.1: Flow diagram of human study protocol.

Pain Pressure Threshold

The pain pressure threshold (PPT) was measured on the primary MTP with an algometer (Baseline Dolorimeter with Circular Probe) with a flat circular surface area of $1.52cm^2$. Pain pressure threshold was compared across groups with a generalized linear model, and within groups with post-hoc paired sample t-test.

Ultrasound Imaging

The participant placed the forearm in a neutral, supine position on a cushioned table beneath the mounted ultrasound transducer. The transducer position on the forearm was standardized throughout the study (regardless of MTP location) to assess changes in the taut band with intervention. The transducer was placed approximately $2cm$ distal to the cubital fossa to include the following structures in B-mode (See Figure 1.1): 1) deep - radius and supinator and pronator teres, 2) lateral border – brachioradialis, 3) medial border - flexor carpi radialis, flexor digitorum superficialis and flexor digitorum profundus). The transducer position was marked on the forearm with a surgical pen for accurate repositioning between pre- and post-intervention imaging.

Five seconds of power Doppler ultrasound images were collected at a frame rate of 5-12 frames per second (FPS) automatically adjusted by the ultrasound unit. The power Doppler window included the entire display. PRF was the only setting that was optimized in the post-intervention image. All other ultrasound settings were unchanged between pre- and post-intervention imaging. The RF frames were processed to obtain power Doppler images. Figure 1.1 provides the experimental setup for ultrasound imaging for the forearm.

From these images the maximum PDI (maxPDI), area and αPDI were quantified.

The maximum PDI was obtained from the frame with highest PDI values and blood flow area (systole), and calculated as the mean intensity of the 97^{th} percentile PDI values. The area and αPDI were obtained with time series analysis of the power Doppler frames: average area was calculated as RMS of the the number of pixels per frame multiplied by the pixel size ($200\mu m$ x $200\mu m$). The pixel size was verified by flow-phantom experiment, not shown here. The RMS of αPDI over all frames represented the average regional blood flow over five seconds. The change in distribution of pixel values pre-post-intervention was observed with histogram representation of the power Doppler images. The RMS value of the quantity of pixels per intensity band (increments of 5 between 25-80 dB) over 5 seconds was normalized to baseline (max pixel values in the lowest intensity band) for group comparison. The power Doppler analysis outcome measures were compared with a generalized estimating equation and Wilcoxon rank-sum and paired-sample t-test post-hoc analysis, depending on normality.

Five seconds of strain elastography images were collected at a frame rate of 15 FPS. The step-size and speed of the motorized arm were adjusted to achieve a tissue compression rate between $4-6Hz$. The tissue compression step-size was optimized post-intervention. All other settings were maintained between pre- and post-intervention imaging. The mean tissue compliance was compared by depth (superficial and deep tissue layers) and across groups. The tissue resistance, and tissue compliance at superficial and deep tissue layers were analyzed with a generalized linear model for between-group comparison with student t-test post-hoc analysis.

Hand Grip Test

A sustained hand grip to voluntary fatigue was measured with sEMG and clench force bulb before and after intervention (MP36 and Biopac Student Lab version 4.13,

Biopac Systems Inc, Goleta CA) using a 3-lead sEMG, disposable electrodes and a soft clench force bulb (Model SS2LB, EL501, and SS56L, Biopac Systems, LLC.). The sEMG signal was filtered with a built-in bandpass filter of $5 - 250Hz$ with a $60Hz$ notch filter, at $2kHz$ sampling rate. The clench force bulb was calibrated with hand -dynamometer (CAMRY digital hand dynamometer 90 Kgs, Camrysalesstore, South El Monte, CA). The participant was instructed, with demonstration, to progressively grip a soft clench bulb 3 times at sub-maximum force for 1-2 seconds each grip, and then grip the bulb at maximum force, sustaining the grip until the voluntary fatigue. No encouragement was provided during the fatigue grip.

Fatigue time was calculated as the time between maximum voluntary contraction (MVC) and grip release. Maximum sEMG amplitude (aEMGmax) was calculated as the RMS of $0.5second$-interval of sEMG data centered at MVC [120]. MVC normalized the force data [%MVC] and aEMGmax normalized the sEMG [%aEMGmax] data and time trends of grip force and aEMG were observed, using the mean and RMS value [120], respectively, of 1-2 second intervals[31] at 20% increments of time [139]. The spectral shape of the EMG signal was assessed to observe how frequencies shift throughout sustained hand grip. The power spectral density (PSD) of 1-2 seconds of sEMG data centered at 20% time points was calculated using a zero-padded Hanning window. The ratio of the energy density in the low frequency ($10 - 55Hz$) and high frequency ($75 - 250Hz$) bands quantified the spectral shift [178], where values above 1 indicates shift towards lower frequencies observed with muscle fatigue [119, 134, 31]. See Appendix C for analysis.

Intervention

The rest group sat quiescent (11 ± 2.04 minutes). The OMT group received muscle energy, strain-counterstrain, balanced ligamentous tension, and the Still method

(8.02 ± 3.67 minutes). The exercise group rested (7.6 ± 2.55 minutes) and then performed repetitive clenches on a soft clench bulb 40 or more times. In an uncontrolled setting, we observed that repetitive hand grips, more than 25, were observed to increased the Doppler velocity in the brachial artery and veins measured approximately 2 cm distal to the cubital fossa in a convenience sample study (results not reported).

Environmental Safety

In order to follow COVID-19 safety protocol, one D.O. and two osteopathic medical student fellows identified MTP location. The same DO and one fellow performed OMT treatments throughout the study. One technician performed all ultrasonic imaging and sEMG data collection. All personnel involved wore appropriate personal protective equipment, as designated by the ATSU IRB.

6.2.3 Principal Component Analysis

Salient features of MTP response to intervention were identified with principal component analysis (PCA) [86, 186, 97], indicating outcome measures with highest effect on variability of the data. The initial PCA analysis, provided in Appendix D, revealed that there was a high degree variability across the MVC results which masked the effect of all other parameters, and that PCA scores were tightly clustered by group. For these reasons all outcome measures were normalized to baseline (Post/Pre ratio), and intervention groups were evaluated separately. The final PCA analyses included 13 parameters listed in Table 6.4.

The first four principal components from each intervention group were identified as the salient parameters. Salient parameters were reviewed with scatter plots of individual data points where values of 2 or more were designated as *responders*. For the $LoHi_{end}$ and TR, values less than 1 were designated as *responders* since a reduction

Outcome Measure	**Description**	**units**
PPT	Pain pressure threshold	kg/cm^2
$maxPDI$	maximum power Doppler intensity value	dB
$Area$	area of detected blood flow	mm^2
αPDI	scaled power Doppler intensity values	$dBmm^2$
TR	tissue resistance	$unitless$
TC_s	superficial tissue compliance	Pa^{-1}
TC_d	deep tissue compliance	Pa^{-1}
HG_t	hand grip duration	sec
MVC	maximum voluntary contraction measured with clench force bulb	kg/cm^2
$aMVCe$	amplitude of sEMG signal during MVC	mV
$HG_{f,end}$	hand grip clench force at the end of the hand grip test	$\%MVC$
$aEMG_{end}$	amplitude of sEMG signal at the end of the hand grip test	$\%aMVCe$
$LoHi_{end}$	low-to-high spectral ratio at the end of the hand grip test	$unitless$

Table 6.2: List and description of 13 outcome measures obtained from the multi-modal approach to quantify MTP response to OMT in the anterior forearm.

in these outcome measures reduce with response to intervention. Baseline values of responders and non-responders were compared with paired-sample t-test to inform participant screening in future work. Non-normal data were log normalized.

Table 6.2 lists the outcome measures obtained from the multi-modal approach.

6.3 Results

From the intake form, self-reported activities included typing, repetitive fine motor tasks and holding postures for long periods. The majority of participants (70.6%) reported a positive pain complaint, and nearly 40% reported that their pain interfered with their daily activities. 44.1% were naive to manual therapy. Of the nearly 55% with prior experience, only 20.6% received therapy within the last month. See Table

6.3.

Variable	**Frequency,% (n)**
Daily Activity	
Typing	79.4(27)
Repetitive, fine motor movement	58.8(20)
Office Work	73.5(25)
Manual/Physical Therapy	29.4(10)
Holding posture for long periods	91.2(31)
Serious Injury	
No	82.4(28)
Yes, yrs since injury 11±13.4	17.6(6)
Treated	14.7(5)
Not Treated	2.9(1)
Positive Pain compliant	
No	29.4(10)
Yes	70.6(24)
Daily Level of Activity Interference from Pain	
No	61.8(21)
Occasionally	8.8(3)
Regularly	29.4(10)
Prior Experience with Manual Therapy	
Never	44.1(15)
At Least Once/Not Regularly	38.2(13)
Regularly	17.6(6)
How recent was your last manual therapy treatment?	
Within the last month	20.6(7)
Within the last year	26.5(9)
2+years	8.8(3)

Table 6.3: Baseline characteristics of participants with MTP in the anterior forearm. Participants self-reported daily activity, past injury, pain complaints, pain interference of daily activity, and prior experience with manual therapy.

6.3.1 MTP locations

MTP were found bilaterally (27 right, 7 left) in all subjects (32 right hand dominant, 1 left-hand dominant and 1 ambidextrous). MTP locations are shown in Figure 6.2.

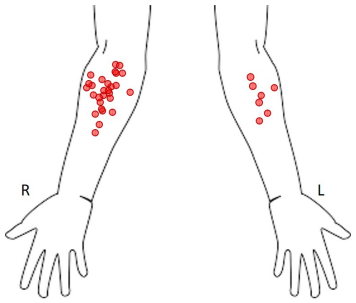

Figure 6.2: Primary MTP locations.

6.3.2 Pain pressure threshold

A significant group-by-phase interaction was found in the pain pressure threshold (p=*0.0005*). PPT significantly increased after OMT intervention (p=*0.021*), compared to rest (p= *0.98*) and exercise (p= *0.45*). See Tables 6.4 and 6.5.

6.3.3 Regional blood flow

No Group-by-phase interaction was found in the regional blood flow metrics. MaxPDI trends showed increases after OMT and decreases after rest and exercise. Area and αPDI trends increased after rest and OMT, and decreased after exercise. See Tables 6.4 and 6.5. There was a notable increase in maxPDI variability after OMT (pre-OMT std=8.11 post-OMT std = 16.77), compared to rest (6.39, 7.68) and exercise (8.11, 7.15). The quantity of low intensity power Doppler values increased after rest and OMT, compared to exercise. See Figure 6.4.

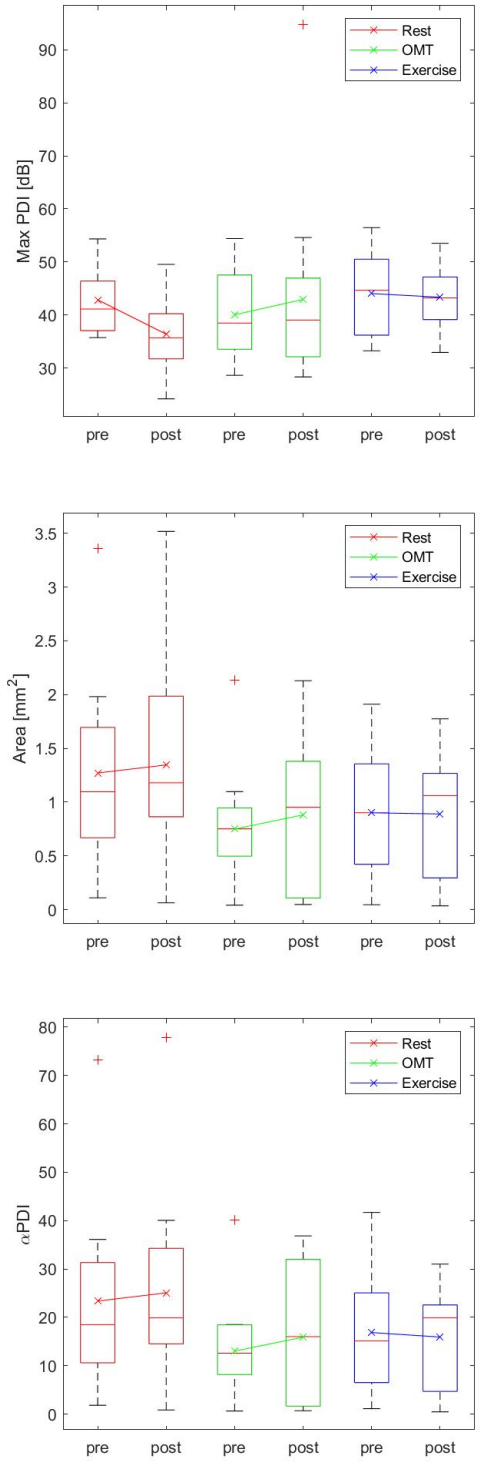

Figure 6.3: Regional blood flow metrics from power Doppler time series analysis.

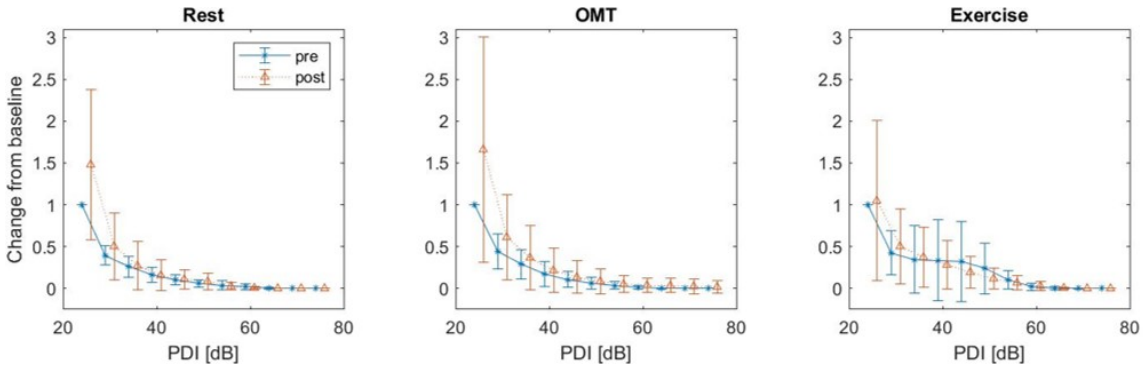

Figure 6.4: Trend lines representing the average (RMS over 3 seconds) quantity of pixels (y-axis) per power Doppler intensity bin (x-axis) before (pre-) and after (post-) intervention. The group means are normalized to baseline (the maximum pixel count in the pre-intervention trend line), and the change from baseline is shown (y-axis). Values shown are represented as mean (markers) and standard deviation (error bars).

6.3.4 Tissue compliance

A significant group by phase interaction was found in the superficial tissue compliance (p=*0.017*), but not in the deep tissue compliance (p=*0.073*) or the tissue resistance estimate (p=*0.549*). Tissue compliance significantly increased after rest (p<*0.0001*) and OMT (p=*0.02*), compared to exercise (p=*0.96*). See Tables 6.4 and 6.5.

6.3.5 Myogenic activity

No significant group by phase interaction was found in the grip time (p=*0.359*), MVC (p=*0.303*), aMVCe (p=*0.642*), sEMG amplitude time trend ($p = 0.844$), grip force time trend ($p = 0.130$), or low-to-high frequency spectral ratio ($p = 0.253$). See Tables 6.4 and 6.5. The low-to-high frequency spectral ratio of the exercise group remained less than 1 throughout both pre- and post-intervention hand grip.

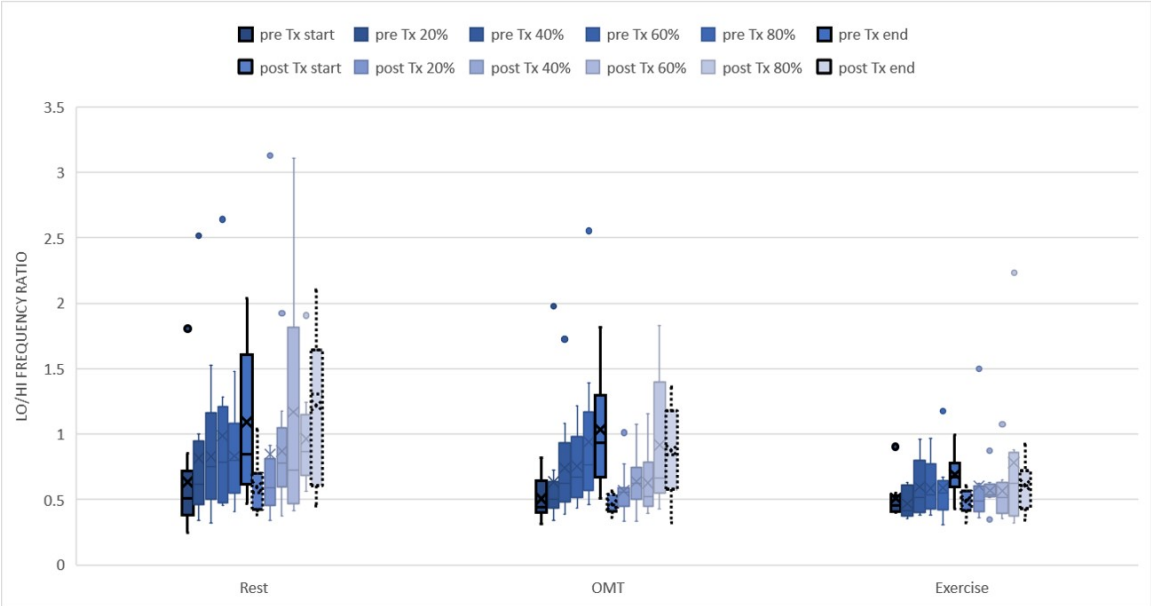

Figure 6.5: sEMG spectral shape trends among among the Rest, OMT and Exercise intervention groups at $0-, 20-, 40-, 60-, 80-$, and 100% time points during hand grip pre- and post- intervention. The spectral shape is indicated by the low-to-high frequency band ratio of the spectral energy density.

		Rest			OMT			Exercise		
		mean (se)	95% CI		mean (se)	95% CI		mean (se)	95% CI	
PPT	pre	1.753 (0.244)	1.274	2.233	1.310 (0.183)	0.951	1.668	1.901 (0.195)	1.518	2.283
	post	1.956 (0.283)	1.402	2.511	2.072 (0.229)	1.624	2.521	1.898 (0.168)	1.568	2.228
maxPDI	pre	42.859 (2.020)	38.900	46.817	40.050 (2.167)	35.802	44.298	44.039 (2.704)	38.740	49.338
	post	36.395 (2.428)	31.636	41.155	42.946 (4.481)	34.162	51.729	43.356 (2.382)	38.686	48.026
Area	pre	1.271 (0.299)	0.684	1.858	0.749 (0.141)	0.473	1.025	0.901 (0.201)	0.506	1.295
	post	1.346 (0.328)	0.704	1.988	0.882 (0.205)	0.480	1.284	0.890 (0.204)	0.490	1.290
aPDI	pre	23.372 (6.588)	10.459	36.285	13.030 (2.650)	7.835	18.225	16.866 (4.284)	8.469	25.263
	post	25.072 (7.092)	11.171	38.972	15.913 (3.848)	8.371	23.456	15.940 (3.717)	8.655	23.224
TR	pre	0.024 (0.004)	0.017	0.031	0.021 (0.003)	0.015	0.026	0.021 (0.002)	0.017	0.026
	post	0.022 (0.003)	0.015	0.028	0.022 (0.003)	0.015	0.028	0.018 (0.002)	0.014	0.022
TC_s [10^{-6}]	pre	3.975 (1.243)	1.538	6.411	3.857 (1.021)	1.856	5.858	5.267 (1.494)	2.338	8.195
	post	5.897 (1.489)	2.979	8.815	5.724 (1.277)	3.222	8.226	5.229 (1.283)	2.714	7.744
TC_d [10^{-6}]	pre	3.712 (0.636)	2.467	4.958	6.529 (2.746)	1.148	11.911	7.469 (2.703)	2.171	12.767
	post	5.693 (0.997)	3.738	7.647	8.488 (3.255)	2.109	14.868	8.174 (1.733)	4.776	11.571
HG_t	pre	73.282 (27.543)	19.298	127.266	88.972 (17.338)	54.990	122.955	57.283 (14.195)	29.461	85.105
	post	58.782 (15.911)	27.595	89.968	132.445 (29.318)	74.981	189.909	78.497 (19.391)	40.492	116.503
MVC [10^4]	pre	4.355 (0.501)	3.373	5.337	4.798 (0.593)	3.637	5.960	4.148 (0.422)	3.320	4.976
	post	4.269 (0.580)	3.133	5.405	4.248 (0.373)	3.517	4.978	3.708 (0.354)	3.015	4.401
aMVCe	pre	0.321 (0.043)	0.237	0.406	0.262 (0.026)	0.212	0.312	0.224 (0.032)	0.161	0.286
	post	0.285 (0.037)	0.212	0.359	0.229 (0.020)	0.190	0.268	0.184 (0.021)	0.143	0.225
aEMGend	pre	0.624 (0.080)	0.467	0.781	0.470 (0.049)	0.374	0.566	0.434 (0.071)	0.294	0.574
	post	0.643 (0.084)	0.478	0.808	0.541 (0.054)	0.435	0.646	0.494 (0.088)	0.321	0.667
$HG_{f,end}$	pre	0.572 (0.069)	0.437	0.707	0.510 (0.046)	0.421	0.600	0.466 (0.065)	0.338	0.593
	post	0.579 (0.069)	0.443	0.715	0.500 (0.038)	0.427	0.574	0.433 (0.062)	0.312	0.554
$LoHi_{end}$	pre	1.077 (0.225)	0.635	1.518	1.070 (0.119)	0.836	1.304	0.691 (0.059)	0.574	0.807
	post	1.195 (0.189)	0.825	1.566	0.919 (0.127)	0.671	1.168	0.606 (0.066)	0.477	0.735

Table 6.4: Pre- and post-intervention outcome measures among the Rest, OMT and Exercise intervention groups. Values are represented by mean (SE) and 95% confidence intervals (CI).

Outcome Measure	Group-by-Phase Interaction	Within-group post-hoc test		
		Rest	OMT	Exercise
PPT	***p=0.0005***	*p=0.98*	***p=0.021***	*p=0.45*
$maxPDI$	*p=0.187*			
$Area$	*p=0.814*			
αPDI	*p=0.716*			
TR	*p=0.549*			
TC_s	***p=0.017***	***p<<0.0001***	***p=0.002***	*p=0.96*
TC_d	*p=0.073*			
HG_t	*p=0.359*			
MVC	*p=0.303*			
$aMVCe$	*p=0.642*			
$HG_{f,end}$	*p=0.130*			
$aEMG_{end}$	*p=0.844*			
$LoHi_{end}$	*p=0.253*			

Table 6.5: Tests for statistical significance among outcome measures with group by phase interaction and post-hoc tests.

6.3.6 Principal component analysis

The PCA analysis showed that each intervention group had a different set of outcome measures that correlated with the first three principal components. Nine of thirteen outcome measures were highly correlated with the first 3 principal components ($PPT, Area, \alpha PDI, TC_s, TC_d, TR, LoHi_{end}$, and $aEMG_{end}$), and contributed to at least 70% of the variability, within the Rest (89.31%), OMT (72.25%) and Exercise (92.18%) groups. See Table 6.6. The complete list of coefficients is provided in Appendix D.2. TC_s occurs as the first principal components in all groups. TC_d occurs in the second principal components for OMT and exercise groups. PPT and $LoHi_{end}$ occurs as first principle component in the Rest group only. $Area$ and αPDI were both highly correlated with PC2 in the OMT group and PC3 in the exercise group, suggesting that these parameters are related and have similar effects on the

variability of the data.

Group	Principal Component #	Highest Correlated Parameter to PC#	Variability %	Running Total %
Rest	PC1	PPT TC_s $LoHi_{end}$	63.99	63.99
	PC2	$LoHi_{end}$ PPT $aPDI$	18.45	82.44
	PC3	$aEMG_{end}$ αPDI	6.88	89.31
OMT	PC1	TC_d	32.24	32.21
	PC2	αPDI $Area$ TC_s	27.88	60.11
	PC3	TC_s PPT	12.14	72.25
Exercise	PC1	TC_d	59.95	59.95
	PC2	TR TC_s	18.11	78.06
	PC3	$Area$ αPDI	14.12	92.18

Table 6.6: Parameters highly correlated with the $1st - 3rd$ principal components per intervention group, and contribution to the variability observed in the data.

Responders

Responders are shown in Figure 6.6 for the 9 parameters that highly correlated with the principle components. PPT responders were primarily located in the OMT-intervention group, excluding one outlier in the rest group who regularly practiced weight training, (Figure 6.6, Table 6.8). Responders among the sample group were found to have significantly lower baseline PPT compared to the non-responders, $p = 0.0007$, (Table 6.7).

Responders for the regional blood flow metrics, area and αPDI, predominantly found in the OMT group (n=7), compared to the rest (n=1) and exercise groups (n=3), see Figure 6.6 and Table 6.8. For the sample population, the responders were found to have lower $area$ and αPDI at baseline, however differences were insignificant, $p = 0.296, p = 0.485$, respectively, (Table 6.7).

For the superficial and deep tissue compliance parameters, responders were found across all intervention groups (Figure 6.6). Responders in the sample group were found to have significantly lower superficial and deep TC baseline values, $p = 0.0089, p < 0.0001$, respectively, (Table 6.7). For tissue resistance, responders from the sample group were found in the rest and OMT-intervention groups, but their baseline values were not found found to be different than non-responders $p = 0.674$, Table 6.7.

For the hand grip test parameters, $aEMGend$ and HG_t, responders were found in the OMT and exercise groups (Figure 6.6). For $aEMGend$, only 1 responder was found so there was not sufficient data to test baseline values. This responder was in the OMT group. For HG_t responders in were found in OMT and exercise groups, but not in the rest group. Responders' baseline values were not significantly different from non-responders, $p = 0.639$, Table 6.7. $LoHi_{end}$ responders were found across all intervention groups. The rest group had distinct and separated clusters of non-responders (>2) and responders (< 1), whereas the OMT and Exercise groups were normally distributed. The $LoHi_{end}$ responders were found across all intervention groups. Responders had a significantly higher baseline values than non-responders, $p < 0.0001$, Table 6.7.

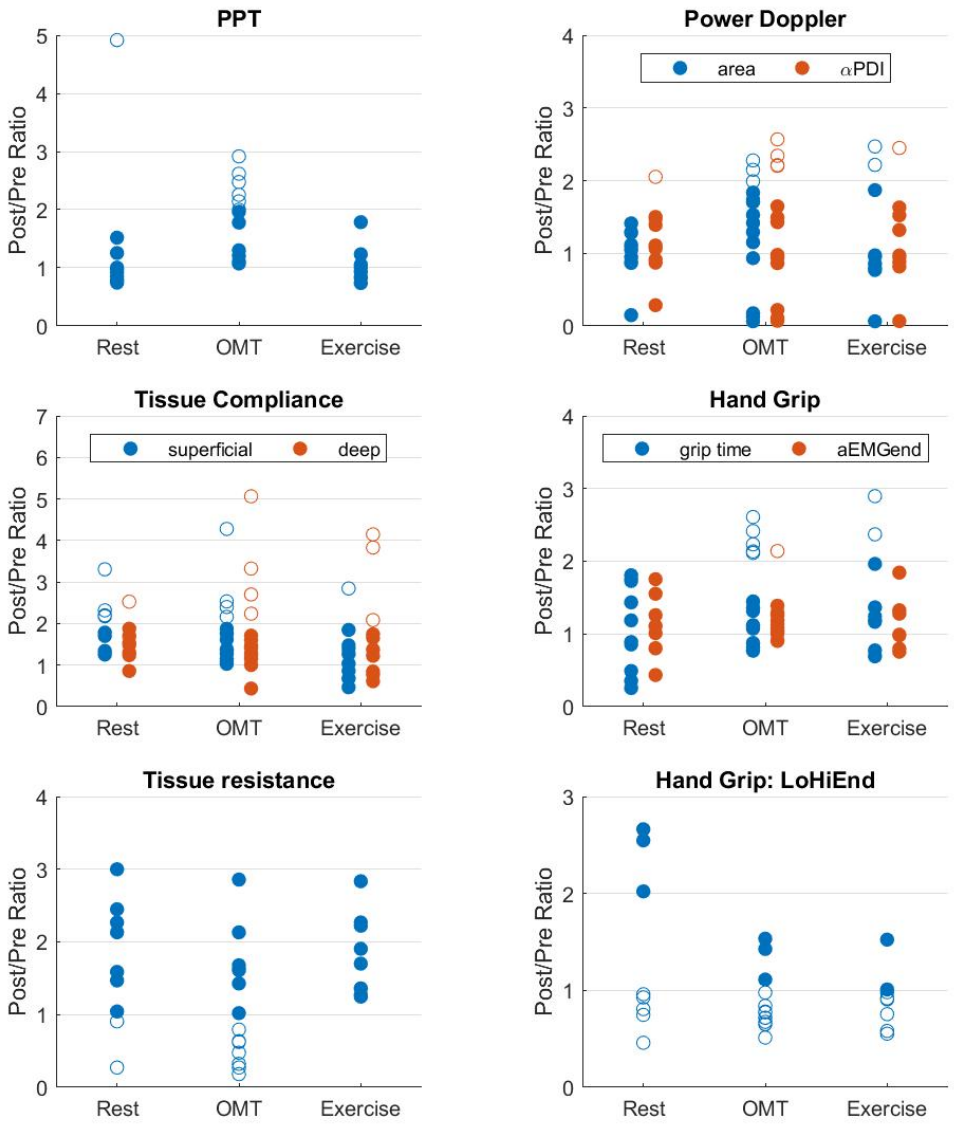

Figure 6.6: Comparison of responders (open circle) and non-responders (solid circle) by each parameter. Values represented are the post-to-pre ratio. Values greater than 2 are designated as responders. Responders for TR and $LoHi_{end}$ parameters were designated as values less than 1 because lower values indicate softer tissue and that the spectrum did not shift towards lower frequencies, respectively.

	Non Responder	CI		Responder	CI		
	mean (se)	lower	upper	mean (se)	lower	upper	*p-val*
PPT	1.81 (0.12)	1.56	2.07	0.84 (0.17)	0.43	1.25	**0.0007**
Area	1.00 (0.14)	0.71	1.30	0.64 (0.14)	0.24	1.04	0.2960
αPDI	18.08 (3.07)	11.76	24.40	13.28 (3.57)	4.10	22.46	0.4848
TR	0.02 (0.00)	0.02	0.03	0.02 (0.00)	0.02	0.03	0.6749
TCs	5.21E-06 (8.57E-07)	3.44E-06	6.98E-06	1.79E-06 (5.84E-07)	4.41E-07	3.14E-06	**0.0089**
TCd	7.34E-06 (1.73E-06)	3.78E-06	1.09E-05	1.56E-06 (2.46E-07)	9.75E-07	2.14E-06	**<0.0001**
HGt	77.38 (13.30)	50.03	104.72	66.01 (22.91)	9.95	122.07	0.6394
$LoHi_{end}$	0.75 (0.10)	0.51	0.98	1.05 (0.11)	0.82	1.28	**<0.0001**

Table 6.7: Comparison of non-responder and responder baseline values, irrespective of intervention group.

	Rest		OMT		Exercise	
	Non-responder	Responder	Non-responder	Responder	Non-responder	Responder
PPT	90.0%, 9	10.0%, 1	78.6%, 11	21.4%, 3	70.0%, 7	30.0%, 3
Area	100.0%, 10	0.0%, 0	78.6%, 11	21.4%, 3	77.8%, 7	22.2%, 2
αPDI	90.0%, 9	10.0%, 1	71.4%, 10	28.6%, 4	88.9%, 8	11.1%, 1
TR	30.0%, 3	70.0%, 7	57.1%, 8	42.9%, 6	40.0%, 4	60.0%, 6
TCs	60.0%, 6	40.0%, 4	71.4%, 10	28.6%, 4	90.0%, 9	10.0%, 1
TCd	90.0%, 9	10.0%, 1	71.4%, 10	28.6%, 4	70.0%, 7	30.0%, 3
aEMGend	100.0%, 8	0.0%, 0	92.3%, 12	7.7%, 1	100.0%, 8	0.0%, 0
HGt	100.0%, 10	0.0%, 0	64.3%, 9	35.7%, 5	80.0%, 8	20.0%, 2
Lo-Hi end	62.5%, 5	37.5%, 3	30.8%, 4	69.2%, 9	62.5%, 5	37.5%, 3

Table 6.8: Comparison of the quantity of non-responders and responders per parameter and intervention group. Values represent the percent and number of subjects for each parameter and group.

6.4 Discussion

The present study implemented a multi-modal approach for objective and non-invasive assessment of MTP response to OMT in the anterior forearm in healthy subjects, compared to rest and exercise. The main findings suggested by the study were:

1. OMT significantly reduced the pain pressure threshold at the MTP site, reduced tissue stiffness of the taut band, found the most subjects with trends of increased regional blood flow and grip time, and significantly reduced muscle fatigue after intervention, compared with rest and light exercise.

2. Rest improved pain, tissue compliance and muscle fatigue.

3. Light exercise improved blood flow, tissue stiffness and muscle fatigue, but increased tissue resistance.

4. Salient outcome measures identified with principal component analysis included at least one parameter from each modality suggesting that the combination of these modalities may be useful in evaluating MTP response to OMT.

5. Maximum voluntary contraction was not useful in observing response to treatment or physical provocation. It highly contributed to the variability of the data and masked other parameters contribution to variability.

6. Tissue compliance and regional blood flow measures were found to contribute to the variability of the data, suggesting that these may be metrics to include in a targeted study to determine the significance of these measures.

7. These data suggested the likelihood that responders may be found in the parameters correlating with high variance in the data. Baseline values of the suggested

responder group had lower pain thresholds, stiffer tissues and muscles fatigued earlier. Targeted study design may be further investigate if these sources of variance have a real statistical difference.

These findings demonstrate that trends, suggesting that objective evidence may be obtained and provides motivation for future MTP intervention research, specifically in the areas of participant screening, treatment effects, and study design.

6.4.1 Participant screening

MTP were identified bilaterally. The self-reported activities were consistent with MTP formation per literature including repetitive fine motor movement and holding postures for long duration [21, 62, 107]. Positive pain complaints without interfering in daily activity aligns with current understanding soft tissue injury, separate from acute injury [64], such as early stages of MTP [68, 104]. The majority of participants had prior experience with manual therapy, but their most recent treatment occurred more than 1 month prior to their study session. These characteristics describe a predominantly asymptomatic population in that MTP has not progressed to the point of disability and seeking care. Asymptomatic populations presenting with latent MTP have been shown to benefit from early manual therapy intervention, reducing pain symptom, improving quality of life, increasing range of motion and improving mental well-being [133]. While patients with chronic MTP are required to study treatment efficacy, investigations of MTP onset and early intervention with osteopathic medicine are also warranted. Screening for asymptomatic responders may be challenging. Responders were more compromised by MTP symptoms - they reported greater pain complaints and described interference with their daily activities compared to non-responders - and while many of the responders had not sought treatment for their specific pain complaints, it was primarily due to lack of motivation or knowledge of

OMT rather than necessity. It may be useful to screen for participants with minimal experience with manual therapy.

6.4.2 Treatment effects

Improvements across each outcome measure were observed after OMT intervention. Pain pressure threshold increased significantly in the OMT group, and all but 1 responder were found in the OMT group. This finding is consistent with literature *in-vivo* [170, 133], and *in-vitro* studies [183, 184, 24]. The mean regional blood flow area and magnitude trended towards an increase after OMT and rest intervention. These results suggest vasodilation and increased tissue perfusion after treatment. Tissue resistance decreased, while superficial and deep tissue compliance increased, suggesting softening of the taut band. The increased grip time and decreased spectral shape suggests improved endurance and reduced muscle fatigue during a sustained hand grip following OMT. These improvements are consistent with hypothesized effects of OMT treatments. Tissue softening is possibly due to a combination of neural signaling in the α- or γ-motoneuron pathways [135, 55]. Contracture knots are thought to be alleviated with passive stretching and pressure [126, 94]. This stretch also serves to resolve the tenderness and spontaneous electrical activity in the taut band [94]. Increased sympathetic activity is thought to increase pain, promote release of ACh from motoneruons with alpha and beta-adrenoceptors[63] and produce vasoconstriction. Pressure on MTP sites induced pain reduction that highly correlated with promoting sympathovagal balance [114] and reduce SEA [94]. Reducing sympathetic activity in the nervous system may also reduce the release of ACh, decrease muscle contraction, promote vasodilation, thus reversing processes promoting MTP formation[137]. Connective tissue activity of myofibroblasts and collagen alter biochemical environments and neuronal signaling [40, 182]. Satellite and endothelial cellular interactions

in response to tissue softening result in vasodilation and improved tissue perfusion [83]. Reduced pain may also be due to alterations in the fascial tissues to allow for gliding against muscle tissue [167]. The results of this study suggest maybe explained by multiple mechanisms that improve circulation, soften tissue and improve muscle function and alleviate pain.

With rest, regional blood flow metrics improved and the superficial tissue softened. The vasodilatory effect after the single bout of exercise (sustained hand grip test) may have also induced softened fascial tissues [167]. The hand grip time reduced and muscles fatigued suggesting that rest did not support improvements in myogenic activity.

With exercise (repeated hand clenches), grip time increased and tissues stiffened which are consistent with prior research [35]. No change was observed in the blood flow metrics or other myogenic activity metrics. This may be explained physiologically because after exercise, increased AcH concentrations are release into the neuromusclular junction, which in turn increases thresholds needed to trigger action potentials that initiate muscle contraction.

Regional blood flow metrics, maxPDI, area and αPDI metrics did not differ by group- variance of area increased following OMT. This might be a result of increased autonomic activity, modulating vasomotor response to establish homeostatic flow. The decrease in maxPDI after rest would conventionally be interpreted as a decrease in vascularity. However, area slightly improved, indicating vasodilation, which should be interpreted as increased vascularity. Increased vessel diameter will decrease blood velocity in the absence of increased supply pressure or flow-volume, producing lower PDI values [96]. Reduced maximum PDI would be interpreted as reduced blood flow if vasodilation is unaccounted.

The αPDI metric captured this effect, suggesting that this standardization method effectively estimated vascularity changes.

The power Doppler intensity trends showed that the slower flow (lower dB intensities) increased in both rest and OMT groups. While the origin of the impeded flow is unknown, we can speculate on why slow flow changes are observed over fast flow. One side effect of slowed or standing blood is the formation of rouleaux, aggregated erythrocytes in a stacked coin formation. This buildup is easily dispersed with shear gradients from normal arterial flow [49]; large blood volume flow changes are not necessary. This might explain the non-significant changes across blood flow metrcis as well as slow flow changes observed.

In-vitro investigations of microvascular damage and regeneration of skeletal muscle tissue [83] demonstrated that upon injury, myofibers were disrupted and capillary networks were fragmented. These changes thereby increased peripheral resistance. During the regenerative phase, capillary networks proliferated in a disorganized fashion and arterioles dilated, increasing tissue perfusion. This proliferation reduced once the tissue had healed, nearly returning pre-injury configurations. While MTP is not formed from acute trauma (i.e., blunt force) [62], peripheral resistance has been demonstrated to increase [151], similar to the early phase of tissue damage with acute injury [83]. The ischemic condition of MTP may be due to suspended state of restricted flow, perhaps resulting from contracture knot compression wherein microvascular structures are still intact. This would fail to trigger wound healing responses that restore vascular flow. Cao et. al. (2013) demonstrated that scratched fibroblasts wound healing advanced with a repetitive strain that simulated therapeutic stretch [24]. It can be speculated that this stretch effect may relieve the compression restoring flow, however these mechanisms must still be investigated.

The increased quantity of lower PDI pixels suggests augmented retrograde flow, venous return or interstitial fluid exchanges, which have been observed with exercise [165]. This study suggests that intervention or physical provocation may more readily be observed in the lower power Doppler intensity profiles. This is consistent with the findings of Sikdar et.al. [151], where blood flow waveforms near MTP sites showed increased retrograde flow compared to those near normal tissue. MTP sites have been identified as hypoechoic regions on B-mode ultrasound, suggesting tissue and microvascular disruption consistent with injury and ischemia [152].

The taut band was found to soften significantly with OMT, however, the tissue resistance estimate did not. This may be due to standardizing the ultrasound imaging to one location on the forearm rather than over the MTP site. In a meta analysis of MTP tissue stiffness related studies, consensus was found that tissue stiffness reduces within 1cm adjacent to the MTP site, from 12-14kPa at the MTP site down to 7-8kPa in adjacent tissue [107]. Evenstill, the tissue compliance estimation method was able to detect and quantify differences across intervention groups whereby tissue compliance reduced. Future work will also investigate SE and TR from the MTP site.

6.4.3 Study Design

Similar results were observed in the myogenic activity and in force generation across all intervention groups. Muscle fatigue reduced with rest, OMT and exercise demonstrated by spectral shape metric ($LoHi_{end}$) responders, however, maximum voluntary contraction (MVC) did not improve with any intervention and was not a salient parameter. Improvements in force were expected with OMT and exercise. Force generation is mediated by sympathetics [137] and OMT is thought to impact neural signalling and sympathetic outflow [75, 47, 145]. Also, relaxed hypertonic muscle tissues and reduced fatigue is observed after a single bout of acute exercise

[140] and with muscle energy treatment [172], improving force generation. The results from this study suggest that the sustained voluntary hand-grip test may have masked treatment effects.

6.4.4 Limitations

MTP category

While the focus of the study was development of an approach, instrumentation, participant screening and study design to assess MTP, described earlier, a major aspect of myofascial trigger point pathology was not investigated - active and latent trigger points were not classified in this study. The distinguishing feature is the nature of pain presentation, i.e. spontaneous and referred as opposed to localized and painful with stimulus. In the present study, only the local pain pressure thresholds were measured and documented. Early MTP research focused on active MTP as latent were interpreted as precursor to active sites and therefore less problematic. Studies have demonstrated increased inflammatory and nociceptive substances [147], increased retrograde blood flow [153], and decreased pain thresholds [58] in active sites compared to latent and normal tissues compared to latent. Future work should classify MTP to have more homogeneous groups.

Inclusion Criteria

The subjects activity level (sedentary to rigorous activity) and overall health status (BMI) were not formally categorized nor screened. It was observed during the individual test sessions that the interventions and grip tests had different effects on highly active vs. sedentary life styles. Highly active participants (engaged in regular weight lifting or martial arts, for example), showed improvements in their hand grip test regardless of intervention group. In these participants the hand grip test pro-

duced a warm-up exercise effect. It is well known that trained and untrained muscles respond differently to an acute bout of exercise. Sedentary participants fatigued during the first hand-grip and their performance in the second hand-grip reduced after exercise, improved with OMT and either improved or reduced with rest. Subjects should be screened for activity level.

Hand Grip Test

This study used a sustained voluntary hand-grip test to assess changes in myogenic activity. However, the fatigue test may not be a suitable test, especially in a symptomatic population. Subjects reporting the highest pain complaints and disruptions to daily activity had difficulty sustaining the grip, regardless of intervention group. In 5 cases sEMG signal length was insufficient for spectral analysis. A better test may be to measure the sEMG signal at rest. Myogenic activity in MTP has been characterized by spontaneous electrical activity in sEMG signal during rest, and at rest compared to before and after a short hand grip [54]. Measuring myogenic activity at rest may improve subject comfort while possibly revealing changes in myogenic activity in tissue with MTP. It is also known this is effect is more prominent in needle-EMG signals compared to surface electrodes. If the goal is to maintain the non-invasive nature of MTP evaluation then participants with high baseline levels of spontaneous electrical activity should be screened. Future work may consider developing tests for contractility [57] or activation times [106], appropriate for symptomatic population.

Participants

Differences between baseline values of the intervention groups were observed, suggesting that the participants represented within each group were not the same. The exercise group showed no fatigue throughout the initial hand grip test, while the rest

and OMT group fatigued. Principle components were different for each group, suggesting that either the sample populations within the intervention groups may have differed or that the interventions differed. This was a sample of convenience and randomization was limited by clinician's schedule and academic schedule of many participants. Future research may better adjust for scheduling challenges to ensure randomization. These results imply the need for improved participant screening and randomization. In future work, care should be taken to ensure participants across all groups match baseline characteristics.

Instrumentation

This proof-of-concept study demonstrated the use of a controlled strain elastography method that is standardized to a biophysical measure. Power Doppler ultrasound imaging requires standardization in order to compare images before and after intervention. For this study, an attempt was made to maintain all imaging parameters during pre- and post-intervention imaging, however, this was not possible in many cases. To accommodate this, a scaling parameter, αPDI, was proposed, which included the pulse-repetition frequency setting. In some cases, blood flow was not detectable as it was below the noise floor of the ultrasound unit. A higher frequency probe can be used to detect slower flows, however, imaging depth maybe compromised with higher frequency transducers.

The sEMG data was collected with a $5 - 250Hz$ band pass filter and $60Hz$ notch filter, which removed a significant portion of spectral content (between 55-75 Hz). Relevant information in the sEMG signal is found between $10 - 500Hz$ [119]. Increasing the frequency content collected and narrowing the $60Hz$ notch filter would provide relevant data that may improve the analysis, whereby the median frequency may more accurately represent the spectral shift [119, 34, 66, 111].

6.4.5 Future work

According to the present study, responders had higher pain at the MTP site, stiffer tissues in the anterior forearm and were easily fatigued. However, limitations with instrumentation may have masked salient features of regional blood flow and myogenic activity that may be useful in screening participants and study design. Future work will focus efforts on improving instrumentation and study design and inclusion/exclusion criteria. This study also reveals that while increasing representation of responders would be beneficial, studies involving non-responders compared to responders metrics may also be of interest.

The participants in the study showed that MTP may present across the range life styles (sedentary to active), wherein response to intervention and physical provocation may vary. Interestingly, four screened participants did not have painful MTP though they met the inclusion criteria (presence of palpable nodules). The study protocol was designed under the assumption that palpable nodules would be painful if all other MTP criteria were met. Since the pain pressure threshold was a measured parameter in this study, participants without elicited pain were excluded. While latent MTP are considered precursory to active sites, there may be an even earlier phase of MTP formation wherein nociceptive input has not yet fully established local hypersensitivity although the nodule is formed. It may be of interest to investigate response of non-painful nodules, perhaps providing insight into a primitive state of MTP and its progression towards severity.

Participant screening excluded participants with severe injury and known neuromuscular disorders. In convenience sample testing preparing for this study (n=5, not reported), inclusion criteria did not exclude prior injury and preliminary results showed greater response to intervention and physical provocation. Future work will

investigate effect of OMT on a more symptomatic population including more severe past injuries, trauma and post-surgery, where MTP also form. Participants should be screened for activity level over injury to increase responders.

6.5 Conclusion

A non-invasive, objective method for assessing MTP treatment with OMT was implemented in a pilot human study. MTP response to OMT in the forearm were detectable and measurable using the proposed approach. The results suggest OMT may provide benefits found in both rest and exercise, which would be useful for a patient population who have a reduced capacity for exercise. Recent studies suggest that MTP alleviation results in enhanced wound healing [184] and improved immune response [43]. Further investigation is needed to better understand how best to investigate myofascial trigger point response to osteopathic manipulative treatment. This study demonstrated that many outcome measures from each modality were considered salient in observing treatment effect across intervention groups. This will enhance understanding of MTP pathology necessary for developing safe and effective treatments. This work may be expanded from the forearm, to other clinically relevant regions of interest. Further investigation is needed to better determine the feasibility in using the methods proposed here for muscle tissue evaluation.

Chapter 7

CONCLUSIONS

The purpose of this thesis was to understand *what* and *how* to measure myofascial trigger point response to treatment or physical provocation. The motivation for this research was described in Chapter 1. Chapters 2 and 3 reviewed muscle tissue anatomy and physiology as it relates to myofascial trigger point formation and an response to an acute bout of exercise. Chapters 4 and 5, described bench-top developments for ultrasound imaging, optimized for superficial muscle tissue vascular and stiffness imaging, respectively. The experimental setup enabled controlled investigation of MTP *in-vivo*. The human subject pilot study, Chapter 6, demonstrated MTP response to treatment compared to rest and exercise, using multi-modal investigation. The findings in this study offered guidance for future MTP research using sEMG and ultrasound.

This pilot study found that further controls are needed in participant screening and randomization. The time of data collection overlapped with the end of one academic year and the start of another. Participants were more fatigued at the end of the academic year compared to those at the start of the next, as depicted in the baseline sEMG metrics. Also, the physician's schedule had to be considered. The physician was more available at the end of the academic year than at the start of the next year, so more participants at the end of the year were placed in the OMT group, and more participants in the start of the next year were placed in the exercise group. As a result, the baseline levels of the exercise group differed from the other groups, skewing the intervention responses.

The number of responders to intervention were low. This is to be expected as the participants were healthy, apart from the presence of MTP. In symptomatic subjects, or subjects with recent injuries, responses to OMT and exercise are expected to be more pronounced. Other factors in participant responses may not be accounted for. A participant may present symptoms responsive to environmental (such as room temperature), and psychological factors (stress), which are challenging to control for. Response to intervention differed greatly between highly active and sedentary participants, and activity level was not screened. The participants were predominantly female. It is noted by osteopathic physicians that pain tolerance and response to intervention varies throughout the menstrual cycle. Other coexistent pain conditions, such as migraines, lower back pain or temporomandibular joints pain may also contribute to response. For the purposes of this study, this medical information was not collected.

The inherent variability of muscle tissue dysfunction presentation and treatment response continue to challenge controlled research methodology. The main therapeutic targets are typically focused on pain and disability as these are the reasons for seeking medical attention. However pain is subjective and alter with many factors. This field would benefit from quantifying bias of pain perception with symptom presentation to help mitigate some of the variability. There is agreement among current researchers that tissue elasticity, circulation and myogenic activity are measurable features of MTP which are considerably more objective than pain perceptions. Pain perception may or may not correlate with these measures. In this present study, pain reductions and softened tissues were observed after OMT, however correlations could not be made. Further studies are needed find correlations between subjective and objective assessment. These observations could potentially offer valuable insights into muscle tissue disorders that are currently challenging to diagnose.

Throughout this study, emphasis was placed on the need to standardize images. During the human study, attempts were made to maintain the PRF setting before and after intervention since this standardization technique is commonly used in muscle tissue investigation with power Doppler ultrasound. However, during the data collection phase, it became apparent that this approach was not suitable, as changes in forearm vascularity necessitated adjustments to the PRF for optimal imaging. An attempt was made to capture the dependence of PD imaging on PRF where both color pixel intensity and area of detected flow were found to alter with PRF. These data demonstrated that Power Doppler ultrasound imaging is vulnerable to user dependent PRF optimization. To mitigate this dependence, a vascularity index was proposed, which captures the variability in color pixel intensity and area over the cardiac cycle, while also incorporating the PRF setting. The proposed a index was found to differentiate flows post-exercise from those at rest compared to PDI alone. Since the approach was developed during the pilot study, the human study contained both optimized and non-optimized power Doppler images. The group results may not reflect vascular changes accurately.

Endothelial function was not evaluated in baseline assessment, such as with reactive hyperemia [56] or an inspiratory gasp test [5]; it was assumed as subjects where considered healthy. In a symptomatic population, such as diabetics, peripheral arterial diseases and edema, endothelial function may be compromised, whereby muscle tissue vascularity may be challenging to image. Further investigation is needed to evaluate the feasibility and applications of using the vascularity index developed here. Chapter 5 demonstrated that strain maps differed with tissue compression rate. During the human study, a tissue compression rate near 4-6 Hz was tested and selected, and maintained between pre- and post- imaging. However, upon closer examination, slower compression rates, 2-3 Hz, provided more tissue deformation between frames,

resulting in improved strain map resolution. For the purpose of this study, the tissue compliance method visualized differences between relaxed and contracted muscles better than strain elastography alone. To fully demonstrate the proposed technique, improvements are needed in controlled strain elastography image acquisition and post-processing algorithms.

The surface EMG data was used to show muscle fatigue during a hand grip test. However, substantial changes in muscle fatigue were not observed. This may be due to the relatively asymptomatic population in this study, where there was little room for improvement as a whole. An alternative use of sEMG investigation may be in evaluating spontaneous electrical activity of MTP in the resting muscle. This might be a useful MTP severity metric. Evaluating the spontaneous electrical activity may provide insights into mechanisms involved in the treatment effect.

Another clinically relevant metric that was observed but not recorded in this study was the range of motion. Many participants demonstrated increased range of motion (supination and protnation) after OMT, compared to rest and exercise. This was observed when the forearm was replaced under the transducer in the supine position after the intervention. Future research might consider both myoelectric activity and biomechanics and as a markers for MTP severity. The forearm of symptomatic patients may not be able to lay supine under the transducer probe for quality SE imaging. Alternate positions should be considered when investigating symptomatic subjects.

This study attempted to identify the best performing metrics using ultrasound and sEMG. Future work may focus on refining the experimental setup and post-processing algorithms, testing the reproducibility, reliability, sensitivity and specificity of outcome measures. Still, there is a need to better understand MTP biomarkers in order to select appropriate diagnostic modalities. Wearables and portable devices may facil-

itate larger studies and investigation of additional anatomical regions. Elastography presents with artifact in superficial tissues within bony structures such as intercostal muscles, lower back pain near spinous or pelvic processes, or deep tissue structures near large vessels and soft tissue organs. Alternative tissue stiffness measurements modalities should be considered.

When considering the burden of musculoskeletal tissue disorders in the general population, simple and effective tools for clinical implementation are desirable. Quasi-quantitative diagnostic utilities in ultrasound imaging are sought after in physical medicine and musculoskeletal research for these reasons. Power Doppler ultrasound and strain elastography are conventionally qualitative imaging modalities. Implementing new techniques using these modalities within clinical settings may be cost-effective because these methods are low cost, easy to use, and time efficient, i.e. requires minimal training and can be acquired at point-of care. This study demonstrated possible modifications for improving their functionality for both the clinician and the researcher in mind.

Multi-modal investigations may provide quality of evidence needed in complementary and integrative medical care. The key contributions of this work includes:

- comprehensive review of myofascial trigger point pathology
- a novel method for quantifying power Doppler ultrasound cine, estimating vascularity in muscle tissue
- a novel strain elastography standardization technique using flexible force sensor integration, estimating tissue compliance
- recommendations and guidance for future work MTP treatment

With further development the proposed approach may apply to broad array of clinical scenarios for musculoskeletal tissue evaluation including physical medicine, biome-

chanics, stroke rehabilitation, neuromuscular diseases, and therapeutic techniques directed towards amelioration of neuromuscular symptoms. The insights gained in this study may support more effective care and management of work-related muscle disorders in clinical practice.

REFERENCES

[1] NIH HEAL Initiative Workshop on Myofascial Pain. 2022.

[2] Ronald S. Adler, Jonathan M. Rubin, J.Brian Fowlkes, Paul L. Carson, and John E. Pallister. Ultrasonic estimation of tissue perfusion: A stochastic approach. 21(4):493–500, 1995.

[3] Micky A Akinrodoye and Forshing Lui. Neuroanatomy, Somatic Nervous System. StatPearls Publishing, 2022-11-01.

[4] Jacob Allen, Yi Sun, and Jeffrey A. Woods. Exercise and the Regulation of Inflammatory Responses. In *Progress in Molecular Biology and Translational Science*, volume 135, pages 337–354. Elsevier, 2015.

[5] John Allen, John R Frame, and Alan Murray. Microvascular blood flow and skin temperature changes in the fingers following a deep inspiratory gasp. 23(2):365–373, 2002-05-01.

[6] G.T Allison and T Fujiwara. The relationship between EMG median frequency and low frequency band amplitude changes at different levels of muscle capacity. 17(6):464–469, 2002-07.

[7] Penelope Allisy-Roberts and Jerry Williams. Imaging with ultrasound. In *Farr's Physics for Medical Imaging*, pages 147–168. Elsevier, 2008.

[8] David J Alvarez. Trigger Points: Diagnosis and Management. 65(4):8, 2002.

[9] Nazar N Amso, Sean R Watermeyer, Neil Pugh, Sharon O'Brien, and Arianna D'Angelo. Quantification of power Doppler energy and its future potential. 76(3):583–587, 2001-09.

[10] Judy E. Anderson. A Role for Nitric Oxide in Muscle Repair: Nitric Oxide–mediated Activation of Muscle Satellite Cells. 11(5):1859–1874, 2000-05.

[11] Lars Arendt-Nielsen and Thomas Graven-Nielsen. Translational musculoskeletal pain research. 25(2):209–226, 2011-04.

[12] Maggie Armstrong, Connor C Kerndt, and Ross A Moore. *Physiology, Baroreceptors*. StatPearls, 2023.

[13] Md Ashikuzzaman and Hassan Rivaz. Second-Order Ultrasound Elastography With L 1-Norm Spatial Regularization. 69(3):1008–1019, 2022-03.

[14] Md Ashikuzzaman, Ali Sadeghi-Naini, Abbas Samani, and Hassan Rivaz. Combining First- and Second-Order Continuity Constraints in Ultrasound Elastography. 68(7):2407–2418, 2021-07.

[15] Md Ashikuzzaman, Ali K. Z. Tehrani, and Hassan Rivaz. Exploiting Mechanics-Based Priors for Lateral Displacement Estimation in Ultrasound Elastography. pages 1–1, 2023.

[16] Donatella Bagagiolo, Debora Rosa, and Francesca Borrelli. Efficacy and safety of osteopathic manipulative treatment: An overview of systematic reviews. 12(4):e053468, 2022-04.

[17] J. Bamber, D. Cosgrove, C. Dietrich, J. Fromageau, J. Bojunga, F. Calliada, V. Cantisani, J.-M. Correas, M. D'Onofrio, E. Drakonaki, M. Fink, M. Friedrich-Rust, O. Gilja, R. Havre, C. Jenssen, A. Klauser, R. Ohlinger, A. Saftoiu, F. Schaefer, I. Sporea, and F. Piscaglia. EFSUMB Guidelines and Recommendations on the Clinical Use of Ultrasound Elastography. Part 1: Basic Principles and Technology. 34(02):169–184, 2013-04-04.

[18] J Gordon Betts, Peter Desaix, Eddie Johnson, Jody E Johnson, Oksana Korol, Dean Kruse, Brandon Poe, James A Wise, Mark Womble, and Kelly A Young. Anatomy & Physiology. page 1420.

[19] Shaloo Bhasin and Peter P. Cheung. The Role of Power Doppler Ultrasonography as Disease Activity Marker in Rheumatoid Arthritis. 2015:1–9, 2015.

[20] W H Breidahl, J S Newman, M S Taljanovic, and R S Adler. Power Doppler sonography in the assessment of musculoskeletal fluid collections. 166(6):1443–1446, 1996-06.

[21] Carel Bron and Jan D. Dommerholt. Etiology of Myofascial Trigger Points. 16(5):439–444, 2012-10.

[22] Arnault H Caillet, Andrew Tm Phillips, Dario Farina, and Luca Modenese. Mathematical relationships between spinal motoneuron properties. 11:e76489, 2022-07-18.

[23] Fleur A. Camfferman, Ginette M. Ecury-Goossen, Jhuresy E. La Roche, Nico deJong, van't Leven, Willem, Hendrik J. Vos, Martin D. Verweij, Kazem Nasserinejad, Filip Cools, Paul Govaert, and Jeroen Dudink. Calibrating Doppler Imaging of Preterm Intracerebral Circulation Using a Microvessel Flow Phantom. 8, 2015-01-13.

[24] Thanh V. Cao, Michael R. Hicks, and Paul R. Standley. In Vitro Biomechanical Strain Regulation of Fibroblast Wound Healing. 113(11):806–818, 2013-11-01.

[25] I Cespedes, J Ophir, H Ponnekanti, and N Maklad. Elastography: Elasticity imaging using ultrasound with application to muscle and breast in vivo. 15:73–88, 1993.

[26] Jérome Chal and Olivier Pourquié. Making muscle: Skeletal myogenesis *in vivo* and *in vitro*. 144(12):2104–2122, 2017-06-15.

[27] Mark A. Chapman, Rachel Meza, and Richard L. Lieber. Skeletal muscle fibroblasts in health and disease. 92(3):108–115, 2016-09.

[28] Anthony G Chila and American Osteopathic Association. *Foundations of Osteopathic Medicine.* Wolters Kluwer Health/Lippincott Williams & Wilkins, 2011.

[29] Kentaro Chino, Ryota Akagi, Michiko Dohi, Senshi Fukashiro, and Hideyuki Takahashi. Reliability and Validity of Quantifying Absolute Muscle Hardness Using Ultrasound Elastography. 7(9):e45764, 2012-09-21.

[30] Kentaro Chino, Ryota Akagi, Michiko Dohi, and Hideyuki Takahashi. Measurement of muscle architecture concurrently with muscle hardness using ultrasound strain elastography. 55(7):833–839, 2014-09.

[31] Mario Cifrek, Vladimir Medved, Stanko Tonković, and Saša Ostojić. Surface EMG based muscle fatigue evaluation in biomechanics. 24(4):327–340, 2009-05.

[32] Tainya Clarcke, Richard Nahin, Patricia Barnes, and Barbara Stussman. National Health Statistics Reports, Number 98, October, 2016, 2016.

[33] Torben Clausen. Na $^{+}$ -K $^{+}$ Pump Stimulation Improves Contractility in Damaged Muscle Fibers. 1066(1):286–294, 2006-03.

[34] Giovanni Corvini and Silvia Conforto. A Simulation Study to Assess the Factors of Influence on Mean and Median Frequency of sEMG Signals during Muscle Fatigue. 22(17):6360, 2022-08-24.

[35] Scott Justin Dankel and Brenna M. Razzano. The impact of acute and chronic resistance exercise on muscle stiffness: A systematic review and meta-analysis. 23(4):473–480, 2020-12.

[36] E. G. Sunethra Dayavansha, Gary J. Gross, Matthew C. Ehrman, Peter D. Grimm, and T. Douglas Mast. Reconstruction of shear wave speed in tissue-mimicking phantoms from aliased pulse-echo imaging of high-frequency wavefields. 150(6):4128–4139, 2021-12.

[37] Kayleigh De Meulemeester, Barbara Cagnie, Jo Van Dorpe, Martin Lammens, Mirko Petrovic, and Patrick Calders. Differences in the Mitochondrial and Lipid Droplet Morphology in Female Office Workers With Trapezius Myalgia, Compared With Healthy Controls: A Muscle Biopsy Study. 98(11):989–997, 2019-11.

[38] Christoph Dietrich, Richard Barr, André Farrokh, Manjiri Dighe, Michael Hocke, Christian Jenssen, Yi Dong, Adrian Saftoiu, and Roald Havre. Strain Elastography - How To Do It? 03(04):E137–E149, 2017-09.

[39] N.A. Dimitrova and G.V. Dimitrov. Interpretation of EMG changes with fatigue: Facts, pitfalls, and fallacies. 13(1):13–36, 2003-02.

[40] John G Dodd, Meadow Maze Good, Tammy L. Nguyen, Andersen I. Grigg, Lyn M. Batia, and Paul R. Standley. In vitro biophysical strain model for understanding mechanisms of osteopathic manipulative treatment. 106(3):157–166, 2006-03.

[41] Amir Dori, Hiba Abbasi, and Craig M. Zaidman. Intramuscular blood flow quantification with power doppler ultrasonography: Muscle Blood Flow Sonography. 54(5):872–878, 2016-11.

[42] E E Drakonaki, G M Allen, and D J Wilson. Ultrasound elastography for musculoskeletal applications. 85(1019):1435–1445, 2012-11.

[43] Huixun Du, Juliet M. Bartleson, Sergei Butenko, Valentina Alonso, Wendy F. Liu, Daniel A. Winer, and Manish J. Butte. Tuning immunity through tissue mechanotransduction. 23(3):174–188, 2023-03.

[44] Francies A. Duck. *Physical Properties of Tissues*. Academic Press Inc., 1990.

[45] Brian E. Earley and Helen Luce. An Introduction to Clinical Research in Osteopathic Medicine. 37(1):49–64, 2010-03.

[46] Sid Edelman. Chapter 1 Ultrasound Physics, 2024.

[47] Alex M. Eingorn and George J. Muhs. Rationale for assessing the effects of manipulative therapy on autonomic tone by analysis of heart rate variability. 22(3):161–165, 1999-03.

[48] Mai Elfarnawany, Stephen Z. Pinter, and James C. Lacefield. Improved Objective Selection of Power Doppler Wall-Filter Cut-Off Velocity for Accurate Vascular Quantification. 38(8):1429–1439, 2012-08.

[49] D. H. Evans, W. N. McDickens, R. Skidmore, and J.P. Woodcock. *Doppler Ultrasound: Physics, Instrumentation and Clinical Applications*. John Wiley & Sons, 1981.

[50] Rasha M. Fawzy, Emtethal A. Said, and Amira I. Mansour. Association of neutrophil to lymphocyte ratio with disease activity indices and musculoskeletal ultrasound findings in recent onset rheumatoid arthritis patients. 39(4):203–206, 2017-10.

[51] Joseph Feher. Spinal Reflexes. In *Quantitative Human Physiology*, pages 400–408. Elsevier, 2012.

[52] Josué Fernández-Carnero, César Fernández-de-las Peñas, prefix=de la useprefix=true family=Llave Rincón, given=Ana Isabel, Hong-You Ge, and Lars Arendt-Nielsen. Bilateral Myofascial Trigger Points in the Forearm Muscles in Patients With Chronic Unilateral Lateral Epicondylalgia: A Blinded, Controlled Study. 24(9):802–807, 2008-11.

[53] Josué Fernández-Carnero, César Fernández-de-las Peñas, de la Llave-Rincón, Ana Isabel, Hong-You Ge, and Lars Arendt-Nielsen. Prevalence of and Referred Pain From Myofascial Trigger Points in the Forearm Muscles in Patients With Lateral Epicondylalgia. 23(4):353–360, 2007-05.

[54] Josué Fernández-Carnero, Hong-You Ge, Yoshiyuki Kimura, César Fernández-de-las Peñas, and Lars Arendt-Nielsen. Increased Spontaneous Electrical Activity at a Latent Myofascial Trigger Point After Nociceptive Stimulation of Another Latent Trigger Point. 26(2):138–143, 2010-02.

[55] Loren Fishman and Jennifer Halstead-Kenny. Integrating complementary/alternative medicine into primary care: Evaluating the evidence and appropriate implementation. page 361, 2015-12.

[56] Robert Fitridge and Mathew Thompson. *Mechanisms of Vascular Disease: A Reference Book for Vascular Specialists*. The University Adelaide, Barr Smith Press, 2011.

[57] Jing Gao, Judy Caldwell, Keeling McLin, Man Zhang, and David Park. Ultrasound Shear Wave Elastography to Assess Osteopathic Manipulative Treatment on the Iliocostalis Lumborum Muscle: A Feasibility Study. 39(1):157–164, 2020-01.

[58] Hong-You Ge and Lars Arendt-Nielsen. Latent Myofascial Trigger Points. 15(5):386–392, 2011-10.

[59] Hong-You Ge, César Fernández-de-las Peñas, and Shou-Wei Yue. Myofascial trigger points: Spontaneous electrical activity and its consequences for pain induction and propagation. 6(1):13, 2011.

[60] J.-L. Gennisson, T. Deffieux, M. Fink, and M. Tanter. Ultrasound elastography: Principles and techniques. 94(5):487–495, 2013-05.

[61] Robert D. Gerwin. Myofascial pain syndromes in the upper extremity. 10(2):130–136, 1997-04.

[62] Robert D. Gerwin. Diagnosis of Myofascial Pain Syndrome. 25(2):341–355, 2014-05.

[63] Robert D. Gerwin, Jan Dommerholt, and Jay P. Shah. An expansion of Simons' integrated hypothesis of trigger point formation. 8(6):468–475, 2004-12.

[64] Maria Adele Giamberardino, Giannapia Affaitati, Alessandra Fabrizio, and Raffaele Costantini. Myofascial pain syndromes and their evaluation. 25(2):185–198, 2011-04.

[65] Francesco Giovagnorio, Carlo Martinoli, and Giulio Coari. Power Doppler sonography in knee arthritis - a pilot study. 20(3):101–104, 2001-04.

[66] M. González-Izal, A. Malanda, I. Navarro-Amézqueta, E.M. Gorostiaga, F. Mallor, J. Ibañez, and M. Izquierdo. EMG spectral indices and muscle power fatigue during dynamic contractions. 20(2):233–240, 2010-04.

[67] Carlo Gotti, Alberto Sensini, Andrea Zucchelli, Raffaella Carloni, and Maria Letizia Focarete. Hierarchical fibrous structures for muscle-inspired soft-actuators: A review. 20:100772, 2020-09.

[68] Rob Grieve, Sue Barnett, Nikki Coghill, and Fiona Cramp. The prevalence of latent myofascial trigger points and diagnostic criteria of the triceps surae and upper trapezius: A cross sectional study. 99(4):278–284, 2013-12.

[69] Liza Grosman-Rimon, William Parkinson, Suneel Upadhye, Hance Clarke, Joel Katz, John Flannery, Philip Peng, and Dinesh Kumbhare. Circulating biomarkers in acute myofascial pain: A case–control study. 95(37):e4650, 2016-09.

[70] Carlos F. Guimarães, Luca Gasperini, Alexandra P. Marques, and Rui L. Reis. The stiffness of living tissues and its implications for tissue engineering. 5(5):351–370, 2020-05.

[71] Hoda Sadat Hashemi and Hassan Rivaz. Global Time-Delay Estimation in Ultrasound Elastography. 64(10):1625–1636, 2017-10.

[72] Roald Havre, Jo Waage, Anesa Mulabecirovic, Odd Gilja, and Lars Nesje. Strain Ratio as a Quantification Tool in Strain Imaging. 8(8):1273, 2018-08-01.

[73] Deborah M. Heath, Inder Raj S. Makin, Chandhana Pedapati, and Jonathon Kirsch. Use of Real-Time Physiologic Parameter Assessment to Augment Osteopathic Manipulative Treatment Training for First-Year Osteopathic Medical Students. 114(12):918–919, 2014-12-01.

[74] Christine A. Henderson, Christopher G. Gomez, Stefanie M. Novak, Lei Mi-Mi, and Carol C. Gregorio. Overview of the Muscle Cytoskeleton. In Ronald Terjung, editor, *Comprehensive Physiology*, pages 891–944. Wiley, 1 edition, 2017-06-18.

[75] Charles E Henley, Douglas Ivins, Miriam Mills, Frances K Wen, and Bruce A Benjamin. Osteopathic manipulative treatment and its relationship to autonomic nervous system activity as demonstrated by heart rate variability: A repeated measures study. 2(1):7, 2008-12.

[76] Elwood Henneman. Relation between Size of Neurons and Their Susceptibility to Discharge. 126(3287):1345–1347, 1957-12-27.

[77] Michael R. Hicks, Thanh V. Cao, David H. Campbell, and Paul R. Standley. Mechanical strain applied to human fibroblasts differentially regulates skeletal myoblast differentiation. 113(3):465–472, 2012-08-01.

[78] Michael R. Hicks, Thanh V. Cao, and Paul R. Standley. Biomechanical strain vehicles for fibroblast-directed skeletal myoblast differentiation and myotube functionality in a novel coculture. 307(8):C671–C683, 2014-10-15.

[79] Ulrich Hoheisel, Siegfried Mense, David G. Simons, and Xian-Min Yu. Appearance of new receptive fields in rat dorsal horn neurons following noxious stimulation of skeletal muscle: A model for referral of muscle pain? 153(1):9–12, 1993-04.

[80] Hsin Hsiu, Wei-Chen Hsu, Bo-Hung Chen, and Chia-Liang Hsu. Differences in the microcirculatory effects of local skin surface contact pressure stimulation between acupoints and nonacupoints: Possible relevance to acupressure. 31(6):829–841, 2010-06-01.

[81] David R. Hubbard and Gregory M. Berkoff. Myofascial Trigger Points Show Spontaneous Needle EMG Activity. 18(13):1803–1807, 1993.

[82] G. Illomei, G. Spinicci, E. Locci, and M. G. Marrosu. Muscle elastography: A new imaging technique for multiple sclerosis spasticity measurement. 38(3):433–439, 2017-03.

[83] Nicole L. Jacobsen, Charles E. Norton, Rebecca L. Shaw, D. D. W. Cornelison, and Steven S. Segal. Myofibre injury induces capillary disruption and regeneration of disorganized microvascular networks. 600(1):41–60, 2022-01.

[84] Bernadette Jaeger and John L. Reeves. Quantification of changes in myofascial trigger point sensitivity with the pressure algometer following passive stretch. 27(2):203–210, 1986.

[85] T Jansson, H W Persson, and K Lindström. Estimation of blood perfusion using ultrasound. 213, 1999.

[86] Ian T. Jolliffe and Jorge Cadima. Principal component analysis: A review and recent developments. 374(2065):20150202, 2016-04-13.

[87] Roland Kadefors. Recruitment of low threshold motor-units in the trapezius muscle in different static arm positions. 42(2):359–375, 1999-02.

[88] Eric R. Kandel, James H. Schwartz, and Thomas M. Jessel. *Principles of Neural Science*. McGraw-Hill, 4 edition, 2000.

[89] Chihiro Kasai, Koroku Namekawa, Akira Koyano, and Ryozo Omoto. Real-Time Two-Dimensional Blood Flow Imaging Using an Autocorrelation Technique. 1985.

[90] Su Ji Kim, Hee Jin Park, and So Yeon Lee. Usefulness of strain elastography of the musculoskeletal system. 35(2):104–109, 2016-04-01.

[91] J Kimura. Part V. Neuromuscular Transmission and Muscle Excitability. In *Electrodiagnosis in Diseaes of Nerve and Muscle: Principles and Practice.*, pages 429–474. 2013.

[92] Lindsey K Koop and Prasanna Tadi. Neuroanatomy, Sensory Nerves.

[93] Ronald J. Korthuis. Skeletal Muscle Circulation. In *Colloquium Series on Integrated Systems Physiology: From Molecule to Function*, volume 3, pages 1–144. 2011.

[94] Dimitrios Kostopoulos, Arthur J. Nelson, Reuben S. Ingber, and Ralph W. Larkin. Reduction of Spontaneous Electrical Activity and Pain Perception of Trigger Points in the Upper Trapezius Muscle through Trigger Point Compression and Passive Stretching. 16(4):266–278, 2008-01.

[95] Frederick Kremkau. *Sonography: Principles and Instruments*. Lauren Wilson, 9 edition, 2016.

[96] Michael M.D. Lawrence-Brown, Kurt Liffman, James B. Semmens, and Ilija D. Sutalo. Chapter 8 Vascular Arterial Haemodynamics. In *Mechanisms of Vascular Disease: A Reference Book for Vascular Specialists*, pages 153–175. The University Adelaide, Barr Smith Press, 2011.

[97] Loong Chuen Lee, Choong-Yeun Liong, and Abdul Aziz Jemain. Partial least squares-discriminant analysis (PLS-DA) for classification of high-dimensional (HD) data: A review of contemporary practice strategies and knowledge gaps. 143(15):3526–3539, 2018.

[98] John W. Leis. *Communication Systems Principles Using MATLAB*. Wiley, 1 edition, 2018.

[99] Arlene Bradley Levine, David Punihaole, and T. Barry Levine. Characterization of the Role of Nitric Oxide and Its Clinical Applications. 122(1):55–68, 2012.

[100] Yufei Li and Jess G. Snedeker. Elastography: Modality-specific approaches, clinical applications, and research horizons. 40(4):389–397, 2011-04.

[101] Lukas D. Linde, Dinesh A. Kumbhare, Maneil Joshi, and John Z. Srbely. The Relationship between Rate of Algometer Application and Pain Pressure Threshold in the Assessment of Myofascial Trigger Point Sensitivity. 18(2):224–229, 2018-02.

[102] Anna Liu, Tong Yu, Katherine Young, Nicholas Stone, Srinivas Hanasoge, Tyler J. Kirby, Vikram Varadarajan, Nicholas Colonna, Janet Liu, Abhishek Raj, Jan Lammerding, Alexander Alexeev, and Todd Sulchek. Cell Mechanical and Physiological Behavior in the Regime of Rapid Mechanical Compressions that Lead to Cell Volume Change. 16(2):1903857, 2020-01.

[103] S. M. Lobmaier, M. Cruz-Lemini, B. Valenzuela-Alcaraz, J. U. Ortiz, J. M. Martinez, E. Gratacos, and F. Crispi. Influence of equipment and settings on myocardial performance index repeatability and definition of settings to achieve optimal reproducibility. 43(6):632–639, 2014-06.

[104] Karen R. Lucas. The impact of latent trigger points on regional muscle function. 12(5):344–349, 2008-10.

[105] Karen R Lucas, Barbara I Polus, and Peter A Rich. Latent myofascial trigger points: Their effects on muscle activation and movement efficiency. 8(3):160–166, 2004-07.

[106] Karen R. Lucas, Peter A. Rich, and Barbara I. Polus. Muscle activation patterns in the scapular positioning muscles during loaded scapular plane elevation: The effects of Latent Myofascial Trigger Points. 25(8):765–770, 2010-10.

[107] Dario F. Mazza, Robert D. Boutin, and Abhijit J. Chaudhari. Assessment of Myofascial Trigger Points via Imaging: A Systematic Review. 100(10):1003–1014, 2021-10.

[108] Lorne M. Mendell. The size principle: A rule describing the recruitment of motoneurons. 93(6):3024–3026, 2005-06.

[109] S. Mense. Referral of muscle pain. 3(1):1–9, 1994-03.

[110] Amir Minerbi and Simon Vulfsons. Challenging the Cinderella Hypothesis: A New Model for the Role of the Motor Unit Recruitment Pattern in the Pathogenesis of Myofascial Pain Syndrome in Postural Muscles. 9(3):e0021, 2018-07-30.

[111] Dong Ming, Xin Wang, Rui Xu, Shuang Qiu, Xin Zhao, Hongzhi Qi, Peng Zhou, Lixin Zhang, and Baikun Wan. sEMG feature analysis on forearm muscle fatigue during isometric contractions. 20(2):139–143, 2014-04.

[112] D.C. Montgomery. *Design and Analysis of Experiments*. John Wiley & Sons, 8 edition, 2012.

[113] Albert F. Moraska, Robert C. Hickner, Wendy M. Kohrt, and Alan Brewer. Changes in Blood Flow and Cellular Metabolism at a Myofascial Trigger Point With Trigger Point Release (Ischemic Compression): A Proof-of-Principle Pilot Study. 94(1):196–200, 2013-01.

[114] Yoshiki Morikawa, Kouich Takamoto, Hiroshi Nishimaru, Toru Taguchi, Susumu Urakawa, Shigekazu Sakai, Taketoshi Ono, and Hisao Nishijo. Compression at Myofascial Trigger Point on Chronic Neck Pain Provides Pain Relief through the Prefrontal Cortex and Autonomic Nervous System: A Pilot Study. 11, 2017-04-11.

[115] Timothy Musila Mutala, Gladys N. Mwango, Angeline Aywak, Dania Cioni, and Emanuele Neri. Determining the elastography strain ratio cut off value for differentiating benign from malignant breast lesions: Systematic review and meta-analysis. 22(1):12, 2022-12.

[116] Harmon L Myers, William H Devine, Christian Fossum, John Glover, Michael Kuchera, Randall S Kusunose, Richard Van Buskirk, Andrew Weil, and Tucson Osteopathic Medical Foundation. *Clinical Application of Counterstrain*. Osteopathic Press, a division of Tucson Osteopathic Medical Foundation, 2012.

[117] Frauke Müggenborg, Ester Moreira De Castro Carletti, Liz Dennett, Ana Izabela Sobral De Oliveira-Souza, Norazlin Mohamad, Gunnar Licht, Harry Von Piekartz, and Susan Armijo-Olivo. Effectiveness of Manual Trigger Point Therapy in Patients with Myofascial Trigger Points in the Orofacial Region—A Systematic Review. 13(2):336, 2023-01-27.

[118] Richard L Nahin. Insurance Coverage for Complementary Health Approaches Among Adult Users: United States, 2002 and 2012. (235), 2016.

[119] Nurhazimah Nazmi, Mohd Abdul Rahman, Shin-Ichiroh Yamamoto, Siti Ahmad, Hairi Zamzuri, and Saiful Mazlan. A Review of Classification Techniques of EMG Signals during Isotonic and Isometric Contractions. 16(8):1304, 2016-08-17.

[120] Osmar Pinto Neto and Evangelos A. Christou. Rectification of the EMG Signal Impairs the Identification of Oscillatory Input to the Muscle. 103(2):1093–1103, 2010-02.

[121] J S Newman, R S Adler, R O Bude, and J M Rubin. Detection of soft-tissue hyperemia: Value of power Doppler sonography. page 5, 1994.

[122] Margareta Nordin and Victor Frankel, H. *Basic Biomechanics of the Musculoskeletal System*. Lea & Febiger, 2 edition, 1989.

[123] J Ophir, I CCspedes, H Ponnekanti, Y Yazdi, and X Li. Elastography: A Quantitative Method for Imaging the Elasticity of Biological Tissues. 13:111–134, 1991.

[124] Salih Ozgocmen and Ozge Ardicoglu. Lipid profile in patients with fibromyalgia and myofascial pain syndromes. 41(5):541–545, 2000.

[125] Salih Ozgocmen and Ozge Ardicoglu. Lipid profiles in patients with fibromyalgia and myofascial pain syndrome. 41(5):541–545, 2000.

[126] Jesus Palomero, Deborah Pye, Tabitha Kabayo, and Malcolm J. Jackson. Effect of passive stretch on intracellular nitric oxide and superoxide activities in single skeletal muscle fibres: Influence of ageing. 46(1):30–40, 2012-01.

[127] Giburm Park, Chan Woo Kim, Si Bog Park, Mi Jung Kim, and Seong Ho Jang. Reliability and Usefulness of the Pressure Pain Threshold Measurement in Patients with Myofascial Pain. 35(3):412, 2011.

[128] Juhani V. Partanen, Tuula A. Ojala, and Jari P.A. Arokoski. Myofascial syndrome and pain: A neurophysiological approach. 17(1):19–28, 2010-02.

[129] Paolo Pedersini, Stefano Negrini, Raquel Cantero-Tellez, Mark D. Bishop, and Jorge Hugo Villafañe. Pressure algometry and palpation of the upper limb peripheral nervous system in subjects with hand osteoarthritis are repeatable and suggest central changes. 33(1):103–111, 2020-01.

[130] Gerald J. Pepe and Eugene D. Albrecht. Microvascular Skeletal-Muscle Crosstalk in Health and Disease. 24(13):10425, 2023-06-21.

[131] Steven Pham and Yana Puckett. *Phsyiology, Skeletal Muscle Contraction*. StatPearls Publishing, 2022.

[132] Una Pongratz and Theresia Licka. Algometry to measure pain threshold in the horse's back – An in vivo and in vitro study. 13(1):80, 2017-12.

[133] Albert Pérez-Bellmunt, Mathias Simon, Carlos López-de Celis, Sara Ortiz-Miguel, Vanessa González-Rueda, and César Fernandez-de-las Peñas. Effects on Neuromuscular Function After Ischemic Compression in Latent Trigger Points in the Gastrocnemius Muscles: A Randomized Within-Participant Clinical Trial. page S0161475420301561, 2021-01.

[134] M. B. I. Reaz, M. S. Hussain, and F. Mohd-Yasin. Techniques of EMG signal analysis: Detection, processing, classification and applications. 8(1):11–35, 2006-12.

[135] Ashley Roberts, Kaylee Harris, Bethany Outen, Amar Bukvic, Ben Smith, Adam Schultz, Stephen Bergman, and Debasis Mondal. Osteopathic Manipulative Medicine: A Brief Review of the Hands-On Treatment Approaches and Their Therapeutic Uses. 9(5):33, 2022-04-27.

[136] Cmt Langdon Roberts, Ma. Effects of Patterns of Pressure Application on Resting Electromyography During Massage. 4(1):4–11, 2011-03-30.

[137] Anna C. Z. Rodrigues, Maria L. Messi, Zhong-Min Wang, Martin C. Abba, Andrea Pereyra, Alexander Birbrair, Tan Zhang, Meaghan O'Meara, Ping Kwan, Elsa I. S. Lopez, Monte S. Willis, Akiva Mintz, D. Clark Files, Cristina Furdui, Ronald W. Oppenheim, and Osvaldo Delbono. The sympathetic nervous system regulates skeletal muscle motor innervation and acetylcholine receptor stability. 225(3):e13195, 2019-03.

[138] Johathan Rubin, M., Ronald S. Adler, Brian J. Fowlkes, Steve Spratt, John E. Pallister, Jian-Feng Chen, and Paul L. Carson. Fractional Moving Blood Volume: Estimation with Power Doppler US. 197(1):183–190, 1995-10.

[139] Thorsten Rudroff, Didier Staudenmann, and Roger M. Enoka. Electromyographic measures of muscle activation and changes in muscle architecture of human elbow flexors during fatiguing contractions. 104(6):1720–1726, 2008-06.

[140] Katja S.C. Röckl, Carol A. Witczak, and Laurie J. Goodyear. Signaling mechanisms in skeletal muscle: Acute responses and chronic adaptations to exercise. 60(3):145–153, 2008-03.

[141] Robert Schleip, Lutz Duerselen, Andry Vleeming, Ian L. Naylor, Frank Lehmann-Horn, Adjo Zorn, Heike Jaeger, and Werner Klingler. Strain hardening of fascia: Static stretching of dense fibrous connective tissues can induce a temporary stiffness increase accompanied by enhanced matrix hydration. 16(1):94–100, 2012-01.

[142] Robert Schleip, Giulio Gabbiani, Jan Wilke, Ian Naylor, Boris Hinz, Adjo Zorn, Heike Jäger, Rainer Breul, Stephanie Schreiner, and Werner Klingler. Fascia Is Able to Actively Contract and May Thereby Influence Musculoskeletal Dynamics: A Histochemical and Mechanographic Investigation. 10:336, 2019-04-02.

[143] Micheal A. Seffinger, edditor. *Foundations of Osteopathic Medicine: Philosophy, Science, Clinical Applications and Research.* Wolters Kluwer Health, 4 edition, 2018.

[144] Małgorzata Serafin-Król, Artur Maliborski, and Medical Radiology Department, Military Institute of Medicine, Warsaw, Poland. Diagnostic errors in musculoskeletal ultrasound imaging and how to avoid them. 17(70):188–196, 2017-09-29.

[145] Nicette Sergueef, Kenneth E. Nelson, and Thomas Glonek. The effect of cranial manipulation on the Traube-Hering-Mayer oscillation as measured by laser-Doppler flowmetry. 8(6):74–76, 2002.

[146] Alap Shah and Abid Irshad. *Sonography Doppler Flow Imaging Instrumentation*. StatPearls Publishing, 2024.

[147] Jay P. Shah and Elizabeth A. Gilliams. Uncovering the biochemical milieu of myofascial trigger points using in vivo microdialysis: An application of muscle pain concepts to myofascial pain syndrome. 12(4):371–384, 2008-10.

[148] Jay P. Shah, Nikki Thaker, Juliana Heimur, Jacqueline V. Aredo, Siddhartha Sikdar, and Lynn Gerber. Myofascial Trigger Points Then and Now: A Historical and Scientific Perspective. 7(7):746–761, 2015-07.

[149] Tsuyoshi Shiina, Kathryn R. Nightingale, Mark L. Palmeri, Timothy J. Hall, Jeffrey C. Bamber, Richard G. Barr, Laurent Castera, Byung Ihn Choi, Yi-Hong Chou, David Cosgrove, Christoph F. Dietrich, Hong Ding, Dominique Amy, Andre Farrokh, Giovanna Ferraioli, Carlo Filice, Mireen Friedrich-Rust, Kazutaka Nakashima, Fritz Schafer, Ioan Sporea, Shinichi Suzuki, Stephanie Wilson, and Masatoshi Kudo. WFUMB Guidelines and Recommendations for Clinical Use of Ultrasound Elastography: Part 1: Basic Principles and Terminology. 41(5):1126–1147, 2015-05.

[150] Rosa M.S. Sigrist, Joy Liau, Ahmed El Kaffas, Maria Cristina Chammas, and Juergen K. Willmann. Ultrasound Elastography: Review of Techniques and Clinical Applications. 7(5):1303–1329, 2017.

[151] S Sikdar, R Ortiz, T Gebreab, L H Gerber, and J P Shah. Understanding the vascular environment of myofascial trigger points using ultrasonic imaging and computational modeling. In *2010 Annual International Conference of the IEEE Engineering in Medicine and Biology*, pages 5302–5305. IEEE, 2010-08.

[152] Siddhartha Sikdar, Jay P. Shah, Tadesse Gebreab, Ru-Huey Yen, Elizabeth Gilliams, Jerome Danoff, and Lynn H. Gerber. Novel Applications of Ultrasound Technology to Visualize and Characterize Myofascial Trigger Points and Surrounding Soft Tissue. 90(11):1829–1838, 2009-11.

[153] Siddhartha Sikdar, Jay P. Shah, Elizabeth Gilliams, Tadesse Gebreab, and Lynn H. Gerber. Assessment of myofascial trigger points (MTrPs): A new application of ultrasound imaging and vibration sonoelastography. In *2008 30th Annual International Conference of the IEEE Engineering in Medicine and Biology Society*, pages 5585–5588. IEEE, 2008-08.

[154] David G Simons. Cardiology and Myofascial Trigger Points. 30(1), 2003.

[155] David G. Simons and Joseph M. Donnelly. *Travell, Simons & Simons' Myofascial Pain and Dysfunction : The Trigger Point Manual*. Wolters Kluwer Health, 3 edition, 2019.

[156] David G. Simons and Janet Travell. Re: Myofascial Trigger Points, a Possible Explanation. 10:106–109, 1981.

[157] David G. Simons, Janet G. Travell, and Lois S. Simons. Travell & Simon's myofascial pain and dysfunction: The trigger point manual, 1999.

[158] E. Smith, C. Azzopardi, S. Thaker, R. Botchu, and H. Gupta. Power Doppler in musculoskeletal ultrasound: Uses, pitfalls and principles to overcome its shortcomings. 24(2):151–156, 2021-06.

[159] John Z. Srbely. New Trends in the Treatment and Management of Myofascial Pain Syndrome. 14(5):346–352, 2010-10.

[160] Dee Sreerangaiah, Michael Grayer, Benjamin A. Fisher, Meilien Ho, Sonya Abraham, and Peter C. Taylor. Quantitative power Doppler ultrasound measures of peripheral joint synovitis in poor prognosis early rheumatoid arthritis predict radiographic progression. 55(1):89–93, 2016-01.

[161] J R Stevenson, J M Blake, T F Douglas, and D M Kercheval. Does continuous passive motion during keyboarding affect hand blood flow and wrist function? A prospective case report.

[162] E. G. Sunethra Dayavansha, Sheryl E. Koch, Jack Rubinstein, and T. Douglas Mast. Shear wave elastography in ex vivo and in vivo skin using high-frequency ultrasound imaging. In *2020 IEEE 20th International Conference on Bioinformatics and Bioengineering (BIBE)*, pages 637–641. IEEE, 2020-10.

[163] Thomas L. Szabo. *Diagnostic Ultrasound Imaging: Inside Out*. Academip Press, 2 edition, 2014.

[164] Yifan Tai, Emma L. Woods, Jordanna Dally, Deling Kong, Robert Steadman, Ryan Moseley, and Adam C. Midgley. Myofibroblasts: Function, Formation, and Scope of Molecular Therapies for Skin Fibrosis. 11(8):1095, 2021-07-23.

[165] Etain A. Tansey, Laura E. A. Montgomery, Joe G. Quinn, Sean M. Roe, and Christopher D. Johnson. Understanding basic vein physiology and venous blood pressure through simple physical assessments. 43(3):423–429, 2019-09-01.

[166] James Teh. Applications of Doppler Imaging in the Musculoskeletal System. 35(1):22–34, 2006-01.

[167] Sarah Tenberg, Kazunori Nosaka, and Jan Wilke. The Relationship Between Acute Exercise-Induced Changes in Extramuscular Connective Tissue Thickness and Delayed Onset Muscle Soreness in Healthy Participants: A Randomized Controlled Crossover Trial. 8(1):57, 2022-12.

[168] Amy Trang and Paras B. Khandar. *Physiology, Acetylcholinesterase.* StatPearls Publishing, 2022.

[169] Janet G. Travell and David G. Simons. *Myofascial Pain and Dysfunction: The Trigger Point Manual*. Williams & Wilkins, 1 edition, 1992.

[170] Diego Turo, Paul Otto, Murad Hossain, Tadesse Gebreab, Katherine Armstrong, William F. Rosenberger, Hui Shao, Jay P. Shah, Lynn H. Gerber, and Siddhartha Sikdar. Novel Use of Ultrasound Elastography to Quantify Muscle Tissue Changes After Dry Needling of Myofascial Trigger Points in Patients With Chronic Myofascial Pain. 34(12):2149–2161, 2015-12.

[171] Matthew W Urban, Ivan Z Nenadic, Shigao Chen, and James F Greenleaf. Discrepancies in Reporting Tissue Material Properties. page 4, 2013.

[172] Joshua A Waxenbaum and Myro Lu. Physiology, Muscle Energy. In *StatPearls [Internet]*. StatPearls Publishing, 2022.

[173] A. Welsh. Quantification of power Doppler and the index 'fractional moving blood volume' (FMBV): Opinion. 23(4):323–326, 2004-04.

[174] Alec W. Welsh, J. Brian Fowlkes, Stephen Z. Pinter, Kimberly A. Ives, Gabe E. Owens, Jonathan M. Rubin, Oliver D. Kripfgans, Pádraig Looney, Sally L. Collins, and Gordon N. Stevenson. Three-dimensional US Fractional Moving Blood Volume: Validation of Renal Perfusion Quantification. 293(2):460–468, 2019-11.

[175] WHO TEAM and Environment, Climate Change and Health. Preventing musculoskeletal disorders in the workplace. Protecting Workers' Health Series No. 5, 2003-06-23.

[176] Naomi Winn, Radhesh Lalam, and Victor Cassar-Pullicino. Sonoelastography in the musculoskeletal system: Current role and future directions. 8(11):868, 2016.

[177] Chueh-Hung Wu, Wen-Shiang Chen, Gi-Young Park, Tyng-Guey Wang, and Henry L. Lew. Musculoskeletal Sonoelastography: A Focused Review of its Diagnostic Applications for Evaluating Tendons and Fascia. 20(2):79–86, 2012-06.

[178] Yassierli and Maury A. Nussbaum. Utility of traditional and alternative EMG-based measures of fatigue during low-moderate level isometric efforts. 18(1):44–53, 2008-02.

[179] Keiichi Yoshida, Yoshiaki Itoigawa, Yuichiro Maruyama, and Kazuo Kaneko. Healing Process of Gastrocnemius Muscle Injury on Ultrasonography Using B-Mode Imaging, Power Doppler Imaging, and Shear Wave Elastography. 38(12):3239–3246, 2019-12.

[180] R. Zahiri-Azar and S. Salcudean. Time-delay estimation in ultrasound echo signals using individual sample tracking. 55(12):2640–2650, 2008-12.

[181] R. Zahiri-Azar and S.E. Salcudean. Motion Estimation in Ultrasound Images Using Time Domain Cross Correlation With Prior Estimates. 53(10):1990–2000, 2006-10.

[182] Manal Zein-Hammoud and Paul R. Standley. Modeled Osteopathic Manipulative Treatments: A Review of Their in Vitro Effects on Fibroblast Tissue Preparations. 115(8):490–502, 2015-08-01.

[183] Manal Zein-Hammoud and Paul R. Standley. Fibroblast proliferation and collagen secretion are required for myofascial release-induced wound healing in three dimensional bioengineered tendons. 19(4):677, 2015-10.

[184] Manal Zein-Hammoud and Paul R. Standley. Optimized Modeled Myofascial Release Enhances Wound Healing in 3-Dimensional Bioengineered Tendons: Key Roles for Fibroblast Proliferation and Collagen Remodeling. 42(8):551–564, 2019-10.

[185] Hui Zhang, Jiao-Jiao Lü, Qiang-Min Huang, Lin Liu, Qing-Guang Liu, and Opoku-Antwi Eric. Histopathological nature of myofascial trigger points at different stages of recovery from injury in a rat model. 35:445–451, 2017.

[186] Y.V. Zontov, OYe Rodionova, O. Ye., S.V. Kucheryavskiy, and A.L. Pomerantsev. PLS-DA – A MATLAB GUI tool for hard and soft approaches to partial least squares discriminant analysis. 203:104064, 2020-08.

APPENDIX A

FLOW PHANTOM SETUP

Experimental Setup

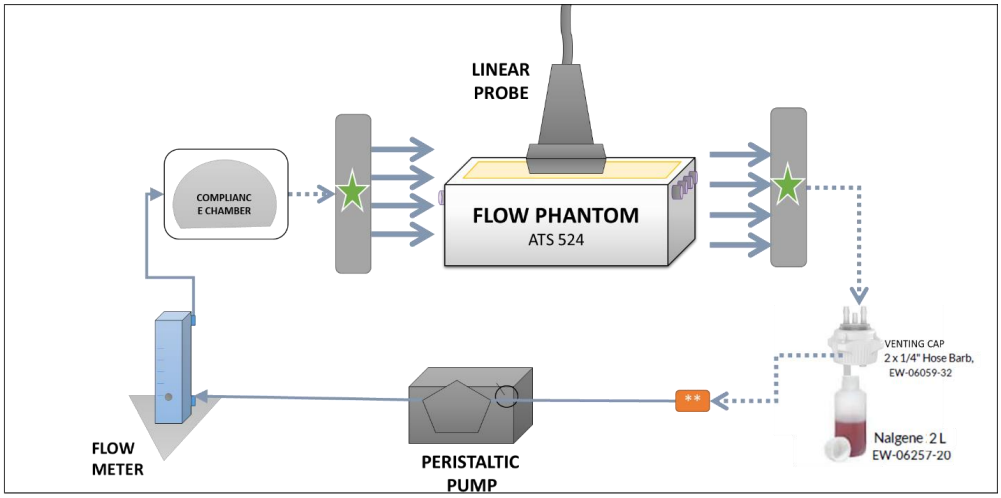
LINEAR
PROBE
COMPLIANC
E CHAMBER
FLOW PHANTOM
ATS 524
VENTING CAP
2 x 1/4" Hose Barb,
EW-06059-32
Nalgene 2 L
EW-06257-20
**
FLOW
METER
PERISTALTIC
PUMP

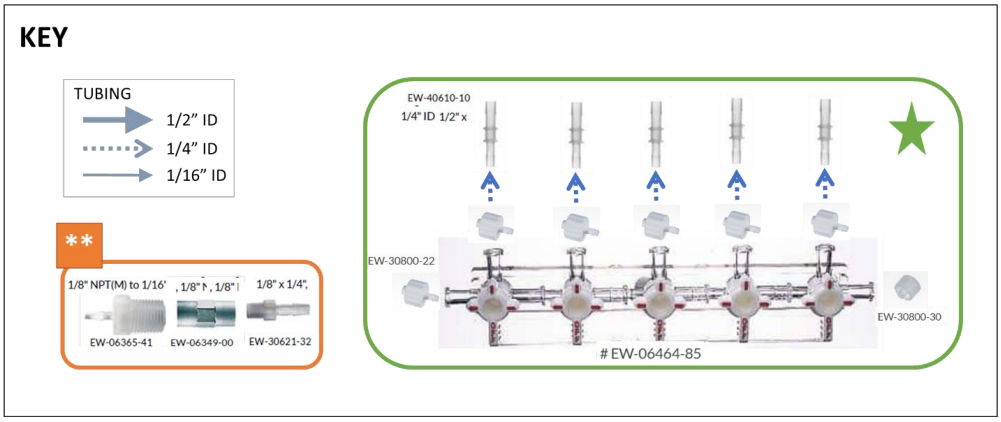
KEY
TUBING
1/2" ID
1/4" ID
1/16" ID
**
1/8" NPT(M) to 1/16'
1/8" x 1/4",
EW-06365-41
EW-06349-00
EW-30621-32
EW-40610-10
1/4" ID 1/2" x
EW-30800-22
EW-30800-30
EW-06464-85

Table 1: Peripheral vascular Doppler flow phantom

MFG	CIRS Inc, Norkoflk, Virginia
Model	ATS 524.
Weight	13 lbs
Dimensions	22 x 14 x 10 cm
Scan surface	17.5x9.8 cm
Max fluid pressure	15 psi (1.05 Kg.cm)
Tissue-Mimicking Material	Urethane Rubber
Tissue-Mimicking Properties	
speed of sound	1450 m/s, measured at 3.5 MHz at 23ºC
attenuation coefficient	0.5 dB/cm/MHz ±10%
flow channels	4 circular shape - 2,4,6,8 cm

Table 2: Pump Drive

Distributor	Cole-Parmer Instrument Co
MFG	MasterFlex
Model	7554-90
Description	Gear only (600 rpm)
Drive Speed Range	20-600 rpm
Max Torque	90 oz-in
Line Voltage	90-130V
Dimensions	220 x 180 x 135 mm
Weight	4.1 kg

Table 3: Pump Head

Distributor	Cole-Parmer Instrument Co
MFG	MasterFlex
Description	Easy-Load II Pump Head
Model	77201-60
Pump Material	PPS/SS
Occlusion	Adjustable
Shaft Length	Short
Tubing	L/S 12,13, 16, 25, 17, 18
Number of rollers	4
Max pump speed	600 rpm
Nominal torque load – Running	Up to 90 oz-in
Dimensions	4 x 4 ¾ (operating), 5 ½ (open) x 2 ¾ in
Weight	0.6 kg

Table 4: Precision pump tubing LS tubing through pump

Distributor	Holland applied technologies
MFG	MasterFlex
P/N	VA-06485-14 Phar Med, Saint-Gobain
Tubing Cross-section	L/S 14
Inside diameter (ID)	1.6 mm (0.6 in)
Flow range with 6-600 rpm drive	1.3-130 mL/min (0.02-20GPH)
Max pressure (continuous)	1.7 bar (25 psi)
Max pressure (intermittent)	2.7 bar (40 psi)
Max vacuum	660 mm Hg
Suction lift	8.8 m H_2O (2 ft H_2O)

Table 5: Tubing Pump through flow meter to Phantom

Distributor	Holland applied technologies
MFG	MasterFlex
P/N	96420-14 Tygon 3350 Silicon, NDRTDN
Tubing Cross-section	L/S 14
Inside diameter (ID)	1.6 mm (0.063)
Max pressure (continuous)	2.7 bar (40 PSI)
Max vacuum	660 mmHg (26 in Hg)
Suction lift	8.8 m H_2O (29 ft H_2O)

Table 6: Doppler Test Fluid (1 gal): Dispersion of plastic particles in glycerin water mixture. Measurements at 23ºC

MFG	ATS Laboratories, Inc.
Model	707
Serial	2170411
Speed of Sound	1571 ± 16 m/sec
Density	1.04 ± 0.01 gm/cc
Viscosity	1.66 ± 0.1 cSt
Particle Size	30 micron mean diameter
Color	Pale yellow
Odor	Slight scent

Doppler Test Fluid

Not a hazardous substance or mixture. While this material is not considered hazardous by the OSHA Hazard Communication Standard (29 CFR 1910.1200), this MSDS contains information regarding the safe handling and proper use of the product.

GHS Label Element
Not a hazardous substance or mixture.

SECTION 3 - COMPOSITION/INFORMATION ON INGREDIENTS

Chemical nature: A dispersion of plastic particles in a water/glycerine mixture.

Hazardous Components: No hazardous ingredients.

SECTION 4 - FIRST AID MEASURES

Inhalation: If breathing is affected, move to fresh air.
Skin contact: Wash with soap and fresh water.
Eye contact: Flush several minutes with fresh water. Seek medical aid if irritation persists.
Ingestion: Do not induce vomiting. Dilute with 1-2 glasses of water. Seek medical opinion.

Components with workplace control parameters: None

Engineering measures: None required

Personal protective equipment:

Hand protection:	Protective rubber or nitrile gloves
Eye protection:	Safety glasses
Skin and body protection:	Choose in accordance with good laboratory hygiene and safety practice.
Respiratory protection:	None required
Other hygiene measures:	In accordance with good laboratory hygiene and safety practice.

SECTION 9 - PHYSICAL AND CHEMICAL PROPERTIES

Appearance:	Liquid
Color:	Clear, some cloudiness from suspended particles
Odor:	Mildly pungent
Odor threshold:	No data available
Flash point:	Not applicable
Ignition temperature:	Not applicable
Lower explosion limit:	Not applicable
Upper explosion limit:	Not applicable
pH:	No data available
Freezing point:	No data available

Boiling point:	No data available
Vapor pressure:	No data available
Evaporation rate:	No data available
Density:	1.040 g/cm^3
Bulk density:	No data available
Water solubility:	Completely miscible
Viscosity:	1.66 Centistokes at 23°C
Relative vapor density:	No data available

SECTION 10 - STABILITY AND REACTIVITY

Reactivity:	Not classified as a reactivity hazard
Chemical stability:	Stable, polymerization will not occur
Possibility of hazardous reactions:	None known
Hazardous decomposition products:	None known
Conditions to avoid:	None known
Materials to avoid:	None known

SECTION 11 - TOXICOLOGICAL INFORMATION

Acute oral toxicity (product):	No data available
Skin irritation (product):	No data available
Eye irritation (product):	No data available
Sensitization (product):	No data available

SECTION 12 - ECOLOGICAL INFORMATION

Additional ecological information (product): No data available

SECTION 13 - DISPOSAL CONSIDERATIONS

EPA Hazardous Waste Code(s):	Not applicable
Waste from residues:	Dispose in accordance with applicable local/municipal/ state or provincial and federal regulations.

SECTION 14 - TRANSPORT INFORMATION

International Regulations

IATA-DGR:	Not regulated as a dangerous good
IMDG-Code:	Not regulated as a dangerous good

Transportation in bulk according to Annex II of MARTIAL 73/78 and IBC Code:

Not applicable for product as supplied.

National Regulations

49 CFR: Not regulated as a dangerous good

SECTION 15 - REGULATORY INFORMATION

Emergency Planning Community Right-To-Know (EPCRA):

CERLA Reportable Quantity:	Not applicable
SARA 302/304 Components:	Not applicable
SARA 311/312 Hazards:	Not applicable
SARA 313 Hazards:	Not applicable

Toxic Substances Control Act (TSCA):

All ingredients in this product are either listed in the TSCA inventory or are not subject to the notification requirements (exempt) per 40 CFR 720 30(h).

Clean Air Act & Related Information:

Non-volatile (wt.) No data available

This product does not contain any hazardous air pollutants (HAP) as defined by the U.S. Clean Air Act, Section 12 (40 CFR 61).

This product does not contain any chemicals listed under the U.S. Clean Air Act, Section 112(r) for Accidental release Protection (40 CFR 68.130, Subpart F)

Resource Conservation and Recovery Act (RCRA):

State laws:

MA Right To Know Components:	None
PA Right To Know Components:	None
NJ Right To Know Components:	None
NJ Trade Secret Registry Number:	None

Canadian Environmental Protection Act:

DSL Status: All ingredients in this product are listed on the Domestic Substances List (DSL).

WHMIS Classification: Not controlled.

California Prop. 65: This product does not contain any chemicals known to the State of California to cause cancer, birth, or any other kind of reproductive defect.

ATS Laboratories, Inc.
404 Knowlton St.
Bridgeport, CT 06608
203-579-2700

SECTION 16 - OTHER INFORMATION

Revision date: 12 April 2016
Print date: 20 April 2016

The component chemicals is this product are primarily water, glycerin and a small quantity of nylon particles. There are also small quantities (< 0.5% concentration) of dispersant and a biocide for which acute toxicity data is available; however, their inclusion in acute toxicity estimate (ATE) for this product (mixture) is not required as their concentration is below 1% and/or the oral limit test is greater than 2000mg/kg body weight. Although not classified as a GHS hazardous mixture, prudent laboratory handling and safety measures should be observed.

HMIS Classification:

Health Hazard:	0
Flammability:	0
Reactivity:	0
PPI:	B

This SDS is compliant with regulations:

(US) OSHA 29 CFR 1910:1200
(Canada) WHIMS
(EU) EU/EEC 1907/2006 (REACH), (EU) EU/EEC 1272/2008 (CLP)

Unlisted ingredients are not "hazardous" per the 29 CFR 1910:1200, WHIMS, or EU/EEC 1907/2006 and are considered trade secrets under US Federal Law (29 CFR, 40 CFR), Canadian Law (Health Canada Regulation) and European Union Directives.

The information provided in the Safety Data Sheet is correct to the best of our knowledge and belief at the time of publication. The information given is designed only as a guidance for safe handling, use, storage, transportation, disposal and release and is not considered a warranty or quality specification. The information relates only to the specific material designated and may not be valid for such material used in combination with any other materials or in any process unless specified in the text.

ATS Laboratories, Inc.
404 Knowlton Street
Bridgeport, CT 06608

Doppler Test Fluid Certification Sheet

Model: 707 **Serial Number:** 21704161

Product Name/Description: Doppler Test Fluid, 1 gal.

Properties: (All measurements @ 23° C)

Speed of Sound:	1577 m/sec
Density:	1.046 gm/cc
Viscosity:	1.64 cSt

Product Specifications:

Speed of sound:	1571 +/- 16 m/sec
Density:	1.04 +/- 0.01 gm/cc
Viscosity:	1.66 +/- 0.1 centistokes
Particle size:	30 micron mean diameter
Color:	Pale yellow
Odor:	Slight scent

The Model 707 Doppler Test Fluid is a dispersion of plastic particles in a glycerin water mixture. Refer to the Safety Data Sheet (SDS) regarding disposal instructions.

Instrumentation used for the certification of the acoustic properties reported above is traceable to the National Institute of Standards and Technology.

Approved: _____ Date: 04/20/2017

FDB 2017 F-04 [v01] I Approved; uncontrolled when printed

APPENDIX B

ELASTOGRAPHY SETUP

Boot Drawing

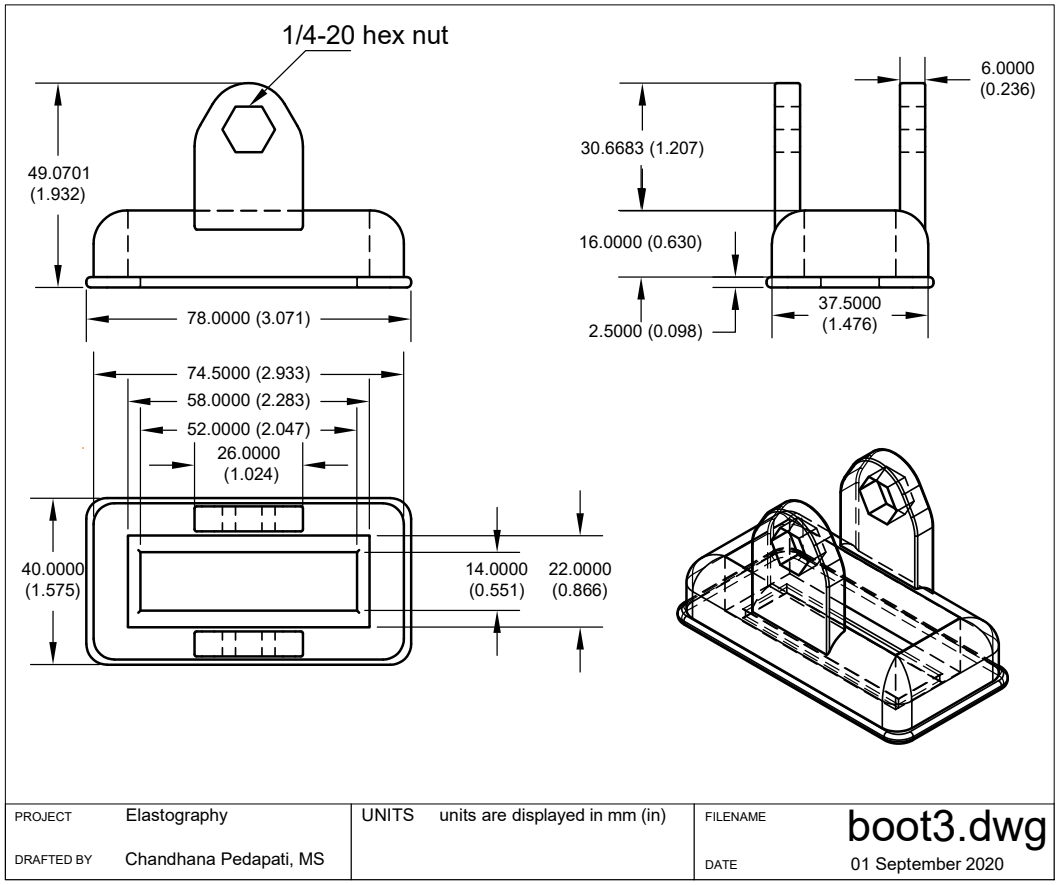

PROJECT	Elastography	UNITS	units are displayed in mm (in)	FILENAME	boot3.dwg
DRAFTED BY	Chandhana Pedapati, MS			DATE	01 September 2020

Project Box

Figure B.1: Project Box containing Actuator Controller and FSR integration

Actuator Controller

Arduino pin assignment

Arduino Boards: OSEPP UNO R3 Plus, Adafruit Moto Sheild v 2.3

PINS	*COMPONENT*	*PERF BOARD*	*PINS*	*COMPONENT*
IOREF			**D0 TX**	
RESET			**D1 RX**	
3V3			**D2**	
5V	**Perf Board**	**Speed, Step, LCD**	**D3**	
GND	**Perf Board**	**Speed, Step, LCD**	**D4**	
GND			**D5**	
VIN			**D6**	
			D7	**Speed CLK**
			D8	**Speed DT**
			D9	**Seed SW**
			D10	**Step CLK**
			D11	**Step DT**
A0			**D12**	**Step SW**
A1			**D13**	
A2			**GND**	
A3			**AREF**	
A4	**LCD SDA (yellow)**		**SDA**	
A5	**LCD SCL (orange)**		**SCL**	

Rotary Encoder Functions

Step Dial: Range: 1-200

Action	**Button Status**	**Step Counter**	**COMMENT**
Initial power up	ON	20	Initial Setting
DIAL Turn Clockwise	ON	Increment by 1	Max 200
DIAL Turn Counter Clockwise	ON	Decrement by 1	Min 1
BUTTON PRESS	OFF	No change	Motor released Step and Speed settings can be adjusted, and will control motor at those settings when turned on.

Speed Dial: Range 10- 100

Action	**BUTTON STATUS**	**Speed Counter**	**COMMENT**
Initial power up	NA	100	Initial Setting
DIAL Turn CW	NA	Increment by 1	Max 100
DIAL Turn CCW	NA	Decrement by 1	Min 10

LCD Display

Rows/Columns	*0*	*1*	*2*	*3*	*4*	*5*	*6*	*7*	*8*	*9*	*10*	*11*	*12*	*13*	*14*	*15*
0	**P**	**W**	**R**		|	**S**	**T**	**E**	**P**	**S**	|	**S**	**P**	**E**	**E**	**D**
1		**O**	**N**		|		**X**	**X**	**X**		|		**X**	**X**	**X**	

Stepper Motor Homing

Manually homing – probe will be placed on the surface of the tissue or phantom

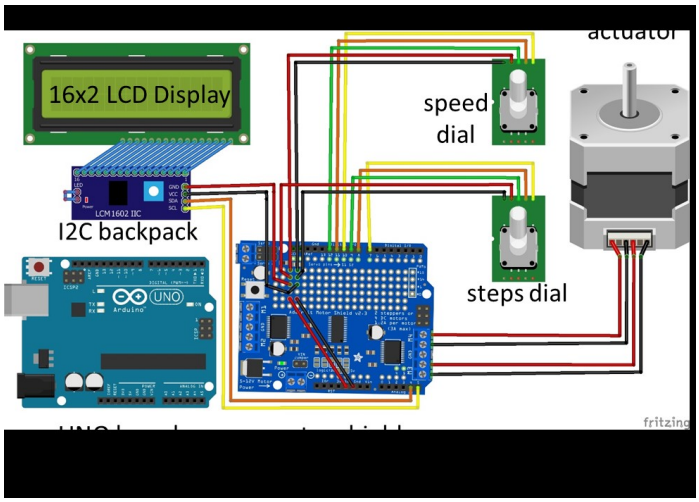

Figure B.2: Actuator Controller Connection Diagram

FSR Integration

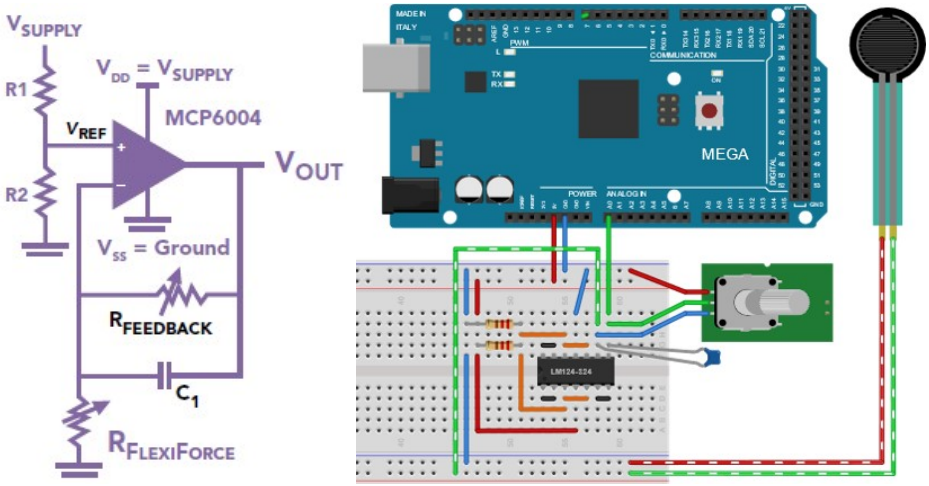

Figure B.3: FSR Schematic and Fritzing Diagrams. FSR integration schematic (left) non-Inverting Op Amp Single source excitation circuit, from Tekscan OEM integration guides, and (right) Fritzing breadboard view.$R_1 = 330k\Omega, R_2 = 100\Omega, C_2 = 47pF, R_{FEEDBACK} = 100k\Omega POT, V_{SUPPLY} = 5.12V$

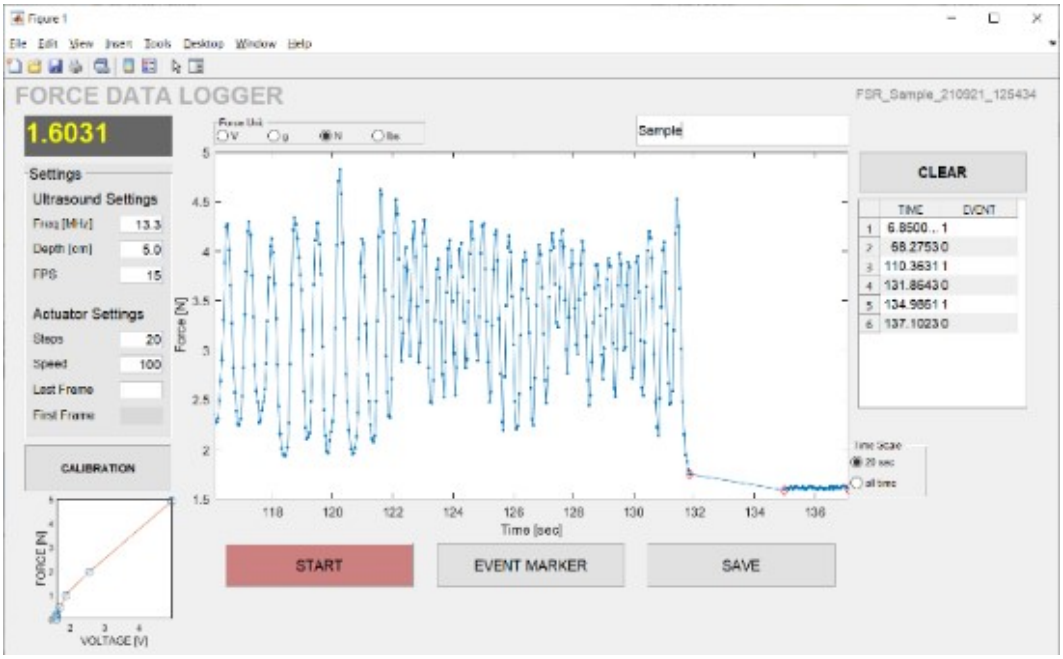

Figure B.4: FSR Data Logging GUI

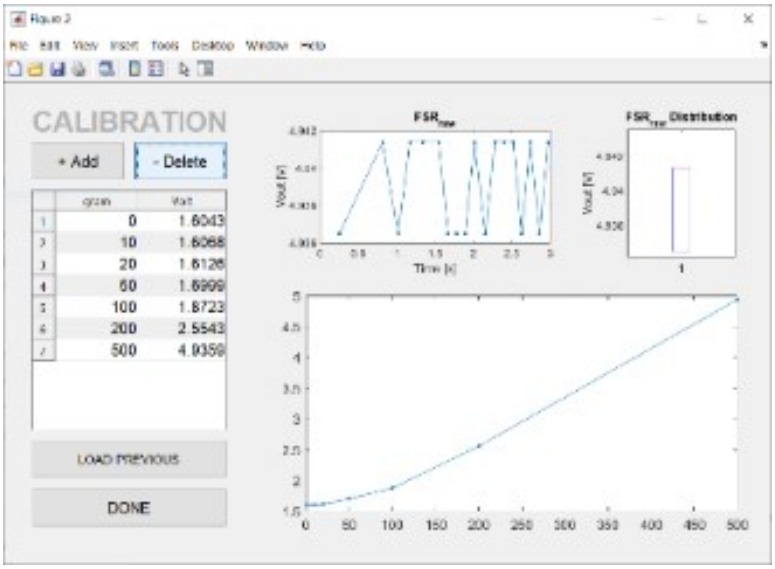

Figure B.5: FSR Calibration GUI

APPENDIX C

PRELIMINARY STUDIES

Power Doppler and Elastography study

Preliminary analysis on color Doppler and Elastography images acquired from BK Ultrasound Ultrasonix Research Unit

December 4, 2017

The brachial artery was imaged in a transverse plane. Color Doppler and elastography images were acquired wherein B mode and RF images were simultaneously acquired with each mode. Two sets of images were acquired, these were baseline and after physical exertion of the upper extremity, in this case, pushups until fatigue. To acquire elastography images, the ultrasound probe was positioned over the brachial artery and moved in a low amplitude oscillatory motion in the z-direction to compress and decompress the investigating tissue. An indicator on the ultrasound unit screen provided feedback on the probe motion for optimal elastography acquisition. It was challenging to continually maintain adequate motion, and it was not determined that elasto images were optimal.

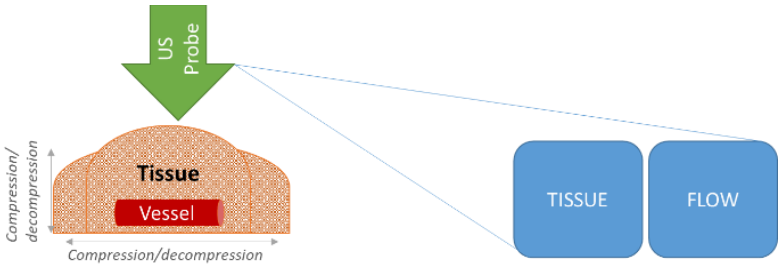

Figure1: Schematic Diagram of ultrasound probe, investigating tissue and ultrasound outputs (blue squares). Elastography images required compression/decompression. Blood flow images were acquired with a stationary probe.

The image formats used in this exercise were '.bpr, .b8, .rf, .cr., .cvv, .epr, .elo. When acquiring color Doppler images, the following file formats are simultaneously captured – .cr, .cvv, and .bpr, .b8 and .rf. When acquiring the elastography images, the following file formats are simultaneously captured – .bpr, .b8, .rf, .epr, .elo.

Table 1: Available file formats from the BK Ultrasond Ultrasounix research unit.

	Pre/NON scan converted	**Post scan converted**	**Scan converted with color coded images**	**Other**
Bmode	.bpr	.b8, .b32		
RF	.rf			
Mmode	.mpr	.m		
Power Doppler		.pw		
Color	.crf	.cvv		
Elastography	.epr	.elo	.el	
TBD	.eft, .col, .ecg			
CWDL IQ signal from CW applying wall filter				.drf

Image formats were transferred to an offline computer loaded with Matlab software. The research unit also comes with Matlab code to read each file format. The color images and corresponding B mode and rf images were read successfully. The elastography images were read successfully, however their corresponding B mode and rf images were not read successfully.

Summary

Blood flow and tissue stiffness were quantified using color Doppler and elastography segmented images respectively. The area containing flow values, non-zero values, were used to calculate regional velocity and variance change from baseline. A post-processing algorithm segmented the elastography image, broke it down into red, green and blue channels and quantified the change from baseline. The next phase is to develop a cross-correlation algorithm to replicate the elastography image. For this, 2 Bmode image frames, from the color Doppler data set were used to calculate cross correlation since the elasto images were likely from a poor quality acquisition.

Regional blood flow changes.

After physical exertion, color Doppler images showed increase in regional flow. Forward flow area increased, and reverse flow, not present in baseline images, was present post exertion.

Output from Reader files provided with US unit

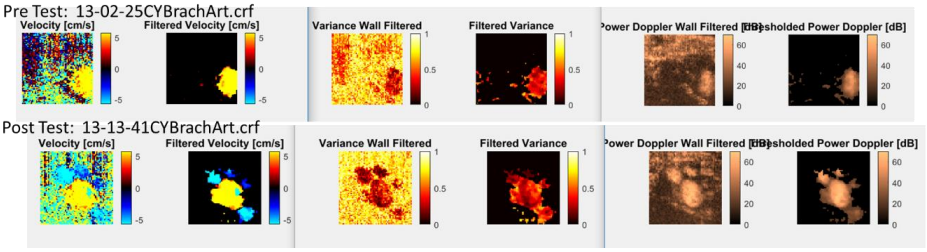

Figure 2: Color Doppler segmented images, read using provided matlab code. (Top row) Baseline images, (bottom row) following exertion images. The velocity, variance and power Doppler can be calculated from the pre scan converted images. The images are shown in sets of two, unfiltered and filtered, in each row, where the filtering is determined by thresholding from number and size of autocorrelation window.

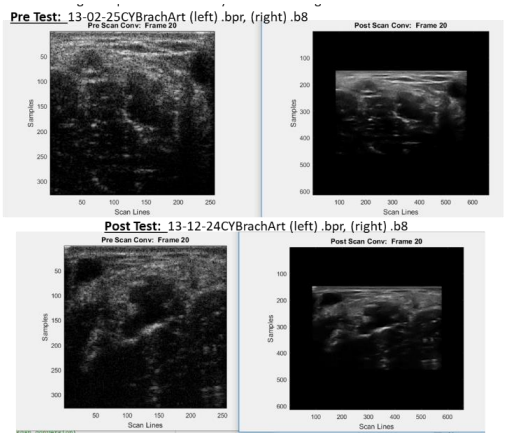

Figure 3: B mode images acquired concurrently with color Doppler mode images. Left side images are pre scan converted images. Right side images are scan converted images.
(top row) baseline, and (bottom row) after physical exertion.

Analysis on Velocity and Variance Data

The figure below shows the filtered color Doppler segmented image, where the color indicates velocity. In the baseline image forward flow is present and reverse flow is not present. In the second image, an increase forward flow region and presence of reverse flow is demonstrated.

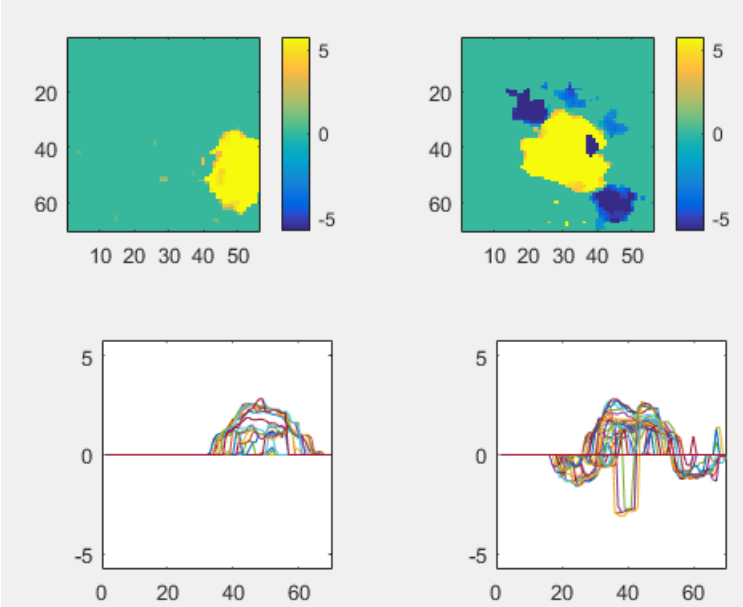

Figure 4: Filtered velocity. (Left) baseline, (Right) after physical exertion. (Top Row) segmented color Doppler image. (bottom row) Scan line plot, (y-axis) amplitude (x-axis) depth, showing that baseline image has only forward flow (positive) values and after physical exertion, the image has both forward flow and reverse (negative) flow. The size of the segmented image was 70x56.

The region containing flow values indicates cross-section area of flow, providing insight on vascular distention, in addition to velocity gradation. The region of flow was calculated by counting the number of pixels with a non-zero value. The table below reports these values, and shows that the region of blood flow more than doubled after physical exertion.

Table 2: Pixel count of color Doppler data in segmented region.

	Baseline	After physical exertion	% change
Non-Zero value Pixel count	386	891	130.8%
Non-zero value to segmentation area ratio	386/(70*56) = 0.0985	891/(70*56) = 0.2273	

The variance of the color Doppler provides information on blood flow turbulence (Kasai 1985). The figure below shows the variance of the color Doppler segmented image.

From Figure 5 and 6 the variance increases after physical exertion. The color Doppler shows increases in region containing flow and increase in color range. Some of the variance may be artifact or erroneous. The histograms also show that the pixel count and range of variance value increases. The box plot additionally shows that while the range of values increases the overall mean decreases.

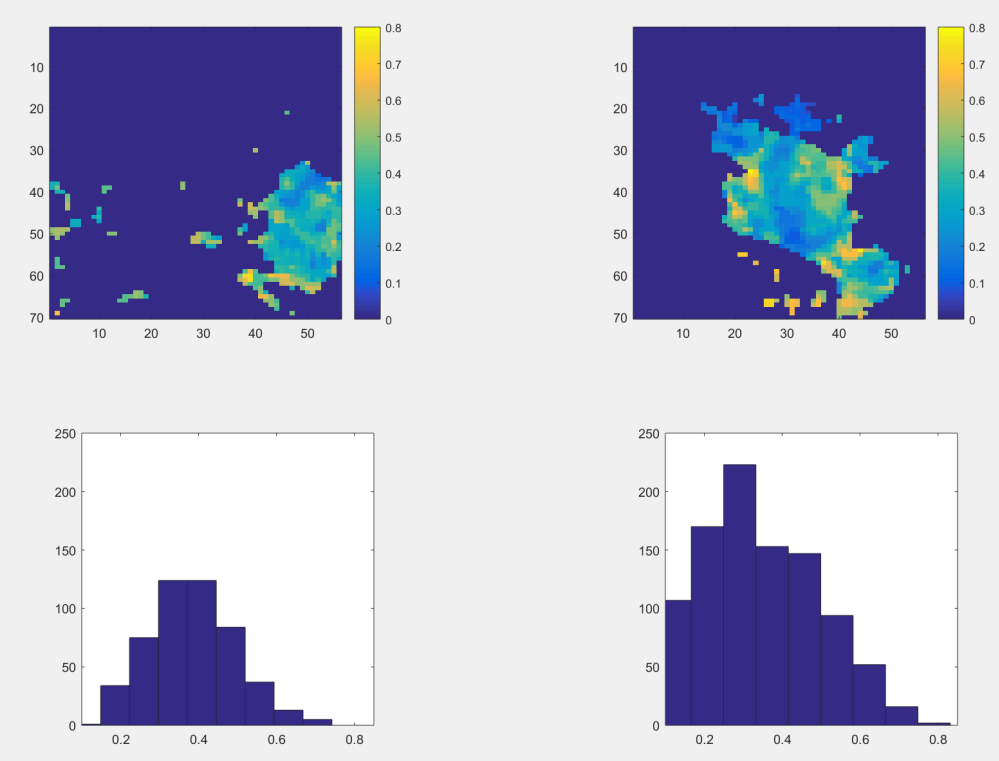

Figure 5: (top row) Variance of segmented color Doppler image, (bottom row) histogram of variance from (left) baseline and (right) after physical exertion.

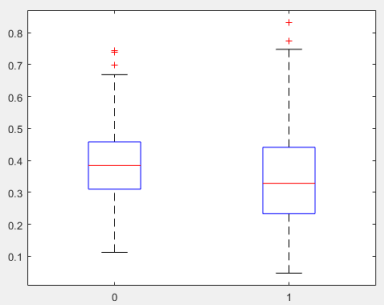

Figure 6: Boxplot of variance excluding zero values, at (0) baseline and after (1) physical exertion, (y-axis) value of variance.

Elastography Images

The elastography images provide tissue hardness information. The original .el file was read, and then a user defined segmented region of the color coded overlay was selected, avoiding the poor acquisition from the deeper tissue, the size of the rectangle was standardized for both baseline and after physical exertion images. The figure below provides the image file output from the ultrasound unit, and read using the provided matlab scripts.

Output from Reader files provided with US unit

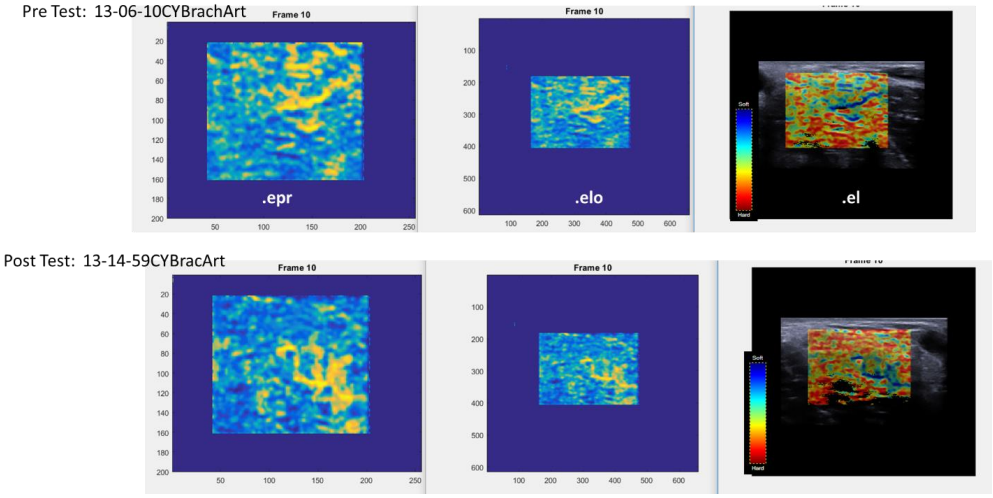

Figure 7: Elastography imaging output from BK Ultrasonix. (top row) basline and (bottom row) after physical exertion. (Left colum) Pre-scan converted. (middle column) scan converted, (right column) scan converted B mode image superimposed color overlay on segmented region, where reds correspond to hard tissue and blue corresponds to soft tissue.

Analysis on Elastography Data

The superimposed color overlay image from Figure 7 was then cropped and broken out into red, green and blue channels, shown below. The mean color value represents the average red intensity value over the cropped area. The table below contains the mean and standard deviation of the color value.

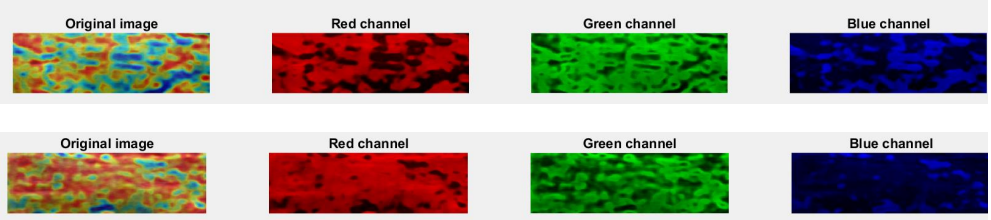

Figure 8: Segmented region from elastography color code superimposed on B mode image, and breakout of red, green and blue channels. (top row) baseline, and (bottom row) after physical exertion. Again, red is hard tissue and blue is soft tissue.

The red value increased by nearly 20%, whereas the blue and green decreased by about 20 and 40% respectively.

Table 3: Color Values Table, where Red, Green and Blue are shown as mean and standard deviation. The percent change is calculated [(after-baseline)/baseline]*100.

	Baseline	After physical exertion	% change
Image Dimension	91 x 301	91 x 301	--
Red	0.4826 ± 0.24	0.5880 ± 0.18	17.93%
Green	0.5336 ± 0.17	0.4456 ± 0.17	-19.75%
Blue	0.3216 ± 0.21	0.2358 ± 0.13	-36.39%

The box plot below illustrates the range of the color values within the cropped images.

Figure 7: Box plot of Red, Green and Blue values in elastography image.

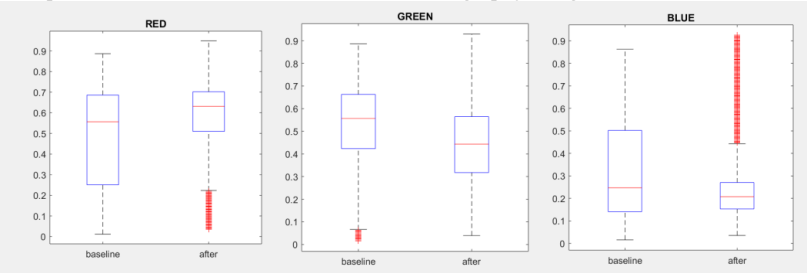

The next phase of this exercise is to calculate the tissue strain using cross correlation methods.

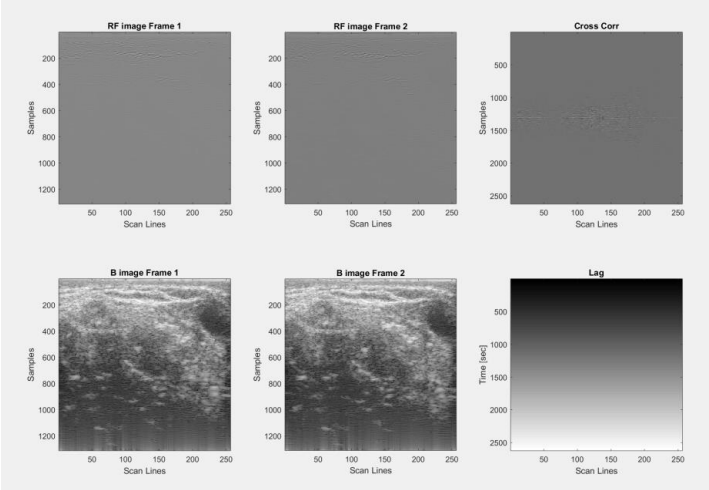

Figure 8: RF obtained images from BK ultrasonix, log compressed images and cross correlation of image by scan line provides frame-to-frame structural position changes, computed in Matlab.

Report 3: Fractional Factorial Design for optimizing ultrasound settings for vascular assessments

IEEE 572 Design of Experiments, Spring 2017

Due Date: 10 April 2017

By: Chandhana Pedapati

Background

In a study by Lobmaier, et al. (2014), the reproducibility and repeatability of myocardial performance index (MPI) using ultrasound modality was investigated. Specifically, the influence of ultrasound equipment settings was reviewed. Optimal ultrasound settings are different for each equipment, and patient specific, so obtaining optimal settings has been a challenge. Each equipment manufacture programs presets into their machines for ease of use. Even still, a further operator dependent fine tuning of these settings are required, and it has been demonstrated that repeatability and reliability may be compromised. These compromises manifest in diagnosis.

Data from two ultrasound units and over 50 fetuses concluded that indeed, ultrasound settings may negatively impact repeatability of this measure, and standardization settings were suggested for optimizing reproducibility. While this study successfully demonstrated a weakness in reproducibility of ultrasound acquired MPI from non-standardized ultrasound settings, this study was inadequate in its method for suggesting standard settings. Table 1 shows the experiment as performed in the study. We can see from this table that the study did not account for factor interaction. Therefore, the settings suggested for standardization may not be optimal.

For this report, I would like to propose a design of experiment for obtaining standardized settings in applications such as this. To this end, a screening experiment using 6 pertinent ultrasound and ultrasound Doppler settings were investigated. The resistivity index (RI) of the carotid artery was calculated from the images, analogous to the MPI.

Design of Experiment

Planning. For this experiment, I identified six factors that seem likely to most impact ultrasound Doppler images. Levels were aggressively distanced around default settings for the carotid vessel preprogramed in the ultrasound unit. Additionally, similar issues in related literature, references listed in the appendix, also identified some of these factors. Initially, this experiment began with 7 factors, however, I found that altering probe frequency was not necessary. Probe frequency adjusts the penetration depth of the acoustic signal, where higher frequencies target superficial structures. Since all of the vessels under investigation were superficial and at the same depth, and after performing a few runs from a 2^(7-4) design, I settled on 12 MHz as a constant, thus reducing the number of factors to investigate. Other constants included screen depth, 2cm, and SV length at 6 where the entire vessel circumference was included in the Doppler acquisition, and the inclusion of a focus at 1.25 cm, approximately centered in the vessel. Also, initially, I wanted to replicate the MPI experiment in the Lobmairer, however, the scans of the heart required for this calculation were beyond my experience level. For this screening experiment, the most time and resource efficient option for demonstrating a fractional factorial analysis was to perform this on an analogous response, and resistivity index (RI) was selected. This common measure makes use of peak systolic velocity (PSV), also and end diastolic velocity (EDV) to assess vascular compliance, similar to the MPI. See Figure 1 for RI equation and waveform characteristics, where PSV and EDV are denoted as S and D respectively. Finally, the right and left carotid arteries were selected, for there accessibility and replication. It is well documented in literature, yet not well understood, that the human body exhibits bilateral asymmetry in flow. Therefore, it is reasonable to select for replication.

One issue that arose during the planning of the experiment was that the pulse wave (PW) Doppler settings were not orthogonal, specifically, the PW PRF and wall filter (WF) adjust with the PW frequency. After some initial experimenting and learning more about the settings, I found that the ultrasound unit automatically adjusted the PRF and the wall filter to suit the PW frequency. I also found that the adjustments were incremental according to the frequency and other settings, delving into which were

beyond the scope of this experiment. So, for this experiment, the hi and lo settings selected for PRF and WF were +/- 2 dial increments and +/- 6 dial increments respectively. The values are shown in Table 1. The ultrasound unit was reset to default after each experimental run to minimize operator error during data collection.

Factors: Table 1 lists the factors and levels.

Response: Resistivity Index (RI)

Experiment type: Resolution III 1/8 Fractional Factorial Design, with 6 factors. The base design has three factors, and there are three design generators. There were 8 runs total, with 2 replicates. The design generators were selected based upon the appendix in the Montgomery textbook, which have a minimum aberration and high resolution (D = AB, E = AC, F = BC).

Experimental setup: Figure 1 shows the ultrasound unit and the subject with linear probe. The head of the subject was slightly turned upward and away from the side where the probe was measuring, in order to expose the carotid artery.

Results

Image characteristics can be washed out or spurious peaks can be accentuated based upon the image resolution, brightness, darkness values, which are controlled by the settings. Figure 2 shows the peak systolic and end diastolic velocity measurements. The systolic peak velocity has the widest range of values measured. Table 2 shows the experimental runs and the RI calculated results. The RI values range between 0.5-1, indicating a healthy compliant vessel.

Analysis

Tables 3-5 show the analysis outcomes. According to the ANOVA, normality plot and linear model coefficients, the factors that are most significant are D, E and F. The A*F interaction appears to be significant as well. D,E and F factors are all settings for the pulse width Doppler, so it is reasonable that these are the most significant factors on RI. The pure error with two replicates was small, indicated by a small MSE value.

Verification

NPP and residuals show that the data are normally distributed. The residuals are somewhat skewed and perhaps a transform would provide a better analysis.

Conclusions

This experiment showed that the interactions were of interest when obtaining optimal ultrasound settings for vascular assessment. Factors that should be investigated further are the pulse width gain, frequency, PRF and wall motion filter. Additional observations are needed to increase internal error, and different vessels should be included in the experiment. Center points, or default settings should also be added to confirm expectations. Also, for waveform analysis an envelope should be included in order to determine waveform characteristics, such as systolic peaks. Many ultrasound units do not have this capability with the ultrasound Doppler. So, in a follow-on experiment I would process the image off-line, producing an envelope based upon the image before calculating RI.

Tables and Figures

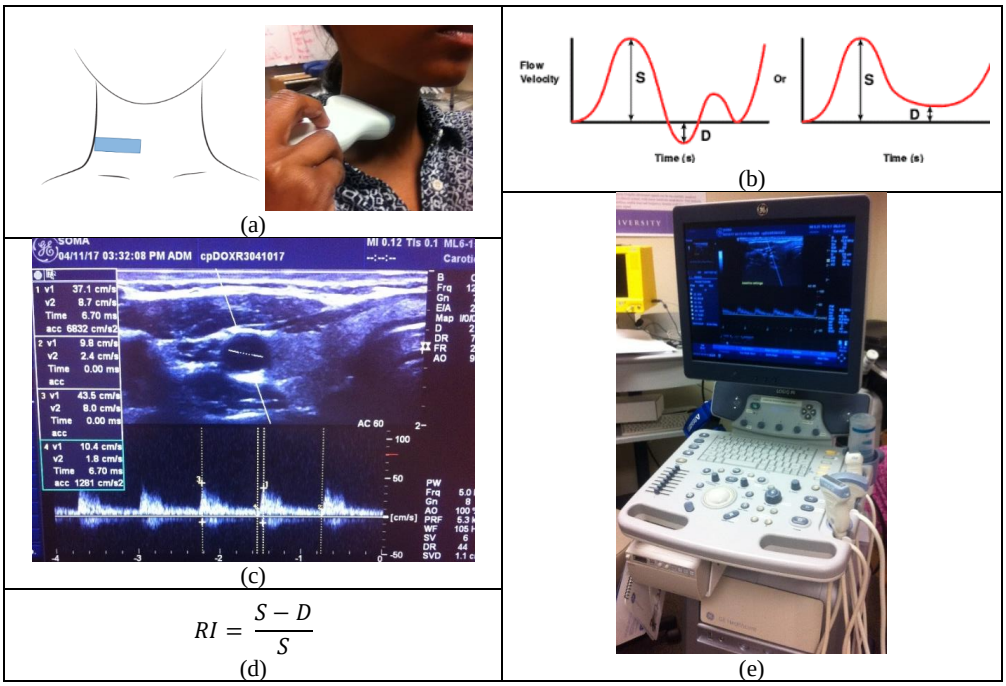

Figure 1: Experimental Setup: (a) Probe positioning for transverse carotid artery ultrasound image, (b) ultrasound Doppler waveform characteristics for RI calculation. (c) B-mode and Doppler Ultrasound with PSV and ESV measurements, (d) Resistivity Index equation, S = peak systolic velocity, D = end diastolic velocity, (e) GE Logiq-P6 Ultrasound unit and ML-6-15 Linear Probe.

Table 1: Factors and Levels

Factor	Standard order Run #	1	2	3	4	5	6	7	8
A	Probe Gain	40	98	40	98	40	98	40	98
B	Dynamic Range	48	48	105	105	48	48	105	105
C	PW Gain	0	0	0	0	32	32	32	32
D	PW Frequency [MHz]	8	5	5	8	8	5	5	8
E	PW PRF [kHz]	12.4	2.6	47.7	4.1	4.1	7.7	2.6	12.4
F	PW Wall Filter [Hz]	750	200	154	83	83	154	200	750

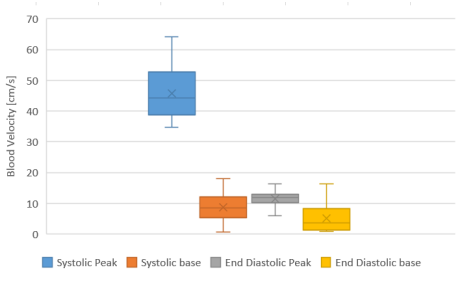

Figure 2: Systolic peak and base, and End diastolic peak and base results

Table 2: Experimental Runs

Tx. Comb.	Run	Run order Vessel 1	Run order Vessel 2	A	B	C	D=AB	E=AC	F=BC	RI Vessel 1	RI Vessel 2	Total RI
def	1	1	5	-1	-1	-1	1	1	1	0.929	1.000	1.929
af	2	8	3	1	-1	-1	-1	-1	1	0.803	0.820	1.622
be	3	5	6	-1	1	-1	-1	1	-1	0.682	0.772	1.455
abd	4	4	2	1	1	-1	1	-1	-1	0.823	0.744	1.567
cd	5	2	7	-1	-1	1	1	-1	-1	0.871	0.582	1.453
ace	6	3	1	1	-1	1	-1	1	-1	0.774	0.794	1.569
bcf	7	6	8	-1	1	1	-1	-1	1	0.662	0.792	1.454
abcdef	8	7	4	1	1	1	1	1	1	1.000	1.000	2.000

Table 3: ANOVA Table

Source	DF	Seq SS	Contributi	Adj SS	Adj MS	F-Value	P-Value
Model	7	0.163534	73.11%	0.163534	0.023362	3.11	0.067
Linear	6	0.163527	73.11%	0.163527	0.027254	3.62	0.048
A	1	0.013646	6.10%	0.013646	0.013646	1.81	0.215
B	1	0.000584	0.26%	0.000584	0.000584	0.08	0.788
C	1	0.000594	0.27%	0.000594	0.000594	0.08	0.786
D	1	0.045067	20.15%	0.045067	0.045067	5.99	0.04
E	1	0.045772	20.46%	0.045772	0.045772	6.09	0.039
F	1	0.057863	25.87%	0.057863	0.057863	7.7	0.024
2-Way Interactions	1	0.000007	0.00%	0.000007	0.000007	0	0.976
A*F	1	0.000007	0.00%	0.000007	0.000007	0	0.976
Error	8	0.060149	26.89%	0.060149	0.007519		
Total	15	0.223682	100.00%				

Table 4: Model Summary

S	R-sq	R-sq(adj)	PRESS	R-sq(pred)
0.08671	73.11%	49.58%	0.240595	0.00%

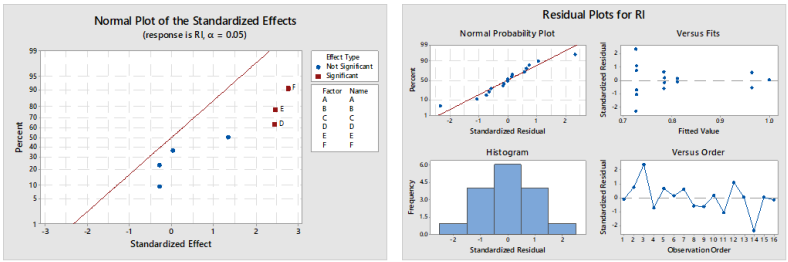

Figure 3: Validation – (right) Normality and (left) Residuals

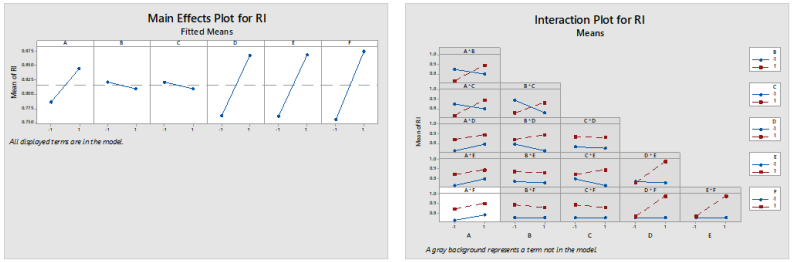

Figure 4: (right) Main effects and (left) Interaction Pots

$$RI = 0.8156 + 0.0292\ A - 0.0060\ B - 0.0061\ C + 0.0531\ D + 0.0535\ E + 0.0601\ F + 0.0007\ A*F$$

Equation 2: Regression Equation in Uncoded Units

Table 5: Coded Coefficients

Term	Effect	Coef	SE Coef	95% CI	T-Value	P-Value	VIF
Constant		0.8156	0.0217	(0.7656, 0.8656)	37.62	0	
A	0.0584	0.0292	0.0217	(-0.0208, 0.0792)	1.35	0.215	1
B	-0.0121	-0.006	0.0217	(-0.0560, 0.0439)	-0.28	0.788	1
C	-0.0122	-0.0061	0.0217	(-0.0561, 0.0439)	-0.28	0.786	1
D	0.1061	0.0531	0.0217	(0.0031, 0.1031)	2.45	0.04	1
E	0.107	0.0535	0.0217	(0.0035, 0.1035)	2.47	0.039	1
F	0.1203	0.0601	0.0217	(0.0101, 0.1101)	2.77	0.024	1
A*F	0.0013	0.0007	0.0217	(-0.0493, 0.0506)	0.03	0.976	1

APPENDIX

Table A1: Experiment Factor Levels, Lobmaier, et al. (2014)

		Natrual Units			Coded Units			
Run Order	Ultrasound Unit	Gain dB	Swap Speed	WMF Hz	Gain dB	Swap Speed	WMF Hz	n
1	Siemens Antares	60	8	187	0	0	0	58
2	Siemens Antares	60	5	187	0	-1	0	58
3	Siemens Antares	50	8	187	-1	0	0	57
4	Siemens Antares	70	8	187	1	0	0	58
5	Siemens Antares	60	8	281	0	0	1	54
6	GE Voluson	-10	5	210	0	0	0	55
7	GE Voluson	-15	5	210	-1	0	0	60
8	GE Voluson	-15	5	90	-1	0	-1	59
9	GE Voluson	-15	5	300	-1	0	1	60
10	GE Voluson	-10	5	300	0	0	1	56

Works Consulted

[1] Kruskal, J. B., Newman, P. A., Sammons, L. G., & Kane, R. A. (2004). Optimizing doppler and color flow US: Application to hepatic sonography. *Radiographics: A Review Publication of the Radiological Society of North America, Inc, 24*(3), 657-675. doi:10.1148/rg.243035139

[2] Lobmaier, S. M., Cruz-Lemini, M., Valenzuela-Alcaraz, B., Ortiz, J. U., Martinez, J. M., Gratacos, E., & Crispi, F. (2014). Influence of equipment and settings on myocardial performance index repeatability and definition of settings to achieve optimal reproducibility. *Ultrasound In Obstetrics & Gynecology, 43*(6), 632-639. doi:10.1002/uog.13365

[3] Torp-Pedersen, S., Christensen, R., Szkudlarek, M., Ellegaard, K., D'Agostino, M. A., Iagnocco, A., . . . Terslev, L. (2015). Power and color doppler ultrasound settings for inflammatory flow: Impact on scoring of disease activity in patients with rheumatoid arthritis: Power and color doppler ultrasound comparison. *Arthritis & Rheumatology, 67*(2), 386-395. doi:10.1002/art.38940

[4] Yang, X., Pugh, N. D., Coleman, D. P., & Nokes, L. D. M. (2010). Are doppler studies a useful method of assessing neovascularization in human achilles tendinopathy? A systematic review and suggestions for optimizing machine settings. *Journal of Medical Engineering & Technology, 34*(7-8), 365-372. doi:10.3109/03091902.2010.497892

Student Lab sEMG Data

Analysis of clench force and surface electromyography (sEMG) during a sustained hand grip test, before and after osteopathic manipulative treatment.

Introduction

Myofascial trigger points (MTP) exhibit changes in myogenic activity such as fatiguability however there are no standardized muscle performance metrics for characterizing this pathology. Surface-electromyography (sEMG) allows for non-invasive real-time monitoring of local myoelectric activity and therefore local fatigue monitoring (Cifrek et al., 2009). MTP related research have used EMG to assess muscle range of motion (Fereira & Satralkar, 2017; Pérez-Bellmunt et al., 2021), contractility (Gao et al., 2020; Ginszt et al., 2020) and strength (Mehdikhani et al., 2018; Pérez-Bellmunt et al., 2021) in MTP studies. While muscle fatigue is regularly evaluated in muscle performance studies, it has not been fully investigated in MTP treatment research. This study aims to better understand what features of the sEMG signal may characterize alterations with MTP treatment, including measures of fatigue.

Motor dysfunction is clinically observed with MTP including: 1) reduced range of motion (Ge & Arendt-Nielsen, 2011), 2) pain and restrictions when passively stretching beyond limited range (Giamberardino et al., 2011), 3) muscle weakness, 4) impaired motor control, and 5) low endurance (Giamberardino et al., 2011). In addition to motor effects, spontaneous electrical activity (SEA) has been measured in the MTP site with both needle and surface EMG (Ge et al., 2011; Giamberardino et al., 2011). SEA present as low noise and intermittent spikes in the EMG signal in the resting muscle. The degree of SEA has been found to vary at different stages of MTP recovery (Giamberardino et al., 2011). The sEMG waveform may be useful in characterizing MTP pathology.

The alterations in the biochemical environment of an MTP compared to normal tissue has been found to contain inflammatory markers, impacting local motor control (Ge & Arendt-Nielsen, 2011; Shah & Gilliams, 2008). Impaired motor control observed with MTP include range of motion, activation, increased fatiguability and muscle weakness. These changes impact local and related muscle groups. Lucas (2008) demonstrated that muscle activation timing is altered in muscles containing latent MTP (LtMTP) as well as functionally related muscles in the posterior shoulder (Lucas, 2008). Treatment or alleviation of MTP has been observed to restore motor control. A second experiment by the same group indicated that treatment with superficial dry needling and passive muscle stretching normalized muscle activation to the level of the control group (no MTP) (Lucas, 2008).

Electromyography of MTP

The sEMG waveform reflects biochemical and physiological changes in the underlying muscle tissue (Cifrek et al., 2009). EMG therefore provides insight into mechanisms involved in muscle tissue pathology and intervention. EMG captures the electrical activity of muscle tissue which includes both neural and motor signals. Action potentials from muscle fibers of a single motor unit is called the motor unit action potential (MUAP) (Reaz et al., 2006). The EMG electrodes detect local depolarization and hyperpolarization from the sarcolemma of the muscle fiber (Vigotsky et al., 2018) and MUAPs (Reaz et al., 2006). The sEMG waveform displays all of the electrical activity from muscle tissue over time, oscillating about a zero DC offset. This complex signal can be decomposed into individual MUAPs, and provide insights on neuromuscular system behavior. The sEMG signal contains frequency content between 0-500 Hz. Noise sources such as ambient noise from electromagnetic radiation and power-line

interference (60 Hz), and motion artifact from electrode and cables (1-10 Hz) impact lower frequencies of the sEMG waveform (Nazmi et al., 2016).

Muscles maintain a low level of activity to ensure resting muscle tone. This signal is depicted as a low amplitude sEMG waveform. Muscle contraction increases the amplitude of the sEMG signa, due to increased electrical signals and quantity of motor units firing. Muscles fatigued from static contraction fire at a lower rate. This is seen as increased sEMG amplitude and spectral shift towards lower frequencies (Cifrek et al., 2009). This shift in frequency, or slowing of the sEMG signal, results from altered pH, or buildup of lactic acid, which is directly proportional to the conduction velocity (Stulen & De Luca, 1981). Increased acidity promotes nociceptor and inflammatory markers and delays the motor unit action potential, thereby decreasing conduction velocity. As conduction velocity decreases the sEMG spectrum shifts towards lower frequencies. Other hypotheses for the observed sEMG signal changes with fatigue involve recruitment/decruitment order. While fast twitch fibers fatigue quickly and switch off, the slower twitch fibers take over, slowing the firing rate, increasing signal amplitude and downshifting the spectrum (Cifrek et al., 2009). Changes in action potential firing frequency can be quantified with time domain and spectral analysis of the sEMG signal.

Metrics

Endurance time is the simplest measure of local fatigue during a sustained isometric contraction (Cifrek et al., 2009; Yassierli & Nussbaum, 2008). The amplitude of the sEMG signal provides information on relative muscle excitation (Vigotsky et al., 2018). The time averaged sEMG amplitude can be calculated with an RMS or average rectified value over a moving window (Vigotsky et al., 2018).

Low frequency band, median frequency and mean frequency are commonly used fatigue indices (Yassierli & Nussbaum, 2008), however the mean frequency is considered less reliable (Corvini & Conforto, 2022). The ideal bandwidth for low frequency metric is specific to the muscle group and motor activity. The appropriate frequency range for sustained grip needs to be determined for each application (Yassierli & Nussbaum, 2008). Table 1 describes frequency bandwidths used for evaluating sEMG signals of muscle tissue in different applications.

Table 1: Frequency bands used for spectral analysis sEMG

Low Frequency	High Frequency	Application
6-30 Hz		with knee extensions (Yassierli & Nussbaum, 2008)
10-45 Hz	>95Hz	Biceps during elbow flexion (Allison & Fujiwara, 2002)

There is a need for objective assessment of myogenic activity in MTP treatment. We hypothesize that changes observed in muscle function after OMT are detectable and quantifiable with sEMG and clench force measurements. The purpose of this study was to evaluate metrics of muscle fatigue to assess the hand grip performance in the human forearm with MTP before and after OMT. The aims of this study are two-fold: 1) determine the appropriate metrics for analyzing myogenic activity during a sustained hand grip, and 2) quantify the effect of OMT on sustained voluntary contraction in a human subject study.

Two tests were performed. In Test 1, a case study was performed to obtain a preliminary analysis of hand grip before and after OMT on a single participant with MTP in the forearm. In Test 2, an expanded analysis of hand grip was applied to student lab data (not-controlled study), before and after OMT. Treatments in Test 1 were completed by an experienced clinician, and in Test 2 were completed by inexperienced first year osteopathic medical students. Figures 5 and 6 provide flow charts of the final analysis used in the hand grip analysis.

Methods

Clench force and sEMG were continuously recorded during a sustained hand grip test to voluntary fatigue, before and after osteopathic manipulative treatment (OMT) in the forearm.

The experimental setup for all tests is shown in Figure 1.

Equipment: Biopac MP36, clench force bulb (SS56L), 3-lead sEMG (SS29L) (BIOPAC Systems, Inc., Goleta, CA).
Biopac Default Settings: EMG: 5-250 Hz with 60Hz notch filter
Sampling frequency: 2kHz

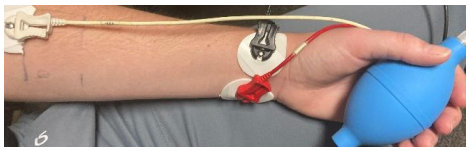

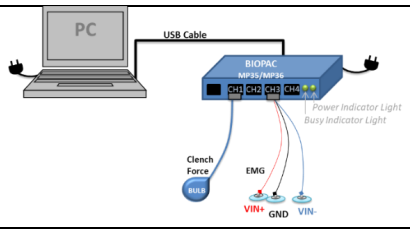

Figure 1: Biopac Systems sEMG and clench force bulb transducers with MP36

Clench force and sEMG Metrics

Time domain metrics:

- maximum voluntary contraction (MVC) – peak grip force
- grip duration (T_{grip}) - time from grip start to grip release
- rise time (T_{rise}) – time from grip start to MVC
- Maximum EMG amplitude (aMVCe) – average rectified EMG amplitude over 0.5 seconds centered at MVC
- Grip force (GF) at 20-, 40-, 60-, and 80% time points
- EMG amplitude (EMGa) at 20-, 40-, 60-, and 80% time points

Spectral analysis metrcis:

- Peak frequency (f_{peak}) – Frequency where maximum PSD occurs
- Median frequency (f_{med}) – the frequency at which the PSD is divided equally on either side
- Mean Frequency (f_{mean}) – average frequency that is calculated as the sum of the product of the power and frequency at each frequency bin divided by the total power
- Total power ($SM0$) – sum of all spectra
- Mean power (S_{mean}) – Average power = SM0/length of Frequency bin
- Spectral moments – $SM1 = \sum_{j=1}^{M} P_j f_j$, $SM2 = \sum_{j=1}^{M} P_j {f_j}^2$, $SM3 = \sum_{j=1}^{M} P_j {f_j}^3$
- Spectral shape Lower band Power to higher band Power = $\frac{P_{lo}}{P_{hi}}$
- Power Spectrum ratio – Power at peak frequency (small bandwidth centered at Fpeak/Ptot
  - Variance of central frequency - $\frac{1}{S0}\sum_{j=1}^{M} P_j\left(f_j - f_{mean}\right)^2 = \frac{S2}{S0} - \left(\frac{S1}{S0}\right)^2$

Test 1: Analysis of hand grip test before and after OMT in controlled setting – case study

A healthy participant with MTP identified in the anterior forearm was treated with OMT to alleviate the MTP. Clinical therapeutic effect was considered alleviation of pain (verbal feedback from participant on scale of 0 to 3), and reduction of palpable nodule and softening of the taut band (subjectively evaluated by clinician). A sustained hand grip to voluntary fatigue was continuously measured with clench force bulb and sEMG. Raw data is shown in Figure 2 (a) and (b).

Grip force and sEMG amplitude (calculated using the average of 1 second intervals) was compared over. See Figure 2 (c) and (d). The spectrum and from the pre- and post-OMT data were compared, Figure 2 (e). The median frequency of the sEMG data in 1-second intervals throughouth the hand grip, were compared, Figure 2 (f).

Test 2: Clench force and sEMG Analysis on student lab data

Osteopathic principles and practice lab data was used to better understand metrics to use for evaluating MTP treatment with OMT. A convenience sample of 10 trials were selected based on increased hand grip duration after treatment, identified with visual inspection of raw data. Raw data of the 10 trials is shown in Figure 3. These trials were not under controlled conditions, rather they were conducted for the purpose of facilitating experiential learning in student lab to highlight the possibility of using objective measurement in showing treatment effect (Heath et al., 2014).

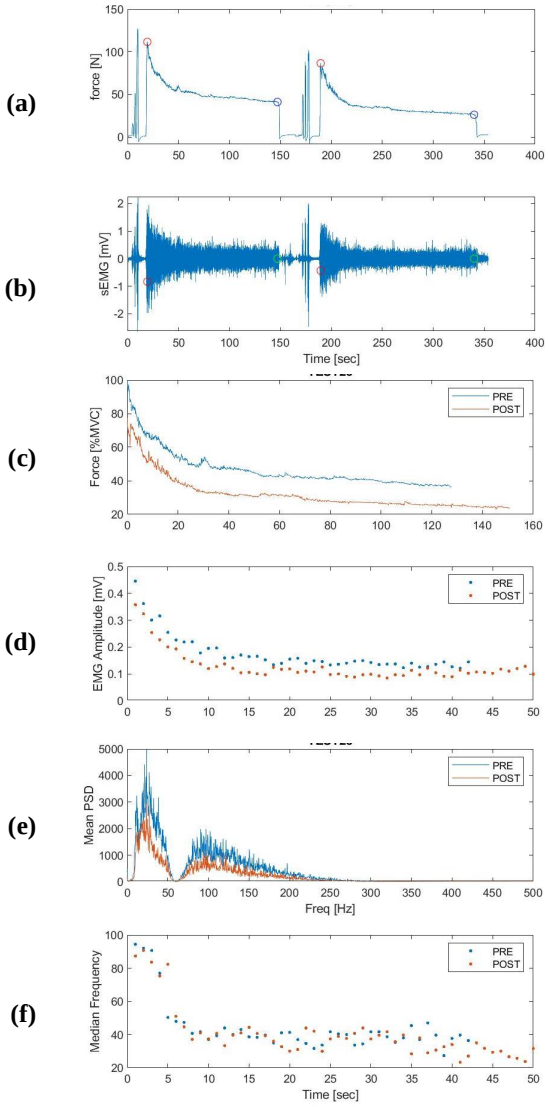

Figure 2: Hand grip test pre- (blue) and post-OMT (orange). Raw data (a) Clench force data (b)sEMG data, where max grip force (red circle) and grip relase (blue circle) are identified. (c) Comparison of pre- and post- grip force. (d) comparison of mean sEMG amplitude in 1 second intervals, x-axis shows time. (e) comparison of pre and post power spectral density. (f) median frequency calculated from 1 second intervals over time.

The rise time of the hand grip was determined as the time from the start and of the hand grip clench to the initial peak force, determined with first derivative and second derivative of clench force data. The duration of the hand grip was defined as the time between the peak force and grip release, where grip release was also determined with first and second derivative of the clench force data. The maximum voluntary contraction (MVC) was determined as the average peak force within 0.5 second, centered on the initial peak clench force. The sEMG amplitude of MVC was calculated as the average of the 0.5 seconds within the same time data time points as MVC. The group results of the 10 trials are shown in Figure 4. Data were normally distributed and compared with paired sample t-test.

Time trends were evaluated at 1-2 second intervals, centered at 20%, 40%, 60% and 80% time points. The time trend metrics included sEMG amplitude (emgAmp), hand grip force (gripforce), peak frequency (fpeak), mean frequency (fmean), median frequency (fmed), average power of the spectrum (Smean), total power (S0), spectral moments 1,2 and 3, (S1, S2, S3), spectral shape (Plohi) - low-to-high frequency band power ratio calculated as the ratio of the power in the low frequency band (10-55 Hz)to the high frequency band (75-250 Hz), power spectrum ratio (PSR), calculated as the peak spectrum divided by the total power (S0), and the variance of the central frequency, calculated as VCF = (S2./S0) - $(S1./S0)^2$. See Table 3

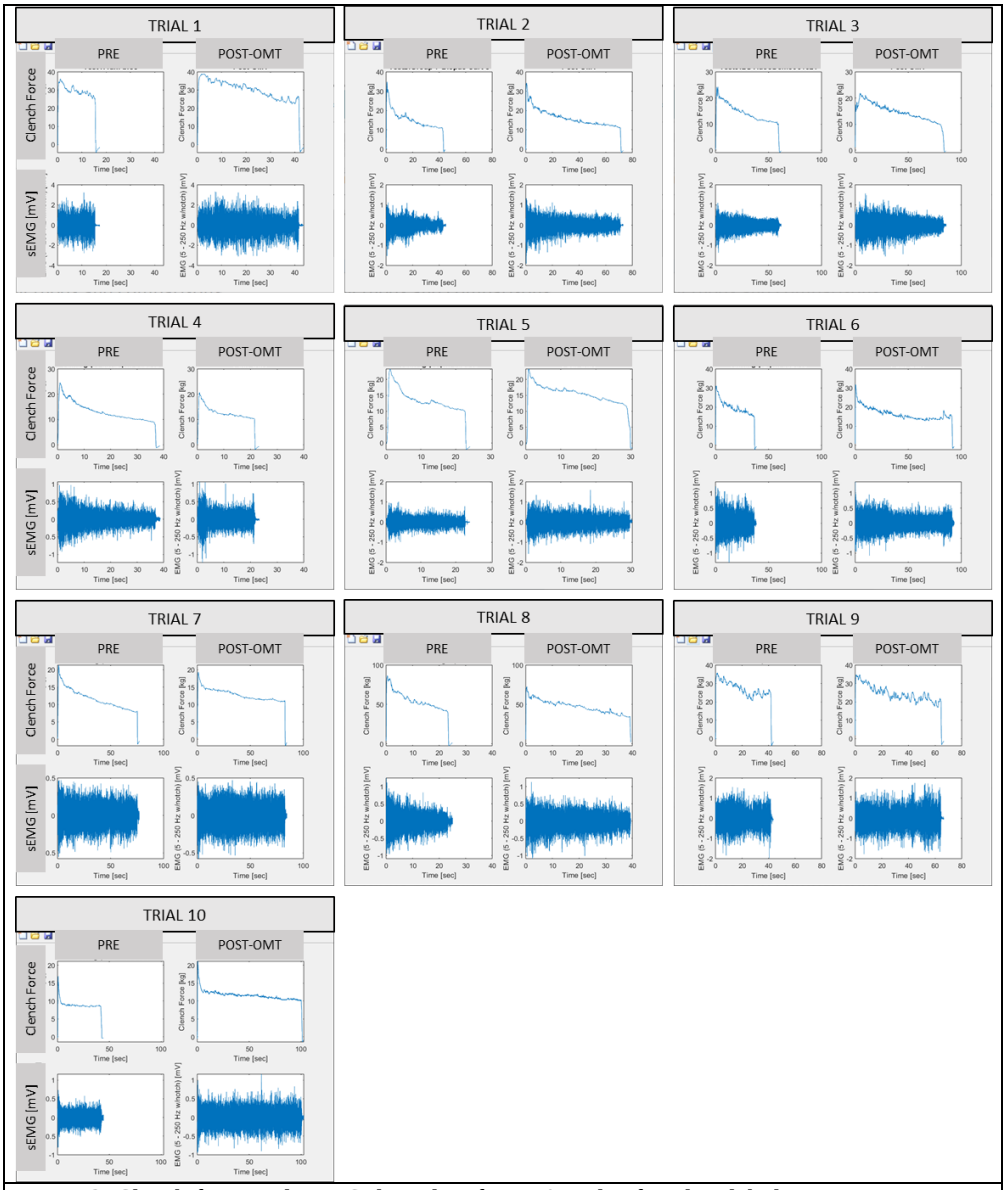

Figure 3: Clench force and sEMG data plots from 10 trails of student lab data

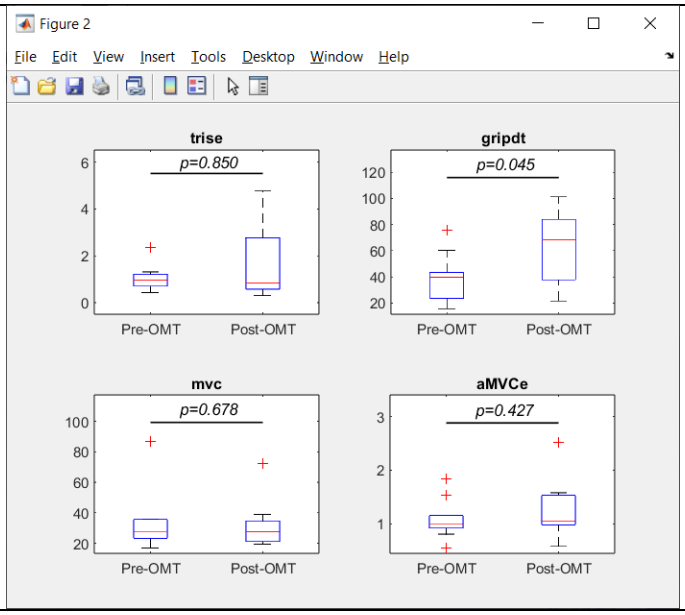

Figure 4: Comparison of hand grip metrics pre- and post-OMT: Rise time (trise), grip duration (gripdt), maximum voluntary contraction (MVC) and amplitude of MVC (aMVCe).

Table 2: Number of tests with increase or decrease in the hand grip metrics.

	trise	gripTime	MVC	aMVCe
increase	4	9	4	7
decrease	6	1	6	3

Table 3: Clench force and sEMG Results

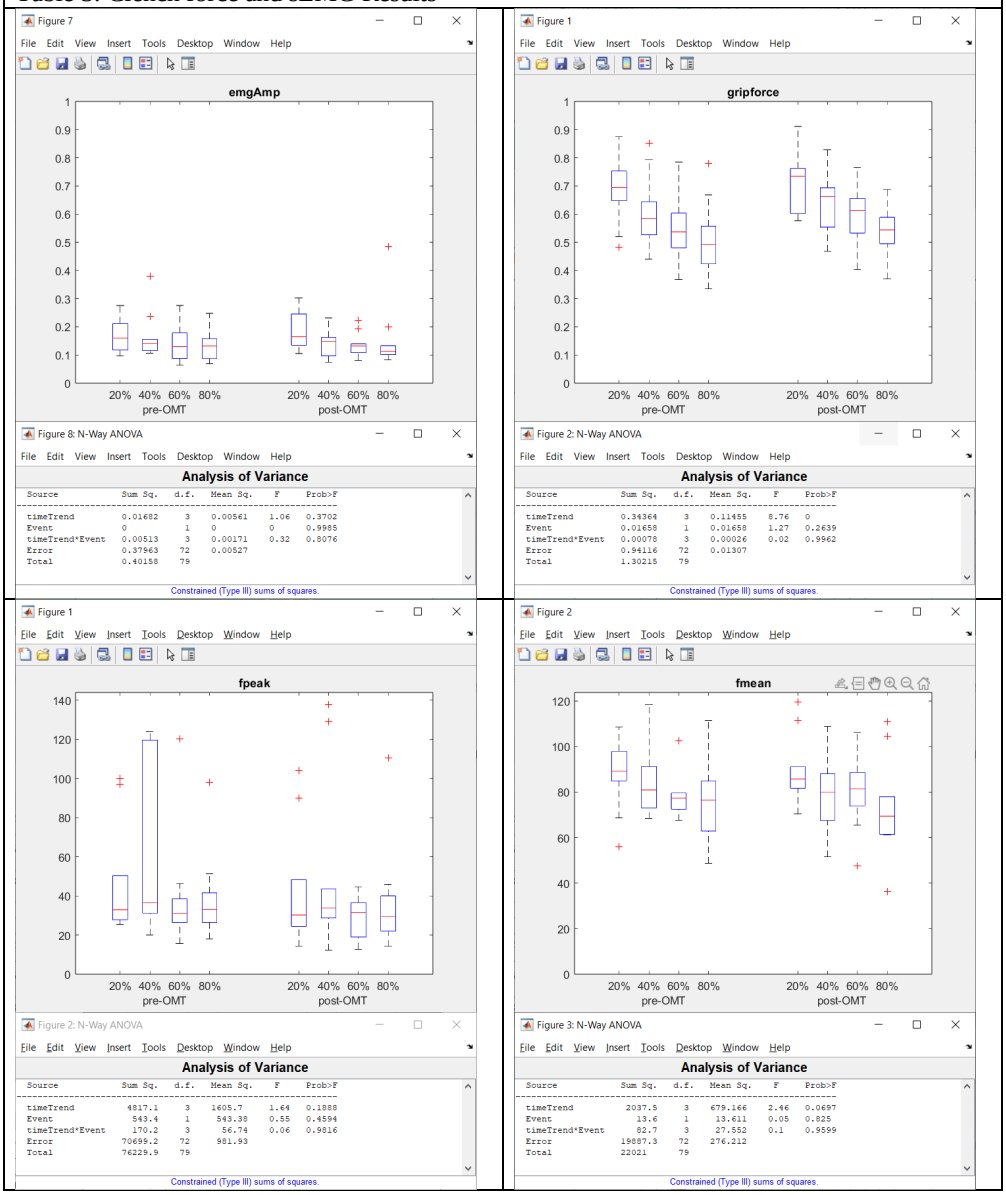

Table 3: Clench force and sEMG Results (cont.)

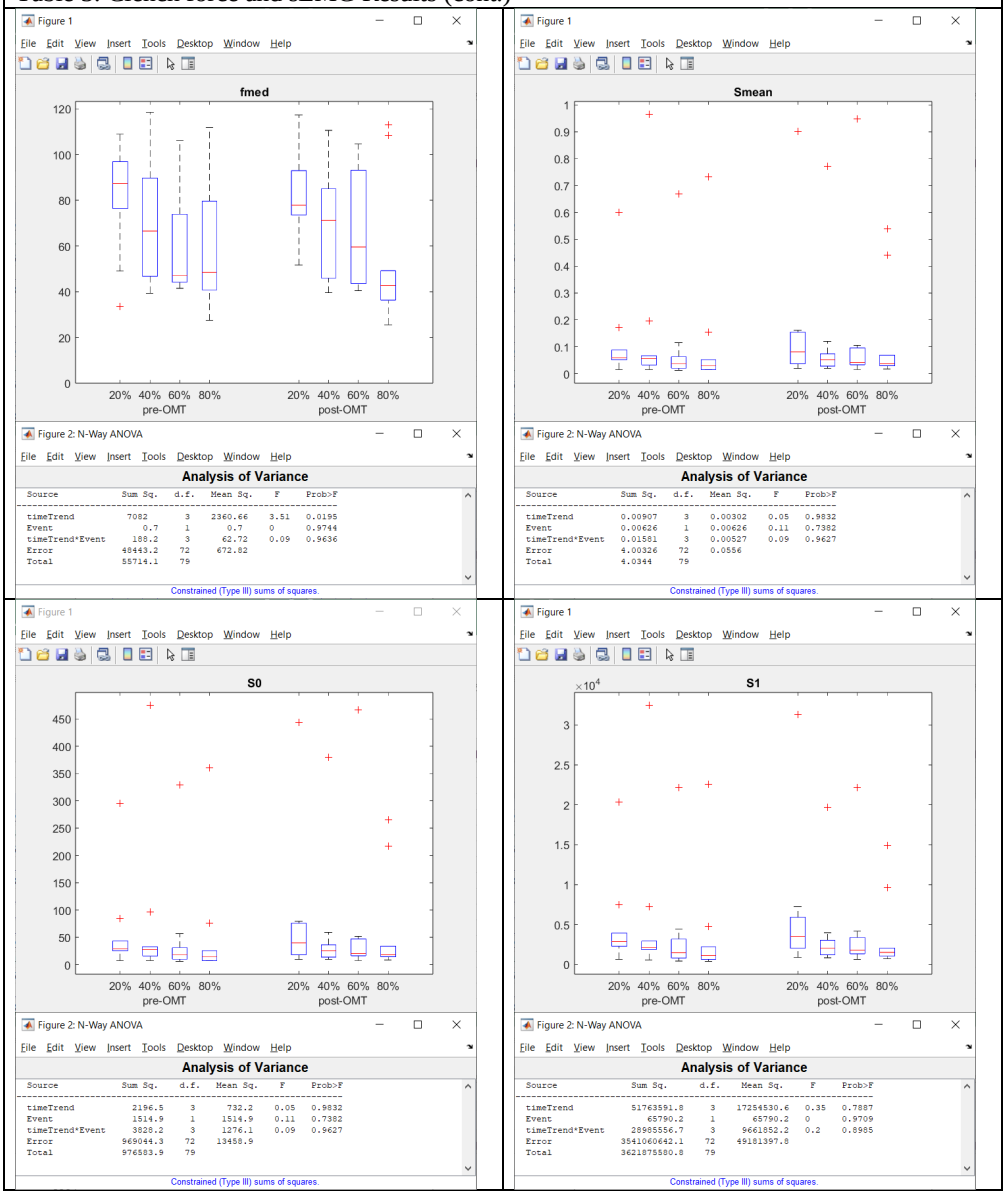

Table 3: Clench force and sEMG Results (cont.)

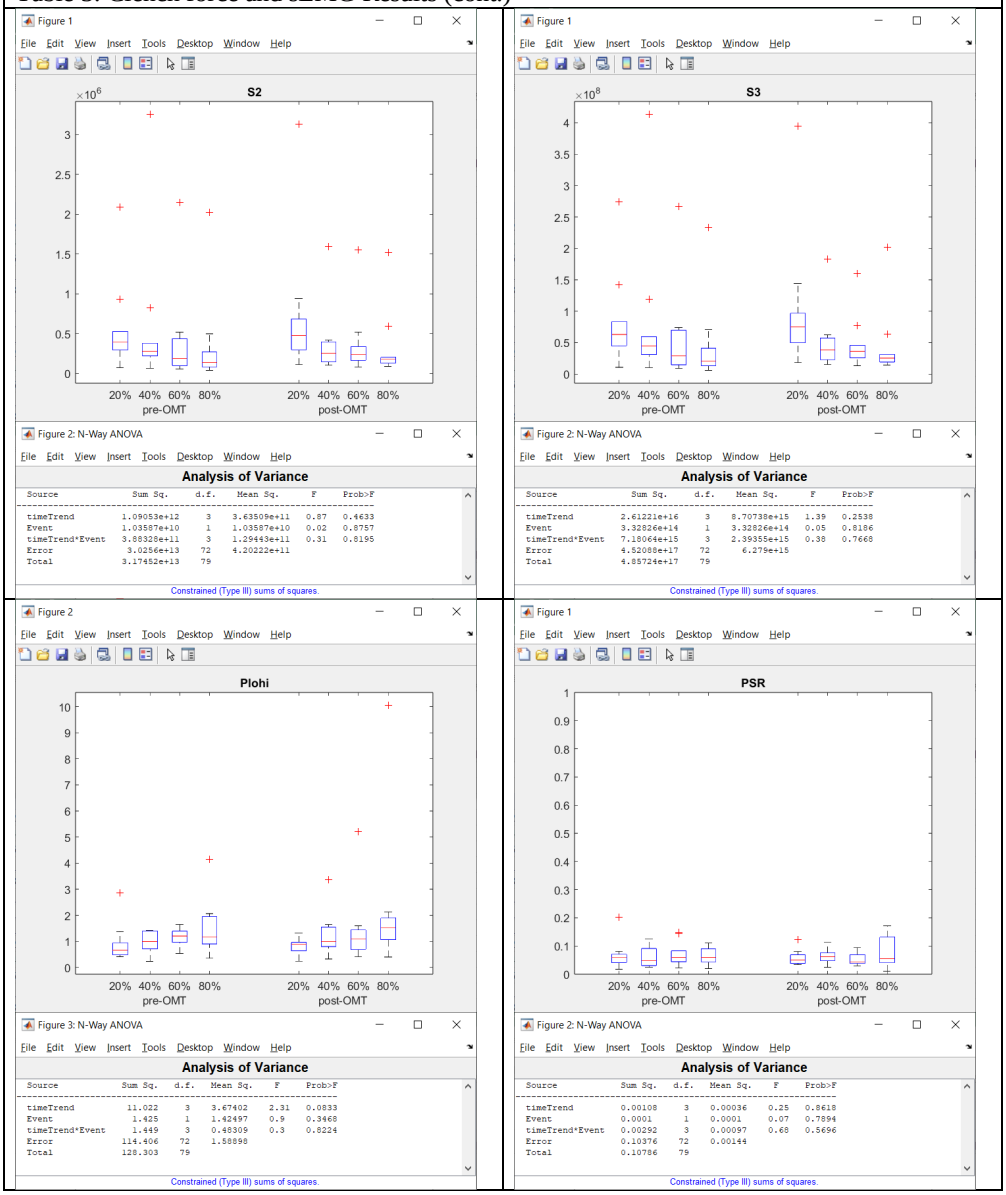

Table 3: Clench force and sEMG Results (cont.)

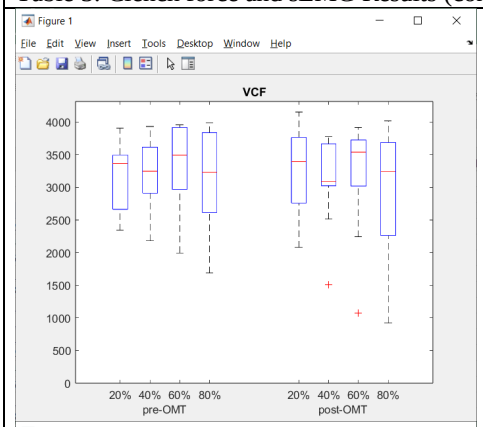

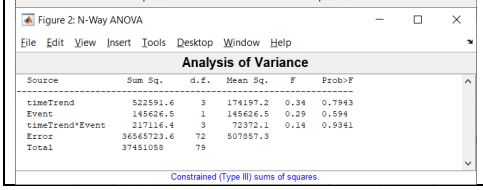

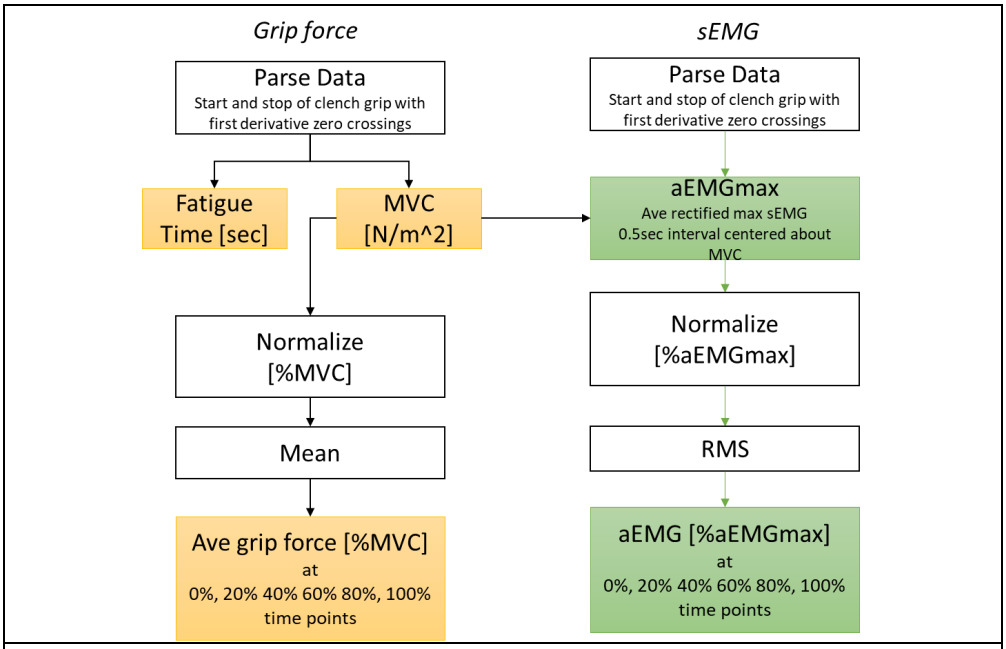

Figure 5: Flow diagram of grip force and sEMG time domain analysis.

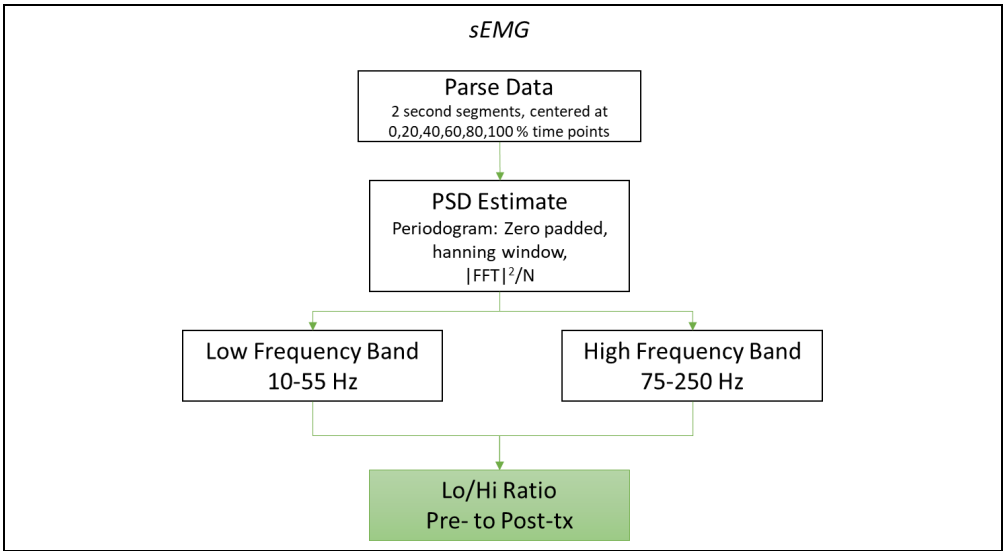

Figure 6: Flow diagram of sEMG spectral analysis.

Results

Test 1. Hand grip duration increased after OMT, but the force generated was lowered after OMT. The sEMG amplitude decreased during the post-OMT hand grip. The spectral content showed that the 60-Hz knotch filter removed a significant portion of data between 50-80 Hz. The median frequency trends were not visably different before and after OMT. As a result, the median frequency could not be assessed accurately. Differences in the median freqiency before and after OMT were not observed.

Test 2. Rise time, MVC and aMVCe were not statistically significant, while grip time was. The hand grip durations increased in the majority of trials. Table 2 shows that the 9 of the 10 participants had an increase in hand grip duration, and 7 had an increase in the MVC amplitude. 6 had a decrease in grip rise time and MVC. The time trends showed significant decreased in grip force ($p<<0.00001$), mean ($p=0.0697$) and median frequencies ($p=0.0195$) and the low-to-high spectral ratio ($p=0.08$) throughout the hand grip, before and after treatment.

The spectral shift detection improved by measuring at 20%, 40%, 60% and 80% time points. Differences in the spectral trends were found with mean, median frequency, however, because of the 60Hz knotch filter, they may not be accurate. The spectral shape metric, defined by the low-to-high spectral ratio excludes the missing data and provided a quantifiable spectral shift index. These data suggest that grip time and spectral shape may be metrics for evaluating changes in muscle activity induced with OMT.

Discussion

Myogenic activity of muscle tissue with MTP has been evaluated in the anterior forearm during a sustained hand grip, before and after OMT. This study demonstrated that changes in

myogenic activity after OMT were detectable and quantifiable with sEMG and clench force measurement. The data from two studies showed that muscles fatigued less after OMT, indicated by increased hand grip time and spectral shifting to a lesser extent. The two studies further suggest that fatigability may be a salient feature of muscle tissue with MTP, as compared to metrics of strength, i.e. grip force trend, maximum voluntary contraction. Strength of contraction was not found to be characteristic of MTP, perhaps due to the sample population being asymptomatic aside from the presence of MTP in the forearm.

Biomechanisms of altered muscle function in MTP.

Both studies indicated that muscle fatigue was affected more than muscle strength, suggesting that specific fiber types may be modulated with intervention. Type I, or slow twitch fibers contribute to muscle endurance, whereas Type-II, fast twitch fibers, contribute to force generation. Muscle fatigue is regularly investigated in exercise-physiology related literature. Interestingly, descriptions of MTP onset are similar to those of exercise on muscle tissue, i.e. hypercontracted regions with inflammation and shorter sarcomere lengths (Ge et al., 2011). Exercise mechanisms may help provide insight into changes in muscle tissues with MTP.

The mechanisms of muscle fatigue include metabolic, structural and energetic changes which arise from inefficient neural signal transmission and insufficient blood circulation (oxygen and nutrition supplies) (Cifrek et al., 2009). Sustained muscle contraction produces metabolic products such as lactic acid, the amount of which is dependent upon the level of force, contraction type (static or dynamic) duration of contraction and local blood supply (Cifrek et al., 2009). Intramuscular pressure from muscle contraction impede blood flow starting with at least 20% maximum voluntary contraction (MVC). Reduced and occluded blood flow impedes removal of metabolic byproducts, altering the pH. In exercise, this produces delayed onset

muscle soreness, which up until recently was not associated with structural changes of muscle fiber damage (Tenberg et al., 2022). With MTP, pH alterations are thought to be a result of alterations in muscle fiber structures. In MTP formation hypothesis, this hypoxic biochemical environment produces an energy crisis, whereby oxygen and nutrition are used up and not replenished although demand persists. Sustained muscle activation eventually results in local ischemia (Ge et al., 2011), wound healing mechanisms and inflammatory marker buildup within the area triggering nociceptors. Unresolved inflammation reduces muscle pain-threshold from increased algetic and cytokines in the muscle and blood, respectively (Ge et al., 2011). These changes ultimately damage the muscle cell membrane thereby increasing calcium and sodium ion influx to the point of overload. This overload is thought to contribute to spontaneous motor endplate activity in the resting muscle (Ge et al., 2011). In muscle tissue with MTP, muscle fiber supply of oxygen and nutrition are reduced, leading to hypoxia and ischemia (Ge & Arendt-Nielsen, 2011). This cascades into a cycle furthering cell damage. Additionally, co-activation of muscles occurs in local pain conditions with MTP (Ge et al., 2011). sEMG signal reflects such changes.

Conclusions

Myogenic activity in muscle tissue with MTP exhibit alterations from tissues after treatment. This study demonstrated that measures of muscle fatigue may be useful in describing characteristics of MTP and MTP treatment. These are readily measurable sEMG and clench force measurements, and described as an increased length of time of hand grip and less spectral shift towards lower frequencies. Muscle weakness is a characteristic feature of MTP, therefore it may be a useful metric in a more symptomatic population. Further controlled studies are needed

for evaluating these metrics for use in MTP research. The changes observed with sEMG may contribute to mechanistic understanding of MTP and MTP treatment.

References

Allison, G. T., & Fujiwara, T. (2002). The relationship between EMG median frequency and low frequency band amplitude changes at different levels of muscle capacity. *Clinical Biomechanics*, *17*(6), 464–469. https://doi.org/10.1016/S0268-0033(02)00033-5

Cifrek, M., Medved, V., Tonković, S., & Ostojić, S. (2009). Surface EMG based muscle fatigue evaluation in biomechanics. *Clinical Biomechanics*, *24*(4), 327–340. https://doi.org/10.1016/j.clinbiomech.2009.01.010

Corvini, G., & Conforto, S. (2022). A Simulation Study to Assess the Factors of Influence on Mean and Median Frequency of sEMG Signals during Muscle Fatigue. *Sensors*, *22*(17), 6360. https://doi.org/10.3390/s22176360

Fereira, O. A., & Satralkar, A. (2017). Effectiveness of Strain Counterstrain Technique and Neural Tissue Mobilisation on Cervicogenic Headache. *Indian Journal of Physiotherapy and Occupational Therapy - An International Journal*, *11*(3), 57. https://doi.org/10.5958/0973-5674.2017.00073.9

Gao, J., Caldwell, J., McLin, K., Zhang, M., & Park, D. (2020). Ultrasound Shear Wave Elastography to Assess Osteopathic Manipulative Treatment on the Iliocostalis Lumborum Muscle: A Feasibility Study. *Journal of Ultrasound in Medicine*, *39*(1), 157–164. https://doi.org/10.1002/jum.15092

Ge, H.-Y., & Arendt-Nielsen, L. (2011). Latent Myofascial Trigger Points. *Current Pain and Headache Reports*, *15*(5), 386–392. https://doi.org/10.1007/s11916-011-0210-6

Ge, H.-Y., Fernández-de-las-Peñas, C., & Yue, S.-W. (2011). Myofascial trigger points: Spontaneous electrical activity and its consequences for pain induction and propagation. *Chinese Medicine*, *6*(1), 13. https://doi.org/10.1186/1749-8546-6-13

Giamberardino, M. A., Affaitati, G., Fabrizio, A., & Costantini, R. (2011). Myofascial pain syndromes and their evaluation. *Best Practice & Research Clinical Rheumatology*, *25*(2), 185–198. https://doi.org/10.1016/j.berh.2011.01.002

Ginszt, M., Zieliński, G., Berger, M., Szkutnik, J., Bakalczuk, M., & Majcher, P. (2020). Acute Effect of the Compression Technique on the Electromyographic Activity of the Masticatory Muscles and Mouth Opening in Subjects with Active Myofascial Trigger Points. *Applied Sciences*, *10*(21), 7750. https://doi.org/10.3390/app10217750

Heath, D. M., S. Makin, I. R., Pedapati, C., & Kirsch, J. (2014). Use of Real-Time Physiologic Parameter Assessment to Augment Osteopathic Manipulative Treatment Training for First-Year Osteopathic Medical Students. *Journal of Osteopathic Medicine*, *114*(12), 918–919. https://doi.org/10.7556/jaoa.2014.179

Lucas, K. R. (2008). The impact of latent trigger points on regional muscle function. *Current Pain and Headache Reports*, *12*(5), 344–349. https://doi.org/10.1007/s11916-008-0058-6

Mehdikhani, R., Olyaei, G. R., Hadian, M. R., Talebian Moghadam, S., & Shadmehr, A. (2018). Evaluation of Electromyographic Activity of Upper Trapezius Muscle Fatigue in Patients with Latent Myofascial Trigger Point: A Randomized Control Trial. *Journal of Modern Rehabilitation*, 209–216. https://doi.org/10.32598/JMR.V12.N4.209

Nazmi, N., Abdul Rahman, M., Yamamoto, S.-I., Ahmad, S., Zamzuri, H., & Mazlan, S. (2016). A Review of Classification Techniques of EMG Signals during Isotonic and Isometric Contractions. *Sensors*, *16*(8), 1304. https://doi.org/10.3390/s16081304

Pérez-Bellmunt, A., Simon, M., López-de-Celis, C., Ortiz-Miguel, S., González-Rueda, V., & Fernandez-de-las-Peñas, C. (2021). Effects on Neuromuscular Function After Ischemic Compression in Latent Trigger Points in the Gastrocnemius Muscles: A Randomized

Within-Participant Clinical Trial. *Journal of Manipulative and Physiological Therapeutics*, S0161475420301561. https://doi.org/10.1016/j.jmpt.2020.07.015

Reaz, M. B. I., Hussain, M. S., & Mohd-Yasin, F. (2006). Techniques of EMG signal analysis: Detection, processing, classification and applications. *Biological Procedures Online*, *8*(1), 11–35. https://doi.org/10.1251/bpo115

Shah, J. P., & Gilliams, E. A. (2008). Uncovering the biochemical milieu of myofascial trigger points using in vivo microdialysis: An application of muscle pain concepts to myofascial pain syndrome. *Journal of Bodywork and Movement Therapies*, *12*(4), 371–384. https://doi.org/10.1016/j.jbmt.2008.06.006

Stulen, F. B., & De Luca, C. J. (1981). Frequency Parameters of the Myoelectric Signal as a Measure of Muscle Conduction Velocity. *IEEE Transactions on Biomedical Engineering*, *BME-28*(7), 515–523. https://doi.org/10.1109/TBME.1981.324738

Tenberg, S., Nosaka, K., & Wilke, J. (2022). The Relationship Between Acute Exercise-Induced Changes in Extramuscular Connective Tissue Thickness and Delayed Onset Muscle Soreness in Healthy Participants: A Randomized Controlled Crossover Trial. *Sports Medicine - Open*, *8*(1), 57. https://doi.org/10.1186/s40798-022-00446-7

Vigotsky, A. D., Halperin, I., Lehman, G. J., Trajano, G. S., & Vieira, T. M. (2018). Interpreting Signal Amplitudes in Surface Electromyography Studies in Sport and Rehabilitation Sciences. *Frontiers in Physiology*, *8*, 985. https://doi.org/10.3389/fphys.2017.00985

Yassierli, & Nussbaum, M. A. (2008). Utility of traditional and alternative EMG-based measures of fatigue during low-moderate level isometric efforts. *Journal of Electromyography and Kinesiology*, *18*(1), 44–53. https://doi.org/10.1016/j.jelekin.2006.08.003

APPENDIX D

HUMAN STUDY SUPPLEMENTAL

IRB Approval Letter

NOTICE of APPROVAL

DATE: 05-10-2022

TO: Chandhana Pedapati

FROM: ATSU, Arizona IRB Committee

SUBJECT: Approval, Protocol IRB Tracking (IRB #2022 -096)

Thank you for the opportunity to review the research proposal, *Effect of Osteopathic Manipulative Treatment in Forearm Muscles.* After reviewing the protocol and attachments, the ATSU, Arizona IRB committee believes that this proposal meets the minimal risk guidelines established by the A.T. Still University Institutional Review Board. Thank you for your time and attention to detail in completing the IRB proposal submission process. Please use the consent forms approved by the ATSU-Arizona IRB, and attached. You may now proceed with data collection.

If any changes are made to the protocol following this approval, you must complete and submit the Review of Changes Form located on the IRB website prior to implementing any changes. A Continuing Review Form reporting study progress is due in the IRB office four weeks prior to the anniversary of protocol approval (date 4 weeks prior to one year renewal date). A Final Report Form is due within 30 days of study completion. The Continuing Review, Final Report and Review of Changes forms are located on the IRB web site.

If you have any questions, please feel free to call or write.

Respectfully,

R Curtis Bay

Curt Bay, PhD
Chair, ATSU, Arizona Institutional Review Board
A.T. Still University
5850 East Still Circle
Mesa, AZ 85206
Main: (480) 219-6000
Office: (480) 219-6037
MesaIRB@atsu.edu

Study Flyer

PARTICIPANTS NEEDED FOR STUDY:

ULTRASOUND IMAGING TO OBSERVE EFFECT OF OSTEOPATHIC MANIPULATIVE TREATMENT ON THE FOREARM

Researchers in ATSU SOMA, are looking for adult volunteers to participate in a research study using ultrasound imaging.

What is this study about?

Researchers are developing a method for imaging the effects of manual therapy in the forearm.

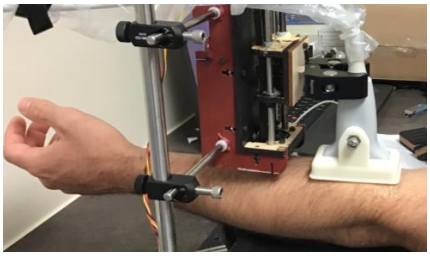

Why Participate?

You will advance our understanding of how manipulative procedures work to reduce muscle discomfort.

You may receive a forearm manipulative treatment.

You will contribute valuable information to advance manual therapy research.

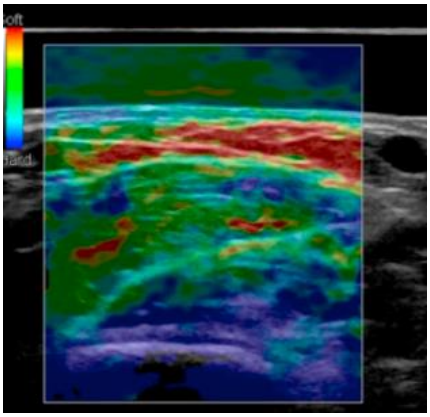

Who can participate?

Men and women aged 18 and up, with forearm pain & stiffness.

Able to attend a 1-hour session

Contact

Chandi Pedapati cpedapati@atsu.edu

Dr. Inder Makin imakin@atsu.edu

Consent Document

Study title	**Effect of osteopathic manipulative treatment in forearm muscles.**
Researcher	Chandhana Pedapati, MS, SOMA Inder Makin, MD, PhD, SOMA ASDOH Deborah Heath, DO, SOMA Tim Durr, OMS IV, SOMA Fellow James Keene, DO, SOMA

We are inviting you to participate in a research study. Participation is completely voluntary. If you agree to participate now, you can always change your mind later. There are no negative consequences, whatever you decide.

Overview

Purpose: The purpose of this study is to look at the effect of manual therapy on the forearm muscles. In this study we are going to use a new ultrasound imaging technique to observe the forearm tissue stiffness and blood flow. And we will compare these images to muscle activity in a simple hand grip fatigue test.

Procedures: In this study, the participant will undergo a clinical osteopathic exam of the forearms, perform a grip test, and be imaged by ultrasound. The experimental group will receive manipulative treatment, the control group will rest, and have no treatment, and the positive control group will perform light exercise (repetitive hand clenches on a soft tension ball) or have a thermal wrap on the forearm.

Time Commitment: The session will take up to 1 hour on one day.

Primary risks: The primary risk associated with this session includes being in close contact with a clinician, and two equipment operators.

Benefits: Participants may receive osteopathic manipulative treatment (OMT) treatment, regardless of which cohort they are randomly assigned to, if they elect to do so.

IRB # 2022-096 Approved

Valid 5/10/2022 to 5/09/2023

Official: R Curtis Bay

What is the purpose of this study?

We want to see if we can detect changes in muscle tissue stiffness and local blood flow in the forearm before and after osteopathic manipulative treatments (OMT). We will use ultrasound imaging and surface EMG to observe changes, if any. For this we have developed custom image processing techniques and built a fixture to hold the ultrasound probe for controlled imaging. We will also measure the muscle activity, in a hand grip fatigue test, before and after treatment. The ultrasound images and the muscle activity before and after treatment will be compared.

What will I do?

- In our lab:
  - We will take history regarding your forearm muscle, such as pain or tightness and activities.
  - We will palpate both of your forearms to identify and mark tight tissue areas, and you will rate your pain to light pressure. The arm with the higher pain score will be used in the rest of the session.
  - We will apply surface EMG stickers to your forearm, and photograph the markings and sensors on the arms.
  - You will perform hand grip test using a soft clench bulb.
  - We will image both of your forearms with ultrasound. Ultrasound gel will be applied. A photograph will be taken of the ultrasound location on your forearm for quality control when imaging is repeated post treatment.
  - You will be randomly selected to receive OMT treatment on the arm with higher rated pain and tightness or receive a warm wrap or rest in a seated position.
  - We will palpate your arm, and you will rate your pain to light pressure, once again.
  - We will re-image your arm again with ultrasound.
  - You will perform the hand grip test again.
  - All markings and gel will be cleaned off at the end of the session.
  - If you are part of the control groups, you will have the option to receive OMT of the forearm.

Risks

Possible risks	How we're minimizing these risks
Breach of confidentiality (your data being seen by someone who shouldn't have access to it)	• Data are de-identified to maintain confidentiality. All identifying information will be removed and replaced with a study ID. • We will store all electronic data on a password-protected, encrypted computer. • We will store all paper data in a locked filing cabinet in a locked office. • We will keep your identifying information separate from your research data, but we will be able to link it to you by using a study ID. We will destroy this link after we finish collecting and analyzing the data.

There may be risks we do not know about yet. Throughout the study, we will tell you if we learn anything that might affect your decision to continue participation.

Other Study Information

Possible benefits	• You may receive a clinical exam and OMT to treat any dysfunction. • Your participation will provide valuable insight in to the effects of OMT, with implications in tissue repair mechanisms and relationship to regional blood` flow.
Estimated number of participants	45
How long will it take?	The total time commitment is 1 hour.
Costs	No costs
Future research	De-identified (all identifying information removed) data may be shared with other researchers.
Recordings / Photographs	We will photograph your forearm only. The photographs will be used for quality checks and to visually record how data was acquired. The photography is necessary to this research. If you do not want to be photographed, you should not be in this study.

What if I am harmed because I was in this study?

If you are harmed from being in this study, please contact us. If it is an emergency, get help from 911 or your doctor right away and tell us afterward.

Confidentiality and Data Security

We will collect the following identifying information for the research: First name, last name, age, gender, date of session, history (any recent or past injury, any current or past pain or discomfort, any on-going functional complaints with forearm). This information is necessary for data management, treatment of dysfunction, and for comparing results.

Where will data be stored?	Any hard copies of paperwork will be stored in a locked cabinet in the research lab at ATSU. All electronic data will be stored on a dedicated ATSU laptop that is password protected, and backed up to an ATSU secured drive which is accessible only to members of the research team analyzing the data.
How long will it be kept?	This data will be kept for 3 years after the completion of the study.

Who can see my data?	**Why?**	**Type of data**
The researchers	To analyze the data.	Identifiable data including patient name with clinical notes including physical history; de-identified data including session notes regarding instrumentation, event timestamps and subject's response to OMT.
The IRB (Institutional Review Board) at ATSU The Office for Human Research Protections (OHRP) or other federal agencies	To ensure we're following laws and ethical guidelines	Same as above.
Anyone (public)	If we share our findings in publications or presentations	• Aggregate (grouped) data • De-identified (no names, birthdate, address, etc.)

Conflict of Interest

This study has no known conflict of interest.

Contact information:

For questions about the research	Chandhana Pedapati, MS	cpedapati@atsu.edu
For questions about your rights as a research participant	IRB (Institutional Review Board; provides ethics oversight)	480-219-6000/ mesairb@atsu.edu
For complaints or problems	Chandhana Pedapati, MS	cpedapati@atsu.edu
	IRB	480-219-6000 / mesairb@atsu.edu

Signatures

If you have had all your questions answered and would like to participate in this study, sign on the lines below. Remember, your participation is voluntary, and you are free to withdraw from the study at any time.

Name of Participant (print)

Signature of Participant Date

Signature of Parent, Guardian or Legally Authorized Representative Date

Name of Researcher obtaining consent (print)

Signature of Researcher obtaining consent Date

Intake Form

OMT on Forearm Study

Demographic and Health Questionnaire

Please complete the following questionnaire honestly and to the best of your ability.

Section 1:

Study ID: Today's Date:

Sex:

Age:

Are you currently taking pain medication (prescription or OTC within the past 48 hours)?

YES NO

If so, please describe: _____

Section 2:

Describe your type of work?

How would you rate your level of daily activity (including Work/Sports/Hobby), using the scale below? _____

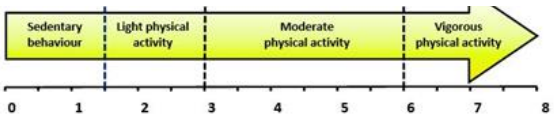

Section 3:

Do you have any pain in (circle areas of pain)?

THUMB FINGERS WRIST HAND FOREARM NECK UPPER BACK

If so, please describe:

Does this pain interfere with your daily activities?

Have you had any serious injury or surgery in your hand, arm, neck or upper back?

If so, what age did it occur? And what, if any treatment did you have?

Have you ever received manual therapies? Never One time A few times Regularly

If yes, how recently?

Examiner Notes:

Data Log

TEST ID **TEST** **DATE**

TEST#_YYYYMMDD

MTP Notes

Symptomatic Arm **R** **L**

Dominant Arm **R** **L**

Mark Location of MTP

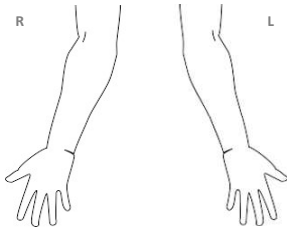

PPT	Pre Tx	Post Tx

DEPTH	

PROTOCOL

NOTES

1. PRE-INTERVENTION

Power Doppler Image

GainC PRF frames

Elastography Image

step size speed frames

Hand Grip Test

Digital Photo

2. Tx

GROUP	Control (No Tx)	Treatment (OMT)	+Control (Ex.)
duration:			

3. POST-INTERVENTION

Power Doppler Image

GainC PRF frames

Elastography Image

step size speed frames

Hand Grip Test

Digital Photo

Data Table

ID	GroupName	PPT_pre	PPT_post	TRpre	TRpost	TC_s_pre	TC_s_post
TEST02	OMT	0.645	1.456	0.024	0.027	1.39E-05	1.59E-05
TEST03	REST	1.470	1.474	0.025	0.015	2.46E-06	4.18E-06
TEST04	OMT	1.678	1.860	0.024	0.033	1.23E-06	2.18E-06
TEST05	Light Exercise	2.835	2.676	0.030	0.021	3.91E-06	5.49E-06
TEST06	REST	2.132	1.588	0.010	0.009	3.54E-06	4.68E-06
TEST07	REST	2.268	1.814	0.015	0.016	7.75E-06	9.72E-06
TEST08	OMT	0.363	0.726	0.043	0.016	1.58E-06	4.01E-06
TEST09	REST	1.588	1.474	0.021	0.036	1.33E-05	1.75E-05
TEST10	OMT	2.858	3.719	0.009	0.007	9.04E-06	1.22E-05
TEST11	REST	1.043	1.021	0.012	0.008	1.48E-06	3.25E-06
TEST12	OMT	2.132	2.291	0.011	0.006	5.96E-06	1.29E-05
TEST13	OMT	1.633	1.792	0.022	0.014	1.15E-06	2.15E-06
TEST14	OMT	1.610	1.769	0.007	0.009	5.63E-07	9.98E-07
TEST15	OMT	1.429	1.726	0.021	0.025	1.63E-06	2.63E-06
TEST16	REST	2.132	2.676	0.044	0.032	8.04E-07	1.86E-06
TEST19	REST	2.449	3.719	0.039	0.022	1.75E-06	3.81E-06
TEST20	REST	3.000	2.350	0.031	0.020	5.28E-06	7.08E-06
TEST21	OMT	1.247	3.266	0.023	0.019	2.94E-07	1.26E-06
TEST22	Light Exercise	2.835	2.381	0.020	0.022	1.99E-06	3.68E-06
TEST23	Light Exercise	2.268	2.268	0.019	0.024	5.20E-06	2.42E-06
TEST24	OMT	1.588	3.402	0.013	0.013	3.10E-06	4.27E-06
TEST25	OMT	1.021	1.814	0.027	0.042	1.89E-06	1.95E-06
TEST26	Light Exercise	1.701	1.406	0.016	0.006	1.47E-05	9.97E-06
TEST27	Light Exercise	1.361	1.270	0.029	0.021	4.94E-07	7.30E-07
TEST28	REST	0.907	0.771	0.017	0.038	2.88E-06	5.14E-06
TEST29	Light Exercise	2.223	2.313	0.029	0.021	7.85E-07	2.23E-06
TEST30	Light Exercise	1.270	2.268	0.029	0.020	5.71E-06	5.92E-06
TEST31	OMT	0.635	1.247	0.013	0.011	5.22E-06	6.67E-06
TEST32	OMT	0.953	2.359	0.017	0.036	2.90E-06	6.96E-06
TEST33	Light Exercise	1.361	1.678	0.014	0.017	1.03E-05	1.32E-05
TEST34	Light Exercise	1.247	1.315	0.008	0.023	8.50E-07	1.08E-06
TEST35	REST	0.544	2.676	0.022	0.022	5.37E-07	1.78E-06
TEST36	OMT	0.544	1.588	0.033	0.043	5.57E-06	6.02E-06
TEST37	Light Exercise	1.905	1.406	0.019	0.007	8.78E-06	7.60E-06

ID	GroupName	TC_d_pre	TC_d_post	maxPDI_pre	maxPDI_post	Area_pre	Area_post
TEST02	OMT	7.77E-07	1.25E-06	31.349	28.336	0.945	1.220
TEST03	REST	4.96E-06	6.44E-06	39.175	37.218	0.110	0.095
TEST04	OMT	1.45E-06	2.48E-06	44.638	94.774	0.751	1.379
TEST05	Light Exercise	5.48E-06	6.70E-06				
TEST06	REST	4.73E-06	7.16E-06	40.900	49.543	0.668	0.864
TEST07	REST	6.44E-06	1.09E-05	46.410	24.200	0.423	0.063
TEST08	OMT	9.68E-06	1.26E-05	54.402	40.381	0.497	0.864
TEST09	REST	4.93E-06	7.54E-06	45.504	46.070	0.795	0.874
TEST10	OMT	3.95E-05	4.84E-05	37.310	32.137	0.751	1.065
TEST11	REST	4.50E-06	8.44E-06	54.345	31.729	1.695	1.485
TEST12	OMT	2.56E-06	8.50E-06	39.650	31.577	0.610	0.107
TEST13	OMT	3.62E-06	4.52E-06	28.636	33.705	0.041	0.048
TEST14	OMT	6.33E-06	8.94E-06	47.541	46.045	2.137	1.996
TEST15	OMT	1.45E-06	3.24E-06	35.242	46.962	0.156	0.311
TEST16	REST	1.09E-06	2.74E-06	51.424	32.134	1.549	1.985
TEST19	REST	2.67E-06	3.97E-06	36.673	29.490	1.981	2.214
TEST20	REST	5.49E-06	6.81E-06	41.355	39.124	3.355	3.517
TEST21	OMT	7.47E-06	3.26E-06	34.933	34.067	0.991	2.129
TEST22	Light Exercise	2.61E-06	5.44E-06	42.865	43.231	0.718	1.774
TEST23	Light Exercise	1.35E-05	8.28E-06	44.668	53.036	0.901	0.876
TEST24	OMT	1.09E-06	5.52E-06	47.684	31.668	0.061	0.104
TEST25	OMT	9.25E-07	1.36E-06	40.553	41.745	0.825	1.880
TEST26	Light Exercise	2.96E-05	2.29E-05	33.260	45.213	0.498	1.103
TEST27	Light Exercise	4.00E-06	6.64E-06	44.731	42.514	1.347	0.087
TEST28	REST	1.17E-06	1.00E-06	37.060	40.250	1.398	1.322
TEST29	Light Exercise	1.75E-06	7.25E-06	34.894	33.846	1.381	1.180
TEST30	Light Exercise	4.13E-06	5.67E-06	53.168	53.521	1.111	1.061
TEST31	OMT	1.38E-05	1.38E-05	52.477	47.522	0.947	0.062
TEST32	OMT	1.16E-06	3.13E-06	33.550	54.602	0.679	1.039
TEST33	Light Exercise	5.70E-06	9.93E-06	49.643	40.913	1.910	1.528
TEST34	Light Exercise	7.58E-07	2.90E-06	56.480	32.944	0.046	0.035
TEST35	REST	1.14E-06	1.95E-06	35.742	34.194	0.734	1.037
TEST36	OMT	1.61E-06	1.85E-06	32.728	37.719	1.097	0.141
TEST37	Light Exercise	7.16E-06	6.05E-06	36.642	44.987	0.195	0.364

ID	GroupName	aPDI_pre	aPDI_post	GripTime_pre	GripTime_post	MVC_pre	MVC_post
TEST02	OMT	15.484	20.326	42.061	101.585	23161.180	25729.678
TEST03	REST	1.835	1.422	282.921	138.750	25635.665	34851.437
TEST04	OMT	12.718	36.050	205.628	220.850	46105.061	40968.064
TEST05	Light Exercise			48.978	141.825	33594.418	31971.127
TEST06	REST	10.610	15.012	28.246	24.155	45300.609	36120.796
TEST07	REST	6.027	0.864	165.918	58.955	35989.285	39960.183
TEST08	OMT	8.187	14.191	87.192	97.633	43672.693	40549.399
TEST09	REST	12.672	14.531	10.578	2.704	76030.116	84192.803
TEST10	OMT	12.495	17.842	27.781	24.352	20999.524	28237.552
TEST11	REST	31.331	26.913	36.777	52.754	47863.972	42367.385
TEST12	OMT	9.570	1.662	46.404	63.061	40737.412	33751.096
TEST13	OMT	0.658	0.705	125.116	326.408	48759.850	35937.907
TEST14	OMT	40.056	35.419	128.961	169.912	43277.148	42157.283
TEST15	OMT	2.430	4.902	20.415	15.705	48256.946	49726.127
TEST16	REST	26.524	34.272	26.918	31.941	41571.658	48557.973
TEST19	REST	36.111	40.051	90.767	158.902	27733.110	24311.871
TEST20	REST	73.152	77.847	45.780	40.704	43010.014	35926.096
TEST21	OMT	18.522	36.839	154.040	169.907	48425.439	47161.738
TEST22	Light Exercise	11.891	31.010	20.001	23.350	41097.007	46696.333
TEST23	Light Exercise	15.129	15.757	126.315	150.065	76504.271	60851.842
TEST24	OMT	0.971	1.493	48.653	102.856	108017.686	76116.937
TEST25	OMT	13.591	31.976	146.152	119.976	78598.110	62396.023
TEST26	Light Exercise	7.682	19.894	91.612	64.152	34688.093	37641.866
TEST27	Light Exercise	25.572	1.262	13.100	10.139	30889.283	29214.622
TEST28	REST	24.332	22.895	28.514	49.315	29786.366	20822.307
TEST29	Light Exercise	24.897	20.129	72.065	98.457	33182.953	27588.764
TEST30	Light Exercise	20.722	20.609	118.177	146.587	40160.019	24594.919
TEST31	OMT	18.522	0.918	21.736	31.456	50066.729	48864.672
TEST32	OMT	10.751	18.426	173.180	369.691	43183.147	27366.335
TEST33	Light Exercise	41.694	28.450	11.103	7.677	49238.632	45817.392
TEST34	Light Exercise	1.140	0.482	5.806	13.761	37960.353	36948.365
TEST35	REST	11.131	16.911	16.401	29.639	62571.711	59772.048
TEST36	OMT	18.466	2.039	18.294	40.843	28479.511	35707.265
TEST37	Light Exercise	3.067	5.863	65.672	128.962	37522.685	29493.560

ID	GroupName	aMVCe_pre	aMVC_post	aEMGend_pre	aEMGend_post	gripEnd_pre	gripEnd_post
TEST02	OMT	0.178	0.162	0.249	0.271	0.427	0.466
TEST03	REST	0.371	0.406	0.305	0.535	0.498	0.702
TEST04	OMT	0.208	0.191	0.469	0.558	0.375	0.415
TEST05	Light Exercise	0.270	0.261	0.520	0.393	0.498	0.351
TEST06	REST	0.339	0.224	0.777	0.863	0.848	0.759
TEST07	REST	0.402	0.325	0.443	0.193	0.245	0.166
TEST08	OMT	0.159	0.137	0.511	0.656	0.617	0.515
TEST09	REST	0.548	0.480				
TEST10	OMT	0.165	0.305	0.481	0.502	0.462	0.446
TEST11	REST	0.514	0.417	0.664	0.533	0.611	0.492
TEST12	OMT	0.404	0.311	0.685	0.627	0.626	0.535
TEST13	OMT	0.313	0.148	0.158	0.338	0.217	0.278
TEST14	OMT	0.342	0.283	0.415	0.375	0.428	0.425
TEST15	OMT	0.310	0.352				
TEST16	REST	0.157	0.250	0.948	0.764	0.737	0.686
TEST19	REST	0.198	0.155	0.741	0.749	0.550	0.496
TEST20	REST	0.254	0.263	0.748	0.942	0.693	0.734
TEST21	OMT	0.141	0.149	0.328	0.334	0.411	0.332
TEST22	Light Exercise	0.263	0.189				
TEST23	Light Exercise	0.398	0.288	0.145	0.192	0.211	0.288
TEST24	OMT	0.341	0.297	0.305	0.423	0.330	0.453
TEST25	OMT	0.393	0.307	0.657	0.660	0.634	0.597
TEST26	Light Exercise	0.166	0.169	0.363	0.669	0.403	0.364
TEST27	Light Exercise	0.141	0.119	0.504	0.662	0.658	0.584
TEST28	REST	0.212	0.122				
TEST29	Light Exercise	0.131	0.145	0.239	0.236	0.227	0.245
TEST30	Light Exercise	0.384	0.271	0.327	0.260	0.426	0.342
TEST31	OMT	0.184	0.185	0.533	0.605	0.614	0.583
TEST32	OMT	0.348	0.197	0.560	0.705	0.747	0.752
TEST33	Light Exercise	0.171	0.164				
TEST34	Light Exercise	0.163	0.122	0.739	0.725	0.608	0.538
TEST35	REST	0.217	0.213	0.366	0.568	0.393	0.596
TEST36	OMT	0.184	0.182	0.755	0.975	0.748	0.705
TEST37	Light Exercise	0.148	0.116	0.637	0.815	0.695	0.754

ID	GroupName	LoHiEnd_pre	LoHiEnd_post	PPT_ratio	TRratio	TC_sRatio	TC_dRatio
TEST02	OMT	0.904642072	0.587243127	2.256	1.159	1.147	1.608
TEST03	REST	0.757569809	0.611296052	1.003	0.601	1.702	1.299
TEST04	OMT	1.401322877	2.000349965	1.108	1.420	1.763	1.709
TEST05	Light Exercise	0.773740994	0.583865135	0.944	0.720	1.403	1.223
TEST06	REST	0.467126067	0.448455402	0.745	0.826	1.323	1.513
TEST07	REST	2.036576722	1.521642923	0.800	1.114	1.255	1.689
TEST08	OMT	0.536657798	0.596805496	2.000	0.368	2.534	1.298
TEST09	REST			0.929	1.689	1.316	1.528
TEST10	OMT	1.252979832	1.053006372	1.302	0.795	1.354	1.226
TEST11	REST	1.508084507	1.39900368	0.978	0.694	2.199	1.876
TEST12	OMT	1.06030553	0.828348479	1.074	0.562	2.161	3.325
TEST13	OMT	1.15132035	0.77732463	1.097	0.630	1.873	1.248
TEST14	OMT	1.816257342	1.303981594	1.099	1.187	1.771	1.413
TEST15	OMT			1.208	1.181	1.619	2.238
TEST16	REST	0.789121709	2.101235322	1.255	0.727	2.318	2.527
TEST19	REST	0.509034277	1.296668513	1.519	0.555	2.177	1.486
TEST20	REST	1.8956988	0.871346618	0.783	0.631	1.340	1.240
TEST21	OMT	0.507054809	0.49592441	2.618	0.841	4.278	0.437
TEST22	Light Exercise			0.840	1.095	1.847	2.084
TEST23	Light Exercise	0.785007138	0.720021843	1.000	1.298	0.467	0.612
TEST24	OMT	0.631304524	0.323797024	2.143	1.043	1.379	5.064
TEST25	OMT	1.313334719	0.856684211	1.778	1.547	1.031	1.466
TEST26	Light Exercise	0.430268469	0.390135409	0.827	0.351	0.679	0.773
TEST27	Light Exercise	0.632049661	0.620094432	0.933	0.726	1.478	1.659
TEST28	REST			0.850	2.193	1.782	0.859
TEST29	Light Exercise	0.602799112	0.918561499	1.041	0.726	2.846	4.147
TEST30	Light Exercise	0.994777367	0.550506435	1.786	0.671	1.037	1.373
TEST31	OMT	0.795507615	0.569327136	1.964	0.822	1.278	1.002
TEST32	OMT	1.758508589	1.359619392	2.476	2.123	2.398	2.701
TEST33	Light Exercise			1.233	1.202	1.282	1.744
TEST34	Light Exercise	0.593093262	0.344786952	1.055	2.831	1.271	3.830
TEST35	REST	0.649932175	1.313805382	4.917	0.997	3.307	1.700
TEST36	OMT	0.779335309	1.195264035	2.917	1.278	1.081	1.147
TEST37	Light Exercise	0.713204433	0.719920824	0.738	0.390	0.865	0.846

ID	GroupName	maxPDIratio	AreaRatio	aPDIratio	GripTimeRatio	MVC_ratio	aMVC_ratio
TEST02	OMT	0.904	1.291	1.429	2.415	1.111	0.913
TEST03	REST	0.950	0.867	0.913	0.490	1.359	1.094
TEST04	OMT	2.123	1.836	0.865	1.074	0.889	0.919
TEST05	Light Exercise				2.896	0.952	0.967
TEST06	REST	1.211	1.293	1.067	0.855	0.797	0.660
TEST07	REST	0.521	0.149	0.286	0.355	1.110	0.807
TEST08	OMT	0.742	1.738	2.342	1.120	0.928	0.864
TEST09	REST	1.012	1.099	1.086	0.256	1.107	0.876
TEST10	OMT	0.861	1.418	1.646	0.877	1.345	1.846
TEST11	REST	0.584	0.876	1.501	1.434	0.885	0.812
TEST12	OMT	0.796	0.175	0.220	1.359	0.829	0.769
TEST13	OMT	1.177	1.152	0.978	2.609	0.737	0.473
TEST14	OMT	0.969	0.934	0.964	1.318	0.974	0.828
TEST15	OMT	1.333	1.990	1.494	0.769	1.030	1.135
TEST16	REST	0.625	1.282	2.051	1.187	1.168	1.590
TEST19	REST	0.804	1.118	1.390	1.751	0.877	0.782
TEST20	REST	0.946	1.048	1.108	0.889	0.835	1.036
TEST21	OMT	0.975	2.149	2.203	1.103	0.974	1.057
TEST22	Light Exercise	1.009	2.470	2.449	1.167	1.136	0.720
TEST23	Light Exercise	1.187	0.972	0.819	1.188	0.795	0.723
TEST24	OMT	0.664	1.705	2.568	2.114	0.705	0.870
TEST25	OMT	1.029	2.278	2.213	0.821	0.794	0.781
TEST26	Light Exercise	1.359	2.216	1.630	0.700	1.085	1.018
TEST27	Light Exercise	0.950	0.064	0.068	0.774	0.946	0.842
TEST28	REST	1.086	0.946	0.871	1.730	0.699	0.576
TEST29	Light Exercise	0.970	0.855	0.881	1.366	0.831	1.100
TEST30	Light Exercise	1.007	0.955	0.949	1.240	0.612	0.706
TEST31	OMT	0.906	0.065	0.072	1.447	0.976	1.008
TEST32	OMT	1.627	1.530	0.940	2.135	0.634	0.566
TEST33	Light Exercise	0.824	0.800	0.970	0.691	0.931	0.955
TEST34	Light Exercise	0.583	0.770	1.321	2.370	0.973	0.748
TEST35	REST	0.957	1.412	1.476	1.807	0.955	0.985
TEST36	OMT	1.152	0.128	0.111	2.233	1.254	0.991
TEST37	Light Exercise	1.228	1.869	1.523	1.964	0.786	0.785

ID	GroupName	aEMGendRatio	gripEnd_ratio	LoHiEnd_ratio
TEST02	OMT	1.086	1.091	0.64914417
TEST03	REST	1.753	1.408	0.806917124
TEST04	OMT	1.189	1.107	1.427472567
TEST05	Light Exercise	0.756	0.704	0.754600235
TEST06	REST	1.110	0.896	0.960030779
TEST07	REST	0.435	0.678	0.747157181
TEST08	OMT	1.284	0.836	1.112078307
TEST09	REST			
TEST10	OMT	1.044	0.966	0.840401693
TEST11	REST	0.802	0.805	0.927669288
TEST12	OMT	0.915	0.855	0.781235649
TEST13	OMT	2.141	1.279	0.67515929
TEST14	OMT	0.904	0.994	0.717949799
TEST15	OMT			
TEST16	REST	0.806	0.931	2.662751889
TEST19	REST	1.010	0.901	2.547310805
TEST20	REST	1.259	1.059	0.45964402
TEST21	OMT	1.016	0.809	0.978048923
TEST22	Light Exercise			
TEST23	Light Exercise	1.326	1.369	0.917216937
TEST24	OMT	1.388	1.370	0.512901479
TEST25	OMT	1.004	0.942	0.652296935
TEST26	Light Exercise	1.844	0.903	0.906725539
TEST27	Light Exercise	1.314	0.888	0.981084985
TEST28	REST			
TEST29	Light Exercise	0.990	1.081	1.523826894
TEST30	Light Exercise	0.796	0.802	0.553396623
TEST31	OMT	1.135	0.951	0.715677794
TEST32	OMT	1.259	1.007	0.773166194
TEST33	Light Exercise			
TEST34	Light Exercise	0.982	0.884	0.581336821
TEST35	REST	1.553	1.515	2.02144998
TEST36	OMT	1.292	0.943	1.533696756
TEST37	Light Exercise	1.279	1.086	1.009417203

PCA 1: All groups

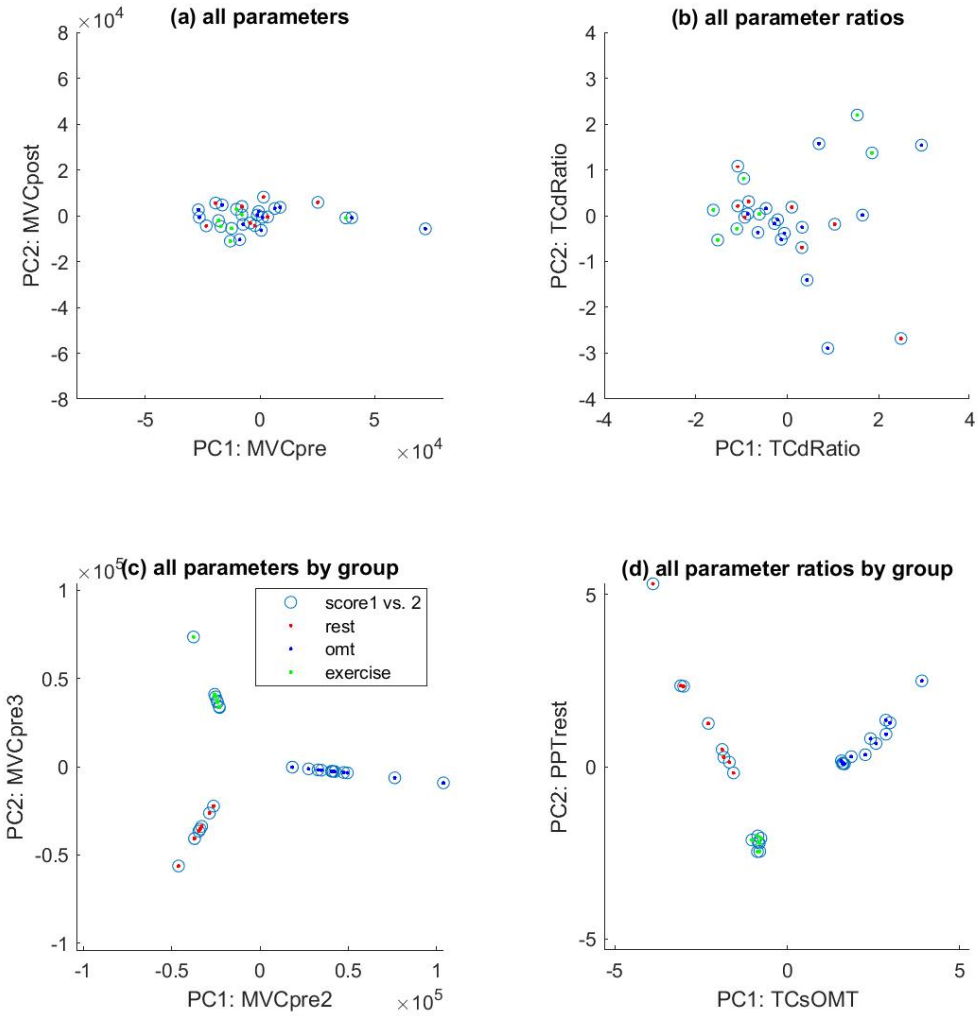

Figure D.1: Score plots of principal component analysis including all parameters from multi-modal analysis with (a) pre-intervention, post-intervention and post-/pre-ratios, (b) post-/pre- ratio only, (c) pre-, post-, and post-/pre- ratios by group, and post-/pre- ratios by group

PCA 2: By Group

Principal Component Analysis by group

The response of myofascial trigger points to osteopathic manipulative treatment (OMT) investigated in the anterior forearm. OMT intervention was compared with rest and exercise intervention. Four modalities were used to assess response before and after treatment – 1) pain pressure threshold of the trigger point measured with algometry, 2) Tissue stiffness (superficial and deep) measured with strain elastography, 3) regional blood flow measured with power Doppler ultrasound, and 4) spectral shape of electromyography signal in an sustained handgrip.

34 participants with myofascial trigger points in the forearm were randomly assigned to one of three intervention groups – 1) Rest, 2) OMT, and 3) light exercise (repetitive hand grip clenches).

Principal component analysis was used to assess the relationship of these parameters by group in 3 methods.

1) Pre and Post parameters only
2) Post/Pre Ratio parameters only
3) Pre, Post and Post/Pre Ratio parameters

Table 1 and 3, and Figures 1 and 3 show that there is very little variability beyond the principal components. All three groups have the same principal component, and nearly similar 2^{nd} and 3^{rd} component.

Table 2.1 shows that each intervention group had unique 1^{st}-4^{th} principal components, indicating that the variability is due to different parameters for Rest, OMT and Exercise groups. The first 4 components were responsible for only 82.6% of the variability in the OMT group, compared to more than 90% in the Rest and Exercise groups. This may indicate that the OMT group had a more variable response to intervention, compared to rest and exercise.

Figure 2.1 illustrates that variability across all three intervention groups is due to 1^{st} principal component.

1. Pre and Post Parameters

Table 1: PCA by group results including pre and post parameters,

Group	Principle Component #	Componenet	Coeff	Explained [%]	Explained Running total [%]
Rest	PC1	MVCpre	0.7508	91.46	91.46
	PC2	MVCpost	0.7508	8.54	100.00
	PC3	GripTime pre	0.9219	1.20E-03	100.00
	PC4	GripTime post	0.9628	3.36E-04	100.00
OMT	PC1	MVCpre	0.8561	97.42	97.42
	PC2	MVCpost	0.856	2.57	100.00
	PC3	GripTime post	0.7788	1.19E-03	100.00
	PC4	GripTime pre	0.6932	1.10E-04	100.00
Exercise	PC1	MVCpre	0.7929	94.48	94.48
	PC2	MVCpost	0.7929	5.52	100.00
	PC3	GripTime post	0.6653	5.19E-04	100.00
	PC4	GripTime post	-0.6502	6.90E-05	100.00

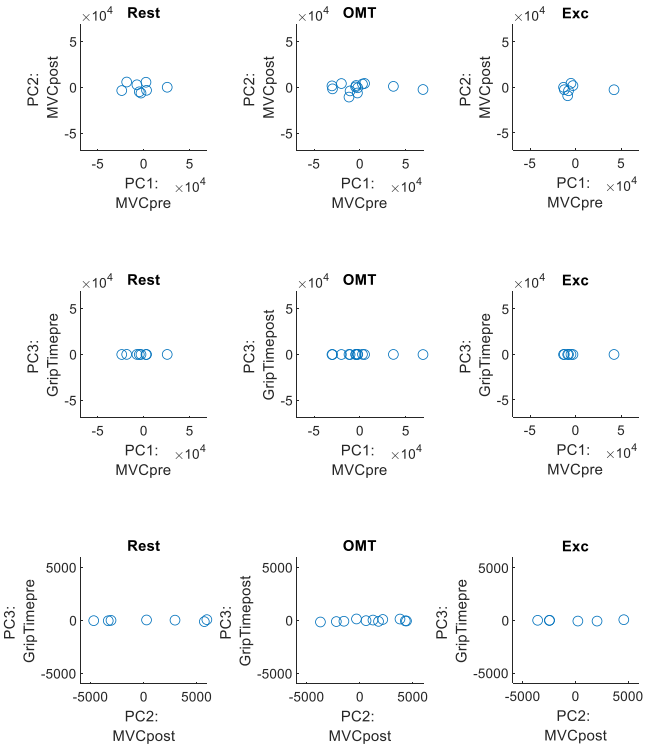

Figure 1: PCA scores plotted to visualize relationship of 1st to 2nd component (top row), 1st to 3rd component (middle row), and 2nd to 3rd component (bottom row), by intervention group.

2. Post/Pre Ratio Parameters

Table 2: Principal Component Analysis Results when evaluating each group separately, and including Post/Pre ratio of parameters.

Group	Principle Component #	Componenet	Coeff	Explained [%]	Explained Running total [%]
Rest	PC1	PPT_ratio	0.7711	63.99	63.99
	PC2	LoHiEnd_ratio	0.6245	18.45	82.44
	PC3	aEMGendRatio	0.5436	6.88	89.31
	PC4	GripTimeRatio	0.5461	4.25	93.56
OMT	PC1	TC_dRatio	0.9263	32.24	32.24
	PC2	aPDIratio	0.6729	27.88	60.11
	PC3	TC_sRatio	0.7054	12.14	72.25
	PC4	PPT_ratio	0.5831	10.32	82.57
Exercise	PC1	TC_dRatio	0.8238	59.95	59.95
	PC2	TRratio	0.6279	18.11	78.06
	PC3	AreaRatio	0.6715	14.12	92.18
	PC4	aEMGendRatio	0.5411	4.21	96.39

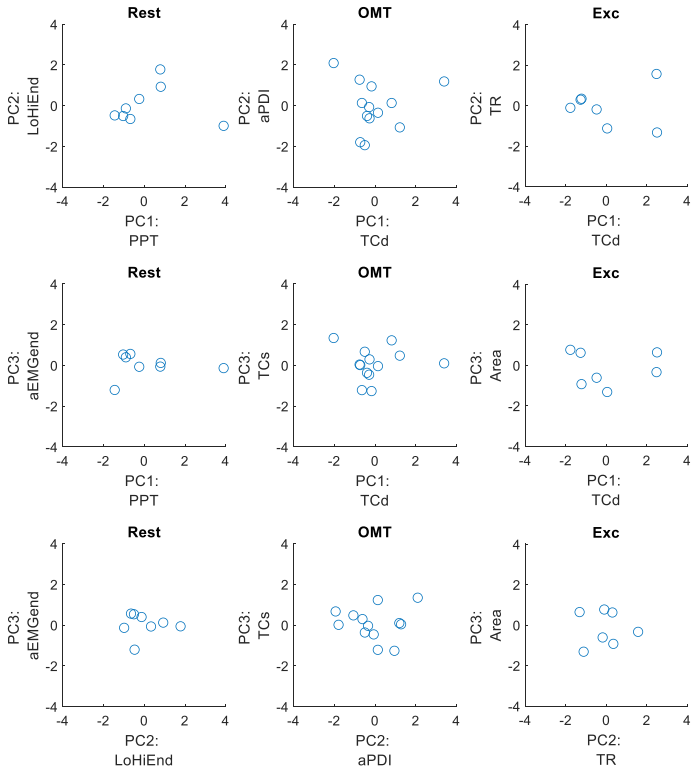

Figure 2: PCA scores plotted to visualize relationship of 1st to 2nd component (top row), 1st to 3rd component (middle row), and 2nd to 3rd component (bottom row), by intervention group.

3. Pre, Post and Post/Pre Ratio Parameters

Table 3: : Principal Component Analysis Results when evaluating each group separately, and including Pre, Post and Post/Pre ratio of parameters.

Group	Principle Component #	Componenet	Coeff	Explained [%]	Explained Running total [%]
Rest	PC1	MVCpre	0.7508	91.46	91.46
	PC2	MVCpost	0.7508	8.54	100.00
	PC3	GripTime pre	0.9219	0.00	100.00
	PC4	GripTime post	0.9621	0.00	100.00
OMT	PC1	MVCpre	0.8561	97.42	97.42
	PC2	MVCpost	0.856	2.57	100.00
	PC3	GripTime post	0.7787	0.00	100.00
	PC4	GripTime pre	0.693	0.00	100.00
Exercise	PC1	MVCpre	0.7929	94.48	94.48
	PC2	MVCpost	0.7929	5.52	100.00
	PC3	GripTime post	0.7132	0.00	100.00
	PC4	GripTime post	-0.6497	0.00	100.00

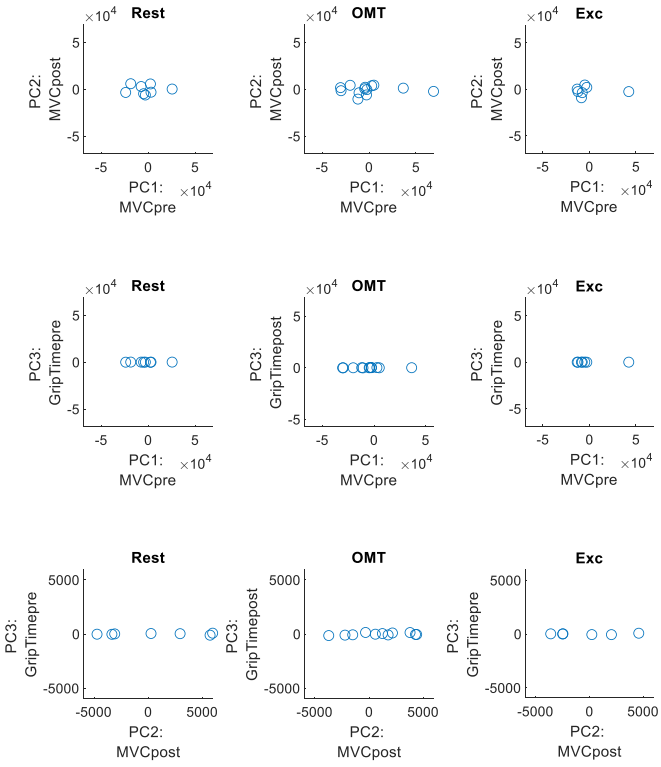

Figure 3: PCA scores plotted to visualize relationship of 1st to 2nd component (top row), 1st to 3rd component (middle row), and 2nd to 3rd component (bottom row), by intervention group.

PCA 2 Coefficients

		PC1	PC2	PC3	PC4
REST	PPT	**0.7711**	**-0.4650**	-0.2235	-0.0428
	TR	0.0065	-0.0965	-0.2869	0.1047
	TCs	**0.3890**	0.0847	-0.0253	-0.0957
	TCd	0.0723	0.3128	-0.2663	**-0.3508**
	maxPDI	0.0108	-0.1071	0.2906	0.1190
	Area	0.1407	0.0973	**0.4619**	0.0976
	aPDI	0.1711	**0.3657**	0.3354	-0.0986
	GripTime	0.2493	0.1766	0.1353	**0.5461**
	MVC	-0.0067	0.0033	-0.0473	-0.3804
	aMVC	0.0405	0.1454	0.0595	**-0.5175**
	aEMGend	0.0900	-0.2217	**0.5436**	-0.2184
	gripEnd	0.1008	-0.1529	0.2401	-0.2419
	LoHiEnd	**0.3428**	**0.6245**	-0.0926	0.0672
OMT	PPT	-0.0306	0.0791	**0.4490**	**0.5831**
	TR	0.0652	-0.0063	0.0328	0.3486
	TCs	-0.2517	**0.4104**	**0.7054**	**-0.4633**
	TCd	**0.9263**	0.1058	0.1287	-0.2245
	maxPDI	-0.0456	-0.0397	0.0407	0.0755
	Area	-0.0293	**0.5643**	-0.1869	0.2116
	aPDI	0.0775	**0.6729**	-0.2304	0.2033
	GripTime	**0.1877**	-0.1897	0.3814	0.4045
	MVC	-0.0794	-0.0493	-0.0747	0.0385
	aMVC	-0.0696	0.0172	-0.1782	-0.0336
	aEMGend	0.0318	-0.0232	0.0797	0.1016
	gripEnd	0.0805	-0.0044	-0.0252	0.0636
	LoHiEnd	-0.1027	-0.0458	0.0609	0.0312
Exercise	PPT	0.0258	-0.0135	-0.1422	**-0.5317**
	TR	0.2937	**0.6279**	**-0.3094**	**0.3196**
	TCs	**0.3490**	**-0.4519**	0.2183	-0.1232
	TCd	**0.8238**	-0.0446	0.2303	0.1049
	maxPDI	-0.1202	-0.0800	0.0988	0.0678
	Area	-0.2241	0.1970	**0.6715**	0.0198
	aPDI	-0.0595	0.3211	**0.5060**	-0.0975
	GripTime	0.1663	0.4344	0.1402	**-0.3715**
	MVC	0.0049	0.0211	0.0494	0.2694
	aMVC	0.0201	-0.0930	0.1136	0.1319
	aEMGend	-0.1193	-0.0243	0.0935	**0.5411**
	gripEnd	-0.0198	0.0031	-0.0101	0.1215
	LoHiEnd	0.0406	-0.2295	0.1510	0.1973

Figure D.2: PCA coefficients, highest correlations are in red bold font, and next highest correlations are in bold font.